

NASA/CR-2002-211428



Health Monitoring for Airframe Structural Characterization

*Thomas E. Munns, Renee M. Kent, and Antony Bartolini
ARINC, Inc., Annapolis, Maryland*

*Charles B. Gause, Jason W. Borinski, Jason Dietz, Jennifer L. Elster, Clark Boyd, Larry Vicari,
and Kevin Cooper
Luna Innovations, Blacksburg, Virginia*

*Asok Ray, Eric Keller, Vadlamani Venkata, and S. C. Sastry
The Pennsylvania State University, University Park, Pennsylvania*

February 2002

The NASA STI Program Office . . . in Profile

Since its founding, NASA has been dedicated to the advancement of aeronautics and space science. The NASA Scientific and Technical Information (STI) Program Office plays a key part in helping NASA maintain this important role.

The NASA STI Program Office is operated by Langley Research Center, the lead center for NASA's scientific and technical information. The NASA STI Program Office provides access to the NASA STI Database, the largest collection of aeronautical and space science STI in the world. The Program Office is also NASA's institutional mechanism for disseminating the results of its research and development activities. These results are published by NASA in the NASA STI Report Series, which includes the following report types:

- TECHNICAL PUBLICATION. Reports of completed research or a major significant phase of research that present the results of NASA programs and include extensive data or theoretical analysis. Includes compilations of significant scientific and technical data and information deemed to be of continuing reference value. NASA counterpart of peer-reviewed formal professional papers, but having less stringent limitations on manuscript length and extent of graphic presentations.
- TECHNICAL MEMORANDUM. Scientific and technical findings that are preliminary or of specialized interest, e.g., quick release reports, working papers, and bibliographies that contain minimal annotation. Does not contain extensive analysis.
- CONTRACTOR REPORT. Scientific and technical findings by NASA-sponsored contractors and grantees.
- CONFERENCE PUBLICATION. Collected papers from scientific and technical conferences, symposia, seminars, or other meetings sponsored or co-sponsored by NASA.
- SPECIAL PUBLICATION. Scientific, technical, or historical information from NASA programs, projects, and missions, often concerned with subjects having substantial public interest.
- TECHNICAL TRANSLATION. English-language translations of foreign scientific and technical material pertinent to NASA's mission.

Specialized services that complement the STI Program Office's diverse offerings include creating custom thesauri, building customized databases, organizing and publishing research results . . . even providing videos.

For more information about the NASA STI Program Office, see the following:

- Access the NASA STI Program Home Page at <http://www.sti.nasa.gov>
- Email your question via the Internet to help@sti.nasa.gov
- Fax your question to the NASA STI Help Desk at (301) 621-0134
- Telephone the NASA STI Help Desk at (301) 621-0390
- Write to:
NASA STI Help Desk
NASA Center for AeroSpace Information
7121 Standard Drive
Hanover, MD 21076-1320

NASA/CR-2002-211428



Health Monitoring for Airframe Structural Characterization

*Thomas E. Munns, Renee M. Kent, and Antony Bartolini
ARINC, Inc., Annapolis, Maryland*

*Charles B. Gause, Jason W. Borinski, Jason Dietz, Jennifer L. Elster, Clark Boyd, Larry Vicari,
and Kevin Cooper
Luna Innovations, Blacksburg, Virginia*

*Asok Ray, Eric Keller, Vadlamani Venkata, and S. C. Sastry
The Pennsylvania State University, University Park, Pennsylvania*

National Aeronautics and
Space Administration

Langley Research Center
Hampton, Virginia 23681-2199

Prepared for Langley Research Center
under Cooperative Agreement NCC1-332

February 2002

Available from:

NASA Center for AeroSpace Information (CASI)
7121 Standard Drive
Hanover, MD 21076-1320
(301) 621-0390

National Technical Information Service (NTIS)
5285 Port Royal Road
Springfield, VA 22161-2171
(703) 605-6000

EXECUTIVE SUMMARY

Structural health monitoring (SHM) is a critical consideration for overall condition monitoring of aircraft systems. SHM of airframes for the identification and characterization of structural degradation presents unique challenges. Traditionally, off-line diagnostic models based on a statistical analysis of material degradation, operating history, and anticipated perturbations in the flight profile have been used to characterize airframe structures. Based on these analyses, a rigorous schedule of inspection and maintenance actions is established to maintain the aircraft in an airworthy condition. However, these existing diagnostic modeling techniques cannot elucidate the condition of individual aircraft. Sensing and characterization of structural condition for specific components of individual aircraft is required to meet the goals of NASA's Single Aircraft Accident Prevention (SAAP) program.

The purpose of this project was to develop a multiplexed airframe structural sensor prototype for on-board characterization of multiple and synergistic failure modes in current and future airframes and to demonstrate the technologies in a laboratory setting. Specifically, the purpose of this study was to establish requirements for structural health monitoring systems, identify and characterize a prototype structural sensor system, develop sensor interpretation algorithms, and demonstrate the sensor systems on operationally realistic test articles. The structural sensing system was designed to provide data sources for ARINC's Aircraft Condition Analysis and Management System (ACAMS), which was developed in a complementary program.

The purpose of introducing SHM into commercial transports is to enhance aviation safety by improving the effectiveness of the operator's continued airworthiness programs. The primary consideration for assessing the effect of SHM systems on continued airworthiness is to determine their potential influence on scheduled maintenance programs and the potential to reduce unscheduled maintenance actions. SHM systems could be an important factor in improving the effectiveness of inspection and maintenance programs and enabling on-condition maintenance. Ultimately, these improvements would increase air carrier profitability by reducing maintenance program costs and increasing aircraft availability.

An important area of emphasis of this project was on sensors to detect aging mechanisms for metallic airframe structures. An understanding of potential damage mechanisms, structural design criteria and fail-safe features, structural maintenance philosophy was needed to assess the efficacy of sensor-based system to monitor structural condition. The structural degradation modes for commercial transport aircraft include low-cycle fatigue (including widespread fatigue damage), high-cycle fatigue, corrosion (and stress corrosion cracking), and accidental damage. The sensor system evaluation and sensor development tasks of this project focused on the principal long-term aging mechanisms for metallic transport aircraft structures—low-cycle fatigue and corrosion.

An array of multiple sensor types will be required to monitor damage events, corrosion and environmental deterioration, and fatigue. This program focused on fiber optic sensors. The selected sensors were evaluated to validate their suitability for monitoring aging degradation; characterize the sensor performance in aircraft environments; and demonstrate placement processes and multiplexing schemes. Corrosion sensors (i.e., moisture and metal ion sensors) and fatigue sensors (i.e., strain and acoustic emission sensors) were developed and evaluated under this program. In addition, a unique micromachined multimeasurand sensor concept was developed and demonstrated. The results show that structural degradation of aircraft materials could be effectively detected and characterized using available and emerging sensors.

A key component of the structural health monitoring capability is the ability to interpret the information provided by sensor system in order to characterize the structural condition. Novel deterministic and stochastic fatigue damage development and growth models have been developed for this program. These models enable real time characterization and assessment of structural fatigue damage.

The goals for implementing SHM systems are to improve aircraft safety and reduce operational and maintenance costs. ARINC recommends that, based on these promising initial results, the development of SHM technology as a key element of an integrated vehicle health management capability should be continued.

ABBREVIATIONS AND ACRONYMS

ACAMS	Aircraft Condition Analysis and Management System
AE	acoustic emission
AFM	atomic force microscopy (AFM)
ARMA	autoregressive moving average
CCD	charged-coupled device
CMC	Carboxymethylcellulose
CMR	certification maintenance requirement
CMV	Continuous maintenance visits
CPC	corrosion preventive compounds
DSB	distributed feedback
EDM	electrostatic discharge machined
EFPI	extrinsic Fabry-Perot interferometry
FAA	Federal Aviation Administration
FAR	federal aviation regulation
FFT	fast Fourier transform
FOQA	flight operations quality assurance
GDM	Gap division multiplexing
HCF	high-cycle fatigue
K-L	Karhunen-Loève
LCF	low-cycle fatigue
LPG	long period grating
MPD	maintenance process data
MSG	maintenance steering group
NASA	National Aeronautics and Space Administration
PEO	poly (ethylene oxide)
PDF	probability density function
SAAP	Single Aircraft Accident Prevention
SCC	stress corrosion cracking
SHM	structural health monitoring

UVa University of Virginia

WDM wavelength division multiplexing

WFD widespread fatigue damage

CONTENTS

INTRODUCTION	1
1.0 BACKGROUND	1
1.1 PURPOSE.....	2
1.2 SCOPE AND APPROACH.....	2
IMPLEMENTATION REQUIREMENTS ANALYSIS.....	4
2.0 INTRODUCTION.....	4
2.1 AIRLINE MAINTENANCE PROGRAMS.....	5
2.1.1 New Aircraft Models (MSG Process)	7
2.1.2 Maintenance Program Implementation	8
2.1.3 Program Review and Reliability Tracking.....	9
2.2 STRUCTURAL DEGRADATION MODES.....	10
2.2.1 Fatigue.....	11
2.2.2 Environmental Damage.....	14
2.2.3 Accidental Damage	15
2.3 INTEGRATION AND UTILIZATION CONSIDERATIONS	16
2.4 DISCUSSION	17
SENSOR SYSTEM DEVELOPMENT AND BASELINE CHARACTERIZATION	19
3.0 INTRODUCTION.....	19
3.1 FATIGUE SENSING.....	20
3.1.1 Bragg Grating Sensors.....	20
3.1.2 EFPI Sensors	21
3.2 CORROSION SENSING	28
3.2.1 LPG Moisture and Humidity Sensors	30
3.2.2 LPG Metal Ion Sensor.....	33
3.3 COMBINED FAILURE MODES	35
3.4 ACCIDENTAL DAMAGE	39
SENSOR DEMONSTRATION AND EVALUATION.....	40

4.0	INTRODUCTION.....	40
4.1	CORROSION SENSOR TESTING.....	40
4.1.1	Simulated Lap Splice Testing.....	40
4.1.2	Sensor Performance under Coatings.....	44
4.2	FATIGUE SENSOR TESTING.....	51
4.2.1	Fiber Bragg Grating Sensors.....	51
4.2.2	EFPI Strain and Extensometer Sensor Tests.....	57
4.3	TABLETOP SENSOR DEMONSTRATION.....	62
4.4	SENSOR SYSTEM IMPLEMENTATION CONSIDERATIONS.....	62
	SENSOR DATA INTERPRETATION.....	65
5.0	INTRODUCTION.....	65
5.1	STATE-SPACE MODEL OF FATIGUE CRACK GROWTH.....	65
5.1.1	State-Space Model Formulation.....	67
5.1.2	Model Validation with Test Data.....	72
5.1.3	Comparison of Computation Time.....	76
5.2	STOCHASTIC MODELING OF FATIGUE CRACK DAMAGE.....	77
5.2.1	Model Formulation and Assessment.....	78
5.2.2	Analysis of Experimental Data.....	82
5.2.3	Risk Analysis and Remaining Life Prediction.....	91
5.3	DISCUSSION.....	94
5.3.1	State-Space Model.....	94
5.3.2	Stochastic Model.....	95
	CONCLUSIONS AND RECOMMENDATIONS.....	96
6.0	INTRODUCTION.....	96
6.1	HEALTH MONITORING SYSTEM REQUIREMENTS.....	96
6.1.1	Maintenance Program Requirements.....	96
6.1.2	Degradation Modes.....	97
6.2	SENSOR SYSTEM DEVELOPMENT.....	98
6.2.1	Corrosion.....	98
6.2.2	Fatigue.....	98
6.2.3	Combined Damage Modes.....	99
6.2.4	Sensor System Implementation.....	99
6.3	SENSOR DATA INTERPRETATION.....	99

6.5	RECOMMENDATIONS.....	101
	REFERENCES.....	102
	APPENDIX: STATE-SPACE MODEL VALIDATION.....	106

Health Monitoring for Airframe Structural Characterization

SECTION 1 INTRODUCTION

1.0 BACKGROUND

Structural health monitoring (HM) is a critical consideration for overall condition monitoring of aircraft systems. In fact, significant inspection and maintenance of structural components is required by the Federal Aviation Administration (FAA) in order to maintain the continued airworthiness of commercial aircraft. For the air carriers, this represents a considerable expense in aircraft maintenance; an expense that could be significantly reduced with the implementation of an effective SHM capability. (Kent and Murphy, 2000).

Traditionally, off-line diagnostic models based on a statistical analysis of material degradation, operating history, and anticipated perturbations in the flight profile have been used to characterize airframe structures. Based on these analyses, a rigorous schedule of inspection and maintenance actions is established to maintain the aircraft in an airworthy condition. However, these techniques cannot elucidate the condition of individual aircraft. Sensing and characterization of structural condition for specific components of individual aircraft is required to meet the goals of NASA's Single Aircraft Accident Prevention (SAAP) program.

There are three key motivations to pursue sensor-based SHM capabilities. First, given the inspection and maintenance techniques currently available, there is a potential that indications of structural degradation could be missed. In general, structural safety inspections can be difficult and tedious because: (1) the feature sizes for cracks and corrosion are often small with respect to the resolution of the inspection methods, (2) crucial structural details are often hidden or buried inside surrounding structure, making access difficult, and (3) inspection of airframe components must include large areas with many features to inspect. Even with the recent advances in automated ground-based nondestructive evaluation methods, the vast majority of inspections are visual. Second, SHM capability could enable on-condition maintenance of airframe structure. On-condition maintenance of structures would simplify periodic checks, improve productivity by minimizing aircraft downtime, and allow the maintenance program to be tailored to the individual aircraft. Finally, SHM is an integral part of a comprehensive condition analysis capability.

Advances in sensors are key enabling technologies to the realization of SHM capability. Recent work has been focused on developing a suite of sensors that can be directly embedded into the material system or attached to a structure with limited increase in cost, weight, shape, or size. These sensors, when properly configured within the airframe structure would create a distributed network capable of measuring strain, pressure, temperature, and other key parameters. This sensor network would be capable of

detecting changes in the operational environment (e.g., thermomechanical loading, flight profile usage, material state, or internal condition) and initiating an appropriate response (e.g., transmitting this information to a centralized signal processing and data management system).

As part of the long-term effort to implement SHM capability, ARINC, in collaboration with NASA, Penn State University, and Luna Innovations, has developed and demonstrated a prototype multiplexed sensor system for airframe structure and compatible real-time damage models for on-board characterization of multiple and synergistic failure modes in current and future airframes. The goal that drove these developments was to monitor structural condition and analyze structural degradation as it occurs, rather than to detect structural failures.

1.1 PURPOSE

The purpose of this project was to develop a multiplexed airframe structural sensor prototype for on-board characterization of multiple and synergistic failure modes in current and future airframes and to demonstrate the technologies in a laboratory setting. Specifically, the purpose of this study was to establish requirements for structural health monitoring systems, identify and characterize a prototype structural sensor system, develop sensor interpretation algorithms, and demonstrate the sensor systems on operationally realistic test articles. The structural sensing system was designed to provide data sources for ARINC's Aircraft Condition Analysis and Management System (ACAMS), which was developed in a complementary program.

In previous work, we have shown that the implementation of advanced health monitoring technologies will depend on (1) acceptance by operators, (2) the ability to gain approval in the FAA certification process, and (3) compatibility with continued airworthiness requirements (Munns, et al., 2000). With these factors in mind, a balance between a technology development perspective and an end-use perspective was maintained throughout the program so that the framework for acceptance, certification, and implementation could be established.

1.2 SCOPE AND APPROACH

The scope of the study included: (1) determination of the operational constraints under which the structural health monitoring system must perform; (2) development of a sensor suite to provide a more comprehensive description of structural condition especially related to known sources of structural degradation (specifically corrosion, fatigue cracking, and stress behavior); (3) demonstration of the sensor technology in a laboratory environment; and (4) development and validation of a dynamic model, formulated in the state-space setting, of fatigue crack propagation in metallic materials.

In order to achieve the goals of the program, the ARINC team completed the following tasks:

- Established requirements for the implementation of structural health monitoring systems
- Identified and characterized a prototype structural sensor system and demonstrated the sensors on realistic test articles
- Developed and validated sensor interpretation algorithms

The approach taken for the implementation requirements analysis included: (1) assessing air carrier maintenance; and (2) identifying and assessing important degradation modes for aging airframe structures that would be targeted by the SHM system.

Based on the analysis of the implementation requirements, a structural sensing system, made up of multiple sensor types, was developed, characterized, and demonstrated. Fiber optic sensors were the predominate sensors used for this study. The selected sensors were characterized to (1) determine their suitability for detecting the important degradation mechanisms; (2) identify methods to multiplex sensors for appropriate coverage; and (3) assess requirements for implementation in an integrated health management environment. Finally, the selected sensors were demonstrated in structural testing environments.

A key component of the structural health monitoring capability is the ability to interpret the information provided by sensor system in order to characterize the structural condition. A novel deterministic state-space fatigue growth model and stochastic model that accounts for the statistical nature of damage development processes were developed to perform real-time characterization and assessment of structural fatigue damage.

The study results are organized into four sections:

- Section 2 includes an analysis of requirements for the implementation of SHM systems
- Section 3 includes sensor system development and baseline characterization
- Section 4 includes sensor demonstration and evaluation
- Section 5 includes sensor data interpretation

The conclusions and recommendations are presented in Section 6.

SECTION 2 IMPLEMENTATION REQUIREMENTS ANALYSIS

2.0 INTRODUCTION

Aging of aircraft structures, or the systematic degradation of structural components resulting from exposure to the service environment was brought to attention of the commercial transport industry as a result of 1988 Aloha Airlines 737 accident (NTSB 1988). This accident raised concerns that structures could lose their inherent fail-safety as a result of fatigue damage or extensive corrosion. In response to this problem, the FAA and the aircraft industry increased the frequency and requirements for periodic inspections for older aircraft models (> 14 years of service). In addition, the damage tolerance and durability requirements of FAR 25 (§25.571) were revised to address aging structure issues. With the combined effects of increased inspection, more stringent maintenance requirements, and increased aircraft utilization—along with the fact that high-time “current generation” aircraft (e.g., 757, 767, A-300, MD-80) are moving into the aging category—SHM capability has become more attractive for application in commercial aviation.

In this context, this section is focused on an analysis of the requirements for integrating an advanced SHM system into an existing air carrier maintenance program. One of the keys to implementation of advanced SHM technologies includes the compatibility of the SHM capability with current and emerging FAA guidelines as well as acceptance by the air carriers and viability of utilizing the SHM system in the airline operational environment. Therefore, we report on SHM system requirements predicated on balancing the characteristics, attributes, capabilities, and limitations of the state of the art in sensor technology, data analysis, and decision support technologies, with existing and projected aircraft maintenance and safety concepts.

There are three main objectives for integrating a sensing and analysis system into aircraft structures:

- Ensure that the component is optimally manufactured to meet all relevant operational specifications and criteria (baseline condition assessment)
- Monitor the condition and performance of the component throughout its service life
- Monitor the structural integrity of the component during its operational utilization

The purpose of this section is to identify requirements for sensing, diagnostics, and prognostics to develop and implement a health monitoring system for commercial airframe structures. These requirements were developed based on an assessment of operators maintenance programs and an analysis of aircraft structural degradation modes.

2.1 AIRLINE MAINTENANCE PROGRAMS

In order to realize the benefits that would be afforded by implementation and utilization of SHM technologies, it was important to understand how these capabilities would be integrated with the current maintenance infrastructure used by the airlines. The first step in this process was to develop an understanding of the maintenance concepts that the airlines currently use before trying to address integration of SHM technology. Once the applicability and reliability of SHM systems has been proven, the overall acceptance by the end user will require integration of SHM systems with existing systems and capabilities.

In order for SHM systems to be an integral part of the operator's structural maintenance programs, they would be required to (1) automate or improve inspections and tests; (2) detect fault precursors so that maintenance or replacement activities can be anticipated and scheduled; and (3) include the data collection and analysis functions associated with maintenance program review.

Operators of commercial aircraft develop and implement maintenance and preventive maintenance programs, not only to comply with regulations and guard against effects of potential life-limiting defects, but also to maximize the availability of individual aircraft (by minimizing aircraft down time) and to protect their considerable capital investment in aircraft and equipment. The objectives of an effective maintenance program are to accomplish the following in a cost-effective manner (ATA 1993):

- Ensure that the inherent component safety and reliability levels are realized
- Restore component safety and reliability to their inherent levels if deterioration occurs
- Obtain information necessary for design improvement of components with lower inherent reliability

The requirements for aircraft utilization have been steadily increasing in recent years. Current schedules and route structures are such that aircraft could see as many as 16 hours per day of service. High utilization aircraft could approach 6000 hours in a year, a number that has been steadily increasing over the past 10–15 years, resulting in fewer opportunities to bring an aircraft in for maintenance (Edwards, 2000).

Although there are distinct differences in detail from airline to airline, most air carriers adhere to similar concepts and protocols when performing maintenance on aircraft structures. Continuous airworthiness maintenance programs are developed by the aircraft operators and approved by the FAA. The basic elements of a continuous airworthiness maintenance program includes the following (FAA 1980):

- Aircraft inspection, including routine inspections, servicing, and tests performed on the aircraft at prescribed intervals
- Scheduled maintenance (i.e., maintenance tasks performed at prescribed intervals), including replacement of life-limited items, components requiring

replacement for periodic overhaul, special inspections, checks or tests for on-condition items, and lubrication

- Unscheduled maintenance (i.e., maintenance tasks generated by the inspection and scheduled maintenance elements, pilot reports, failure analyses, or other indications of a need for maintenance)
- Engine, propeller, and appliance repair and overhaul
- Structural inspection program and airframe overhaul
- Required inspection items (i.e., safety-critical items)
- Maintenance manuals

There has been a gradual evolution of aircraft maintenance philosophy to embrace reliability control methods as an integral part of an approved aircraft maintenance program (FAA 1988). This transition is evident in the three approaches to preventive maintenance currently applied to commercial transport components—hard time, on-condition, and condition monitored—as described in the following paragraphs.

Early (first-generation) air carrier maintenance programs were developed under the assumption that each functional component needed periodic disassembly for inspection. This led to the implementation of hard time maintenance processes, where components are removed from service when they reach a predetermined service parameter (e.g., flight hours, flight cycles, or calendar time).

However, the majority of aircraft components do not exhibit old-age wear-out that would be conducive to hard time maintenance. The principal reliability pattern for complex aircraft systems is high initial failure rates, followed by random incidence of failure throughout the remaining life (Edwards 2000). Replacing such components at a prescribed age actually reduces overall reliability because the poor initial reliability is introduced more often. This led to the implementation of on-condition maintenance processes, where periodic visual inspection, measurements, tests or other means of verification are used to establish component condition without disassembly, inspection, or overhaul.

Finally, the industry and regulatory authorities developed methods to establish maintenance program requirements by tracking component failure rates and maintaining an acceptable level of reliability. Reliability methods identified components that respond to neither hard time nor on-condition approaches. This led to the implementation of condition monitoring maintenance processes, where component performance is monitored and analyzed, but no formal services or inspections are scheduled.^a

Airline maintenance programs include all three maintenance approaches as appropriate. SHM systems could provide benefit to the operators in each of the maintenance scenarios

^a This definition of condition monitoring differs from the definition traditionally used in nondestructive evaluation or process controls. The traditional definition implies that parameters that would provide evidence of impending failure events are monitored. For the current definition performance relative to an alert value indicating failure is monitored.

described above. First, hard time components could be converted to one of the reliability-based approaches by identifying faults that are precursors to failure and monitoring the components using a SHM system. Second, SHM systems could be used to automate the inspection, measurements, and tests for on-condition components. Finally, SHM systems could be used to detect the precursors to failure for condition-monitored components so that maintenance or replacement activities could be anticipated and scheduled.

Maintenance tasks are developed and implemented for individual components by component manufacturers and operators based on detailed analyses of component performance, potential failure modes and consequences, and reliability of similar components in service. The approaches used by air carriers to identify maintenance tasks are outlined in the following sections.

2.1.1 New Aircraft Models (MSG Process)

Operators recommend initial maintenance tasks for new aircraft based on a detailed analysis approach (ATA 1993). Each major subsystem is considered by a maintenance steering group (MSG), which consists of senior maintenance engineers from each carrier that will operate the aircraft type, as well as representatives of the manufacturer and the FAA. The MSG identifies significant maintenance tasks in critical systems using a rigorous evaluation process that includes the following general steps:

- Identify subsystem function
- Predict potential failure modes based on analysis or experience with similar designs
- Analyze the failure modes using an established logic that considers consequences of failure (e.g., affects safety, undetectable, operational impact, economic impact)
- Write maintenance tasks and intervals based on the above assessment (e.g., lube/service, crew monitoring, operational check, inspection/functional check, remove and restore, or remove and discard)

Structural designs are evaluated to identify potential structural failure processes, assess the ability to detect indications of each failure mechanism, and determine the potential consequences of each failure event (or multiple events acting simultaneously). Inspection, maintenance, and modification tasks for structures are developed based on the results of these analyses.

Once the MSG has identified the maintenance tasks, individual carriers add to or modify the tasks for their operations to develop a maintenance list. At the same time, the manufacturer develops a maintenance manual, which includes structural airworthiness limitations, certification maintenance requirements (CMR)^b, and servicing and lubrication

^b CMRs are required periodic tasks that are established during airworthiness certification as operating limitations of the type certificate.

requirements. Based on their maintenance manual, the manufacturers develop maintenance process data (MPD) and maintenance task cards. The air carriers use these resources to develop their maintenance program.

2.1.2 Maintenance Program Implementation

Once maintenance tasks and intervals have been established, the air carrier must develop an implementation plan, consistent with their operations and capabilities, to accomplish scheduled maintenance tasks for each aircraft. In addition, the maintenance program must have mechanisms to accomplish unscheduled maintenance so problems that arise out of sequence with scheduled maintenance can be dealt with. The goals of an effective SHM system are to anticipate required actions for scheduled maintenance visits and to save the operators maintenance costs by reducing unscheduled maintenance actions.

2.1.2.1 Scheduled Maintenance

A typical maintenance program has a series of scheduled maintenance “checks,” where maintenance tasks are grouped so that they can be accomplished with minimal downtime. The checks for a typical maintenance program are shown in Table 2-1. There are a number of approaches to implementing inspection and maintenance intervals that comply with manufacturers’ suggestions and are complementary with the carriers’ operations. The following are examples of approaches to organizing maintenance tasks into checks (Ake 2000):

- Block program – the aircraft is divided into inspection areas (zones) or systems and all of the A-level or C-level checks are accomplished at an appropriate visit.
- Segmented program – each check interval is broken up into subintervals. For example, instead of performing one large A-check at 4000 hours, the carrier can perform 4 smaller checks at 1000, 2000, 3000, and 4000 hours. Either way, the required work is done within the specified time.
- Phased program – similar to a segmented program except that all A-level segments are completed within each B-level increment, and similarly for higher-level checks.
- Continuous maintenance visits (CMV) program – individual tasks are assigned an initial check and a prescribed interval. For example a task might start at the second C-check (C2) and be repeated at every third C-check from then on (3C interval).

The FAA does not prescribe how the operators must organize their tasks, so an acceptable maintenance program could be organized using any of these methods or by combining the methods.

Table 2 –1. Typical Airline Scheduled Maintenance and Service Plan

When Service is Performed	Type of Service Performed	Impact on Airline Service
Prior to each flight	“Walk-around” – visual check of aircraft exterior and engines for damage, and leakage	None

Every 2-7 days	Service check (line maintenance opportunity) - service consumables (engine oils, hydraulic fluids, oxygen) and tire and brake wear	Overnight layover
Every 25-40 days	A-checks (line maintenance check) - detailed check of aircraft and engine interior, service and lubrication of systems (e.g., ignition, generators, cabin, air conditioning, hydraulics, structures, and landing gear)	Overnight layover
Every 45-75 days	B-checks (packaged A-checks) – torque tests, internal checks, and flight controls	Overnight layover
Every 12-15 months	C-checks (base maintenance visit) - detailed inspection and repair of engines and systems	Out of service 3-5 days
Every 2-5 years (depending on usage or mandatory inspection/modification requirements)	Heavy maintenance visit (or maintenance program visit) – corrosion protection and control program and structural inspections/modifications	Out of service up to 30 days

Source: Based on New Materials for Next-Generation Commercial Transports, NMAB-476, National Research Council, Washington, DC: National Academy Press (1996).

2.1.2.2 Unscheduled Maintenance

Unscheduled corrective maintenance is usually performed when damage, defects, or degradation are discovered during operational inspections and checks by aircrew, maintenance, or support personnel (e.g., pre- and post-flight inspections and service checks). In most cases, the problem will be immediately corrected under an engineering order or action. Such unscheduled corrective maintenance activities are normally accomplished by air carrier or contractor maintenance technicians following the calibration, repair, and overhaul procedures published in the airline maintenance manual, aircraft structural repair manuals, and work cards. Whenever possible, minor maintenance and repairs are performed on the flight line (i.e, without returning the aircraft or component to the maintenance shops). Unscheduled maintenance requirements always have the potential to cause costly departure delays.

2.1.3 Program Review and Reliability Tracking

Commercial operators establish and maintain continuous monitoring and surveillance programs to ensure that inspection and maintenance programs are, and continue to be, effective. The requirement to establish and maintain a continuous monitoring and surveillance program effectively establishes a quality control or internal audit function to assure that everyone involved in the inspection and maintenance program is in compliance with the operator's manuals and applicable regulations.

Reliability-based maintenance programs allow inspection and maintenance intervals and methods to be set (and modified) based on demonstrated reliability (FAA 1988). Typically, operators track the mean time to unit failure to identify reliability trends. These

data are used to upgrade the maintenance program and to identify design flaws that should be addressed by the manufacturer.

SHM systems could be an integral part of an airline's monitoring and surveillance and reliability tracking programs. In order to integrate SHM with these activities, the system would need to include the data collection and analysis functions associated with structural maintenance program review and augment air carrier Flight Operations Quality Assurance (FOQA) programs.

2.2 STRUCTURAL DEGRADATION MODES

In order to provide the benefits to the air carriers' structural maintenance programs as described in the previous subsection, the SHM system must have the following capabilities:

- Detecting structural deterioration or damage that could affect structural integrity
- Determining the location and then characterizing the extent and severity of these undesirable conditions
- Assessing the adverse effect of these conditions on the performance of the structure
- Initiating mitigating or corrective actions to restore the structure to airworthy condition

An understanding of potential damage mechanisms, structural design criteria and fail-safe features, and structural maintenance philosophy is needed in order to assess the efficacy of sensor-based system to effectively monitor structural condition. This section describes important structural degradation modes considered in commercial transport aircraft and sensing strategies that would allow a SHM system to detect and characterize structural degradation. This review of aging mechanisms considered most of the common airframe materials, including aluminum, steel, and composites, but was primarily concerned with aluminum airframe structure, which has received the bulk of the attention from the aging aircraft community. Materials and constructions for aircraft engine structures are not considered in this report.

Three principal degradation modes—accidental damage, environmental deterioration (such as corrosion), and fatigue damage—are considered in developing structural inspection and maintenance tasks. These three modes (and combinations thereof) are inclusive of virtually all of the degradation mechanisms observed for aircraft structure.

The majority of structural components in large commercial transport aircraft and most large military aircraft are designed to be fail-safe, relying on multiple, redundant load paths or crack arrest features to preclude catastrophic failures in the event of fatigue, corrosion, manufacturing defects, or accidental damage. Fuselage structural design provides an example of how the fail-safe design philosophy has been used to provide damage tolerance in a fatigue environment (Johnston and Helm 1998). These structures are typically constructed of thin, ductile aluminum alloys (e.g., 2024-T3), where the skin

thickness varies from about 0.036 inches to 0.08 inches depending on aircraft type and size. The fuselage is built up from aluminum alloy sheets connected by riveted lap-splice joints with circumferential tear straps, usually a higher strength aluminum alloy (e.g., 7075-T6), riveted to the inside of the fuselage to prevent a single crack from propagating across multiple frames. The combination of the ductile skin and the tear straps make the aircraft fuselage structure extremely tolerant of damage in the presence of a single long crack. If a single long crack were to develop in the fuselage (through either accumulation of fatigue damage or a discrete source damage), the tear straps would cause the crack to turn and allow the aircraft to decompress in a controlled manner. The damage-tolerant nature of the construction enables the structure to maintain sufficient residual strength in the presence of a long crack to allow the crack to be detected before reaching critical size.

In some cases, fail-safe requirements are impractical for specific components. In these cases, FAR 25 requires that safe-life analyses be performed. This structure must be shown by analysis, supported by test evidence, to be able to withstand the operational cycles without detectable cracks.

2.2.1 Fatigue

There are two primary types of fatigue observed for metallic structures on commercial aircraft—low-cycle fatigue (e.g., from flight maneuver and gust loading) and high cycle fatigue (e.g., from vibratory excitation from aerodynamic, mechanical, or acoustic sources) (NRC 1997).

2.2.1.1 Crack Growth

Monitoring of low-cycle fatigue (LCF) cracking from pre-existing flaws or defects has been part of the inspection and maintenance regimen for many years. Commercial aircraft structures are designed assuming that the maximum probable sized flaw or defect is located in the most critical area of the structure. Critical areas are generally identified during airframe full-scale fatigue tests or by comparison with similar designs. Safety limits are calculated as the time for a crack to grow from the assumed initial flaw size to the critical size leading to rapid fracture. Therefore, inspections are required to identify and track cracks.

Under given initial design operating conditions, stress levels and materials are selected so that the safety limits will not be reached within the life of the airframe. However, operations outside the intended flight envelop or beyond the intended service life could lead to increases in the number of critical areas and could increase the possibility that fatigue cracking will not be detected. Fatigue damage must be detected and monitored so repairs can be made before the crack reaches critical length. If cracks are found that are below critical size, inspection intervals are shortened to ensure that needed repairs can be made before the crack approaches critical length.

The vigilance and added cost required to track fatigue-critical areas and perform inspections and maintenance are particularly burdensome for single-load-path structures

(e.g., rotorcraft and military fighters). There are currently no effective means (short of full scale fatigue testing) to identify new critical areas as they develop as a result of usage.

Failure from fatigue crack growth from an initial material flaw is of lesser concern in large transports because the majority of the structures have been designed to be fail-safe. However, fatigue damage must be detected and monitored so repairs can be made before the crack reaches critical length.

Based on the structural design and maintenance considerations described above, the required approach for monitoring fatigue crack growth is to (1) detect the presence of subcritical fatigue cracks, (2) isolate and characterize the damage, and (3) monitor the crack growth. The SHM system must be able to predict when the crack will be likely to reach critical length and initiate maintenance before the crack becomes critical.

2.2.1.2 Widespread Fatigue Damage

Although fail-safe structure is designed to tolerate fatigue damage, widespread fatigue damage (WFD) can compromise fail-safe structural design features. Widespread fatigue damage is the simultaneous presence of small cracks initiating from normal quality structural details. WFD can exist as multiple site damage, where cracks are present in the same structural element, or multiple element damage, where cracks are present in adjacent structural elements. In the case of a fuselage lap splice, small cracks developing at multiple rivet holes in a lap-splice joint might prevent the tear straps from turning the crack, compromising their damage tolerance.

To maintain airworthiness in fail-safe structure, the onset of WFD must be avoided. The onset of WFD is defined as the point in time when cracks are of sufficient size and density to cause the residual strength of the structure to degrade to where it will no longer sustain the required loads in the event of a primary load-path failure or a large partial damage incident (NRC 1997).

Areas of commercial aircraft fuselage structure that have been found to be susceptible to WFD include (Hidano and Goranson 1995):

- longitudinal skin joints, frames, and tear straps
- circumferential joints and stringers
- frames
- aft pressure dome outer ring and dome web splices
- other pressure bulkhead attachments to skin and web attachment to stiffener and pressure decks
- stringer-to-frame attachments
- window surround structure
- over-wing fuselage attachments
- latches and hinges of nonplug doors
- skin at runout of large doublers

Wing and empennage structure that have been found to be susceptible to WFD include (Hidano and Goranson 1995):

- skin at runout of large doublers
- chordwise splices
- rib-to-skin attachments
- stringer runout at tank end ribs

Managing WFD requires predicting the onset of WFD in an accurate and timely manner. This involves the prediction of initiation and growth of small fatigue cracks (or the interpretation of full-scale fatigue test data and service fatigue data), the prediction of fail-safe residual strength, and the evaluation of the potential effects of environmentally induced corrosion on crack initiation and growth and residual strength. A number of models and analyses have been developed to assess WFD (Harris et al. 1996).

The SHM system must be capable of detecting crack initiation or small crack propagation to effectively monitor materials degradation from WFD. Candidate sensors would (1) identify when a fatigue crack has initiated or when an existing crack grows, and (2) monitor damage development. Monitoring structures for WFD will require development and implementation of techniques to rapidly detect small fatigue cracks over large areas of the structure prior to the onset of WFD. Required capabilities include methods to detect second- or inner-layer cracks, methods to detect hidden corrosion that could lead to the initiation of cracks, and analytic methods for assessing the fail-safe residual strength of monitored structures. Inspection for WFD is particularly difficult because the crack sizes that can significantly degrade strength can be as small as 1mm (depending on alloy type and structural design) and there are many susceptible structural details to monitor.

2.2.1.3 High Cycle Fatigue

High-cycle fatigue (HCF), resulting from exposure to high-frequency load cycles from aerodynamic, mechanical, and acoustic sources, is generally handled during initial design for airframes of commercial aircraft, but can represent a serious threat to structural integrity. The amplitude of HCF load cycles is lower than operation load cycles, but the high frequency can lead to significant damage in very short times. HCF conditions can lead to crack initiation in unflawed structure or rapid propagation from even very small initial flaws.

Even though excitations that could result in HCF are generally identified and corrected during initial design and structural testing, changes in (1) the response of the structure (e.g., due to wear, corrosion, loose fasteners, repairs, and LCF crack growth) or (2) operational environment of the aircraft could lead to HCF in service. Because of the nature of HCF damage, the only workable strategy to monitor structural health is to sense the conditions for HCF and effect repairs to avoid crack initiation and growth.

2.2.2 Environmental Damage

The predominant environmental damage mechanism for metallic structures is corrosion. The main concern with corrosion of metallic airframes is that, if left undetected, the potential for synergy with other degradation mechanisms that could, in turn, lead to structural failure. For this reason, significant effort and expense is focused on the inspection and repair of corrosion damage, especially for hidden corrosion located in inaccessible areas (NRC, 1997). There are a wide variety of corrosion types that routinely occur in aircraft structures: uniform (or general) corrosion, galvanic corrosion, pitting corrosion, fretting corrosion, crevice (filiform and faying surface) corrosion, intergranular (including exfoliation) corrosion, and stress corrosion. The different types of corrosion can have very different characteristics and consequences, making detection and assessment very complicated. Though nondestructive evaluation for corrosion detection is becoming available, corrosion is still often detected using visual inspection methods. Unfortunately, visual inspection has been shown to have inconsistent reliability, even with experienced inspectors (Spencer, 1996). This means that corrosion can remain undetected, especially for internal or inaccessible structures. Because of the difficulty in detecting and characterizing corrosion, the commercial airline industry has elected to manage corrosion primarily through prevention and control.

The commercial aircraft industry has developed corrosion prevention and control plans for each specific airplane type. In developing these plans, the industry established standards to assess corrosion severity, ranging from Level I, where corrosion can be repaired with no structural consequences, to Level III, where corrosion presents a major or systematic threat to airworthiness. An example of corrosion severity standards (Boeing, 1994) is provided below:

“Level I corrosion. (1) Corrosion damage occurring between successive inspections that is local and can be re-worked/blended-out within allowable limits as defined by the manufacturer; or (2) corrosion damage occurring between successive inspections that is widespread and can be reworked/blended-out well below allowable limits as defined by the manufacturer; or (3) corrosion damage that exceeds allowable limits and can be attributed to an event not typical of the operator’s use of other airplanes in the same fleet (e.g., mercury spill); or (4) operator experience over several years has demonstrated only light corrosion between successive inspections but latest inspection and cumulative blend-out now exceed allowable limit.

Level II corrosion. (1) Corrosion occurring between successive inspections that requires a single re-work/blend-out which exceeds allowable limits, requiring a repair/reinforcement or complete or partial replacement of a principal structural element, as defined by the original equipment manufacturer’s structural repair manual, or other structure listed in the baseline program; or (2) corrosion occurring between successive inspections that is widespread and requires a single blend-out approaching allowable re-work limits.

Level III corrosion. Corrosion found during the first or subsequent inspections, which is determined (normally by the operator) to be an urgent airworthiness concern requiring expeditious action. Note: When level III

corrosion is found, consideration should be given to action required on other airplanes in the operator's fleet. Details of the corrosion findings and planned action(s) should be expeditiously reported to the appropriate regulatory authority."

The intent of corrosion prevention and control plans is to ensure that corrosion will not be allowed to progress to the point where it will be a threat to structural safety (e.g., no greater than level I) and to reduce operator's maintenance costs. Corrosion that is found is exposed, repaired, and corrosion prevention coatings or compounds are reapplied.

Stress corrosion cracking (SCC) is an environmentally induced, sustained-stress cracking mechanism. SCC is most commonly found in components fabricated from forgings and machined plate of high-strength steel and aluminum alloys in high-strength tempers (e.g., 7075-T6 and 2024-T3). SCC is sensitive to residual tensile stresses from heat treatment or fit-up, but can also result from operating loads. If SCC occurs, components are usually very difficult and costly to replace (e.g., large structural forgings), so the emphasis has been on precluding SCC through corrosion prevention and control as described above. Generally, components that are susceptible to SCC have been identified through analysis or service records. As with LCF crack growth, SCC is of lesser concern for fail-safe structures than for safe-life structures.

The strategy for monitoring for corrosion damage using SHM technology is to focus on early detection of incipient corrosion or, preferably, detection of when the corrosion prevention scheme has failed. Candidate sensors would (1) identify when corrosion protection has broken down to a point where moisture can intrude, and (2) identify the presence of corrosion by detecting corrosion products. This monitoring approach has two objectives. The first objective is to identify and correct corrosion damage before it becomes a threat to structural integrity. The second objective is to enable inspection for hidden corrosion without unnecessarily disturbing intact structure.

2.2.3 Accidental Damage

Accidental damage is the one structural degradation mechanism that is not considered to be an aging mechanism. This damage could be result of unexpectedly severe operating conditions, operations and maintenance handling, or thermal and environmental exposure. Examples of some of the rare events that could lead to accidental damage include:

- Unexpected flight or maneuver loads
- Overload from actuation system failures
- Lightning attachment
- Bird strikes
- Hail or foreign object impacts
- Damage from in-flight failure of other components
- Ramp and maintenance damage

An integrated SHM system will be required to include a sensing approach to monitor for discrete damage incidents and to trigger the appropriate sensors to characterize the extent of damage in case an event is detected. Because this program focused on detection and characterization of structural aging mechanisms, accidental damage was not systematically addressed.

2.3 INTEGRATION AND UTILIZATION CONSIDERATIONS

Integration and utilization of a SHM system for commercial aircraft structures will be dependent upon the ability of the SHM system to reliably detect and isolate the faults associated with aging degradation mechanisms. As previously discussed in this section, the importance of integration of the SHM system into existing maintenance programs is also key due to requirements for acceptance by the FAA and economic viability of technology insertion.

The air carriers already have rigorous series of mandated inspections that are periodically performed either through teardown and visual inspection, or via automated nondestructive evaluation (NDE) techniques. In order for an *in situ* SHM to be accepted by the FAA and the air carriers, it will be essential to demonstrate that the SHM technology provides at least equivalent detection capability as current ground-based NDE techniques. Further, the air carriers are likely to critically analyze the economic viability and return-on-investment of insertion of advanced SHM technologies into their maintenance processes prior to committing to implementation.

Conventional NDE techniques are usually ground-based, implying that they are used during the periodic maintenance checks described earlier in this section and are impractical for in situ health monitoring. Further, because of the localized nature of most NDE technologies, they generally require a priori knowledge of where damage is most likely to occur and require a direct line of sight to damaged regions. Damage deep below the surface of the structural is frequently beyond the detection capability of most NDE techniques.

SHM differs from conventional NDE in that it is concerned with the overall health of the structure and therefore represents a broader and more ambitious set of goals. Most notably, SHM seeks to perform in situ, nearly continuous monitoring and analysis of structures during flight. As discussed earlier in this section, there are multiple degradation modes that can react alone or in combination to degrade the condition of the aircraft structure. These factors, together, suggest that a multi-variant sensor suite consisting of non-intrusive, low-power, low-weight distributed sensor systems and processors are required for analysis. In addition, the sensors should lend themselves to be massively multiplexed, and environmentally rugged for in-flight operation. Distributed fiber optic sensing systems have the potential to address each of these integration requirements.

Properly integrating and configuring SHM architectures is a challenging task. The natural inclination is to employ designs that rely on using the maximum possible number of sensor devices without considering important issues such as sensor fidelity and reliability,

signal collection and distribution efficiency, and information processing and analysis capacity. However, this strategy may not be justifiable from either the operational or cost-benefit perspectives (Kent and Murphy 2000). Consequently, a disciplined systems engineering approach to develop a system that selectively monitors critical structures and optimizes sensor placement is needed to develop the requirements for a SHM system that could be implemented for commercial transports.

The practical constraints on volume, weight, sensor response time, and capacity, balanced with economic viability of integration, ultimately drive the size and configuration of the SHM system. Specifically, this means that the type, number, location, and distribution of individual sensor elements are practically limited. Though the specific sensor configuration and distribution will be specific to the particular aircraft configuration (e.g., make/model), component design, and individual user maintenance support concept; our previous research has indicated that economic viability of implementation of a SHM system will drive the sensor placement to be optimally located only within regions of the aircraft where current inspections are tedious, labor-intensive, or otherwise costly (Kent and Murphy, 2000).

As the integrated structures undergo repair, in order to maintain the same level of internal interrogation (i.e., statistically identical probability of detection), maintenance procedures must be incorporated which allows for sensor repair, replacement, or alternatively, off-equipment inspection.

Much of the recent research and development of “SHM systems” has focused on sensor and demodulation electronics. However, the sensor suite used for data acquisition only provides the front-end of the analysis necessary for comprehensive health monitoring. It is imperative to translate the raw sensor data to the physical behavior of the structure that maps to a fault condition. Ideally, the sources resident in the multi-variant sensor suite would be analyzed in near real-time to map the sensor state to the physical state or condition of the material. The physical parameters in material-space would then be accumulated to mutually reinforce or deny the existence of identified possible fault characteristics of the structure. This latter analysis is the subject of ARINC’s ACAMS processing models and algorithms performed under a complementary program (ARINC 2001).

2.4 DISCUSSION

The purpose of introducing SHM into commercial transports is to improve the effectiveness of the operators’ continued airworthiness programs while, at the same time, reducing the overall maintenance support cost. The ultimate consideration for assessing the effect of SHM systems on continued airworthiness will be their potential to improve scheduled maintenance programs and reduce unscheduled maintenance actions. SHM systems could be an important factor in improving the effectiveness of inspection and maintenance programs and enabling on-condition maintenance.

Detection, location, and characterization of structural degradation are the keys to SHM. For example, since most internal damage, especially fatigue-related damage, occurs incrementally over relatively small spatial scales, global manifestations of damage may not be detectable by traditional inspection and monitoring techniques until well after the damage has reached a critical state that compromises the functional or physical integrity of the structure. For this reason, SHM systems must sense damage defects with extremely small signatures relative to the global response of the structure.

Because of the myriad of structural damage mechanisms described above, an array of multiple sensor types will likely be required to effectively monitor the range of damage events, corrosion and environmental deterioration, and fatigue. For example, an aluminum splice joint could have moisture, corrosion product, and pH sensor elements distributed adjacent to the splice joint to monitor corrosion; strain sensors along rows of fasteners and in-plane acoustic emission sensors to detect fatigue cracking events and monitor crack growth; and strain; and out-of-plane acoustic emission sensors to detect discrete damage events.

As will be described in Section 3 of this report, one of the focus areas of this project was on sensors to detect aging mechanisms for metallic airframe structures (i.e., fatigue and corrosion). Although not addressed in this program, detection of accidental damage and environmental deterioration of composite and bonded structures will also be important to the development of comprehensive SHM capability.

SECTION 3 SENSOR SYSTEM DEVELOPMENT AND BASELINE CHARACTERIZATION

3.0 INTRODUCTION

The initial step in the development of structural health monitoring capability was to investigate the viability of using a combination of existing sensors and available information for structural condition assessment. A sensing approach, based on the potential damage mechanisms, component design criteria, and operators' maintenance practices, was developed to monitor selected aircraft structures. It was determined that multiple types of structural sensors were needed to detect the indications of degradation described in the previous section. In some cases, where no existing adequate sensors were identified that could meet the requirements for a comprehensive SHM strategy, new sensors and sensor systems were developed and characterized. This section describes the sensor approach, sensor development, and the baseline sensor characterization that was completed during this program. Each sensor type (including those currently available and those developed under this program) is described in relation to detection of the specific structural damage mechanisms for which it is intended.

For the most part, this program focused on fiber optic sensors. These sensors are attractive for the SHM application because of their small size and the ability to multiplex sensor elements. In addition, fiber optic sensor systems are not likely to interfere with adjacent flight systems and are not susceptible to electromagnetic interference effects.

Optical fiber systems have been developed during the past twenty-five years for applications in long-distance, high-speed digital information communication. Sensors using optical fiber technology have been developed over the past fifteen years for applications in the characterization of materials and structures, civil structures, industrial process control, and biomedical systems (Murphy et al. 1991; Claus et al. 1992).

In an optical fiber, injected light is guided by a dielectric cylindrical core surrounded by a dielectric cladding, (see Figure 3-1). Light is transmitted as a field down the fiber, which acts as a waveguide, with energy mostly confined in the core, but with an evanescent field that extends into the cladding. If the incident angle, θ_i , exceeds a critical angle, θ_c , the light energy starts to be attenuated in the cladding. Electric field continuity across the core/cladding interface, particularly in step-index fibers, dictates the allowable modes in a given fiber. This project was performed with single-mode fibers, which carry only a narrow range of wavelengths, with the rest attenuated in the cladding (Jones 1996).

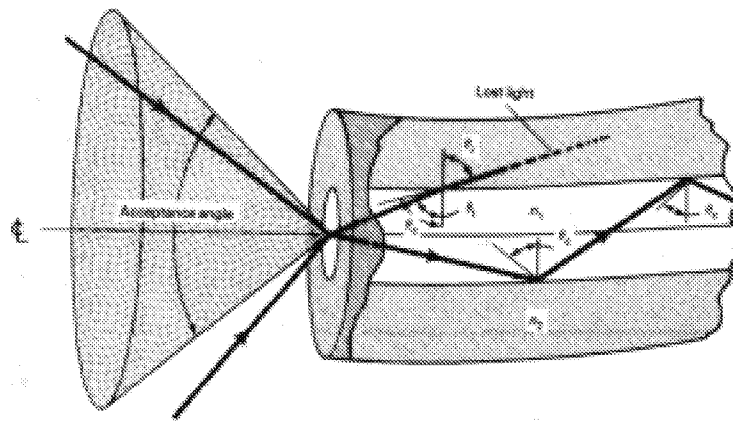


Figure 3-1. Schematic representation of an optical fiber waveguide. Source: Stroman 1991.

3.1 FATIGUE SENSING

As described in Section 2, the structural health monitoring system must be capable of detecting crack initiation or initial crack propagation in order to effectively monitor materials degradation from fatigue. Monitoring structures for WFD will require development and implementation of techniques to rapidly detect small fatigue cracks over large areas of the structure prior to the onset of WFD. Inspection for WFD is particularly difficult because the crack sizes that can significantly degrade strength can be as small as 1mm (depending on alloy type and structural design) and because of the many susceptible structural details to monitor.

The focus of fatigue sensing in this program was on Bragg grating strain sensors (Froggatt et al. 2001; Froggatt and Moore 1998) and fiber-optic strain and acoustic emission sensors based on extrinsic Fabry-Perot interferometry (EFPI) (Poland et al. 1994). Developmental acoustic emission sensors were considered for detecting crack initiation and short crack growth. EFPI fiber-optic strain gage sensors and Bragg grating strain sensors were investigated for monitoring subsequent crack growth and representative strains.

3.1.1 Bragg Grating Sensors

NASA has developed a fiber-optic sensing system that uses optical frequency-domain reflectometry to measure the wavelength of light reflected from many (hundreds or thousands) of low reflectivity Bragg gratings distributed along single mode fibers (Childers et al. 2001). If the Bragg gratings are attached to a structure the shift in measured wavelength can be used to infer the elongation attributable to thermal expansion or applied strain.

NASA's distributed fiber optic sensing system consisted of a laser diode source, a four-channel optical network, detectors, and a desktop computer for data acquisition. The laser diode was a continuously tunable, mode-hop free, external cavity design found in the telecommunications industry. The laser was tuned in a 12 nm range centered about 1550

nm. The total laser power was approximately 5mW with approximately 1.0 mW transmitted to each channel.

The fibers have a large number of Bragg gratings etched at regular intervals into the fiber core with a 246nm UV laser using a two-beam interferometer. The raw signal for each fiber includes spectra for all of the gratings on that fiber. Because the spectrum for each grating is modulated by a signal with a unique frequency that is a result of the grating's position, each grating can be viewed independently. The individual spectrum can be extracted by bandpass filtering around a specific frequency using fast Fourier transformation (Childers et al. 2001). Strain is inferred from the change in wavelength of the centroid of the grating spectrum with respect to an initial (zero or baseline) value.

The primary benefit of the distributed Bragg grating system is the ability to achieve high-density sensor placement at a low sensor cost.

3.1.2 EFPI Sensors

Extrinsic Fabry-Perot interferometry (EFPI) is a versatile technique for a variety of fiber-optic sensor applications. EFPI-based sensors use a distance measurement technique based on the formation of a low-finesse Fabry-Perot cavity between the polished end face of a fiber and a reflective surface, shown schematically in Figure 3-2. A portion of the incident light (determined by the difference between the index of refraction of air and the fiber) is reflected at the fiber/air interface (R_1). The remaining light propagates through the optical path between the fiber and the reflective surface and is reflected back into the fiber (R_2). The optical path length is the physical gap between the end of the fiber and the reflective surface multiplied by the index of refraction of the material in the gap. These two reflected waves interfere constructively or destructively based on their wavelength and the optical path length difference; that is, the interaction between the two light waves in the Fabry-Perot cavity is modulated by a change in the gap distance or change in refractive index of the material in the gap. The resulting light signal then travels back through the fiber to a detector where the signal is converted into an electrical signal and then demodulated to produce a distance measurement.

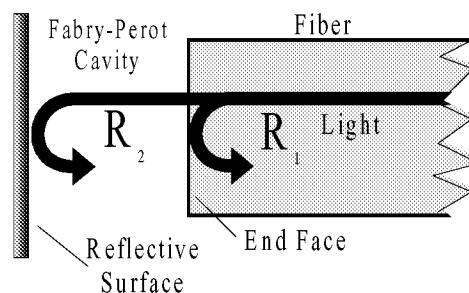


Figure 3-2. Extrinsic Fabry-Perot interferometer concept.

The demodulation of the signals from an EFPI cavity can be performed with a variety of methods. Intensity-based interferometric and spectral interrogation methods are described in this report.

An intensity-based interferometric demodulation system using single wavelength interrogation is shown in Figure 3-3. A laser diode supplies coherent light to the sensor head and the reflected light is detected at the second leg of the optical fiber coupler. The output can then be approximated as a low-finesse Fabry-Perot cavity in which the intensity at the detector is,

$$I_r = |A_1 + A_2|^2 = A_1^2 + A_2^2 + 2A_1A_2 \cos\Delta\phi$$

if A_1 and A_2 are the amplitudes of R_1 and R_2 and $\Delta\phi$ is the phase difference between them. The output is sinusoidal, with a peak-to-peak amplitude and offset that depends on the relative intensities of A_1 and A_2 , as depicted in Figure 3-4. The drop in detector intensity is due to the decrease in coupled power from the sensing reflection as it travels farther away from the single-mode input/output fiber. Minute displacements can be characterized by tracking the output signal. The disadvantage of this type of demodulation system is the non-linear transfer function and directional ambiguity of the sinusoidal output. For example, if gap changes occur at a peak or valley in the sinusoidal signal (e.g. at π , 2π , 3π , ...) they will not be detected because the slope of the transfer function is zero at those points. The sensitivity of the system correspondingly decreases at points near multiples of π . One approach to solving these problems is to design the sensor head so that at the maximum gap the signal does not exceed the linear region of the transfer function. However, confining operation to the linear region places difficult manufacturing constraints on the sensor head by requiring the initial gap to be positioned at the Q-point of the transfer function curve. Also, the resolution and accuracy are limited when the signal output is confined to the linear region.

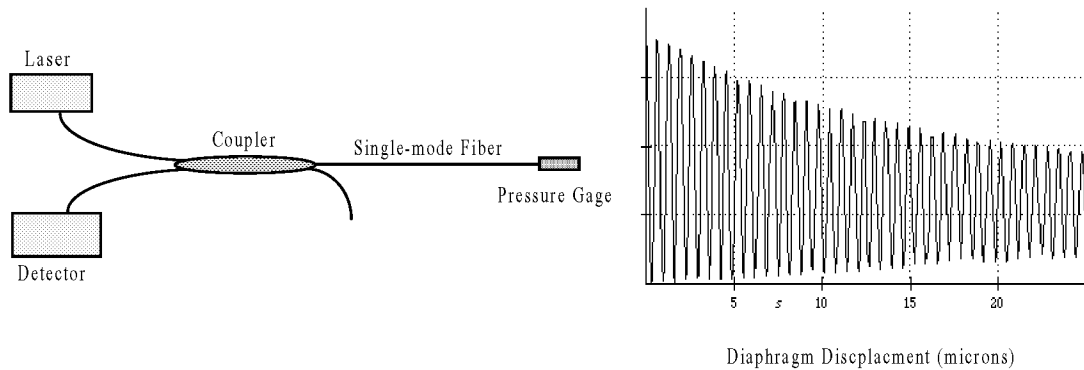


Figure 3-3. Intensity-based interferometric demodulation system using single wavelength interrogation. Source: Murphy et al. 1991.

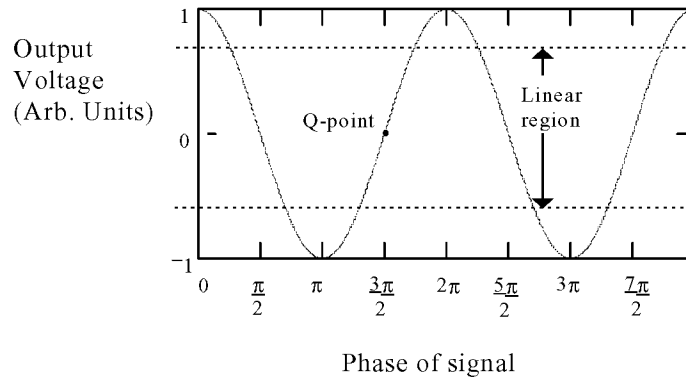


Figure 3-4. Output of an intensity-based interferometric signal over a period.

One approach to solving the non-linear transfer function and directional ambiguity problems of intensity-based signal demodulation is white light interferometry (Dakin and Culshaw 1988). White-light interferometry is an optical cross-correlation technique capable of very accurately determining the path imbalance between two arms of an interferometer (Zuliani et al. 1991). For the case of the EFPI sensor, white-light interferometric techniques provide the exact optical path length between the fiber endfaces that form the Fabry-Perot cavity. The configuration of the absolute EFPI system is shown in Figure 3-5. The white light source is transmitted to the sensor where it is modulated by the Fabry-Perot cavity. The modulated spectra is then physically split into its component wavelengths by a diffraction grating, which is measured by a charged-coupled device (CCD) array.

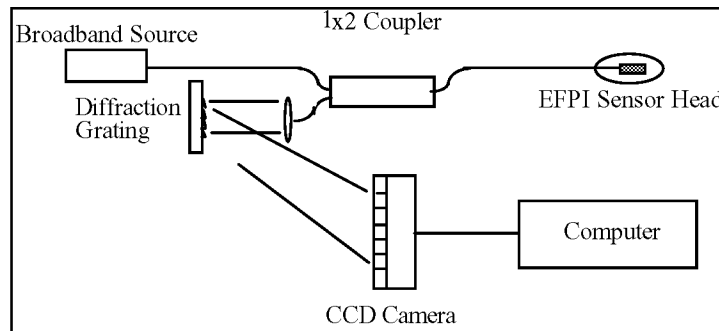


Figure 3-5. Spectral interferometric sensing system.

A representation of the spectral interrogation method is shown in Figure 3-6. An optical path length is calculated from the spectra using a Luna Innovations-proprietary algorithm, which includes an FFT that transforms the signal from a wavelength domain to a gap domain. The location of the maximum of the main peak is the absolute optical gap of the EFPI cavity.

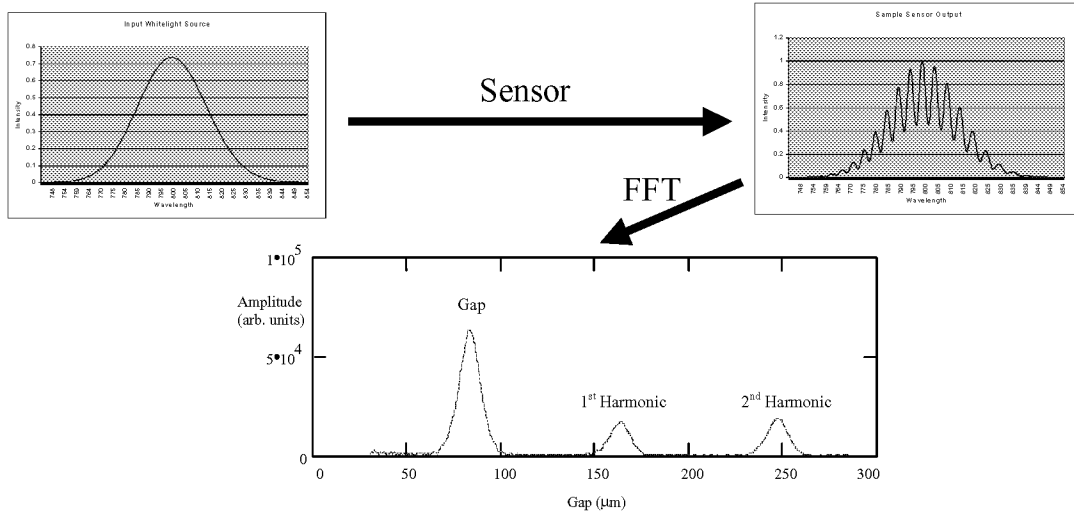


Figure 3-6. Depiction of spectral interrogation system method.

Spectral interrogation has become the preferred method for demodulation of EFPI sensors, and is the type of demodulation system that is primarily used in this study.^c The determination of absolute gap removes the ambiguity typical of intensity based demodulation. Also, the system can be cycled off and on and the data can be gathered again from that point, without having to re-determine the equilibrium point.

3.1.2.1 EFPI Strain Sensors and Extensometers

EFPI-based fiber-optic strain sensors and extensometers (Poland et. al. 1994) were evaluated for monitoring fatigue crack growth. A schematic representation of the EFPI sensor head used in these sensors is shown in Figure 3-7. The EFPI measurement method is described above. Small movements in the hollow core cause a change in the gap distance, which changes the phase difference between the sensing and reflecting waves. If the hollow core tube is attached to a material, and the gauge length of the sensor is known, strain in the material can be accurately measured (Meller 1996). Given an intensity-based demodulation, EFPI technology provides an absolute gap measurement that does not rely on comparison to an initial null-load.

^c The notable exception is that an alternative high frequency demodulation system, described in Section 3.1.2.2, was required for the EFPI acoustic emission sensors.

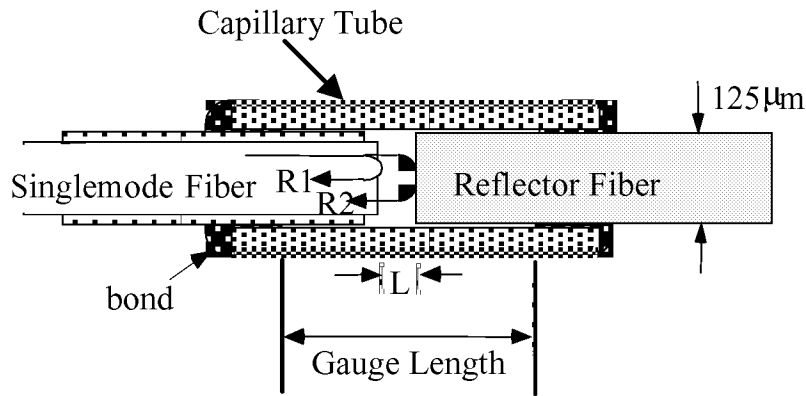


Figure 3-7. EFPI strain sensor head.

The following sensor types were considered for the SHM application to aircraft structure:

- EFPI strain gages. These are commercially available, miniature fiber optic strain gages with outer diameter of 350 μm and gage lengths ranging from 2 mm to 20 mm. The typical sensor range is $\pm 5,000$ microstrain and the resolution is 50 nanostrain for a 4 mm gage length.
- EFPI extensometers. These are commercially available, miniature fiber optic extensometers, gage lengths range from 8mm to 20mm. The sensor range is typically $\pm 20,000$ microstrain and the resolution is 25 nanostrain for an 8 mm gage length.

Because the accuracy of EFPI strain sensors with respect to conventional foil strain gages has been established in side-by-side comparisons in previous programs, the focus of this program was to investigate the performance of these sensors in fatigue environments and the ability to multiplex multiple sensors. The results of these investigations are presented in Section 4 of this report.

3.1.2.2 EFPI Acoustic Emission Sensors

Acoustic emissions are the stress waves that are produced as a result of internal structural changes from damage development and accumulation (Huang et. al. 1998). Available acoustic emission (AE) transducers have been shown to be effective in the evaluation of fatigue damage, including initiation and propagation events (Fang and Berkovits 1994). The purpose of this research was to investigate the efficacy of modifying small, lightweight EFPI-based AE sensors with a high frequency demodulation system to measure in-plane stress waves resulting from acoustic emissions of fatigue cracks. The objective for SHM was to have an in-plane AE sensor that could be permanently attached to aircraft structures.

Demodulation of the EFPI AE sensors required a specialized high-frequency demodulation system. The high-frequency demodulation system is based on dual-wavelength interrogation, and is suitable for single point or multiplexed configurations at frequencies up to 10 kHz and above. The architecture for the design is shown in Figure 3-

8. This system used narrow-band light sources (1300 nm F-P laser diodes), a DSP processor and grating filters to provide relative, yet unambiguous, measurement of cavity displacement. Two lasers of appropriate output wavelength were selected to generate quadrature phase shifted signals for a given sensor cavity length. The reflected laser signals from the sensor head were then separated out at the detector end using photoinduced Bragg grating filters. The quadrature signals were sent to the digital signal processor for high-speed demodulation into an output analog signal that represented sensor displacement.

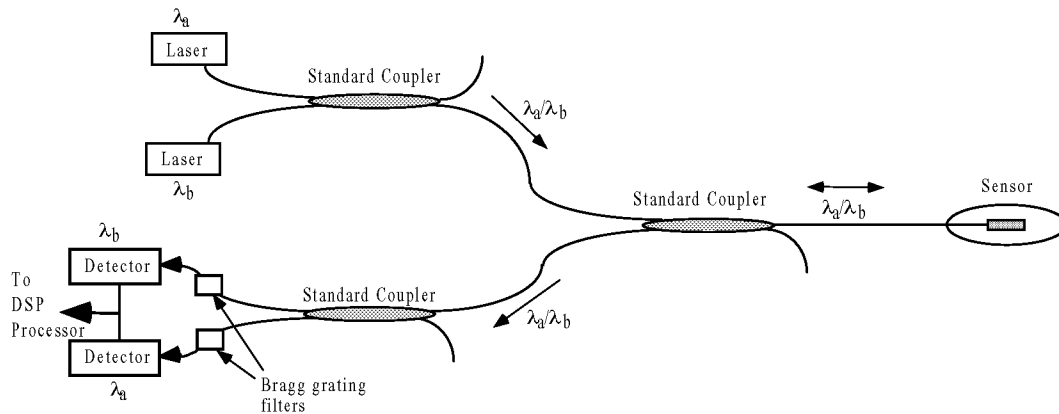


Figure 3-8. High Frequency Interrogation System Architecture.

Although this demodulation system satisfied the need for the high frequency response necessary for the EFPI AE sensors, the demodulation system can only accommodate a single sensor. Multiplexing the EFPI AE sensors can only be achieved through the use of a mechanical switch, which would allow monitoring of only one channel at a time.

A thin walled aluminum specimen (0.050" x 2" x 12") was used for the baseline characterization of the in-plane AE sensor. The sensor was mounted 2" from the edge of the plate using a phenol salicylate bonding agent. For comparison, a Physical Acoustics (PAC) piezo-electric AE sensor R15 (150 kHz resonant device) was also attached to the plate at the same position. The signals from the sensors were acquired with a 4-channel oscilloscope. For initial evaluation, a pencil lead break (PLB) was performed 2" from both of the sensors. Figure 3-9 illustrates typical waveforms collected using the R15 (bottom curve) sensor and EFPI sensor (top curve). The results of PLB verified operation of the fiber optics, showing that the EFPI sensor response was comparable to that of the conventional AE sensor.

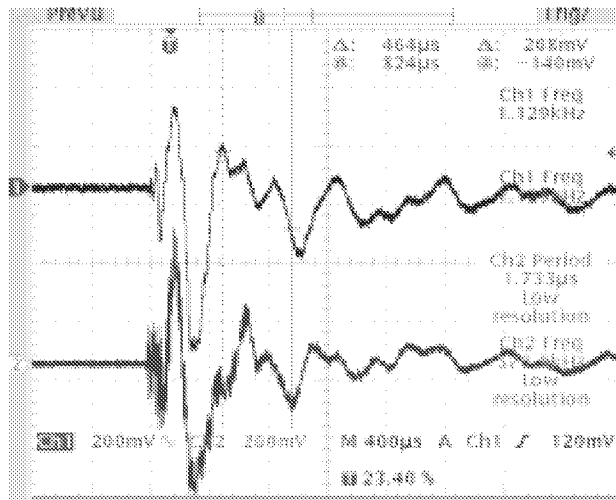


Figure 3-9. Signals acquired with in-plane EFPI AE Sensor (channel 1, top) and Conventional R15 (channel 2, bottom) from 0.5 mm PLB.

Unfortunately, though these initial results indicated comparable low-frequency performance between the EFPI AE and the conventional AE sensor that made the EFPI system appear promising, comparative analysis between the EFPI and R15 sensor at higher frequencies indicated that the sensitivity of the EFPI sensor is approximately 10 dB less than conventional AE sensor. In addition, the noise level is very high (i.e., the signal-to-noise ratio is about 30 dB). This was extremely problematic for the application to detection of the high frequency events that are characteristic of fatigue crack damage.

The results described above, along with independent exploratory testing performed on a fatigue test article, indicated that the system would not have sufficient sensitivity at high frequencies to detect certain AE events, including fatigue crack initiation and propagation. Three primary causes were identified for the inadequate high-frequency (i.e., above 100 kHz) sensitivity: (1) impedance mismatching between the demodulation system and the data acquisition electronics; (2) poor signal-to-noise ratio of the demodulation electronics; and (3) high attenuation of sensor response above 100 kHz. The impedance mismatch was resolved by using a buffering amplifier between the demodulation system and the acquisition system input channels. However, this was not a suitable solution because it further reduced the signal-to-noise ratio of the system. Though Luna Innovations subsequently made dramatic improvements in the electronics that allow the detection of moderate-level, high frequency events, this EFPI AE sensor is still not suitable to detect extremely low-level events such as are characteristic of fatigue crack propagation.

It should be noted that the improved EFPI AE sensor still offers reasonable potential for detection of lower-level events. Such event signatures are reportedly characteristic of other structural degradation mechanisms, such as accidental damage.

3.2 CORROSION SENSING

As described in Section 2, the strategy for monitoring for corrosion damage was to focus on early detection of incipient corrosion or, preferably, detection of when the corrosion prevention scheme has failed. The corrosion sensors that were investigated in this study were intended to (1) identify when corrosion protection has broken down to a point where moisture can intrude, and (2) identify the presence of corrosion by detecting corrosion by-products. This monitoring approach has two objectives. The first objective was to identify and correct corrosion damage before it became a threat to structural integrity. The second objective was to enable inspection for hidden corrosion without unnecessarily disturbing intact structure^d.

The focus of corrosion sensing in this program was LPG optical fiber sensors. These sensors, which are cladded with tailored coatings that react with target chemical species, have been shown to effectively discern the presence of significant moisture, metal ions indicative of corrosion products or the pH of a potential electrolyte solution (Elster et al. 1998, 1999). As described above, LPG sensors can be multiplexed, that is, multiple sensing elements can be deposited on a single optical fiber. Moisture and metal ion corrosion sensors were considered and demonstrated in this program.

The long period grating (LPG) sensor is a spectral loss element that has a longer period of index modulation than traditional Bragg grating sensors. This results in the opportunity for interactions between an evanescent optical wave from the fiber with the surrounding media. The optical wave is scattered at a particular wavelength based on the refractive index of the surrounding environment so that the resulting optical response through the fiber is characteristic of the material in the vicinity of the fiber. The LPG-based sensors characterized in this program operate based on the use of specially designed affinity coatings that exhibit a measurable change in the refractive index that modulates the LPG when brought in contact with certain molecules. As the coating absorbs target molecules, the refractive index changes, causing a shift in the wavelength of the scattered light. Figure 3-10 shows a representative spectrum shift with refractive index change for a LPG sensing element. By tracking the wavelength of the spectral loss minima, both qualitative and quantitative measurements can be accomplished.

^d Anecdotal evidence from several air carrier sources has indicated that required corrosion inspections necessitated the disassembly of intact structure with pristine corrosion protection. The carriers expressed concern that, following re-assembly, there was no way to ensure that the integrity of the corrosion protection of re-assembled structure remained pristine.

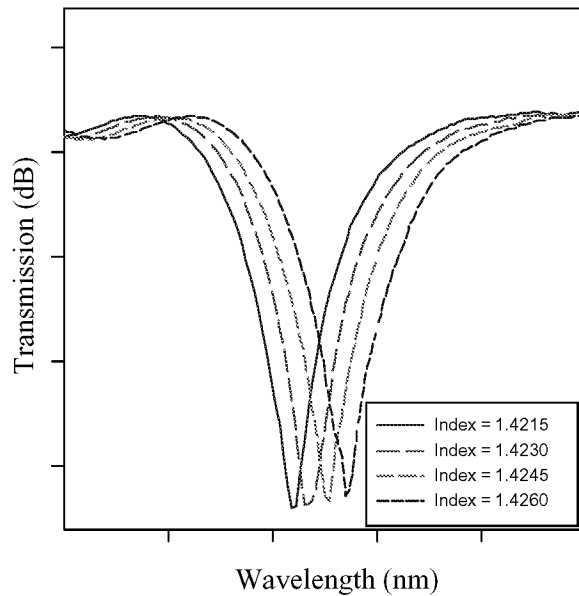


Figure 3-10. Long period grating (LPG) transmission spectrum.

The foundation for the signal conditioning system is a scanning Fabry-Perot interferometer, which is commercially available from several suppliers. The Fabry-Perot filter is a bandpass device that transmits a small segment of the spectrum. By scanning the filter through a range of wavelengths using a piezo-modulator, the entire LPG profile can be continuously measured. The LPG signal conditioning system architecture is shown in Figure 3-11.

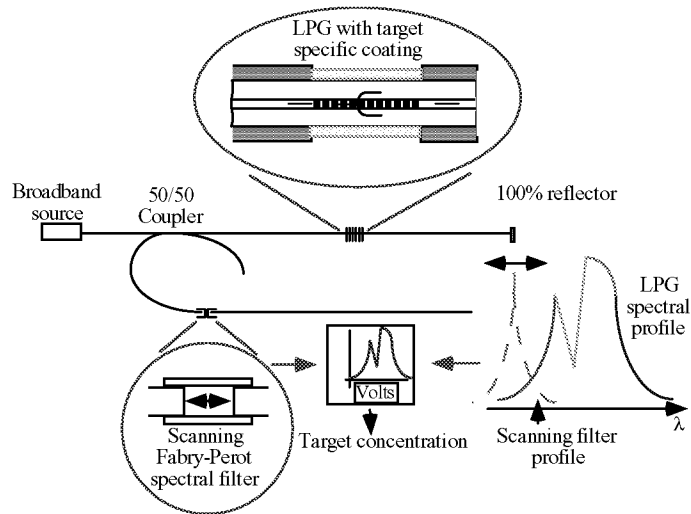


Figure 3-11. LPG signal conditioning system architecture.

A sensor demodulation and data acquisition system (i.e., the Lunascan-3000), which consisted of a signal conditioning box, a 1x8 optical switch, and a computer interface, was developed to track the wavelength of the LPG spectral loss minima with time. The latest graphical user interface for the LPG-based chemical sensors is shown in Figure 3-12. Although shown for moisture sensors, this system has been designed to monitor multiple types of sensors at multiple locations. Wavelength and power thresholds can be selected for each channel in order to establish test limits.

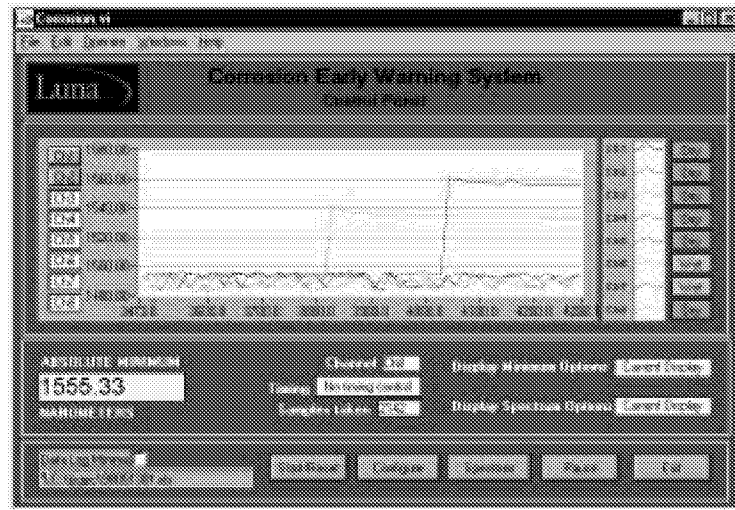


Figure 3-12. System software used to interrogate eight long period gratings (LPGs) simultaneously and plot the wavelength of the LPG spectral loss dip with time.

An advantage of the LPG is that the operating wavelength can be tailored using different grating periodicities. LPG sensors can be written at various wavelengths and demodulated using standard wavelength division multiplexing (WDM) techniques. The multiplexing allows on the order of tens of LPG sensors to be fabricated in a single fiber with each sensor interrogated at its own particular wavelength.

3.2.1 LPG Moisture and Humidity Sensors

For our current application, as was described in Section 2, the commercial air carriers approach to corrosion management relies on ensuring that the corrosion protection finish that protect the aircraft structure from moisture intrusion remains intact. Therefore, we investigated sensors that could be placed beneath the corrosion protection finish to detect moisture. Moisture intrusion beneath the corrosion protection finish would indicate a breakdown in the integrity of the finish and the existence of a condition that could lead to corrosion if left uncorrected.

At the outset of this program, a commercial sensor from Luna Innovations was available to detect the presence or absence of moisture in the vicinity of the sensor. In this class of sensors, detection of water was accomplished by coating an LPG sensor element with poly (ethylene oxide) [PEO], formed from the polymerization of ethylene oxide

monomers. This PEO derivative is a water-absorbing hydrogel coating that swells in the presence of moisture. The coating thickness was previously optimized by Luna Innovations for high responsiveness and reversibility (Elster 1998). In the presence of water, the PEO hydrogel coating absorbs water and swells, leading to a decrease in the refractive index surrounding the cladding. This change in the refractive index then results in a loss of power in the optical response and a dip in the optical spectrum. This scheme provides for on/off water detection only, since the hydrogel initially used was sensitive only to relative humidity levels higher than 95%. Though this sensitivity for the existing sensor configuration was deemed sufficient for application to detection of moisture intrusion beneath a corrosion protection finish (since moisture would be in direct contact with the sensor if the finish was compromised), an investigation of the practical limitations on measurement range and sensitivity of the moisture sensor was warranted.

To accomplish these investigations, alternative compositions of polymer coatings were considered so that measurement sensitivities to relative humidity levels lower than 70% were demonstrated. At the same time, we found that the modified sensors provided a measurable shift in the frequency at which the spectral loss occurs, as a function of relative humidity. Figure 3-13 illustrates the shift of spectral loss of the newly refined moisture/humidity sensor. As shown, the spectral loss dip shifts to higher frequencies with increased relative humidity. In addition to indicating the presence of moisture in the vicinity of the sensor, with appropriate calibration, the sensor can now be used to quantify the relative level of moisture content in contact with the sensor. This has significant implications in the application to health monitoring since previously water had to be in direct contact with the sensor in order for moisture to be identified.

The plot shown in Figure 3-14 shows the shift in the spectral loss dip of the refined moisture sensor as a function of exposure to moisture. As the level of moisture content in the vicinity of the sensor increases, the wavelength of the spectral loss minima increases; conversely, the wavelength of the spectral loss dip decreases as the relative moisture content surrounding the sensor decreases.

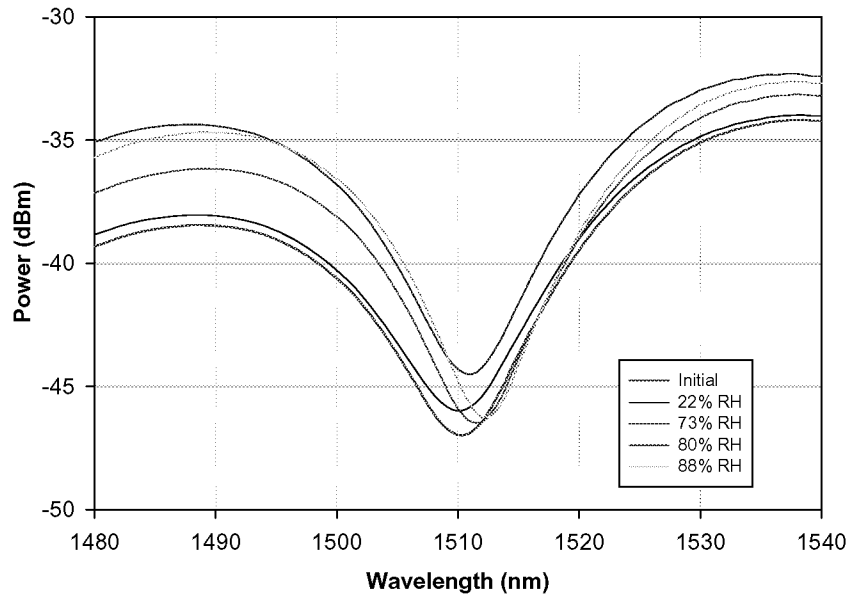


Figure 3-13. Sensogram plot showing response of LPG-based RH sensor increased relative humidity.

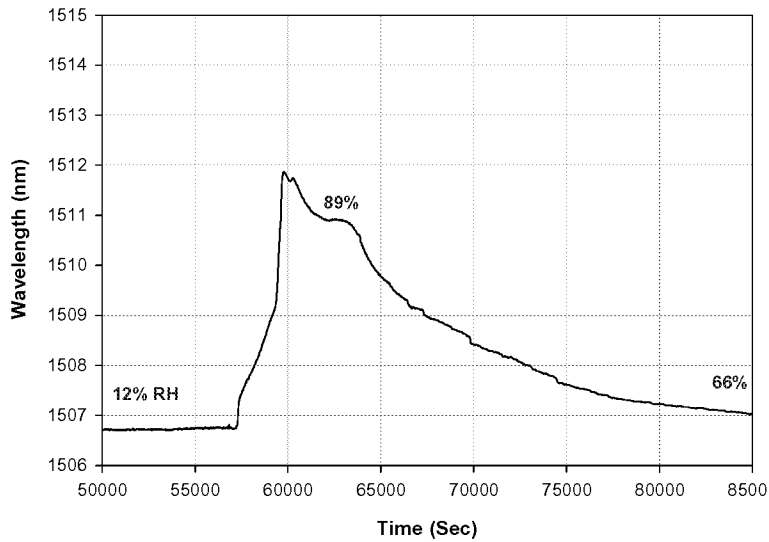


Figure 3-14. Plot of spectral loss wavelength as a function of time showing response of LPG-based humidity sensor due to increased relative humidity.

The manufacturer provides an internal calibration and calibration codes that translate wavelength to relative humidity (RH). These codes can be entered into the software and calculated and logged with time. Real-time RH data can be acquired by using the calibration codes to calculate and log the relative humidity.

3.2.2 LPG Metal Ion Sensor

In order to sense the metal ions associated with corrosion by-products, a chelating polymer coating with an affinity for 2^+ metal-ions is applied to the surface of the LPG sensing element. When metal-ions are present they form inter-chain and intra-chain cross-links with the carboxyl groups in the chelating polymer, significantly reducing the phase volume of the polymer chains. This cross-linking increases the polymer density of the coating and results in an increase in refractive index at the surface of the fiber, causing a shift in the wavelength out-coupled by the LPG. This program tested the capability of the metal-ion sensor to detect various concentrations of Cu^{2+} , Mg^{2+} , and Fe^{2+} . These ions are corrosion by-products for aircraft-grade aluminum alloys and structural steel alloys.

The LPG-based metal-ion sensor can be tailored for increased sensitivity to metal-ion concentrations or increased saturation levels. Figure 3-15 shows a typical response of an LPG-based metal-ion sensor to various concentrations of CuSO_4 . The sensors were exposed to 1 milli-molar (mM), 2.5 mM, and 5 mM concentrations of CuSO_4 for approximately 100 seconds. There was an apparent difference in the kinetic response (slope of the curve and equilibrium state) for the various concentrations. The sensor exhibited an 11 nm shift during the first 50 seconds for the 1 mM concentration solution, a 20 nm during the first 50 seconds for the 2.5 mM solution, and a 20 nm during the first 50 seconds for the 50 mM concentration. This indicates that the sensor saturated at ion concentrations between those present in 2.5 mM and 5 mM CuSO_4 solutions.

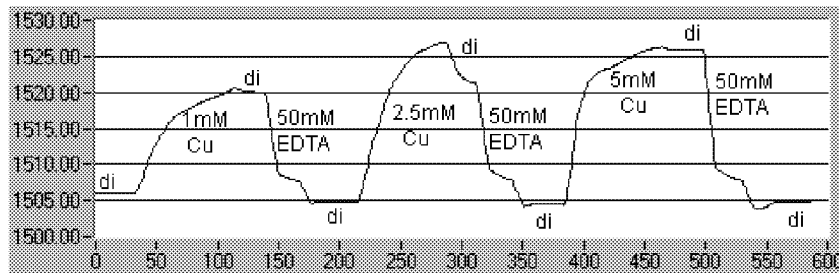


Figure 3-15. Metal-ion sensor response (Wavelength in nm vs. time in seconds) exposed to different concentrations of CuSO_4 before soaking in water.

Figure 3-16 shows the repeatable response of a metal-ion sensor to 10 mM CuSO_4 . The sensor displays very good repeatability with no indicated loss of sensitivity over time or regeneration cycles.

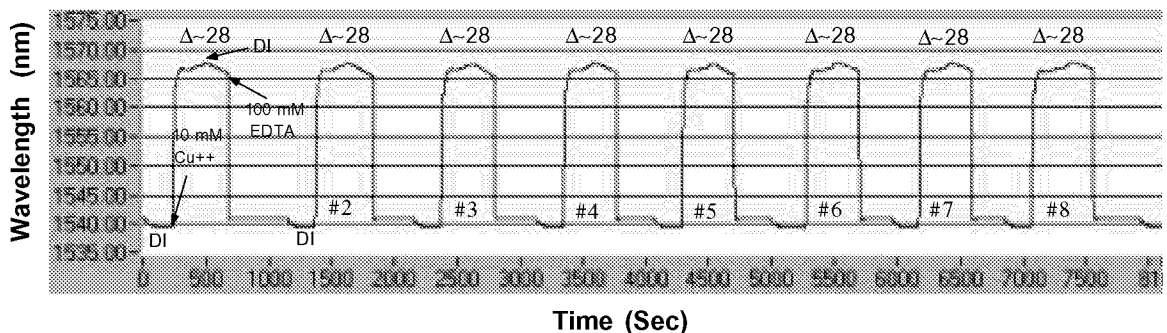


Figure 3-16. Repeatable response of a metal-ion sensor to 10mM concentration of CuSO_4 and regeneration with EDTA.

The LPG-based metal-ion sensors are sensitive to all 2^+ metal-ions. To demonstrate this, the LPG metal ion sensors were exposed to solutions of various types and concentrations of 2^+ metal ions. As shown in Figure 3-17, the LPG metal ion sensor responds to MgCl_2 , exhibiting a 3.2 nm shift in 10 mM MgCl_2 with repeatable results. The plot shown in Figure 3-18 shows the response of the sensor to FeCl_2 , exhibiting a 53nm shift in 100 mM FeCl_2 , 38 nm shift in 50 mM FeCl_2 , 25 nm shift in 10 mM FeCl_2 , and 10 nm shift in 1 mM FeCl_2 .

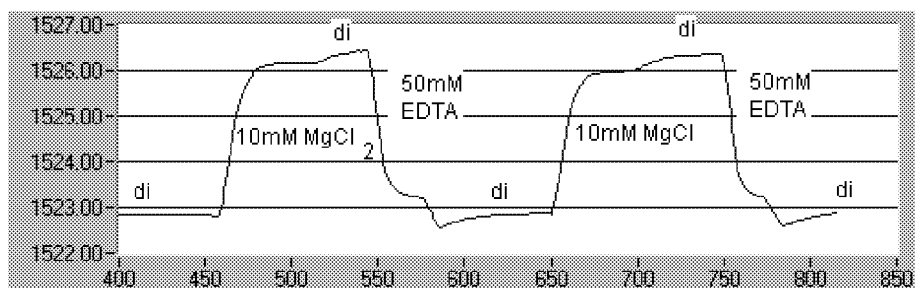


Figure 3-17. Metal-ion sensor response (wavelength in nm vs. time in sec.) exposed to 10 mM concentrations of MgCl_2 data acquired after soaking in DI water for 9 days and let dry.

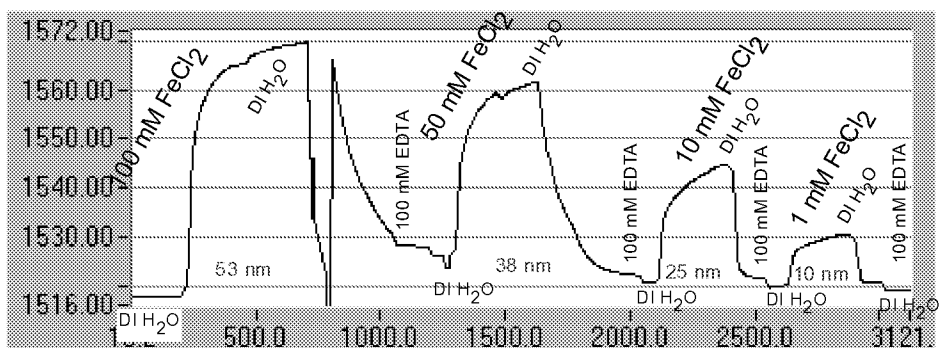


Figure 3-18. Sensogram (wavelength in nm vs. time in sec.) showing detection of various concentrations of Fe^{2+} .

The sensitivity of the metal ion sensor can be tailored to various concentrations of 2^+ metal ions. It is critical to know what concentration levels to expect or critical concentration levels to measure within the measurement environment. In previous experiments, the LPG-metal-ion sensor has been demonstrated to have a $10\ \mu\text{M}$ sensitivity to Cu^{2+} , a $0.5\ \mu\text{M}$ sensitivity to Fe^{2+} , and a $0.15\ \text{mM}$ sensitivity to Mg^{2+} .

3.3 COMBINED FAILURE MODES

As discussed in Section 2, individual faults (such as corrosion and fatigue damage) can interact synergistically to form a combined failure mode. Therefore, it is expedient to consider sensor systems that would allow measurement of multiple parameters and mechanisms.

A multimeasurand microsensor device, based on silicon micromachining and EFPI technologies, has been developed and demonstrated as a custom prototype. A description of the development of the prototype multimeasurand microsensor follows.

3.3.1 Multimeasurand MicroSensor Development

Microcantilever beams, typically used in atomic force microscopy (AFM), are extremely sensitive to mass loading. The force constant of the beam, which depends on the overall dimensions and material properties, defines the mass loading sensitivity. Figure 3-19 shows the dimensions of the cantilever beams used in the prototype sensor development. These cantilevers were adapted and fitted with optical demodulation to create single-point multi-measurand sensors for parameters such as temperature, vibration/acoustic emission, and moisture.

The sensing elements consisted of micromachined micro-cantilever beams attached to a silicon base. The cantilevers were positioned over optical fibers with end faces polished to a 45° -angle. A V-groove was made in the base using anisotropic etching to accurately position the optical fibers beneath the cantilever beams. The end faces of the optical fibers were angle-polished at 45° so that the light would propagate perpendicularly out of the fiber. The light reflected off of the cantilever surface and was coupled back into the fiber, creating an EFPI cavity. By measuring the length of this interferometric cavity, the deflection or movement of the cantilever was very accurately detected. When required for the desired measurement, the beams were coated on one side with a coating that was sensitive to the target environment in order to cause a tip deflection.

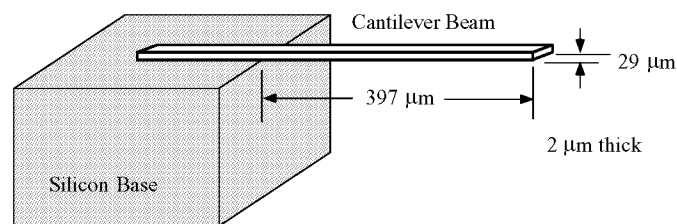


Figure 3-19. Dimensions of the cantilever beams used in sensor fabrication.

A temperature-sensing element was fabricated by coating one side of the cantilever beam with gold, which was polished to maintain good reflectivity. The differential thermal expansion between the gold-coated and uncoated surfaces of the cantilever caused a strain and resulting tip deflection with temperature. This temperature sensor was then cycled from 30°C to 90°C to determine the response characteristics of the beam with temperature. The temperature response is shown in Figure 3-20, showing an approximate 3.5nm displacement per 1°C change in temperature. The demodulation system had a 0.2nm resolution, resulting in a sensor resolution of 0.05°C.

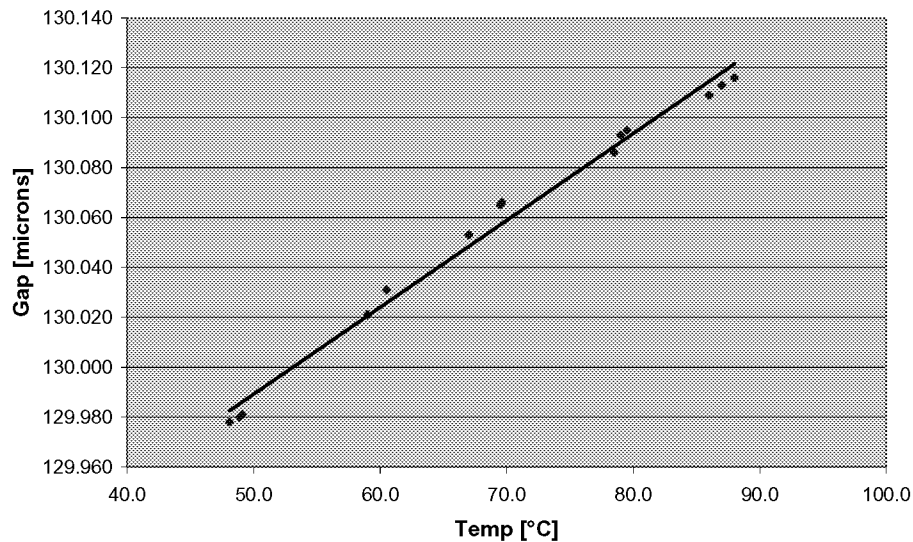


Figure 3-20. Temperature measurement using microcantilever beam and fiber optic demodulation system

A resonant-frequency out-of-plane vibration/acoustic emission sensing element was fabricated using micromachining technology. The sensitivity and resonant frequency of the sensors were precisely controlled through the micromachining process. A 120 kHz resonant frequency microcantilever vibration/AE sensing element was constructed and tested for sensitivity and frequency response. The sensor was mounted on a ¼”-thick aluminum panel using cyanoacrylate adhesive. A piezoelectric transducer was located on the panel and used to excite the sensor at known frequencies. The high-frequency (1 MHz) demodulation system described above was used to demodulate the sensor. The noise floor was found to be 50 mVpp, and the maximum detected signal was approximately 1 Vpp, yielding a signal to noise ratio of 13 dB. The frequency response of the sensor was isolated around the resonant frequency of the cantilever with a bandwidth of approximately 20 kHz, as shown in Figure 3-21.

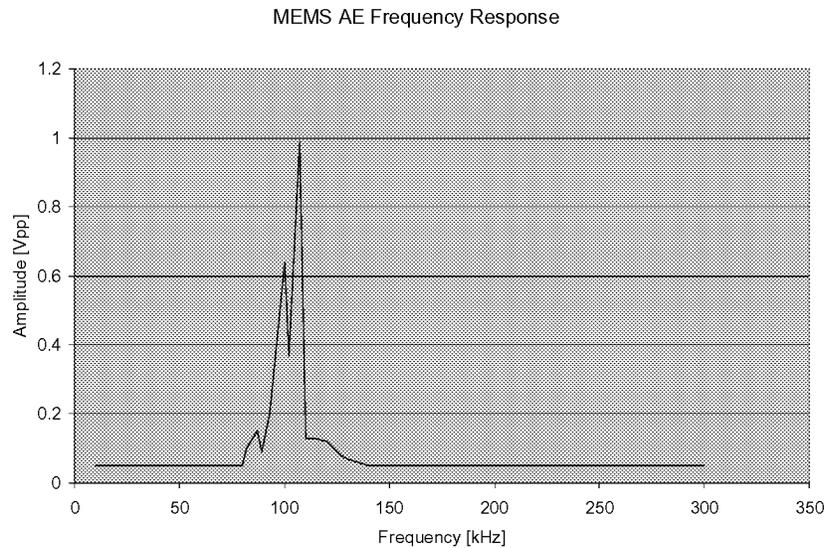


Figure 3-21. Vibration/AE sensor frequency response.

Finally, a moisture sensing element, shown in Figure 3-22, was fabricated. This sensor used collapsing hydrogel coatings, as described above for the LPG moisture sensors, on one side of the cantilever to cause tip deflection to detect the presence of moisture. The coatings swell in the presence of moisture, causing surface strain and a tip deflection that is measured by the optical interferometric system.

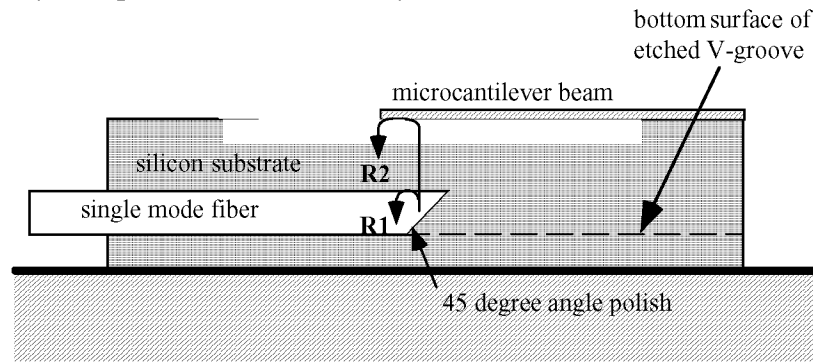


Figure 3-22. Interferometric displacement sensor for microcantilever beam moisture sensor.

In order to test the moisture sensing element, the sensor was mounted to a glass slide and cycled between the wet and dry states using de-ionized, purified water. The returned optical spectrums for the moisture sensor in the dry and wet states are shown in Figure 3-23.

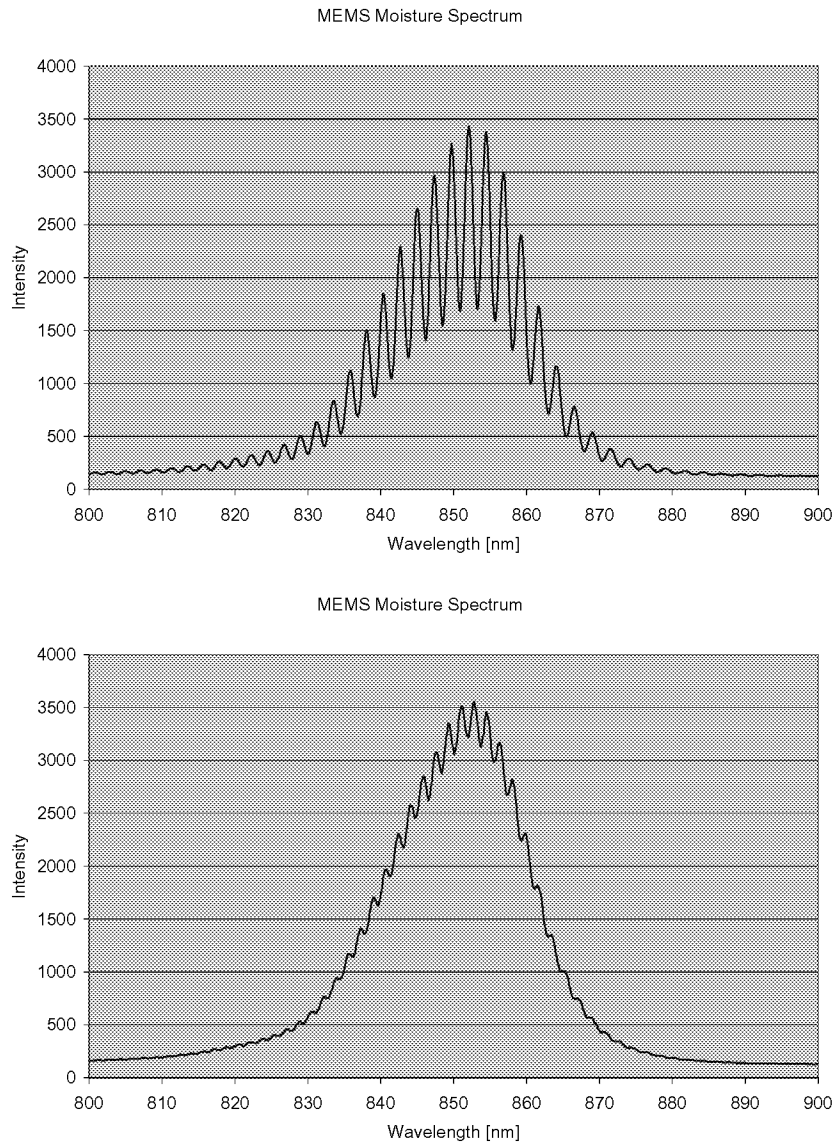


Figure 3-23. Microcantilever Moisture Sensor response in the dry (top) and wet (bottom) states.

The engineering value output (in terms of gap in microns) for the sensor in the dry state was measured to be 153 μm and 210 μm in the wet state. The engineering value output over a period of approximately 3 minutes for alternate wet/dry cycling is shown in Figure 3-24.

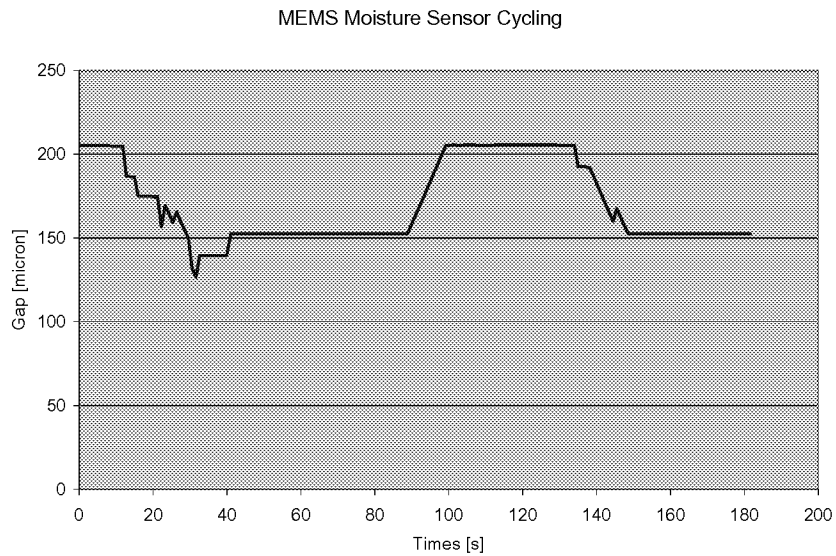


Figure 3-24. MEMS EFPI moisture sensor output.

3.4 ACCIDENTAL DAMAGE

The sensing approach for accidental damage would monitor for discrete damage incidents and trigger the appropriate sensors to characterize the extent of damage in case an event is detected. This program was focused on sensing and characterization of aging mechanisms for metal structure, not accidental damage. However, as described above, sensors developed for fatigue and corrosion detection and characterization might also be used to monitor accidental damage.

SECTION 4 SENSOR DEMONSTRATION AND EVALUATION

4.0 INTRODUCTION

The sensors described in Section 3 were evaluated to (1) validate their suitability for monitoring aging degradation, (2) characterize the sensor performance, including testing of operationally realistic configurations; and (3) demonstrate placement processes and multiplexing schemes. Corrosion sensors (i.e., LPG moisture and metal ion sensors) and fatigue sensors (i.e., EFPI strain and extension, Bragg grating strain, and EFPI acoustic emission sensors) were tested and evaluated under this program.

In this section, we describe the testing and results for embedded sensors in lap joint test specimens subjected to simulated corrosion and fatigue conditions. In addition, we describe the results of testing of the performance of corrosion sensors when subjected to corrosive inhibitive coating characteristic of aircraft structure.

4.1 CORROSION SENSOR TESTING

Testing of the LPG metal ion and moisture sensors for detection of incipient corrosion or the presence of a corrosive environment was performed. In these tests, we investigated the performance of the sensors in a simulated lap joint structure exposed to a corrosive environment. In addition, we evaluated the performance of the sensor under several corrosive preventative coatings, characteristic of those used to inhibit corrosion in aircraft structure.

4.1.1 Simulated Lap Splice Testing

Detection of incipient corrosion in inaccessible areas of an aircraft structure is one of the keys to an effective corrosion management strategy. For example, early detection of corrosion in lap joints is particularly valuable because small amounts of corrosion cannot be seen from the surface but can combine with fatigue-induced defects to accelerate damage to the structure. Therefore, researchers at the University of Virginia (UVa) have conducted experiments to validate the detection capability of LPG-based metal ion sensors in simulated lap joints.

Luna Innovations and UVa used chloride or sulfate salts and a modified lap joint simulant solution (20 mM chloride as AlCl_3 , plus 4 mM nitrite, 4 mM bicarbonate, and 2 mM fluoride as the sodium or aluminum salts, pH ~ 9) to calibrate the metal ion sensors. Sensors embedded in 2024-T3 aluminum alloy simulated lap joints were exposed to CuCl_2 solution (contains Cu^{2+} ions), HCl solution (aggressive corrosion environment), and water (benign environment). The simulated lap joint used in these studies is shown in Figure 4-1.

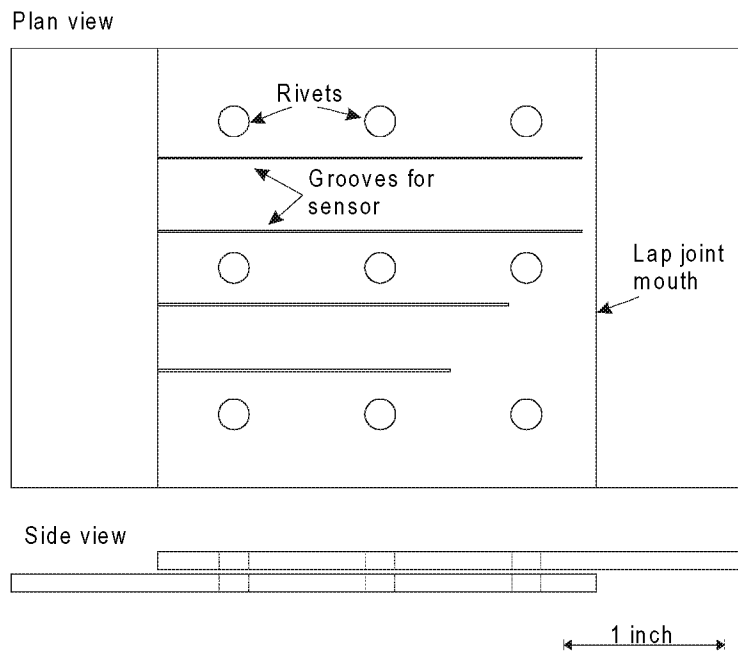


Figure 4-1. Schematic of non-clad 2024-T3 simulated lap joint.

In order to validate the ability of the metal ion sensor to detect 2+ ions, the simulated lap joint was exposed in a 10 mM CuCl_2 solution. The entire exposure cycle, shown in Figure 4-2, consisted of a pre-exposure test of the sensor (detailed in Figure 4-3), assembly of the sensor in the lap joint, exposure by partial immersion in CuCl_2 solution, and post-exposure testing (detailed in Figure 4-4).

As shown in Figure 4-2, and in finer detail in Figure 4-3, the metal ion sensor responded to exposure in the CuCl_2 solution. Not long after initial exposure, a sharp increase in the wavelength minimum, associated with the mechanical effects of the constraint of the sensor element within the lap joint, was noted. After one hour of exposure, the lap joint was moved to a dry beaker, and after about 17 hours in air the lap joint was re-immersed in the Cu^{2+} solution for another six hours. After another 30 minutes exposure to ambient air, the lap joint was disassembled and cycled through the solutions as shown in detail in Figure 4-4. The initial post-exposure signal in water, which was greater than that of post-exposure in 10 mM CuSO_4 , was biased by the level of Al^{3+} ions from corrosion and Cu^{2+} remaining at the sensor.

To demonstrate the ability of the metal ion sensors to detect corrosion products in situ, it was imperative that the test article be exposed in a solution corrosive to aluminum and aluminum alloys, but also one that did not cause an independent response from the sensors. A 1 mM HCl environment satisfied these criteria. Sensor response to the HCl solution within the lap joint would be negligible because the metal ion sensors did not respond to the presence of solutions with H^+ or Cl^- ions.

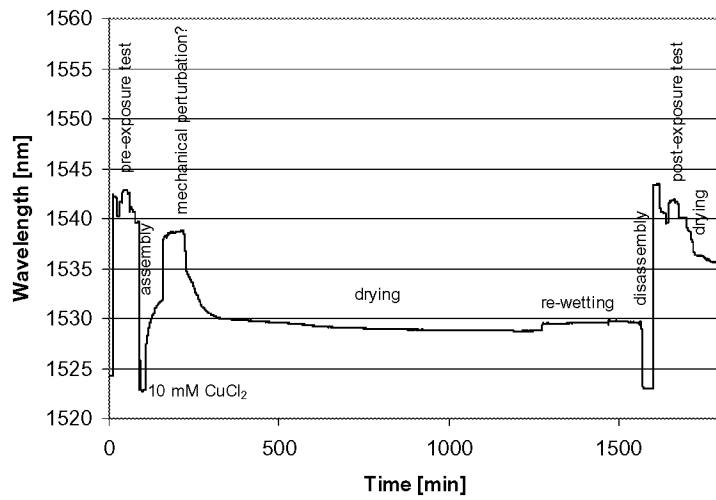


Figure 4-2. Exposure sequence and response of LPG-based metal ion sensor in lap joint exposed to 10 mM CuCl₂.

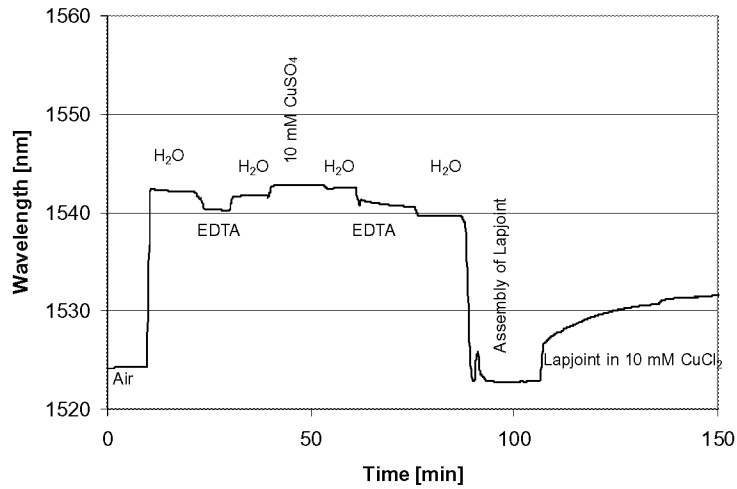


Figure 4-3. Detail view of initial part of Figure 4-2 showing pre-test calibration with Cu²⁺ ion solutions, water and EDTA (for sensor regeneration).

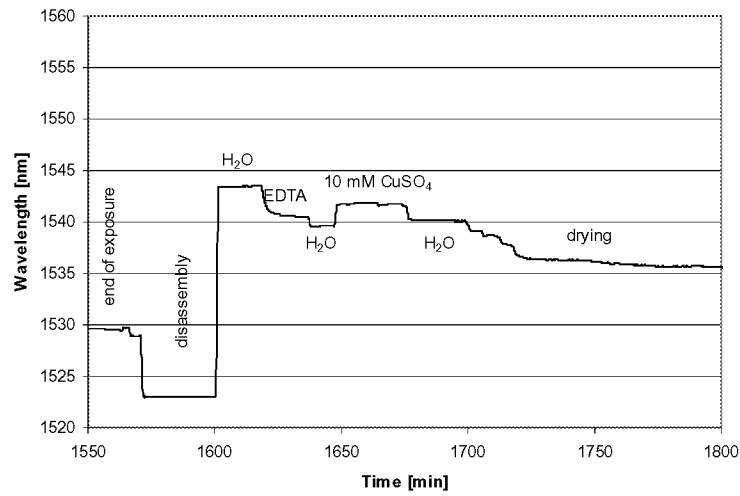


Figure 4-4. Detail view of post-test analysis with Cu^{2+} ion solutions, water and EDTA (for sensor regeneration).

The instrumented lap joints exposed to 1 mM HCl (Figure 4-5) showed an initial rapid increase in spectral loss wavelength due to moisture exposure and a subsequent gradual increase in spectral loss dip wavelength after 80 hours exposure. These results indicate that the LPG-based metal ion sensors are capable of detecting the presence of corrosion by-products (i.e., cations) within an occluded region such as lap joint.

As shown in Figure 4-6, no increase in the wavelength of the spectral loss minimum was observed after the initial increase due to moisture exposure for the lap joint exposed to pure water.

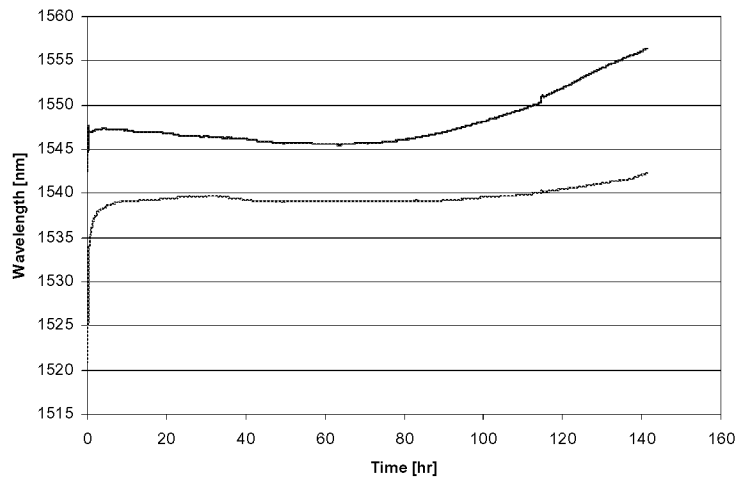


Figure 4-5. Signal response from two metal ion sensors embedded in the same lap joint and partially immersed in 1 mM HCl.

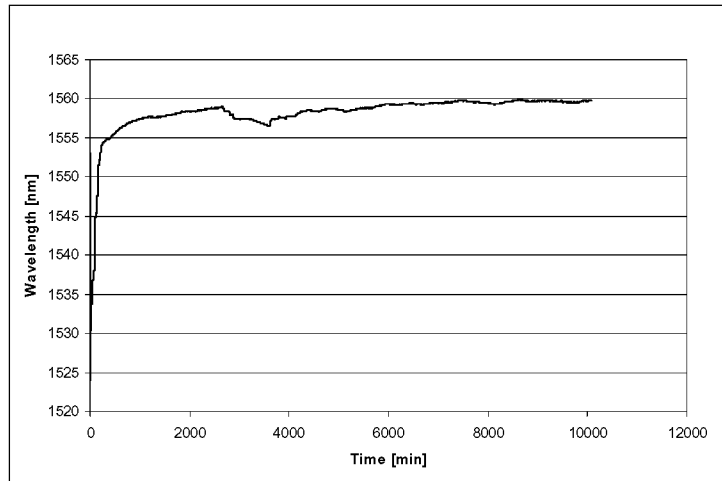


Figure 4-6. A single metal ion sensor embedded in a lap joint and partially immersed in high purity water.

Concentration calibrations for metal ions of interest (Cu^{2+} , Al^{3+} , Mg^{2+} , Zn^{2+}) were inconclusive because of difficulties in fabricating sensors with reproducible sensitivity. These difficulties arose from changes in the coating procedure for the sensors fabricated for validation testing from those used in previous tests. Although the metal-ion sensors that were demonstrated in validation testing were verified to respond to 2^+ ion solutions, quantitative measurements of ion concentration were not demonstrated.

4.1.2 Sensor Performance under Coatings

As was described in the previous sections of this report, corrosion management in commercial aviation is expected to include assessment of the continued integrity of preventative coatings^e used to inhibit corrosion. Such finishes, including CPCs, paints, and sealants, are intended to limit moisture intrusion so that aircraft structure is not subjected to conditions favorable to the formation of corrosion. For health monitoring, sensors may be placed beneath a CPC in order to monitor the integrity of the corrosion inhibitor. However, since the functionality of LPG-based corrosion sensors are based on interaction of the sensor with a surrounding media, it is important to determine what, if any, effect the presence of the finish itself may have on the sensor response.

The objective of this experiment was to determine the effects of three aircraft finishes (CPC, aircraft sealant, and aircraft primer) on the operation of embedded LPG-based corrosion sensors. As baseline, the optical response from bare LPGs (i.e., LPG having no affinity coating) were measured upon immersion in water as well as each of the finishes. Beyond this baseline, two additional configurations of LPG-based sensors were evaluated:

^e Throughout the discussion of these tests, the corrosive protective coatings will be referred to as *finishes* to minimize confusion between the sensor coating and corrosive inhibiting coating (finish) applied to the test article.

- PEO coated moisture sensors
- Carboxymethylcellulose (CMC) coated 2⁺ metal ion sensors.

Each of the three corrosive protective finishes were applied to the LPG sensors, as described below. The test articles with LPG-based moisture sensors were then immersed in water for several months; the test articles with LPG-based metal ion (cation) sensors were immersed in a 100 mM CuSO₄ solution. A broad band light source was used to illuminate each fiber optic sensor and the optical response from the sensor was measured using an optical spectrum analysis. Effects of the finishes on the operation of the LPG were determined by analyzing the spectrum plots of the sensors over time in comparison to the original optical response of the sensors.

CPC Finish Preparation

- Individually dip-coat LPG sensors (bare, PEO coated, or CMC coated) into CPC bath.
- Repeat until finish fully covers LPG surface element.
- Visually inspect finish for full coverage over sensor element.
- Verify that the initial LPG sensor peak disappears to ensure complete coverage.
- Dry for 24 hours before immersion in solution.

Sealant Finish Preparation

- Individually dip-coat sensors in bath of aircraft sealant.
- Repeat until finish fully covers surface of sensor element.
- Visually inspect surface for full coverage.
- Dry for 48 hours prior to testing

Aircraft Primer Finish Preparation

- Adhere each sensor to glass slide, being sure to keep adhesive one half inch away from the LPG sensor element
- Paint LPG sensor and glass slide with aircraft primer.
- Visually inspect sensor element for full coverage.
- Dry for 48 hours prior to testing.

Recall that the theory of LPG operation suggests that a dip in the spectral content (a spectral loss peak) will be observed when the affinity coating (i.e., PEO or CMC coating) of the LPG sensor comes in contact with a lower index of refraction media. As previously mentioned, uncoated sensors were tested in water and metal ion baths, as a baseline. As expected, with no affinity coating on the sensor no spectral loss peak was observed (see Figure 4-7), regardless of the type of finish applied. This verifies the expected result that the uncoated LPG alone is unresponsive to changes in the surrounding media.

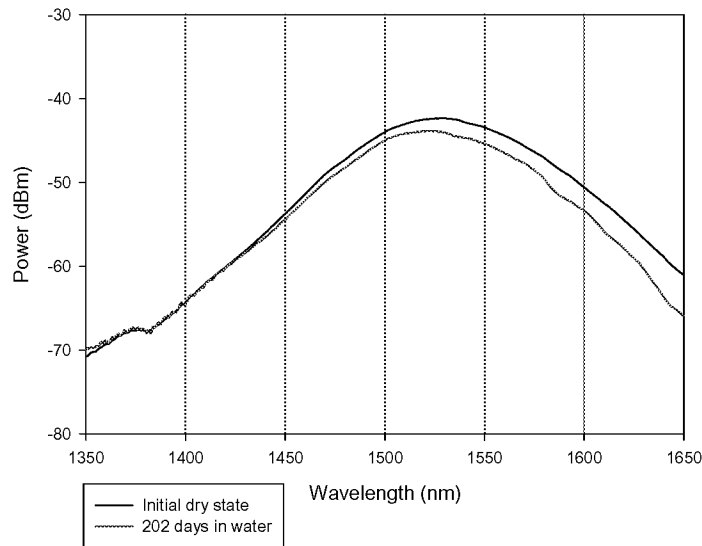


Figure 4-7. Initial and water-exposed results for bare LPG sensors coated with CPC.

Alternatively, when the sensor is clad with an appropriate affinity coating, a spectral loss minima is expected to be observed when the sensor comes in contact with a lower index of refractive media. Each of the finishes used in these experiments has a relatively *high* refractive index resulting in an initial reduction of the spectral loss peak in the optical response of the sensor. This was observed for all sensors/finish configurations. When the lower refractive index water or metal ion solution penetrates the finish to come into contact with the LPG sensor element, a spectral loss peak will be observed in the optical response. Therefore, spectral loss peaks are indicative of a sensor response to the presence of water or metal ions in contact with the sensor element. The test results, summarized in Table 4-1, indicate that embedded sensor elements were able to sense target molecules that were able to penetrate the corrosion protection systems.

Table 4-1. Summary of Experimental Results for Coated LPG Sensing Elements

	CPC	Aircraft Sealant	Aircraft Primer
Bare LPG sensors in water	0/4 sensors exhibit spectral loss peak	0/3 sensors exhibit spectral loss peak	0/2 sensors exhibit spectral loss peak
LPG-based moisture sensors in water	0/4 sensors exhibit spectral loss peak	3/3 sensors exhibit spectral loss peak	2/4 sensors exhibit spectral loss peak
LPG-based metal-ion sensors in CuSO ₄ solution	0/3 sensors exhibit spectral loss peak	1/2 sensors exhibit spectral loss peak	3/3 sensors exhibit spectral loss peak

To understand these results, it was necessary to consider the effectiveness of the coating at preventing intrusion of the moisture or the metal ion solution to the underlying sensor, as well as the effect of the finish on the sensor response. That is, a lack of response (i.e., no observed spectral loss peak) in a sensor could be interpreted as either (1) the sensor did not respond to the presence of the target molecule after the given finish was applied,

or (2) the finish provided an effective barrier to water or metal ion penetration. These considerations are discussed in further detail below.

Representative plots showing the sensor performance and response compared with initial conditions are shown in Figures 4-8 and 4-9 for the test articles coated with aircraft sealant. All three LPG-based water sensors responded within 18 days, indicating that water or Cu^{2+} had penetrated to the sensing element. In addition, one of the two LPG-based metal-ion sensors responded to the presence of copper in 57 days. Specifically, the results indicate that:

- LPG-based moisture sensors coated with aircraft sealant showed a distinct spectral loss minima within 18 days after water exposure (Figure 4-8). The wavelength of the minima shifted to lower wavelengths for the first 45 days, after which the spectral loss dip stabilized to a constant position. The initial response in 18 days resulted from the PEO coating first being exposed to water. The peak gradually shifted left as the moisture content at the surface of the LPG increased and the PEO coating reached saturation.
- One of the LPG-based metal ion sensors coated with aircraft sealant showed a small spectral loss after only two days immersion in a 100 mM CuSO_4 solution. The loss increased over time and a distinct peak became apparent after 57 days (Figure 4-9). The peak began to decrease in power from 57 days until the end of the testing period. The second test of LPG-based metal-ion sensors also indicated a spectral loss around two days that increased to its maximum at 57 days, but never became a well-defined peak. The loss began to decrease in power from 57 days until the end of the testing period. The finish thickness of the sealant varied slightly between sensors and may have been the reason that only one of the two sensors displayed a well-defined peak. The decrease in the spectral loss for both sensors after 57 days was attributed to degradation in the reflective gold coating on the end face of the fiber from the CuSO_4 solution.

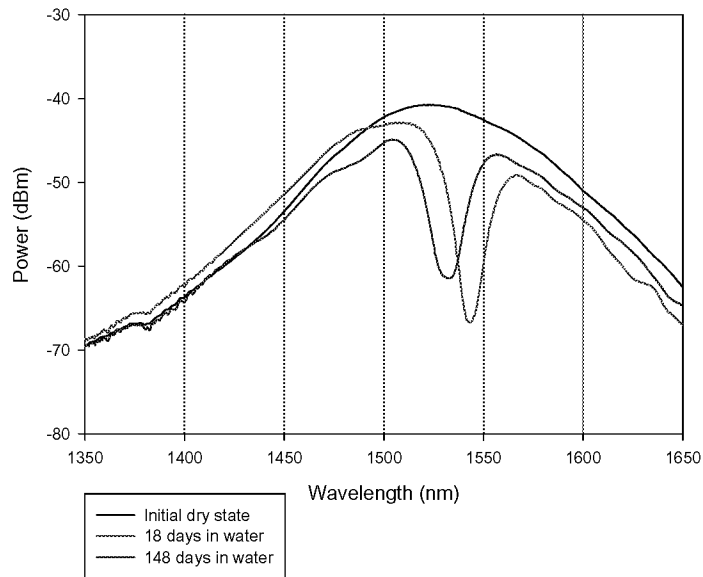


Figure 4-8. Initial and water-exposed results for LPG-based moisture sensors coated with aircraft sealant.

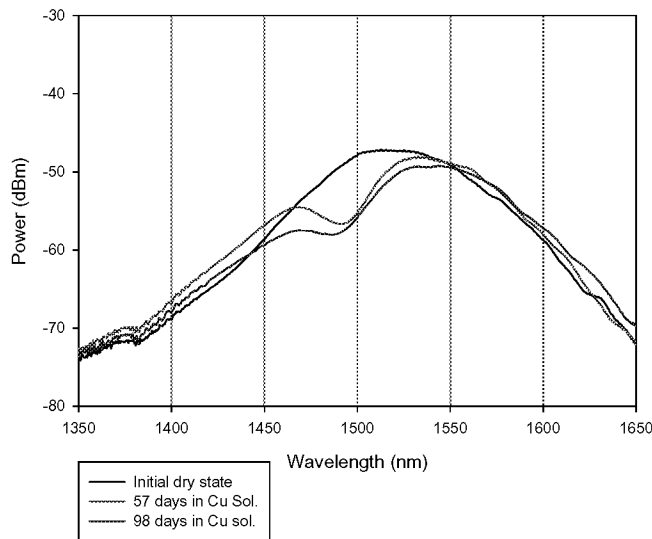


Figure 4-9. Initial and CuSO₄-exposed results for LPG-based metal ion sensors coated with aircraft sealant.

Representative plots showing the sensor performance and response compared with initial conditions are shown in Figures 4-10 and 4-11 for the test articles finished with aircraft primer. Two of the four LPG-based moisture sensors responded in only 18 days. In addition, all three of the LPG-based metal-ion sensors responded in 57 days.

Epoxy-based aircraft primers, by themselves, are not generally considered to be effective barriers to moisture penetration. In fact, in aircraft applications, the corrosion protection in primers is usually derived from addition of corrosion inhibitors to the primer

formulation. Therefore, in these experiments, we expect the sensors should indicate moisture or metal ion intrusion. Specifically, the results indicate that:

- Two of the LPG-based moisture sensors coated with aircraft primer showed a distinct appearance of a peak after 18 days immersion in water (Figure 4-10). The peak became more defined by 43 days and remained constant for the remainder of the testing period. These LPG-based water sensors were able to detect the presence of water through the aircraft primer paint coating. The remaining two sensors also showed slight spectral losses over the entire testing period, but these losses are as well defined and did not qualify as an unambiguous response. Variability in surface preparation, primer application, or resulting finish thickness could have contributed to the difference in sensor response. Additional testing would be required to resolve these results.
- LPG-based metal-ion sensors coated with aircraft primer showed a distinct appearance of a peak after 13 days immersion in the CuSO_4 solution (Figure 4-11). These responses remained constant for the remainder of the testing period. The quick response of the metal-ion sensors indicates that both the primer and the CMC coating surrounding the LPG-based sensing element became saturated after a short exposure. The LPG based metal-ion sensors were able to detect the presence of Cu^{2+} ions through the aircraft primer.

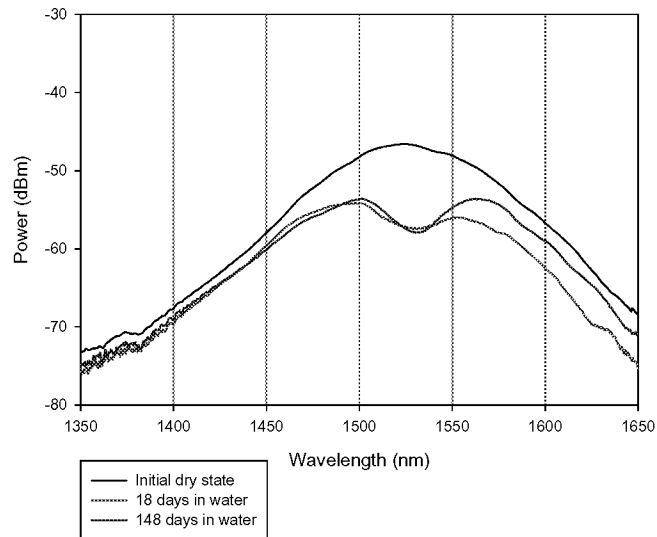


Figure 4-10. Initial and water-exposed results for LPG-based moisture sensors coated with aircraft primer.

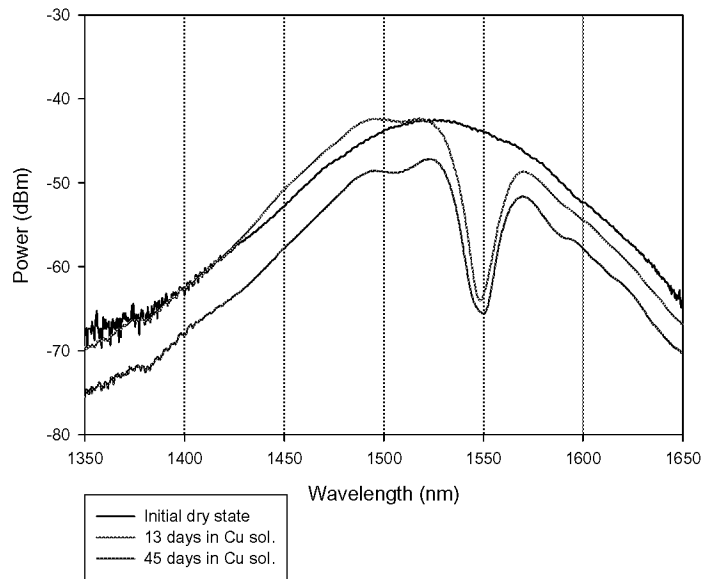


Figure 4-11. Initial and CuSO_4 -exposed results for LPG-based metal ion sensors coated with aircraft primer.

Finally, representative plots showing the sensor performance and response compared with initial conditions are shown in Figures 4-12 and 4-13 for the CPC coated test articles. The results indicate that:

- LPG-based moisture sensors coated with CPC showed a broad, shallow dip after 27 days water exposure, which became slightly more distinct throughout the remainder of the test (Figure 4-12). Though this dip represents a change in the optical response through the fiber sensor, it cannot be unambiguously identified as a spectral loss peak that is indicative of the presence of moisture.
- LPG-based metal-ion sensors coated with CPC showed no change with immersion in CuSO_4 solution for 98 days (Figure 4-13). These results indicate that the LPG sensing element did not indicate the presence of Cu^{2+} .

Independent research indicates that the CMC finish is often a quite effective barrier to short-term intrusion of corrosive environments. Therefore, it is likely that the CMC finish simply did not allow intrusion of the target molecules through the CMC to reach the LPG sensor. However, verification of this result would require removal of the finish and an independent chemical analysis for the presence of the specific constituents be performed.

Overall, the LPG sensors appear promising for detection of incipient corrosion or the presence of a corrosive environment even beneath characteristic aircraft finishes. However, these results do indicate that there is an apparent effect on the sensitivity of the LPG sensor response depending on the thickness of the finish; this must be further investigated in order to tailor the LPG sensor for a specific finish application.

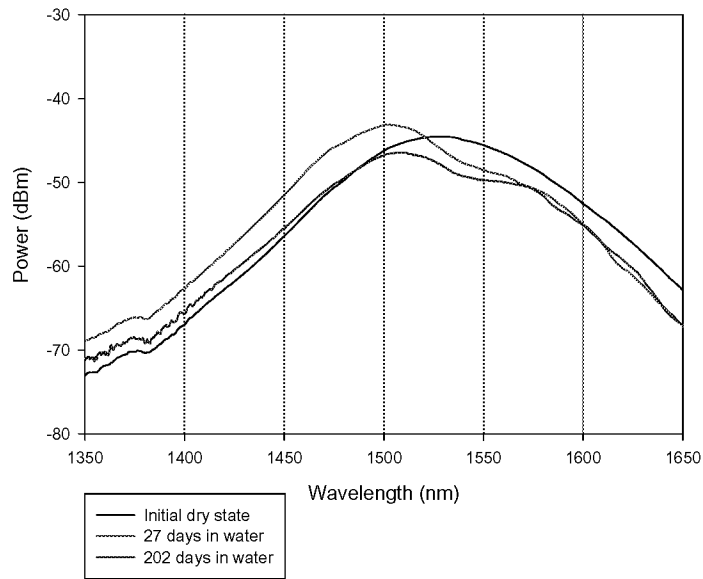


Figure 4-12. Initial and water-exposed results for LPG-based moisture sensors coated with CPC.

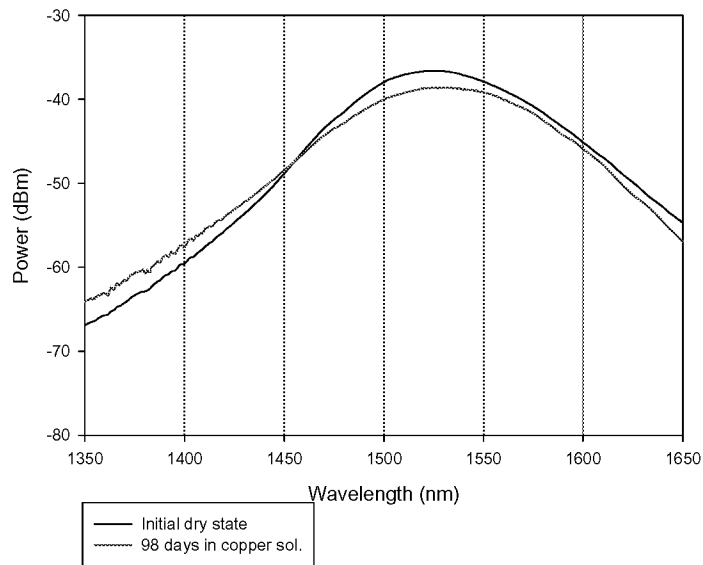


Figure 4-13. Initial and CuSO_4 -exposed results for LPG-based metal ion sensors coated with CPC.

4.2 FATIGUE SENSOR TESTING

4.2.1 Fiber Bragg Grating Sensors

Distributed fiber Bragg grating sensors (Froggatt and Moore 1998) were evaluated for monitoring fatigue crack growth in a sample designed to simulate a body lap splice. The purpose of this testing was to establish that an array of distributed Bragg grating sensors could be used to detect and characterize fatigue cracks by monitoring changes in strain distribution and signal response signatures.

The lap splice test articles were constructed to simulate a typical axial fuselage lap joint. The sample had three rows of rivets with 1-inch spacing. The initial EDM (electrostatic discharge machined) notches were 0.25 inch from either side of a selected fastener in the critical row. The initial test article configuration is shown in Figure 4-14.

Three distributed Bragg grating fibers were attached to the test article in accordance with the procedures outlined below. The gratings were distributed and numbered as shown in Figure 4-15. The sample was installed in an Instron test frame at the NASA Langley Research Center's Structural Test Laboratory and subjected to constant amplitude fatigue cycles (325 lbs to 6500 lbs; 10Hz). The cycling was stopped periodically so that strain surveys could be taken at minimum and maximum static loads. Crack length was measured using wide-field optical microscopy. Fatigue cycling was continued until catastrophic failure. (Note: Prior to beginning the test, it was discovered that one of the sensing fibers had broken. The decision was made to go ahead with the test and ignore the results from the failed sensors.)

Sensor Installation Procedure

- Degrease and clean surface using Hypersolve and alcohol.
- Mask and micro-sandblast using 50 micron Al_2O_3 abrasive powder.
- Remove abrasive powder residue and clean with alcohol.
- Spraycoat entire test area with M-Bond 600.
- Air dry 10 minutes at room temperature.
- Raise temperature to 200°F (Heating rate 4°F/min, maximum). Cure for 1 hour
- Clean the basecoat surface using alcohol.
- Mask and micro-sandblast the basecoat sufficiently to remove glazed appearance.
- Remove abrasive powder residue and clean with alcohol.
- Place the fibers on the surface such that the strain sensing (indexed) areas of the fibers are in the pre-determined locations.
- Tape sensor fibers in place per standard practice.
- Spraycoat the sensing fibers using M-Bond 600.
- Air dry 10 minutes at room temperature.
- Raise temperature to 200°F (Heating rate 4°F/min, maximum). Cure for 1 hour

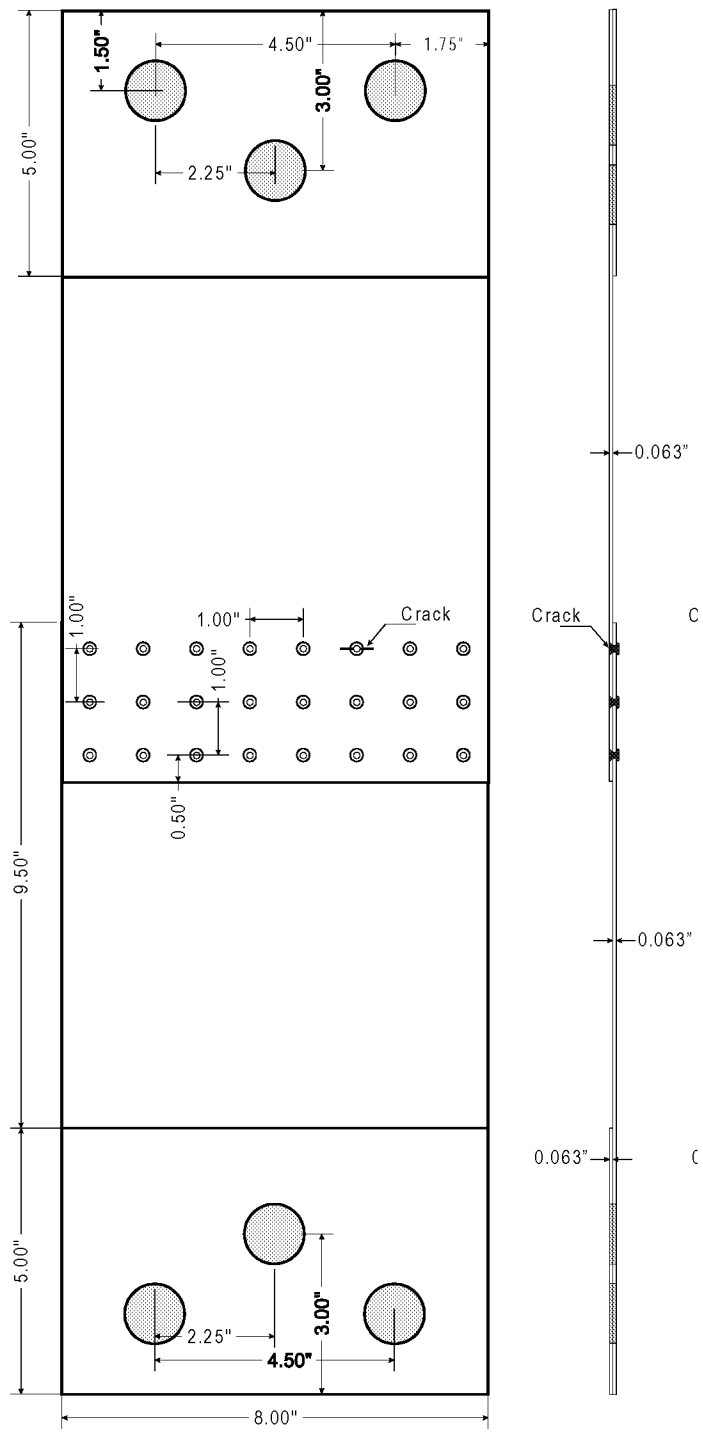


Figure 4-14. Simulated lap splice specimen. A 0.25 EDM cut was made at the indicated fastener (3rd fastener from right on top row) to act as a crack starter. The specimen was fabricated from 0.063 in. 2024-T3 aluminum sheet.

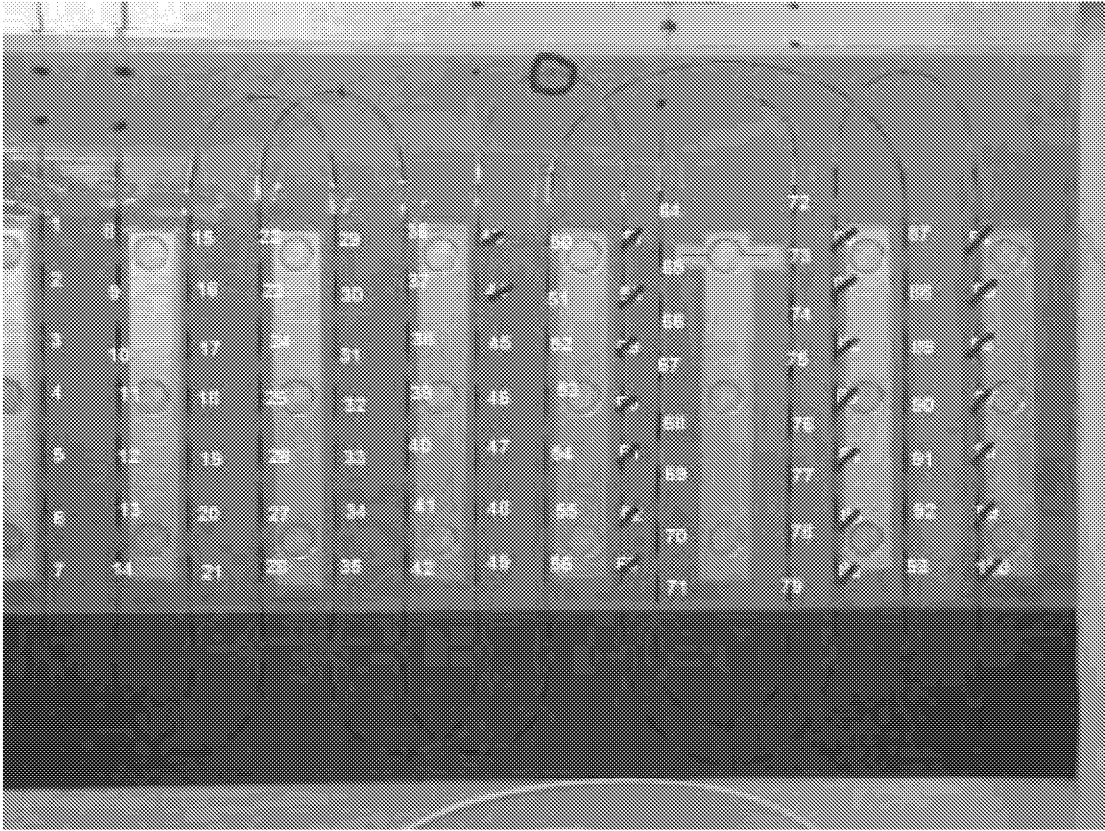


Figure 4-15. Bragg grating location and numbering. The gratings marked in red were ignored because the optical fiber was broken prior to the testing.

The data were post-processed using NASA-developed analytical tools (Childers et. al. 2001) to recover individual grating spectra and calculated strains. A typical grating spectrum is shown in Figure 4-16. Strain was calculated from the change in the characteristic wavelength (centroid of the grating spectra signal) compared with a baseline value.

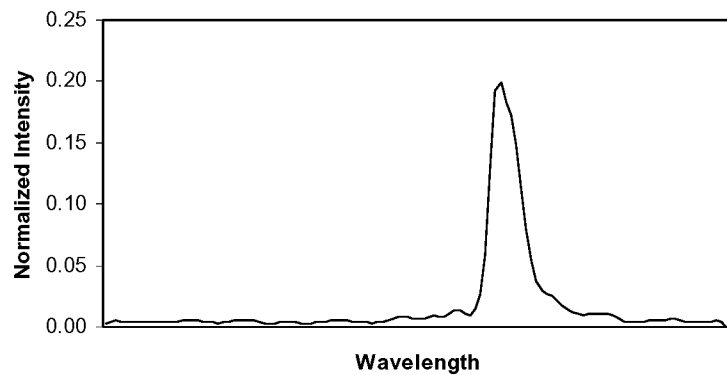


Figure 4-16. Typical grating spectrum.

Typical results from the strain survey for the sensors surrounding the notched fastener and an adjacent fastener are shown in Figure 4-17. The data show the fractional increase in strain as the crack initiates from the edge of the EDM notch and grows to, and past, the adjacent fastener.

These results were used to develop test logic and diagnostic inference models (DIMs), consistent with the ACAMS approach, to assess behaviors and relationships among sensors and the associated damage state (ARINC 2001). Tests were established by relating increases in measured strain to an observed damage. For many applications, DIMs can be expressed as single outcome models, either supporting or denying the existence of a particular fault. However, multi-outcome tests were required for this application because the test could suggest more than one fault condition (i.e., no fault, a small crack at an adjacent fastener, a large crack at an adjacent fastener, a large crack at a distant fastener, or a failed sensor), depending on the magnitude of the change in strain. A list of possible faults that could be supported or denied by each Bragg grating sensor location was developed for these multi-outcome tests. The dependencies among these outcomes were established and a DIM was coded and run on the developmental ACAMS processor using outcomes derived from the fatigue test results. The evidence supporting the existence of the identified faults was accumulated. The ACAMS processor was able to detect and isolate the fatigue cracks growing from the pre-existing notches and was able to detect when the cracks progressed to the fasteners adjacent to the fasteners.

Further analysis indicated a correlation between the test outcomes from the strain-based tests established for the dependency models and the recovered grating signals. Representative grating signals and their correlation with damage state test outcomes from the dependency model are shown in Figure 4-18.

The results of the initial testing of distributed fiber Bragg grating strain system indicate that distributed strain sensing can be utilized to detect and characterize the damage resulting from structural fatigue of a realistic structural element. The feature of the Bragg sensor that allows the system to be massively multiplexed offers the unique capability to provide detailed strain mapping throughout a region of interest, such as the vicinity of the crack tip. This has significant positive implications both for application to SHM when the exact location of a crack may not be known a priori, as well as for application for structural characterization under damage conditions. Such quantitative information can provide critical information to aid in an understanding of operational structural behaviors.

Additional detailed testing is underway to validate this approach, improve the understanding of the testing variables and their influence on sensor responses, and refine the diagnostic models.

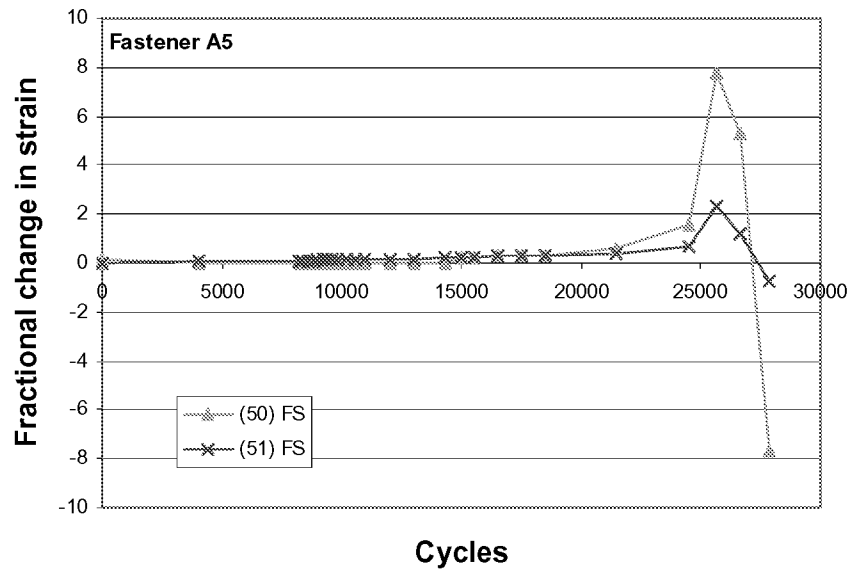
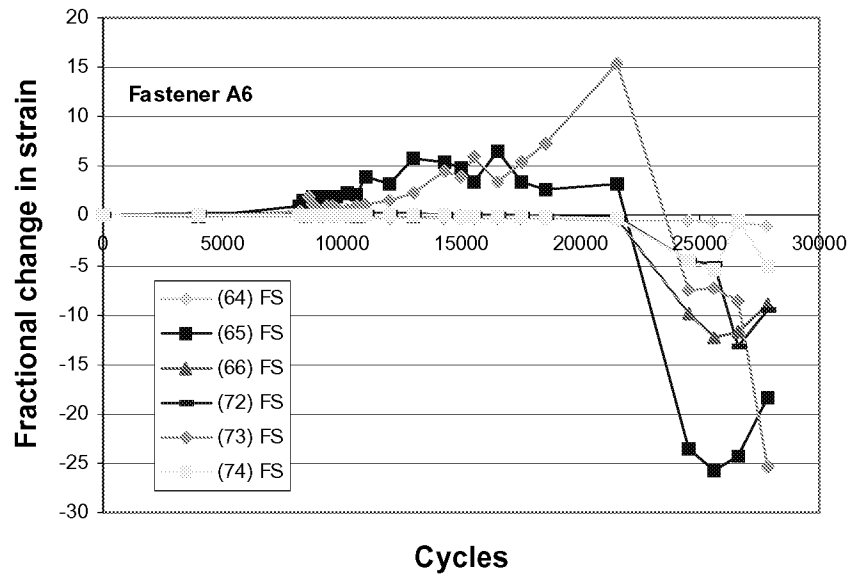


Figure 4-17. Fractional change in strain versus fatigue cycles for gratings surrounding the notched fastener (top) and an adjacent fastener (bottom). The strain increases as the crack approaches the sensor. Large negative changes were attributed to failure of the sensor fiber.

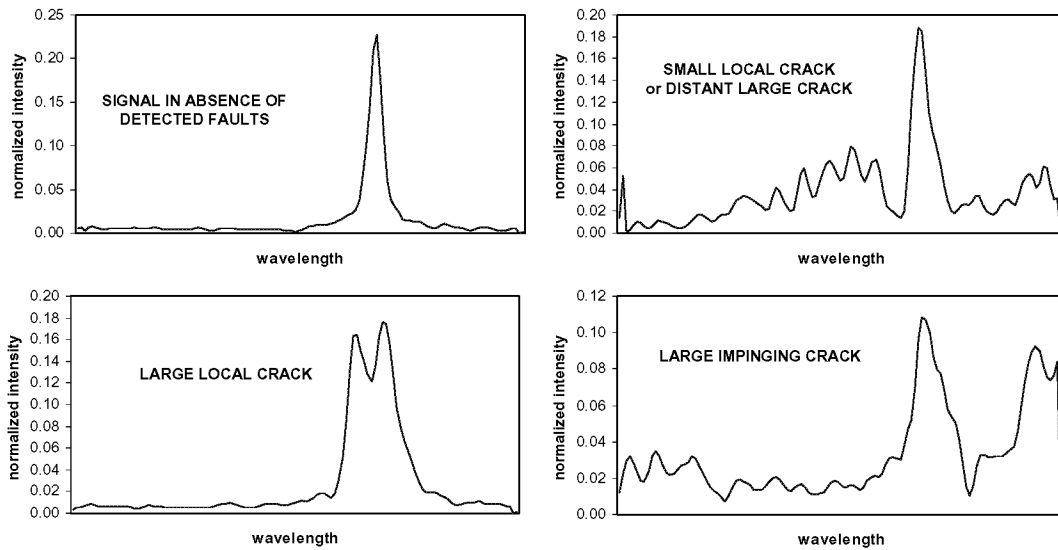


Figure 4-18. Recovered grating signals and the correlation with damage states.

4.2.2 EFPI Strain and Extensometer Sensor Tests

Test specimens (Figure 4-19) were machined from 0.125 in thick, 2024-T3 aluminum and 7075-T6 sheet with a center notch consisting of an EDM-notched 0.125-in. hole. Strain gage sensors and extensometers were attached to the center-notched tension specimen as shown in Figure 4-19. All sensors were oriented parallel to the principal load axis; one sensor between the notch and the load frame along the centerline of the sample that runs parallel to the principal loading direction (sensor #6) and the rest distributed along the centerline perpendicular to the principal load direction (sensors #1-5).

The coupons were subjected to constant amplitude fatigue (load control) until failure in a MTS fatigue test frame at Penn State University. Load cycles were applied at a frequency of 10Hz. Every 200 cycles, the cycle rate was reduced to 1Hz for three cycles to allow strain or crack length measurements to be taken. Because of the high cycling rates and resulting data rate requirements, strain sensor and extensometer measurements were accomplished by individual demodulation systems (as described above for EFPI sensors) and data were captured by the laboratory’s data acquisition system. Crack growth was monitored using a Questar QM100 step zoom long-distance microscope. Digital images were captured every 6,000–10,000 cycles and crack length was measured from the digital images.

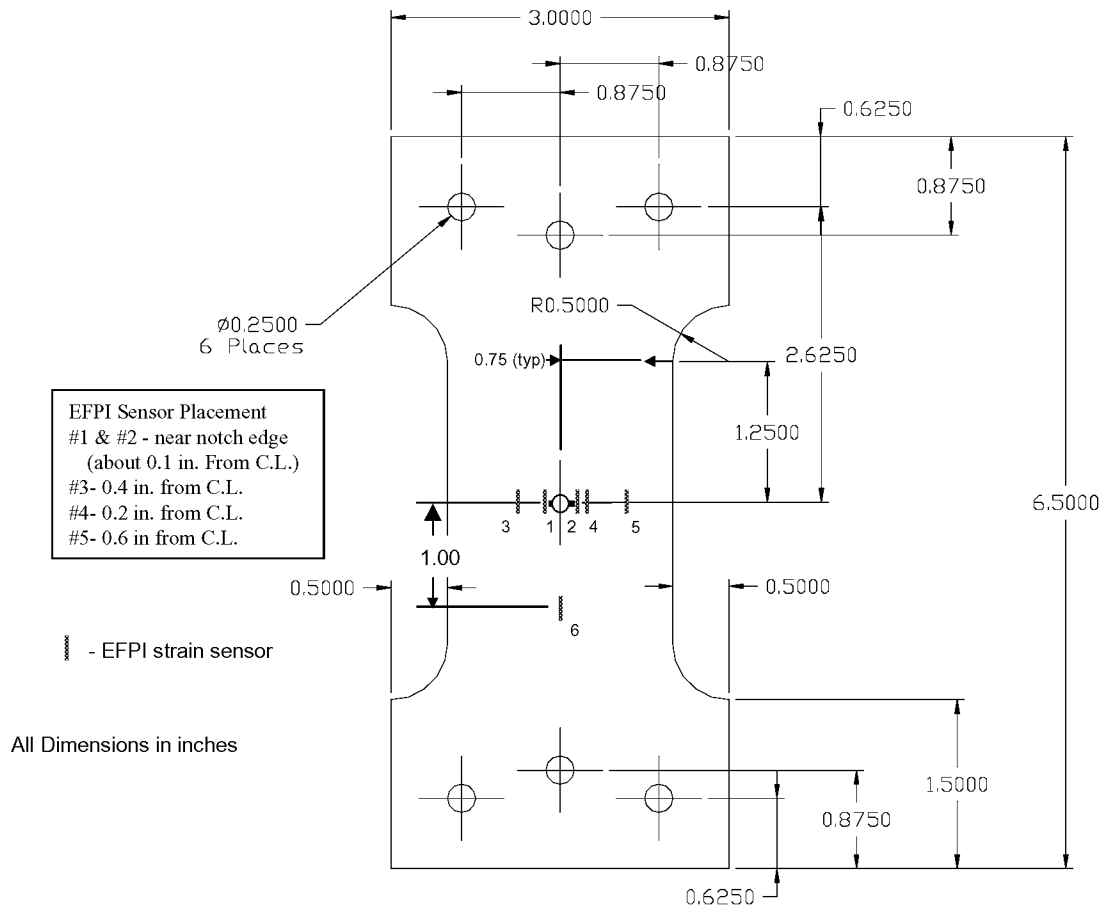


Figure 4-19. Sample configuration and sensor placement for center crack fatigue testing. Sensor 1 was an EFPI extensometer. All others were EFPI strain sensors.

The results from fatigue tests of center notched 2024-T3 and 7075-T6 samples are depicted in representative data in Figure 4-20, 4-21, and 4-22. Figure 4-20 shows strain measurements from sensors distributed along the likely crack path (i.e., distributed at the reduced cross-section) and remote from the notch area for 2024-T3 (Figure 4-20a) and 7075-T6 (Figure 4-20b) alloys. These data show a gradual increase in strain resulting from the reduced sample cross-section as the fatigue crack progresses, followed by a more rapid increase as the crack impinges on, and passes, the sensors. Figure 4-21 shows strain measurements from the sensor at the sample centerline parallel to the principal load axis. These data show a significant decrease in strain as the imposed strain is redistributed around the growing crack in the later phases of the test. Finally, Figure 4-22 shows the results from an extensometer placed near the notch of the 7075-T6 sample. These data show gradual increase in apparent strain (i.e., deflection averaged over the sensor gauge length) as the crack opens). The extensometer on the 2024-T3 specimen did exhibit this behavior, indicating that sensor placement near the notch was critical.

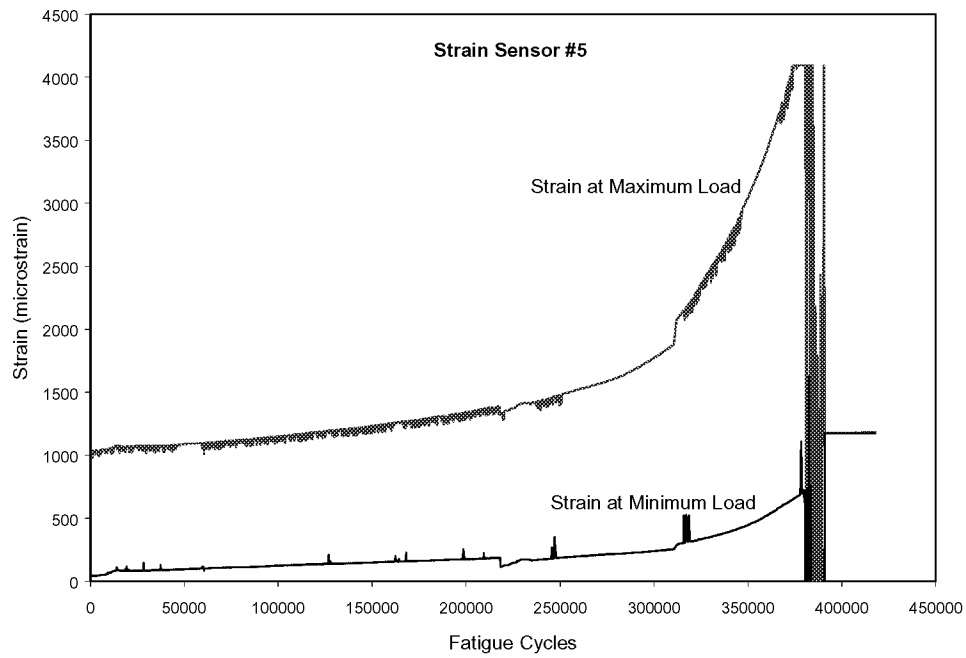
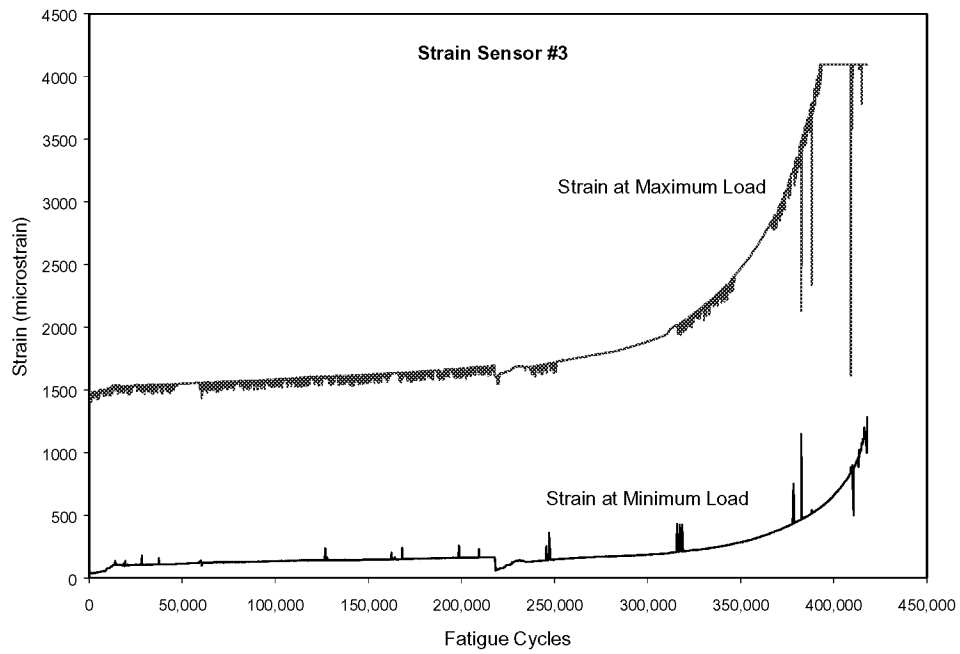


Figure 4-20a. Results from EFPI strain sensors 3 and 5 (placed along reduced cross-section remote from notch area) for 2024-T3 specimen.

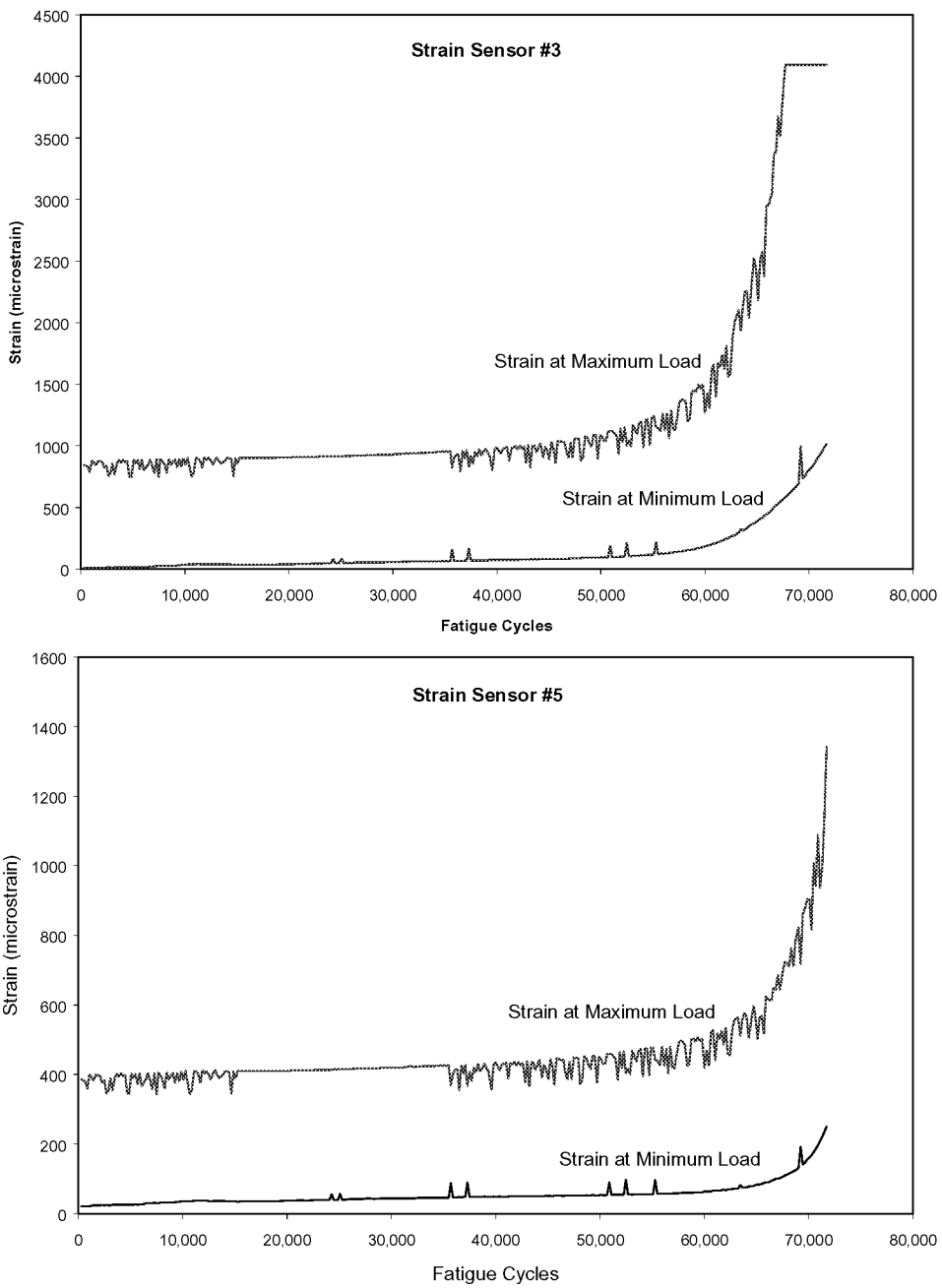


Figure 4-20b. Results from EFPI strain sensors 3 and 5 (placed along reduced cross-section remote from notch area) for 7075-T6 specimen.

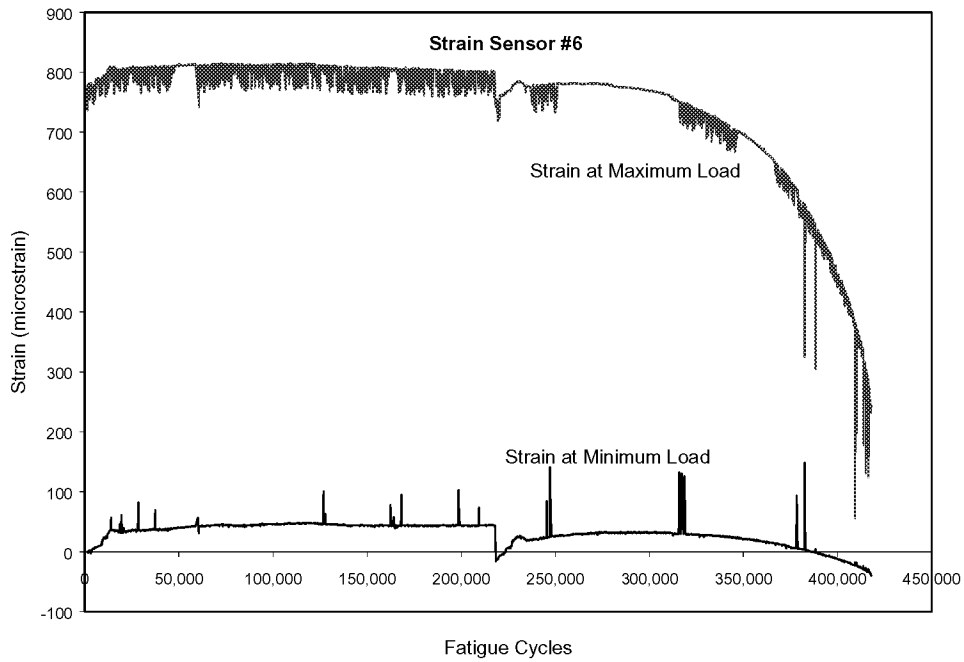


Figure 4-21. Strain vs. fatigue cycles for sensor #6, showing the decrease in strain as the applied load is redistributed around the growing fatigue crack.

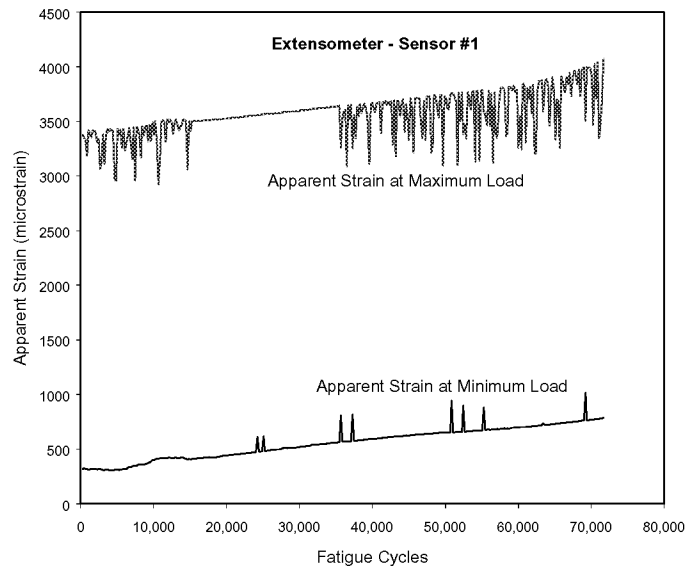


Figure 4-22. Apparent strain vs. fatigue cycles for sensor #1, showing the crack opening deflection of the growing fatigue crack.

The center-notch fatigue tests of EFPI strain sensors and extensometers showed that the presence of growing fatigue cracks could be inferred from information gathered from strategically placed sensors. The test results provided indication of load redistribution around a growing defect because the measured strains were shown to be sensitive to crack tip position. Although the results from extensometers were mixed, there are indications that they could provide a very important measure of crack opening deflection that would be helpful in monitoring critical crack growth.

4.3 TABLETOP SENSOR DEMONSTRATION

In addition to the detailed testing and demonstration of the sensor functionality under simulated fatigue and corrosion testing, the sensors developed under this program were demonstrated at the NASA Langley Research Center. These demonstrations, which occurred July 9-11, 2001, showed:

- The response of the LPG metal ion sensor to various +2 ion solutions. The sensors were shown to be fully recoverable after exposure to the ion solution.
- The EPFI AE sensor detection of a simulated impact on an aluminum substrate
- Multiplexed EFPI strain sensors using gap division multiplexing
- The LPG moisture sensor response to the presence of water.

In addition, a prototype single Si-chip, multi-microcantilever beam sensor consisting of three sensing elements and three fiber leads was fabricated for demonstration. The prototype sensor was demonstrated to monitor wet and dry moisture state, vibration/AE, and temperature. For the purpose of the demonstration, the sensing elements were monitored separately by independent demodulation systems.

Finally, in a related demonstration of the ARINC ACAMS capability, the data and sensor signals from the simulated lap joint fatigue testing described above were used to predict the behavior of the fatigue crack. In this final demonstration, using ARINC's proprietary prognostic algorithms, we were able to project the future location of the fatigue crack, on average, 4000 cycles prior to the actual propagation (ARINC 2001).

4.4 SENSOR SYSTEM IMPLEMENTATION CONSIDERATIONS

This section has summarized the sensor system testing for application to SHM. The results show that structural degradation of aircraft materials can be effectively detected and characterized using available sensors. As was described in the previous section, implementation of SHM systems will require the fusion of information from arrays of multiple sensor types acting in concert. Therefore, the ability to multiplex sensors and to combine different sensors into a coherent system is crucial to any future implementation.

Table 4-2 presents a summary of the integration capabilities for the fiber optic sensor technologies developed or evaluated under this program. The fiber optic sensors evaluated in this project operate on one of three wavelengths—830nm, 1300nm, and 1550 nm. Each sensor technology utilizes a separate band and therefore a different transmission fiber. As a result, in the current state of sensor technology multiple sensor types cannot be multiplexed on a single optical fiber.

Table 4-2. Summary of Current Fiber Optic Sensor Technology

Sensor Technology	Wavelength	Multiplexing	System Refresh Rate	Comments
EFPI Strain	830nm	8 channels, switched (see Note 1)	1 Hz	Using 1 Fiberscan + 1 Mux 8
		4 channels, in-line	15 Hz	Using 1 Fiberscan, in-line multiplexing
		1 channel	60 Hz	Using 1 Fiberscan
Acoustic Emission	1300nm	1 channel	400 kHz	Using 1 single-channel FOSS NDE system
LPG Corrosion	1550nm	8 channels, switched (see Note 1)	1 Hz	Using 1 Lunascan + 1 Mux 8
		3 channels, in-line	30 Hz	Using 1 Lunascan, in-line multiplexing
		1 channel	100 Hz	Using 1 Lunascan

Note 1 1x8 switched multiplexors can be cascaded in arrangements up to 64 sensors

The EFPI strain technology operates at 830nm source/fiber. Multiplexing of EFPI strain sensors can be achieved in two ways: 1) optical switching and 2) in-line multiplexing. Optical switching uses a MEMS device to circuit switch between fiber legs each having up to 8 sensors, polling each of these sensors using a single demodulation system in a round-robin fashion. Gap division multiplexing (GDM) can be used to provide serial, in-line multiplexing (i.e., placing more than one sensor on a single optical fiber) of EFPI strain sensors. Up to 4 EFPI sensors can be multiplexed using this technique. While a significant system cost saving per channel can be realized by multiplexing the number of sensors that share sources and demodulation systems, each multiplexing techniques degrades the system performance by reducing bandwidth in proportion to the number of multiplexed sensors.

The EFPI acoustic emission technology utilizes 1300 nm source/fiber and does not currently lend itself to multiplexing. As described earlier in this section, the EFPI AE sensor technology is based on an intensity system, which allows only one sensor per channel (or per fiber).

The corrosion sensor technology is based on the LPG concept and uses a 1550 nm source and fiber. Like the EFPI technologies, these sensors can be multiplexed through optical switching and in-line multiplexing. The current in-line multiplexing capability is limited to 3 sensors. As with the EFPI strain system, reduction in bandwidth is proportional to the number of multiplexed channels.

The distributed Bragg grating strain system is capable of measuring a large number of sensors (potentially, up to 10,000 strain sensors) along a single optical fiber, with a single demodulation system. This multiplexing capability results in the lowest projected system cost.

Although there are numerous benefits to spectral interrogation systems used in the EFPI and LPG technologies, there are some aspects of the design that effect measurements in flight environments. One significant drawback is the speed of the system, which is at least three orders of magnitude slower than relative interrogation systems (~100 Hz compared to >1 MHz). The source of the problem is the speed of the spectrometer internal to the system, which uses a CCD array to measure the intensities of the wavelengths. Although this is a problem in many applications where events occur faster than 100 Hz, and up to hundreds of kilohertz, the kinetics of low-cycle fatigue and corrosion processes on commercial aircraft make it unlikely that the system speed will become an implementation concern for the majority of applications.

Sensor system hardware considerations also need to be considered in an eventual implementation. The hardware requirements include a miniature spectrometer, a DSP processor card (DSP, peripheral components, A/D circuitry, etc.), and a laser diode source for each system. Currently, the light source and optical component technologies are based on available off-the-shelf components and are limited in their temperature tolerance and sensitivity. In the past, thermo-electric coolers have been used to compensate for the temperature extremes in service applications.

SECTION 5 SENSOR DATA INTERPRETATION

5.0 INTRODUCTION

A key component of the structural health monitoring capability is the ability to interpret the information provided by sensor system to characterize the structural condition. The diagnostic inference models described for the lap splice testing in the previous section represent one method for relating sensor outcomes to potential faults to assess the state of structural health. Physical models are another tool that will be required to establish system structural health and to project how structural degradation will likely progress.

This section describes a deterministic state-space fatigue growth model and stochastic model that accounts for the statistical nature of damage development processes. These models were developed to perform real-time characterization and assessment of structural fatigue damage.

5.1 STATE-SPACE MODEL OF FATIGUE CRACK GROWTH

Modeling of fatigue crack growth has been a topic of intensive research for several decades. Based on different experimental data, many models (e.g., Anderson 1995, Bannantine et al. 1990, Suresh 1991) have been proposed for fatigue life prediction. Fatigue crack growth models have been used for damage mitigating control of complex mechanical structures such as aircraft (Ray and Caplin 2000), rocket engines (Dai and Ray 1996; Holmes and Ray 1998), and power plants (Kallappa et al. 1997; Holmes and Ray 2001).

Modeling of fatigue crack growth under variable-amplitude loading usually relies on a memory-dependent physical variable (e.g., crack opening stress, or reference stress) that requires storage of information on the load history. In current state of the art of fatigue crack growth modeling, the finite interval over which the load history is considered to be relevant may vary with the type of loading as well as with the rules employed for cycle counting. Nevertheless, this memory-dependent variable can be modeled in a finite-dimensional state-space setting by an ordinary difference (or differential) equation. The complete information on the state at the current cycle is realized as a combination of the partial information on the state and the history of the input (i.e., cyclic stress) excitation at finitely many previous cycles.

The state-space model is a nonlinear dynamical model of fatigue-crack growth under variable-amplitude loading in ductile alloys following the state-space approach (Patankar and Ray 2000). The crack growth equation in the state-space model is structurally similar to Paris equation (Paris and Erdogan 1960) modified for crack closure, which has been extensively used in fatigue crack growth models such as FASTRAN (Newman 1992) and AFGROW (Harter 1999). Under variable-amplitude loading, these models usually rely on a memory-dependent physical variable (e.g., crack opening stress or reference stress) that requires storage of information on the load history. For example, the crack-opening stress

in the FASTRAN model (Newman 1992) is assumed to depend on the load history over an interval of about 300 cycles. Another example is the strain-life model in which the reference stress obtained by the rainflow method relies on cycle counting that, in turn, depends on the load history (Dowling 1983). The model predictions, in general, become more accurate if the load history is considered over a longer period, although a short recent history of the applied load might be adequate in some cases for crack growth modeling. An extreme example is constant-amplitude cyclic loading where storage of the load history over the previous cycles may not be necessary. It is not precisely known to what extent information storage is necessary for calculating the memory-dependent variable in a fatigue crack growth model under *a priori* unknown variable-amplitude (e.g., single-cycle, block, spectrum, or random) loading. The state at the current cycle is realized as a combination of the state and the input (i.e., cyclic stress) excitation at finitely many previous cycles. Equivalently, the state becomes a function of the fading memory of the input excitation, which can be generalized to an autoregressive moving average (ARMA) model that is equivalent to a state-space model (Ljung 1999). Unlike the existing crack growth models, the state-space model does not require a long history of stress excitation to calculate the crack-opening stress. Therefore, savings in the computation time and memory requirements are significant.

Although the structure of the state-space model's crack growth equation is similar to that of FASTRAN (Newman 1992), it adopts a novel approach to generate the (cycle-dependent) crack opening stress under variable-amplitude loading. As such, the crack length computed by these two models could be different for given variable-amplitude loadings, even though the results are nearly identical under the same constant-amplitude loading.

The state-space model was formulated to satisfy the following requirements:

- Capability to capture the effects of single-cycle overload and underload, load sequencing, and spectrum loading
- Representation of physical phenomena of fracture mechanics within a semi-empirical structure
- Compatibility with plant dynamic models for health management and life extending control
- Validation by comparison with fatigue test data and a well known code of fatigue crack growth
- Computer code development for real-time execution on standard platforms

The first two requirements were satisfied as the state-space model was formulated based on fracture-mechanistic principles of the crack closure concept. The third requirement was also satisfied because the plant dynamic models are usually formulated in the state-space setting or autoregressive moving average (ARMA) setting (Ljung 1999). The remaining two requirements were satisfied by validating the state-space model with fatigue test data for different types of variable-amplitude and spectrum loading on 7075-T6 and 2024-T3 alloys (Porter 1972; McMillan and Pelloux 1967). The model predictions

were also compared with those of AFGROW and FASTRAN, which are well-known codes for fatigue crack growth prediction that are widely used in the aircraft industry.

5.1.1 State-Space Model Formulation

5.1.1.1 Nomenclature

A_k^j	parameter in the empirical equation of S_k^{oss} for $j=1, 2, 3, 4$
a	crack length
C	parameter in the crack growth equation
E	Young's modulus
$F(\bullet, \bullet)$	crack length dependent geometry factor
$h(\bullet)$	crack growth function in crack growth equation
k	current cycle of applied stress
m	exponent parameter in the crack growth equation
m	number of cycles of a particular stress level in the load block
n	number of cycles of a particular stress level in the load block
R	stress ratio of minimum stress to maximum stress
S^{flow}	flow stress
S^{\max}	maximum stress within a cycle
S^{\min}	minimum stress within a cycle
S^o	crack opening stress
S^{oss}	crack opening stress under constant amplitude load given by empirical equation.
S^{ult}	ultimate tensile strength
S^y	yield stress
t	specimen thickness
$U(\bullet)$	the Heaviside function
w	half-width of center-cracked specimen or width of compact specimen
α	constraint factor for plane stress/strain
α^{\max}	maximum value of α
α^{\min}	minimum value of α
Δa^{\max}	crack increment above which $\alpha = \alpha^{\min}$
Δa^{\min}	crack increment below which $\alpha = \alpha^{\max}$
Δa_k	crack increment ($= a_k - a_{k-1}$)
ΔK^{eff}	effective stress intensity factor range
ε^{thr}	positive lower bound for absolute value of maximum stress $\{S_k^{\max}, k \geq 0\}$.
η	decay rate for S^o

5.1.1.2 Model Development

The state-space model was formulated based on the crack closure concept where the state variables are the crack length a and the crack-opening stress S^o . A difference equation

for S_k^o has been constructed in such a way that, under different levels of constant amplitude load, the forcing function S_k^{oss} at the k^{th} cycle matches the crack opening stress derived from the empirical relation (Newman 1984) given as:

$$S_k^{oss} = S^{oss}(S_k^{\max}, S_k^{\min}, \alpha_k, F(c_{k-1}, w))$$

$$= \begin{cases} (\max\{(A_k^0 + A_k^1 R_k + A_k^2 R_k^2 + A_k^3 R_k^3), R_k\}) S_k^{\max}, & R_k \geq 0 \\ (A_k^0 + A_k^1 R_k) S_k^{\max}, & \text{otherwise} \end{cases}, \quad (\text{SS-1})$$

where

$$R_k = \frac{S_k^{\min}}{S_k^{\max}} U(S_k^{\max}) \quad \text{for all } k \geq 0 \quad (\text{SS-2})$$

$$A_k^0 = (0.825 - 0.34\alpha_k + 0.05\alpha_k^2) \left[\cos\left(\frac{\pi}{2} \frac{S_k^{\max} F(c_{k-1}, w)}{S^{\text{flow}}}\right) \right]^{1/\alpha_k} \quad (\text{SS-3})$$

$$A_k^1 = (0.415 - 0.071\alpha_k) \left(\frac{S_k^{\max}}{S^{\text{flow}}} F(c_{k-1}, w) \right) \quad (\text{SS-4})$$

$$A_k^2 = \begin{cases} 1 - A_k^0 - A_k^1 - A_k^3 & \text{if } R_k \geq 0 \\ 0 & \text{if } R_k < 0 \end{cases} \quad (\text{SS-5})$$

$$A_k^3 = \begin{cases} 2A_k^0 + A_k^1 - 1 & \text{if } R_k \geq 0 \\ 0 & \text{if } R_k < 0 \end{cases} \quad (\text{SS-6})$$

The following constitutive relation in the form of a piecewise bilinear first order difference equation has been proposed (Patankar and Ray 2000) for recursive computation of the crack opening stress S_k^o at the completion of the $(k-1)^{\text{th}}$ cycle:

$$S_k^o = \left(\frac{1}{1+\eta} \right) S_{k-1}^o + \left(\frac{\eta}{1+\eta} \right) S_k^{oss} + \left(\frac{1}{1+\eta} \right) U(S_k^{oss} - S_{k-1}^o) (S_k^{oss} - S_{k-1}^o) \quad (SS-7)$$

$$+ \left(\frac{1}{1+\eta} \right) [1 - U(S_k^{oss} - S_{k-1}^o)] U(S_{k-1}^{\min} - S_k^{\min}) [S_k^{oss} - S_k^{oss}(S_k^{\max}, S_{k-1}^{\min})]$$

where $\eta = \frac{tS^y}{2wE}$ (SS-8)

The Heaviside function $U(x) = \begin{cases} 0 & \text{if } x \leq 0 \\ 1 & \text{if } x > 0 \end{cases}$

and the forcing function S_k^{oss} is calculated from the semi empirical formula given by Eq. (SS-1) as if constant amplitude stress cycles (S_k^{\max}, S_k^{\min}) were applied.

S_k^{oss} generated from the semi-empirical Eq. (SS-1) is used to construct the (piecewise bilinear) forcing function to the dynamics of crack opening stress S_k^o in Eq. (SS-7). Under constant amplitude stress excitation, S_k^{oss} is the steady state solution of S^o . However, under variable amplitude stress excitation, S_k^{oss} is different from the instantaneous crack opening stress S_k^o .

Following an overload cycle, the duration of crack retardation is controlled by the dynamics of S^o in the state-space model, and hence determined by the stress independent parameter η defined in equation (SS-8).

The last term on the right hand side of Eq. (SS-7) accounts for the effects of reverse plastic flow. The overload condition and the reverse plastic flow condition are mutually exclusive. The former feature is mathematically represented by the Heaviside function $U(S_k^{oss} - S_{k-1}^o)$ in the third term on the right hand side of Eq. (SS-7). Moreover, depletion of the normal plastic zone occurs when an underload occurs. The underload effects have been incorporated via another Heaviside function $U(S_{k-1}^{\min} - S_k^{\min})$.

5.1.1.3 Prediction of Sequence Effects

Figure 5-1 shows the effects of a single cycle overload on S^o , as predicted by the state-space model in Eq. (SS-7). The model predictions are qualitatively similar to the experimental data of Yisheng and Schijve (1995) except for the lack of a sharp negative spike in S^o immediately after the application of an overload. The sharp transients of S^o that occur only for a few cycles have no significant bearing on the overall crack growth.

Because the dynamics of S° is described by a first order difference equation, S° attains a peak value in the cycle following the application of a single cycle overload. The positive edge of this resulting pulse is effective whereas, unlike a linear system, the negative edge is rendered ineffective by the Heaviside function $U(S_k^{oss} - S_{k-1}^\circ)$. The last term on the right hand side of Eq. (SS-7) is inactive throughout in this case. When $U(S_k^{oss} - S_{k-1}^\circ)$ is zero, S° decreases at a rate determined by the dimensionless parameter η . The amplitude of the input pulse on the right hand side of Eq. (SS-7) depends on the amount of overload and the current value of S° , which leads to retarded crack growth during the constant amplitude load that follows the overload.

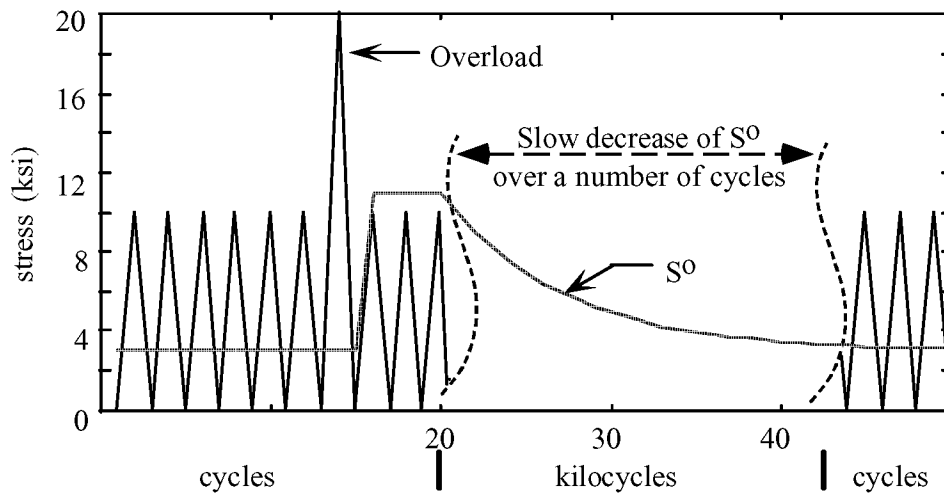


Figure 5-1. Overload Response of Crack Opening Stress as Predicted by the State-Space Model (Patankar and Ray 2000).

In contrast to a single cycle overload, a single cycle underload makes the Heaviside function $U(S_k^{oss} - S_{k-1}^\circ)$ ineffective while the last term on the right hand side of Eq. (SS-7) is effective along with the Heaviside function $U(S_{k-1}^{\min} - S_k^{\min})$ that accounts for reverse plastic flow and the resulting depletion of plastic zone. When the load returns to its normal range from an underload, the Heaviside function $U(S_k^{oss} - S_{k-1}^\circ)$ again becomes effective while the last term on the right hand side of Eq. (SS-7) is inactive. This brings S° back to its normal value. Thus S° is low only for one cycle during single cycle underloads, which hardly impacts on overall crack growth if underloads are sufficiently closely spaced.

Figure 5-2 shows the effect of an underload followed by an overload. The difference between this case and the pure overload case is that, when the specimen encounters an overload, the preceding underload causes S° to be abnormally low. Thus, the crack has very little protection from growing during the overload cycle and consequently the crack increment during the overload cycle is significant. The response following the overload is similar to the single cycle overload case described before.

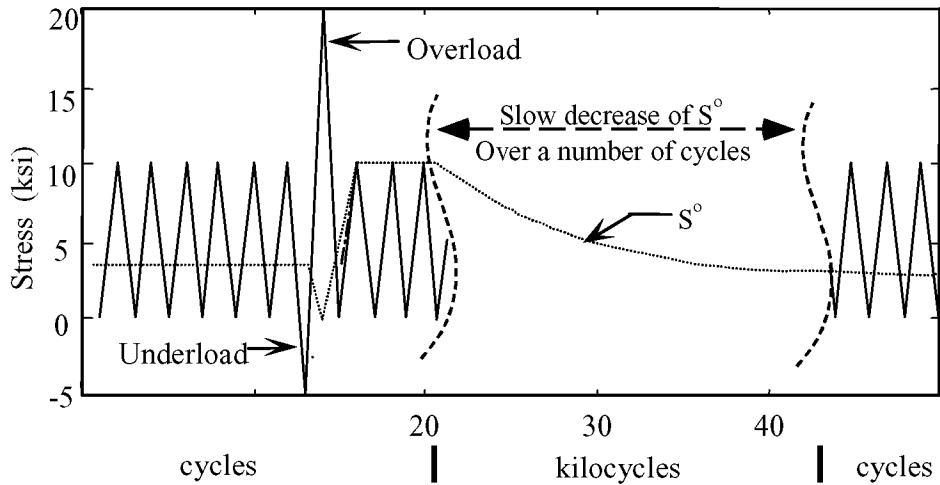


Figure 5-2. Underload-Overload Response of Crack Opening Stress as Predicted by the State-Space Model (Patankar and Ray 2000)

Figure 5-3 shows how S^o is affected by an overload immediately followed by an underload. In the overload-underload cycle, S_k^{\max} is identical to that for pure overload but the corresponding S_k^{\min} is smaller. Consequently, S_k^{oss} is smaller for overload-underload than that for a single cycle overload. In effect, the forcing function that is multiplied by the Heaviside function $U(S_k^{\text{oss}} - S_{k-1}^o)$ in Eq. (SS-7) assumes a smaller value for overload-underload than that for a single cycle overload, while the last term on the right hand side of Eq. (SS-7) is inactive. A single cycle overload retards crack growth more effectively than a similar overload immediately followed by an underload. Thus the benefits of an overload monotonically diminish with increase in the magnitude of the following underload.

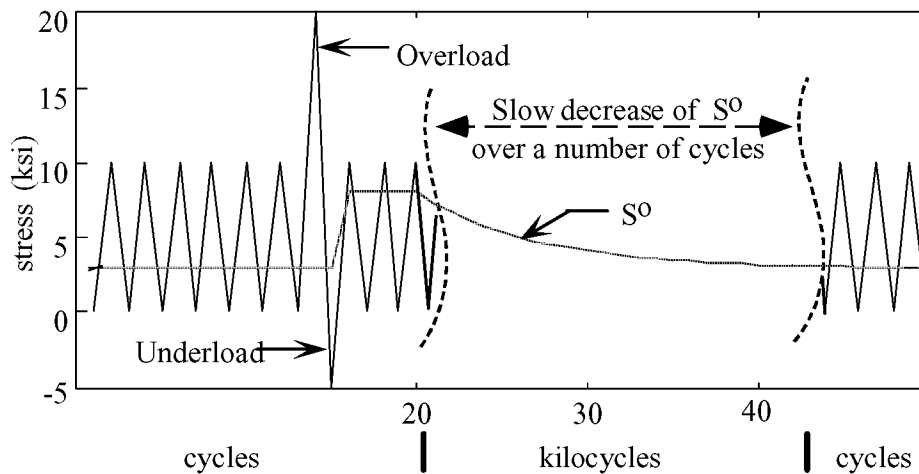


Figure 5-3. Overload-Underload Response of Crack Opening Stress as Predicted by the State-Space Model (Patankar and Ray 2000).

5.1.2 Model Validation with Test Data

The state-space model has been validated with the fatigue test data of: (1) 7075-T6 aluminum alloy specimens under different types of variable amplitude cyclic loading (Porter 1972); and (2) 2024-T3 aluminum alloy specimens under spectrum loading (McMillan and Pelloux 1967), which are available in open literature. The state-space model predictions have been compared with those of FASTRAN (Newman 1992) and several other crack-tip-plastic-zone-based models (e.g., Wheeler, Willenborg, and Chang) that are available in the AFGROW software package (Harter, 1999). On all the AFGROW models, predictions of the Walker equation with Willenborg retardation model were found to yield, on the average, closest agreement with the test data of McMillan and Pelloux as well as Porter. The complete set of validation comparisons (Sastry 2000) is presented in Appendix A. The results are summarized below.

Porter (1972) collected fatigue test data on center-notched 7075-T6 aluminum alloy specimens made of 305 mm wide, 915 mm long, and 4.1 mm thick panels, for which $E = 69600 \text{ MPa}$, $\sigma^y = 520 \text{ MPa}$, and $\sigma^{ult} = 575 \text{ MPa}$. The initial crack size ($2a$) was 12.7 mm and the experiments were conducted in laboratory air. The profile of block loading for data generation is shown at the top of Figures 5-4 and 5-5 where the positive integers, n and m , indicate that a block of n constant-amplitude cycles is followed by a block of m cycles of a different constant-amplitude.

Figures 5-4 and 5-5 show comparisons of the state-space model predictions with Porter data and the predictions of FASTRAN model and AFGROW (Walker equation with Willenborg retardation model) that calculate the crack opening stress in a different way. The analyses on each of FASTRAN, AFGROW, and the state-space models have been conducted with identical initial crack length with the assumption of no loading history. The curves in Figure 5-4 are generated with the parameters $n = 50$ and $m = 1$ with different values of the overload σ_2 and underload σ_1 superimposed on constant-amplitude stress cycles of 103.43 MPa and 51.72 MPa for repeated overload-underload spectra. Similarly, the curves in Figure 4-5 are generated with the parameters $n = 50$ and $m = 1$ with different values of the overload σ_2 and underload σ_1 superimposed on constant-amplitude stress cycles of 103.43 MPa and 51.72 MPa for repeated underload-overload spectra.

The state-space and FASTRAN models produce nearly identical results under constant-amplitude cyclic stresses, because the procedure for calculating S^{OSS} is similar in both models while the AFGROW model yields somewhat different results. For variable-amplitude cyclic stresses, the state-space model predictions are quite close to both the experimental data and predictions of the FASTRAN model, as seen in Figures 5-4 and 5-5. These plots indicate that the accuracy of the state-space model relative to the experimental data is comparable to that of the FASTRAN model. On the average, for repeated overload and underload, accuracy of the state-space model is comparable to that of FASTRAN and AFGROW. The results show that the state-space model (and, to lesser extent, FASTRAN) demonstrates the difference between the effects of overload-

underload and underload-overload on crack growth in agreement with the test data. In contrast, the AFGROW model does not show any appreciable difference when corresponding results are compared. The predictions of the state-space model are apparently superior to those of AFGROW for sequence effects.

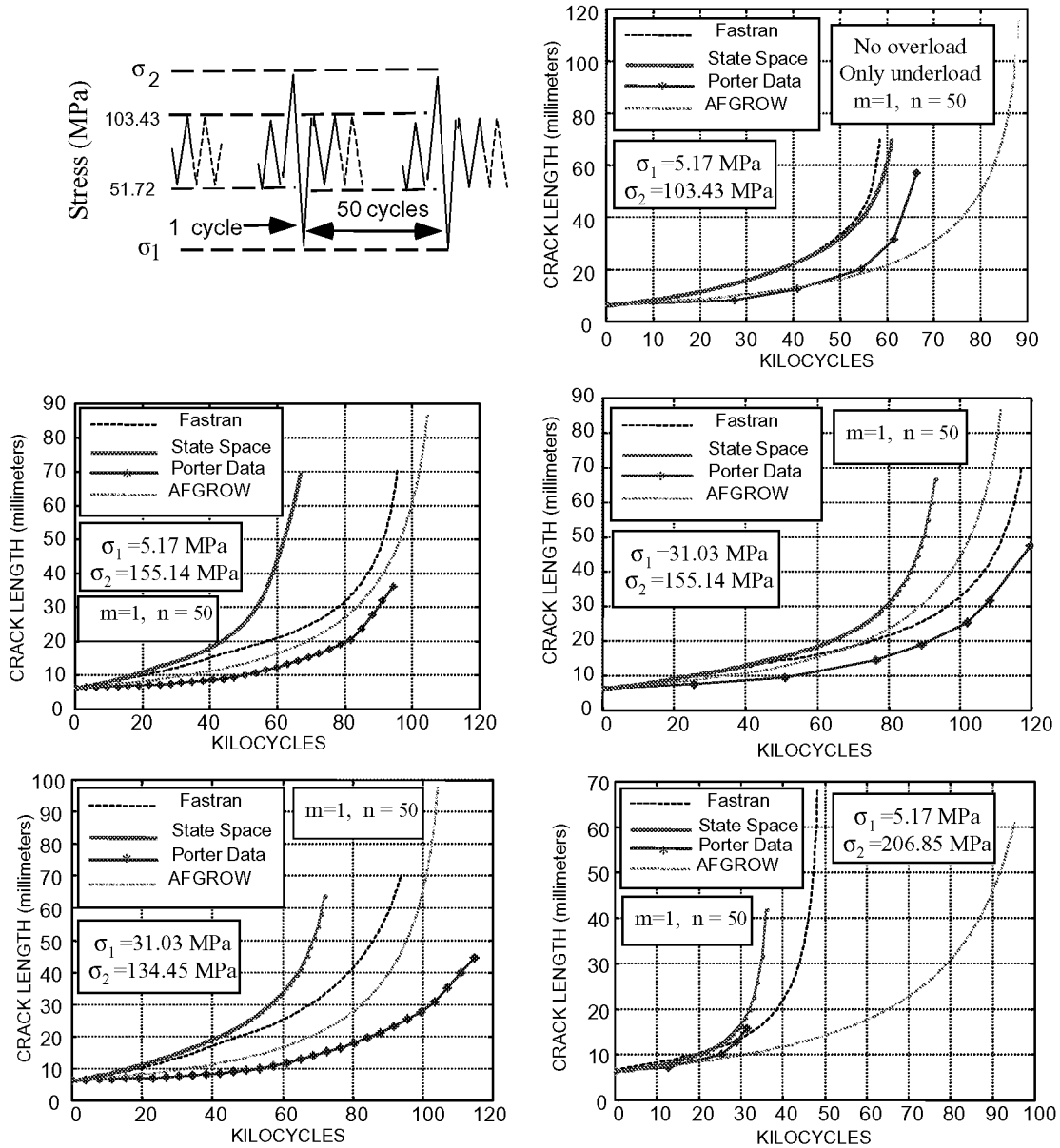


Figure 5-4. Comparison of analytic model predictions with published overload-underload) fatigue data. Data source: Porter 1972.

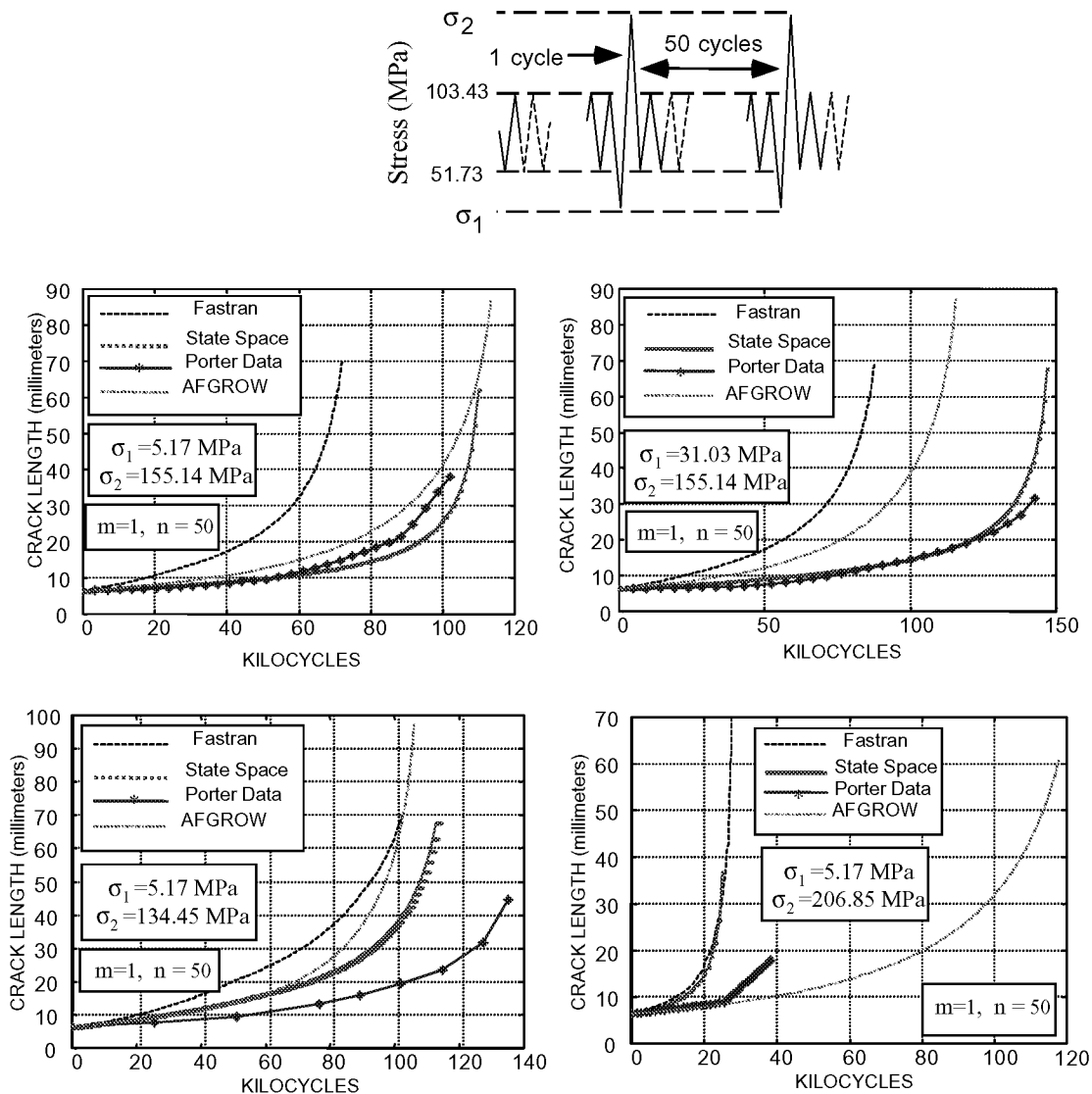


Figure 5-5. Comparison of analytic model predictions with published overload-underload) fatigue data. Data source: Porter 1972.

McMillan and Pelloux (1967) generated fatigue data under complex spectrum loads for center-notched 2024-T3 aluminum alloy specimens made of 229 mm wide, 610 mm long, and 4.1 mm thick panels. Fatigue testing was accomplished in a vertical 125 kip electrohydraulic fracture jig of Boeing design. The testing system was capable of applying loads with an absolute error within $\pm 1\%$ of the maximum programmed load. The initial crack size ($2a$) was 12.7 mm and the experiments were conducted in laboratory air.

Figure 5-6 shows predictions of the state-space, FASTRAN, and AFGROW models with selected four of the thirteen spectral data sets of McMillan and Pelloux. The state-space model predictions are closest to the experimental data in twelve out of the thirteen cases of spectrum loads except for the data set P10.

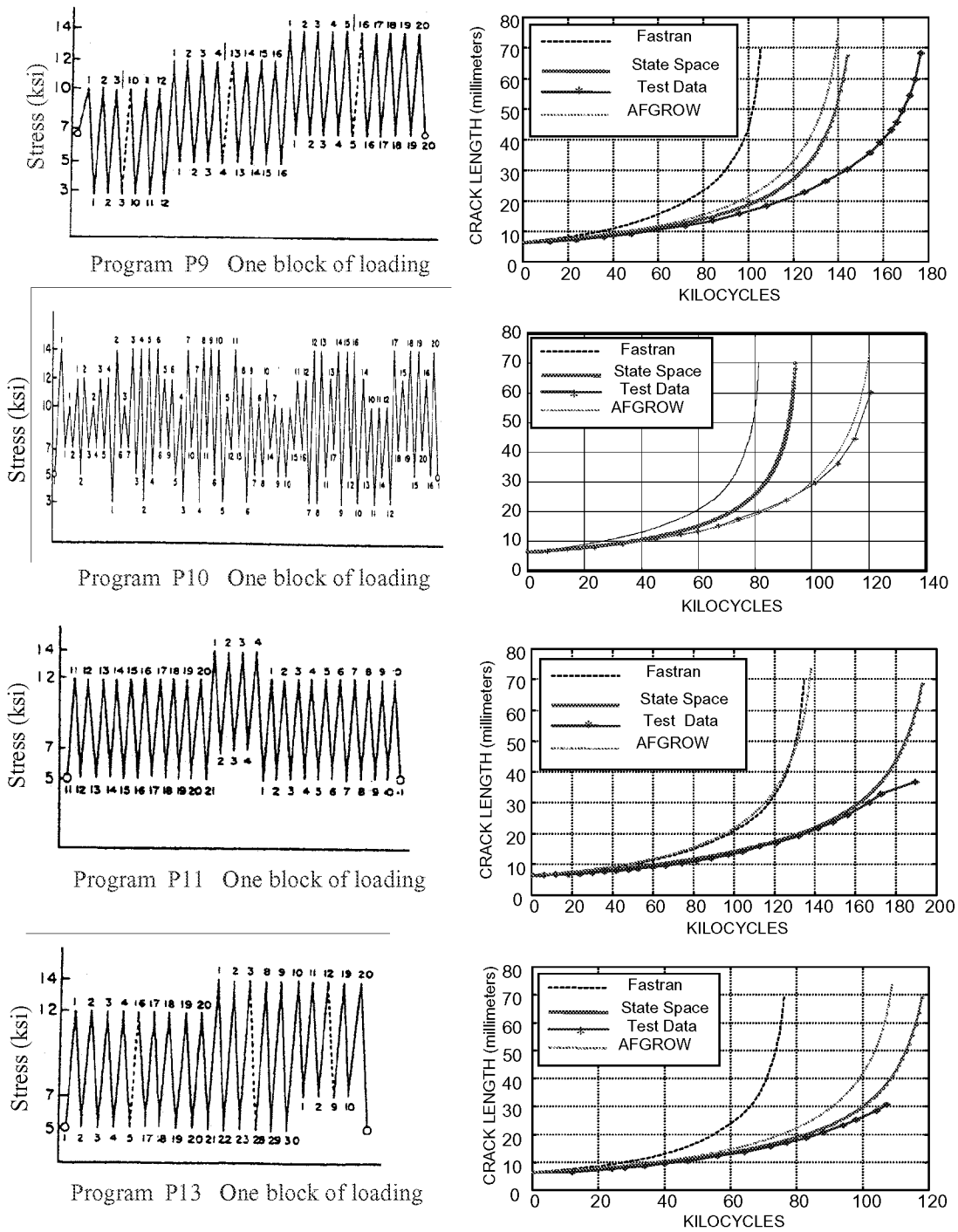


Figure 5-6. Comparison of analytic model predictions with published spectrum fatigue data. Data source: McMillan and Pelloux 1967.

Modest disagreements (in the range of approximately 10%) between the state-space model predictions and the test data are reasonable because the number of samples (e.g., in the order of three or four) over which the test data are averaged is small. The agreement of model predictions with experimental data strongly supports the state-space model and its fundamental hypothesis that the crack opening stress can be treated as a state variable.

5.1.3 Comparison of Computation Time

Table 5-1 and Table 5-2 list typical computation time required for calculation of crack growth under programmed loads for Porter data and McMillan and Pelloux data, respectively, on a 450 MHz Intel Pentium PC platform. In the thirteen cases reported in Table 5-2, the state-space model predicts a longer life than FASTRAN by a few thousand cycles. In the case of spectrum P10, both models run for approximately the same number of cycles which provides a fair comparison of their computation time. The execution time per spectrum block for both the models indicates that the state-space model is about 10 times faster than FASTRAN for each of the thirteen spectrum load cases.

Table 5-1. Execution Time for Overload-Underload Cases

Repeated Load Blocks (N cycles @ 68.95 Mpa; 1 cycle @ 103.43 Mpa Min. stress 3.45 Mpa)	Time in Seconds on a 450 Mhz Pentium	
	State- Space Model	FASTRAN Model
N=1000	1.20	4.80
N=300	1.10	4.50
N=50	0.50	2.30

Table 5-2. Execution Time for Spectrum Load Cases

Load Description	State-Space Model (Time in Seconds)	FASTRAN Model (Time in Seconds)
Program P1	0.65	4.09
Program P2	0.69	4.55
Program P3	0.50	5.70
Program P4	0.48	4.10
Program P5	0.47	5.07
Program P6	1.17	5.51
Program P7	1.28	5.10
Program P8	0.97	6.41
Program P9	0.79	7.16
Program P10	0.50	5.60
Program P11	1.07	5.36
Program P12	0.64	6.53
Program P13	0.66	5.31

The state-space model recursively computes the crack opening stress as a state variable as a simple algebraic function of the maximum and minimum stress excitation in the present cycle as well as the minimum stress and the crack opening stress in the immediately preceding cycle. In contrast, the FASTRAN model computes the crack opening stress as a function of contact stresses and crack opening displacements based on the stress history.

Since the state-space model does not need storage of load history except the minimum stress in the previous cycle, the memory requirements are much lower than those of FASTRAN that does require storage of a relatively long load history. Consequently, both computer execution time and memory requirement of the state-space model are significantly smaller than those of the FASTRAN model. Specifically, the state-space enjoys the following advantages over other crack growth models:

- Smaller execution time and computer memory requirements as needed for real-time health management and life extending control (Holmes and Ray 1998)
- Compatibility with other state-space models of plant dynamics (e.g., aircraft flight dynamic systems and rocket engine systems) and structural dynamics of critical components as needed for synthesis of life-extending control systems (Holmes and Ray 1998)

5.2 STOCHASTIC MODELING OF FATIGUE CRACK DAMAGE

Traditionally, the risk index and remaining service life (Bolotin 1989) of machinery are calculated off-line based on statistical models of material degradation, operating history, and anticipated disruptions in the plant operation (e.g., postulated stress levels). Because the predicted service life of operating machinery is likely to be altered in the event of unscheduled operations, on-line computation of damage statistics allows continual refinement of the risk index and remaining life prediction as time progresses. In this context, this report focuses on stochastic modeling of fatigue crack damage in metallic materials, which is a major source of failures in structural components of operating machinery (Özekici 1996).

Stochastic modeling of fatigue crack phenomena in ductile alloys is a relatively new area of research, and a list of the literature representing the state of the art is cited by Sobczyk and Spencer (1992) as well as in the March 1996 issue of *Engineering Fracture Mechanics*. Bogdonoff and Kozin (1985) proposed a Poisson-like independent-increment jump model of fatigue crack phenomena. The underlying principle of this model agrees with the theory of micro-level fatigue cracking. An alternative approach to stochastic modeling of fatigue crack damage is to randomize the coefficients of an existing deterministic model to represent material inhomogeneity (Ditlevsen 1986). Another alternative approach is to augment a deterministic model of fatigue crack growth with a random process (e.g., Lin and Yang 1985; Spencer *et al.* 1989; Ishikawa *et al.* 1993). The fatigue crack growth process is thus modeled by nonlinear stochastic differential equations in the Itô setting (Kloeden and Platen 1995). Specifically, Kolmogorov forward and backward diffusion equations, which require solutions of nonlinear partial differential equations, have been proposed to generate the statistical information required for risk

analysis of mechanical structures (Tsurui and Ishikawa 1986; Bolotin 1989). These nonlinear partial differential equations can only be solved numerically and the numerical procedures are computationally intensive as they rely on fine-mesh models using finite-element or combined finite-difference and finite-element methods (Sobczyk and Spencer 1992). Casciati *et al.* (1992) have analytically approximated the solution of Itô equations by Hermite moments to generate a probability distribution function of the crack length.

Formulation and assessment of a stochastic model of fatigue crack damage in ductile alloys that are commonly encountered in aircraft structures is presented in the following subsections. The fatigue crack damage at an instant (i.e., at the end of a stress cycle) is expressed as a continuous function of the current and initial crack lengths. The (non-stationary) probability distribution of crack damage is obtained in a closed form without numerically solving stochastic differential equations in the Wiener integral or Itô integral setting. Model predictions are shown to be in close agreement with the fatigue test data of 2024-T3 and 7075-T6 aluminum alloys. Finally, an illustration is provided to describe how the stochastic model can be used in making decisions for risk analysis and life prediction that are necessary for health management and life extending control of mechanical systems.

5.2.1 Model Formulation and Assessment

5.2.1.1 Nomenclature

C	autocovariance; covariance matrix	Y_d	desired operational profile
C	crack length	Δ	incremental range
\bar{c}_M	critical crack length	δ	increment operator
\bar{c}_0	threshold of initial crack length	$\delta(\cdot)$	unit impulse function
$F(\cdot)$	probability distribution function	ε	confidence level for risk analysis
f	final condition	ϕ	eigenvector
H	hypothesis	ξ	dummy variable
K	stress intensity factor	Λ	(diagonal) eigenvalue matrix
M	number of hypotheses	λ	eigenvalue
m	exponent parameter of the model	μ	expected value
O	initial condition; opening condition	ρ	multiplicative white noise
$P[\cdot]$	probability measure	σ	standard deviation
R	stress ratio (S^{\min}/S^{\max}); autocorrelation	τ	dummy variable
S	stress	Ψ	discretized fatigue crack damage
T	maximum time of operation	ψ	continuous fatigue crack damage
t	time (cycles)	Ω	multiplicative parameter of the model
X	random vector	ζ	sample point (test specimen)
x	random variable		

5.2.1.2 Modeling of Fatigue Crack Damage

Fatigue crack growth models have been formulated by fitting estimated mean values of fatigue crack length, generated from ensemble averages of experimental data, as functions of time in units of cycles (Paris and Erdogan 1963; Schjive 1976). Following Sobczyk and Spencer (1992) and the pertinent references cited therein, the stochastic model of fatigue crack damage presented in this report, is built on the structure of the following mean-value model (Anderson 1995; Suresh, 1991):

$$\begin{aligned}\delta\hat{c}(t) &= h(\Delta K_{\text{eff}}(t)) \delta t; \text{ for } t \geq t_0 \text{ and given } \hat{c}(t_0) \\ \Delta K_{\text{eff}}(t) &= \Delta S(t) \sqrt{\pi \hat{c}(t)} F(\hat{c}(t)) \\ \Delta S(t) &= S^{\text{max}}(t) - S^0(t)\end{aligned}\tag{1}$$

where t is the current time upon completion of a stress cycle, t_0 is the initial time (e.g., when the machine component is put in service after a major maintenance or inspection), $\hat{c}(t)$ is the estimated mean value of (time-dependent) crack length, $\delta\hat{c}(t)$ is the increment of the estimated mean crack length over one cycle after time t , δt indicates the time increment over that cycle, $h(\bullet)$ is a non-negative continuous function that is dependent on the material and geometry of the stressed component, and $\Delta S(t)$ is the effective stress range during one cycle (after time t) with the corresponding crack opening stress $S^0(t)$ and peak stress $S^{\text{max}}(t)$. The (dimensionless) correction factor F is dependent on geometrical configuration (e.g., thickness, width, and the crack type in the stressed component) and the crack length. For example, $F = \sqrt{\sec(\pi \hat{c}(t) / (2w))}$ for center-cracked specimens of half-width w . There are several empirical and semi-empirical methods (e.g., Newman 1984) for calculating S^0 . For constant-amplitude load, Ibrahim et al. (1986) formulated a simple algebraic relation to obtain S^0 as a function of peak stress S^{max} and stress ratio $R \equiv S^{\text{min}} / S^{\text{max}}$.

It has been shown that for a given geometry (i.e., thickness and width) of center-cracked specimens, the function $h(\bullet)$ can be expressed as a product of two functions, $h_1(\Delta S(t))$ and $h_2(\hat{c}(t))$ (Anderson 1995; Suresh 1991). Accordingly, for center-cracked specimens with $0 < \hat{c}(t) < w \forall t \geq t_0$, Eq. (1) is modified via series approximation of the $(m/2)^{\text{th}}$ power of the secant term in the correction factor F as:

$$\delta\hat{c}(t) = \hat{\Omega} \Delta S(t)^m \hat{c}(t)^{m/2} \left(1 - m \left(\frac{\pi}{4w} \right)^2 \hat{c}(t)^2 \right)^{-1} \delta t; \text{ } t \geq t_0 \text{ and given } \hat{c}(t_0)\tag{2}$$

where the constant parameters $\hat{\Omega}$ and m are dependent on the specimen material, geometry, and fabrication. For constant-amplitude load, Eq. (2) reduces to the well-known Paris equation (Suresh 1991). For varying-amplitude load, Patankar and Ray

(2000) have shown the validity of Eq. (2) under time-dependent stress range $\Delta S(t) \equiv (S^{\max}(t) - S^o(t))$ by having $S^o(t)$ as a state variable.

Ditlevsen (1986) has shown that, under constant load amplitude the randomness of fatigue crack growth accrues primarily from parametric uncertainties. The stochastic process of crack growth is largely dependent on two second-order random parameters—a multiplicative process $\Omega(\zeta, \Delta S)$ and an exponent parameter $m(\zeta)$. Ditlevsen (1986) has suggested the possibility of one of the above two random variables being a constant for all specimens ζ . Statistical analysis of the experimental data for 2024-T3 and 7075-T6 aluminum alloys reveals that the random exponent $m(\zeta)$ can be approximated as a constant for all specimens (i.e., $m(\zeta) = m$ with probability 1) at different levels of constant stress range ΔS for a given material. Based on this observation and the (deterministic) model structure in Eq. (2), we postulate the following constitutive equation for fatigue crack growth in the stochastic setting (Sobczyk and Spencer 1992), which is, in part, similar to what was originally proposed by Paris and Erdogan (1963) in the deterministic setting:

$$\delta c(\zeta, t) = \Omega(\zeta, \Delta S(t)) (\Delta S(t))^m c(\zeta, t)^{m/2} \left(1 - m \left(\frac{\pi}{4w} \right)^2 c(\zeta, t)^2 \right)^{-1} \rho(\zeta, t) \delta t; t \geq t_o \text{ and given } c(\zeta, t_o) \quad (3)$$

where the second order random process $\Omega(\zeta, \Delta S)$ represents uncertainties of a test specimen ζ for a stress range ΔS (i.e., Ω is a constant for a given specimen under a constant stress range); the second order noise process $\rho(\zeta, t)$ represents uncertainties in the material microstructure and crack length measurements that vary with crack propagation even for the same specimen ζ . The multiplicative uncertainty $\rho(\zeta, t)$ in the crack growth process is assumed to be a stationary white noise process that is statistically independent of $\Omega(\zeta, \Delta S)$. The rationale for this assumption is that inhomogeneity of the material microstructure and measurement noise associated with each test specimen, represented by $\rho(\zeta, t)$, are statistically homogeneous and are unaffected by the uncertainty $\Omega(\zeta, \Delta S)$ of a particular specimen caused by, for example, machining operations. With no loss of generality, $\mu_\rho \equiv E[\rho(\zeta, t)] = 1$ is set via appropriate scaling of the parameters in Eq. (3).

Because the number of cycles to failure is usually very large in the crack growth processes (even for low-cycle fatigue), a common practice in the fracture mechanics literature is to approximate the difference equation of crack growth by a differential equation. Therefore, for $t \geq t_o$, Eq. (3) is approximated as the following stochastic differential equation:

$$\left(c(\zeta, t)^{-m/2} - m \left(\frac{\pi}{4w} \right)^2 c(\zeta, t)^{-m/2} \right) dc(\zeta, t) = \Omega(\zeta, \Delta S(t)) (\Delta S(t))^m \rho(\zeta, t) dt; t \geq t_o \text{ and given } c(\zeta, t_o) \quad (4)$$

which is integrated pointwise (i.e., for the individual ζ 's) as follows:

$$\int_{c(\zeta, t_0)}^{c(\zeta, t)} \frac{d\xi}{\xi^{m/2}} - m \left(\frac{\pi}{4w} \right)^2 \int_{c(\zeta, t_0)}^{c(\zeta, t)} \frac{d\xi}{\xi^{-2+m/2}} = \int_{t_0}^t d\tau (\Delta S(\tau))^m \Omega(\zeta, \Delta S(\tau)) \rho(\zeta, \tau); \text{ given } c(\zeta, t_0) \quad (5)$$

to yield the following solution

$$\left(\frac{c(\zeta, t)^{1-m/2} - c(\zeta, t_0)^{1-m/2}}{1 - \frac{m}{2}} \right) - m \left(\frac{\pi}{4w} \right)^2 \left(\frac{c(\zeta, t)^{3-m/2} - c(\zeta, t_0)^{3-m/2}}{3 - \frac{m}{2}} \right) = \int_{t_0}^t d\tau \Omega(\zeta, \Delta S(\tau)) (\Delta S(\tau))^m \rho(\zeta, \tau) \quad (6)$$

where the constant parameter, m , is in the range of 2.5 to 5 for ductile alloys and many metallic materials ensuring that $(1 - m/2) < 0$ and $(3 - m/2) > 0$ in Eq. (6). A stochastic process, $\psi(\zeta, t; t_0)$, was introduced to represent the (dimensionless) fatigue crack damage as a function of the crack length $c(\zeta, t)$ after normalization relative to the physical parameter, w , of the stressed specimen:

$$\begin{aligned} \psi(\zeta, t; t_0) &\equiv \left(\left(\frac{c(\zeta, t)^{1-m/2} - c(\zeta, t_0)^{1-m/2}}{1 - \frac{m}{2}} \right) - m \left(\frac{\pi}{4w} \right)^2 \left(\frac{c(\zeta, t)^{3-m/2} - c(\zeta, t_0)^{3-m/2}}{3 - \frac{m}{2}} \right) \right) w^{(m/2)-1} \\ &= \left(\frac{(c(\zeta, t)/w)^{1-m/2} - (c(\zeta, t_0)/w)^{1-m/2}}{1 - \frac{m}{2}} \right) - m \left(\frac{\pi}{4} \right)^2 \left(\frac{(c(\zeta, t)/w)^{3-m/2} - (c(\zeta, t_0)/w)^{3-m/2}}{3 - \frac{m}{2}} \right) \end{aligned} \quad (7)$$

It follows from Eq. (7) that $\psi(\zeta, t; t_0)$ is a continuous function of the crack length process $c(\zeta, t)$. Because $c(\zeta, t)$ is a measurable function, $\psi(\zeta, t; t_0)$ is also a measurable function although the two measure spaces are different. The probability distribution of $\psi(\zeta, t; t_0)$, conditioned on the initial crack length $c(\zeta, t_0)$, leads to a measure of fatigue crack damage at the instant t . The conditional probability distribution $F_{\psi|c(\zeta, t_0)}(\bullet; t|\bullet)$ that depends on the stress history $\{\Delta S(\tau): \tau \in [t_0, t]\}$ plays an important role in risk analysis and remaining life prediction.

Next, the special case of constant stress range ΔS , for which experimental data of random fatigue are available for model validation and parameter identification, was considered. A combination of Eqs. (6) and (7) yields the following simplified relation for constant ΔS :

$$\psi(\zeta, t; t_0) = w^{(m/2)-1} (\Delta S)^m \Omega(\zeta, \Delta S) \left(t - t_0 + \int_{t_0}^t d\tau (\rho(\zeta, \tau) - 1) \right) \quad \text{with probability 1} \quad (8)$$

Given that $E[\rho(\zeta, t)] = 1$, $E[(\rho(\zeta, t_1) - 1)(\rho(\zeta, t_2) - 1)] = \sigma_\rho^2 \delta(t_1 - t_2)$, $m(\zeta) = m$ with probability 1, and $\rho(\zeta, t)$ is statistically independent of $\Omega(\zeta, \Delta S)$, it follows from Eq. (8) that:

$$\begin{aligned} \mu_\psi(t; t_0) &\equiv E[\psi(\zeta, t; t_0)] \\ &= w^{(m/2)-1} (\Delta S)^m \mu_\Omega(\Delta S) (t - t_0) \end{aligned} \quad (9)$$

$$\begin{aligned} R_{\psi\psi}(t_1, t_2; t_0) &\equiv E[\psi(\zeta, t_1; t_0) \psi(\zeta, t_2; t_0)] \\ &= w^{m-2} (\Delta S)^{2m} \left(\mu_\Omega^2(\Delta S) + \sigma_\Omega^2(\Delta S) \right) \left((t_1 - t_0)(t_2 - t_0) + \sigma_\rho^2 (\min(t_1, t_2) - t_0) \right) \end{aligned} \quad (10)$$

where $\mu_\Omega(\Delta S) \equiv E[\Omega(\zeta, \Delta S)]$ and $\sigma_\Omega^2(\Delta S) \equiv \text{Var}[\Omega(\zeta, \Delta S)]$. The autocorrelation function $R_{\psi\psi}(t_1, t_2; t_0)$ in Eq. (10) is continuous at $(t_1, t_2)|_{t_1=t_2=t}$ for all $t \geq t_0$. Hence, the process $\psi(\zeta, t; t_0)$ is mean-square continuous based on a standard theorem of mean-square calculus (Jazwinski 1970; Wong and Hajek 1985).

It follows from Eqs. (9) and (10) that the autocovariance function of $\psi(\zeta, t; t_0)$ for constant ΔS is:

$$\begin{aligned} C_{\psi\psi}(t_1, t_2; t_0) &= w^{m-2} (\Delta S)^{2m} \left(\sigma_\Omega^2(\Delta S) (t_1 - t_0)(t_2 - t_0) + \left(\mu_\Omega^2(\Delta S) + \sigma_\Omega^2(\Delta S) \right) \sigma_\rho^2 (\min(t_1, t_2) - t_0) \right) \\ \Rightarrow \text{Var}[\psi(\zeta, t; t_0)] &\equiv \sigma_\psi^2(t; t_0) = w^{m-2} (\Delta S)^{2m} \sigma_\Omega^2(\Delta S) (t - t_0)^2 \left(1 + \frac{\mu_\Omega^2(\Delta S) + \sigma_\Omega^2(\Delta S)}{\sigma_\Omega^2(\Delta S)} \frac{\sigma_\rho^2}{(t - t_0)} \right) \text{ for } t > t_0 \end{aligned} \quad (11)$$

5.2.2 Analysis of Experimental Data

Published fatigue test data were analyzed to validate the model structure in Eqs. (3) and (4). The statistical signal processing technique of Karhunen-Loève (K-L) expansion (Fukunaga 1990) was used for selecting the dominant features of the stochastic crack growth process. The idea was to decompose a (mean-square continuous) second order stochastic process into mutually orthogonal components conceptually similar to what was achieved in Fourier expansion. In K-L expansion, the coefficients are uncorrelated random variables and the orthonormal basis functions are deterministic.

Experimental data of random fatigue crack growth in 2024-T3 aluminum alloy (Virkler et al. 1979) and 7075-T6 aluminum alloy (Ghonem and Dore 1987) were used for model assessment. These tests were conducted under different constant load amplitudes at ambient temperature. The Virkler data set was generated for 68 center-cracked specimens (of half-width $w=76.2$ mm) at a single constant-amplitude load amplitude with peak nominal stress of 60.33 MPa (8.75 ksi) and stress ratio $R \equiv S_{\min} / S_{\max} = 0.2$ for about 200,000 cycles; the resulting $\Delta S \equiv (S^{\max} - S^0) = 21.04$ MPa. The Ghonem data sets were generated for 60 center-cracked specimens each (of half-width $w=50.8$ mm) at three

constant load amplitudes: (1) Set 1 with peak nominal stress of 70.65 MPa (10.25 ksi) and $R=0.6$ for 54,000 cycles, and the resulting $\Delta S = 15.84$ MPa; (2) Set 2 with peak nominal stress of 69.00 MPa (10.00 ksi) and $R=0.5$ for 42,350 cycles, and the resulting $\Delta S = 17.80$ MPa; and (3) Set 3 with peak nominal stress of 47.09 MPa (6.83 ksi) and $R=0.4$ for 73,500 cycles, and the resulting $\Delta S = 13.24$ MPa. The crack opening stress S^o is calculated via the correlation of Ibrahim et al. (1986).

Because only finitely many data points at ℓ discrete instants of time are available from experiments, an obvious choice is discretization over a finite horizon $[t_o, t_f]$ so that the stochastic process $\psi(\zeta, t; t_o)$ now reduces to an ℓ -dimensional random vector denoted as $\Psi^D(\zeta)$. Consequently, the covariance function $C_{\psi\psi}(t_1, t_2; t_o)$ in Eq. (11) is reduced to a real positive-definite $(\ell \times \ell)$ symmetric matrix $C_{\Psi\Psi}^D$. Because the experimental data were taken at sufficiently close intervals, $C_{\Psi\Psi}^D$ contains pertinent information of the crack damage process. The ℓ real positive eigenvalues are ordered as $\lambda_1 \geq \lambda_2 \geq \dots \geq \lambda_\ell$, with the corresponding eigenvectors, $\phi^1, \phi^2, \dots, \phi^\ell$, that form an orthonormal basis for signal decomposition. The K-L expansion also ensures that the ℓ random coefficients of the basis vectors are statistically orthogonal (i.e., zero-mean and mutually uncorrelated). These random coefficients form a random vector $X(\zeta) \equiv [x_1(\zeta) \ x_2(\zeta) \ \dots \ x_\ell(\zeta)]^T$ having the covariance matrix $C_{XX} = \text{diag}(\lambda_1, \lambda_2, \dots, \lambda_\ell)$ leading to decomposition of the discretized signal as:

$$\Psi^D(\zeta) = E[\Psi^D(\zeta)] + \sum_{j=1}^{\ell} (\phi^j x_j(\zeta)) \quad (12)$$

Ray et al. (1998) observed that the statistics of crack length are dominated by the random coefficient corresponding to the principal eigenvector (i.e., the eigenvector associated with the largest eigenvalue) and that the combined effects of the remaining eigenvectors are small. Therefore, the signal $\Psi^D(\zeta)$ in Eq. (12) is expressed as the sum of a principal part and a residual part:

$$\Psi^D(\zeta) = \underbrace{\hat{\Psi}^D(\zeta)}_{\text{principal part}} + \underbrace{\sum_{j=2}^{\ell} (\phi^j x_j(\zeta))}_{\text{residual part}} \quad (13)$$

If the random vector $\Psi^D(\zeta)$ is approximated by the principal part

$$\hat{\Psi}^D(\zeta) \equiv E[\Psi^D(\zeta)] + \phi^1 x_1(\zeta), \quad (14)$$

then the resulting (normalized) mean square error (Fukunaga, 1990) is:

$$\varepsilon_{\text{rms}}^2 \equiv \frac{\text{Trace}\left(\text{Cov}\left[\left(\Psi^D(\zeta) - \hat{\Psi}^D(\zeta)\right)\right]\right)}{\text{Trace}\left(\text{Cov}\left[\Psi^D(\zeta)\right]\right)} = \frac{\left(\sum_{j=2}^{\ell} \lambda_j\right)}{\left(\sum_{j=1}^{\ell} \lambda_j\right)} \quad (15)$$

The K-L expansion of fatigue test data shows that $\varepsilon_{\text{rms}}^2$ in Eq. (15) is in the range of 0.018 to 0.035 for all four data sets. Furthermore, the principal eigenvector ϕ^1 , associated with the largest eigenvalue λ_1 , closely fits the ramp function $(t - t_o)$ in each case and the proportionality constants are directly related to the parameter $\sigma_{\Omega}^2(\Delta S)$ in Eq. (11) for the respective values of ΔS for the individual data sets. Ditlevsen (1986) also observed somewhat similar properties by statistical analysis. Nevertheless, the K-L expansion provided deeper physical insight as seen below.

The terms on the right hand side of Eq. (13) are compared with those of Eq. (8) to generate the following equivalence between the discrete-time model from test data and the postulated continuous-time model:

$$\phi^1 x_1(\zeta) \sim \left\{ (\Delta S)^m (\Omega(\zeta, \Delta S) - \mu_{\Omega}(\Delta S))(t - t_o) : t \in [t_o, t_f] \right\} \quad (16)$$

$$\underbrace{\sum_{j=2}^{\ell} \left(\phi^j x_j(\zeta) \right)}_{\text{discrete-time model derived from test data}} \sim \underbrace{\left\{ \left((\Delta S)^m \Omega(\zeta, \Delta S) \right) \int_{t_o}^t d\tau (\rho(\zeta, \tau) - 1) : t \in [t_o, t_f] \right\}}_{\text{postulated continuous-time model}} \quad (17)$$

The entities in Eqs. (16) and (17) are mutually statistically orthogonal. It follows from Eq. (11) that the uncertainties associated with an individual sample resulting from $\Omega(\zeta, \Delta S)$ dominate the cumulative effects of material inhomogeneity and measurement noise due to $\int_{t_o}^{t_f} d\tau (\rho(\zeta, \tau) - 1)$ unless $(t_f - t_o)$ is very small. Therefore, from the perspectives of risk analysis and remaining life prediction (where $(t_f - t_o)$ is expected to be large), an accurate identification of the parameters $\mu_{\Omega}(\Delta S)$ and $\sigma_{\Omega}^2(\Delta S)$ of the random process $\Omega(\zeta, \Delta S)$ is crucial and the role of $\rho(\zeta, t)$ is much less significant. This observation is consistent with the statistical analysis of fatigue test data by Ditlevsen (1986) where the random process described by Eq. (17) was treated as the zero-mean residual.

5.2.2.1 Model Parameters and Probability Distributions

The model parameters m , μ_{Ω} , σ_{Ω}^2 , and σ_p^2 in Eqs. (9) and (10) were identified based on the four data sets described above. The exponent parameter m is first identified as an ensemble average estimate from the slope of the logarithm of crack growth rate in Eq. (3) for both materials, 7075-T6 and 2024-T3. A database for the random process $\Omega(\zeta, \Delta S)$ was generated following Eq. (6) over a period $[t_o, t_f]$ as:

$$\Omega(\zeta, \Delta S) = \frac{\left(\frac{c(\zeta, t)^{1-m/2} - c(\zeta, t_0)^{1-m/2}}{1 - \frac{m}{2}} \right) - m \left(\frac{\pi}{4w} \right)^2 \left(\frac{c(\zeta, t)^{3-m/2} - c(\zeta, t_0)^{3-m/2}}{3 - \frac{m}{2}} \right)}{\left((t_f - t_0) + \int_{t_0}^{t_f} d\tau (\rho(\zeta, \tau) - 1) \right) (\Delta S)^m} \quad (18)$$

Given that $\Omega(\zeta, \Delta S)$ is not explicitly dependent on time by construction of Eq. (4) and $E[\rho(\zeta, \tau) - 1] = 0$, the parameter $\mu_\Omega(\Delta S)$ was the ensemble average estimate from the data sets for each type of material. Because the parameters $\sigma_\Omega^2(\Delta S)$ and σ_ρ^2 could not be separately identified from Eq. (18) alone, the additional information of the eigenvalues, $\lambda_1, \lambda_2, \dots, \lambda_\ell$, of $C_{\Psi\Psi}^D$ generated by Karhunen-Loève analysis was used. Taking expected values of Euclidean norms of the terms on both sides of Eqs. (16) and (17) and making use of Eq. (15), the following relations were obtained based on the experimental data over a period $[t_0, t_f]$:

$$\text{Var}[(\Delta S)^m \Omega(\zeta, \Delta S)] (t_f - t_0)^2 \approx \lambda_1 \Rightarrow \sigma_\Omega^2(\Delta S) \approx \frac{(\Delta S)^{-2m} \lambda_1}{(t_f - t_0)^2} \quad (19)$$

$$(\Delta S)^{2m} \left(\sigma_\Omega^2(\Delta S) + \mu_\Omega^2(\Delta S) \right) \sigma_\rho^2 (t_f - t_0) \approx \sum_{j=2}^{\ell} \lambda_j \Rightarrow \sigma_\rho^2 \approx \frac{\sum_{j=2}^{\ell} \lambda_j}{\lambda_1 + \left((t_f - t_0) (\Delta S)^m \mu_\Omega(\Delta S) \right)^2} < \frac{\varepsilon_{\text{rms}}^2}{1 - \varepsilon_{\text{rms}}^2} \quad (20)$$

The parameters μ_Ω , σ_Ω^2 , and σ_ρ^2 were evaluated via Eqs. (18), (19) and (20) for different ranges of fatigue crack data (i.e., different values of t_0 and t_f). The results were consistent for modest changes in t_0 and t_f , confirming that $\Omega(\zeta, \Delta S)$ is a random variable for a given constant ΔS and that $\rho(\zeta, t)$ is stationary white noise. Testing with large changes in t_0 and t_f could not be accommodated because of the limited ranges of sample paths in the experimental data sets.

The following generalized parametric relations were postulated for different levels of (constant-amplitude) stress excitation for a given material:

- $\mu_\Omega(\Delta S) \equiv E[\Omega(\zeta, \Delta S)]$ is independent of ΔS (i.e., μ_Ω is a constant and $E[(\Delta S)^m \Omega(\zeta, \Delta S)] = (\Delta S)^m \mu_\Omega$)
- $\sigma_\Omega^2(\Delta S) \equiv \text{Var}[\Omega(\zeta, \Delta S)]$ is proportional to $(\Delta S)^{-2m}$ (i.e., $\text{Var}[(\Delta S)^m \Omega(\zeta, \Delta S)]$ is a constant)
- $\text{Var} \left[(\Delta S)^m \int_{t_0}^t d\tau (\rho(\zeta, \tau) - 1) \right]$ is small compared to $\text{Var}[(\Delta S)^m \Omega(\zeta)(t - t_0)]$ for large $(t - t_0)$

The above three relations are consistent with the experimental data sets of Ghonem and Dore (1987) for 7075-T6 aluminum alloy. The third relation follows from Eq. (11), providing an approximation for risk analysis and remaining life prediction described in a subsequent subsection. The first two relations could not yet be verified for 2024-T3 aluminum alloy because the Virkler data set provides only one level of stress range. These relations are expected to be valid for ductile alloys and many other metallic materials because the nature of dependence of the model parameters on the material microstructure and specimen preparation (i.e., machining operations) is similar. Estimates of the model parameters for 2024-T3 and 7075-T6 aluminum alloys are summarized in Table 5-3.

Table 5-3. Estimated Model Parameters

Data Set and Material Type	Stress Range ΔS (MPa)	m (dimensionless)	μ_{Ω} (SI units)	$(\Delta S)^m \sigma_{\Omega} / \mu_{\Omega}$ (SI units)	μ_{ρ} (dimensionless)	$(\Delta S)^m \sigma_{\rho} / \mu_{\rho}$ (SI units)
Virkler Data (2024-T3)	21.04	3.4	6.4×10^{-7}	5.634×10^4	1.0	4.980×10^2
Ghonem Data #1 (7075-T6)	15.84	3.6	7.7×10^{-7}	7.573×10^4	1.0	8.426×10^2
Ghonem Data #2 (7075-T6)	17.80	3.6	7.7×10^{-7}	7.573×10^4	1.0	8.426×10^2
Ghonem Data #3 (7075-T6)	13.24	3.6	7.7×10^{-7}	7.573×10^4	1.0	8.426×10^2

Several investigators have assumed that the crack growth rate in metallic materials is lognormal-distributed (e.g., [Sobczyk and Spencer 1992]). Others have treated the crack length to be lognormal-distributed (e.g., [Ray et al. 1998]) based on the assumption that the crack growth process is highly correlated. The results of K-L expansion in Eqs. (12) to (17) are in agreement with these claims because $\Omega(\zeta, \Delta S)$, which dominates the random behavior of fatigue crack growth, can be considered as a perfectly correlated random process whereas the white noise $\rho(\zeta, t)$ is a perfectly uncorrelated random process. Yang and Manning (1996) have presented an empirical second-order approximation of crack growth by postulating lognormal distribution of a parameter that does not bear any physical relationship to ΔS but is, to some extent, similar to $\Omega(\zeta, \Delta S)$ in the present model.

The random process $\Omega(\zeta, \Delta S)$ was hypothesized to be a two-parameter ($r=2$), lognormal-distributed (Bogdonoff and Kozin 1985) process, and its goodness of fit is examined by both χ^2 and Kolmogorov-Smirnov tests of experimental data. Each of the four data sets was partitioned into $L=12$ segments to assure that each segment contains at least 5 samples. With $(L-r-1)=9$ degrees of freedom, the χ^2 -test shows that for each of the four data sets, the hypothesis of two-parameter lognormal-distribution of $\Omega(\zeta, \Delta S)$ passed the 10% significance level which suffices the conventional standard of 5% significance level. For each of the four data sets, the hypothesis of two-parameter lognormal-distribution of $\Omega(\zeta, \Delta S)$ also passed the 20% significance level of the Kolmogorov-Smirnov test.

Next, a probability distribution of $\rho(\zeta, t)$ was hypothesized. Because the crack length and crack growth rate are guaranteed to be non-negative, Eq. (3) enforces that the random noise $\rho(\zeta, t)$ must also be non-negative with probability 1 for all t . As a viable option, it could be hypothesized that the two-parameter lognormal distribution for $\rho(\zeta, t)$ was similar in structure to that of $\Omega(\zeta, \Delta S)$. Then, the right hand side of Eq. (4) becomes lognormal-distributed because the product of two lognormal variables is lognormal. The result is that the rate of fatigue crack damage (see Eqs. (4) and (8)) is lognormal distributed.

5.2.2.2 Model Prediction

Figure 5-7 compares the analytically derived lognormal-distributed probability density functions (pdf's) of $\Omega(\zeta, \Delta S)$ with the corresponding histograms generated from experimental data by approximately compensating the relatively small second-order statistics of the noise $\rho(\zeta, t)$. Referring to Table 5-3, the mean μ_{Ω} in the model is identical for the three data sets of 7075-T6 while the corresponding variance is different in each set. This is because $\sigma_{\Omega}^2(\Delta S)$ is inversely proportional to $(\Delta S)^{2m}$ and ΔS is different for each data set— σ_{Ω}^2 is largest for the Ghonem data set #3 for which $\Delta S = 13.24$ MPa is smallest and σ_{Ω}^2 is smallest for the Ghonem data set #2 for which $\Delta S = 17.80$ MPa is largest of the three data sets. However, for 2024-T3, no such comparison could be made because only one ΔS is available in the Virkler data set.

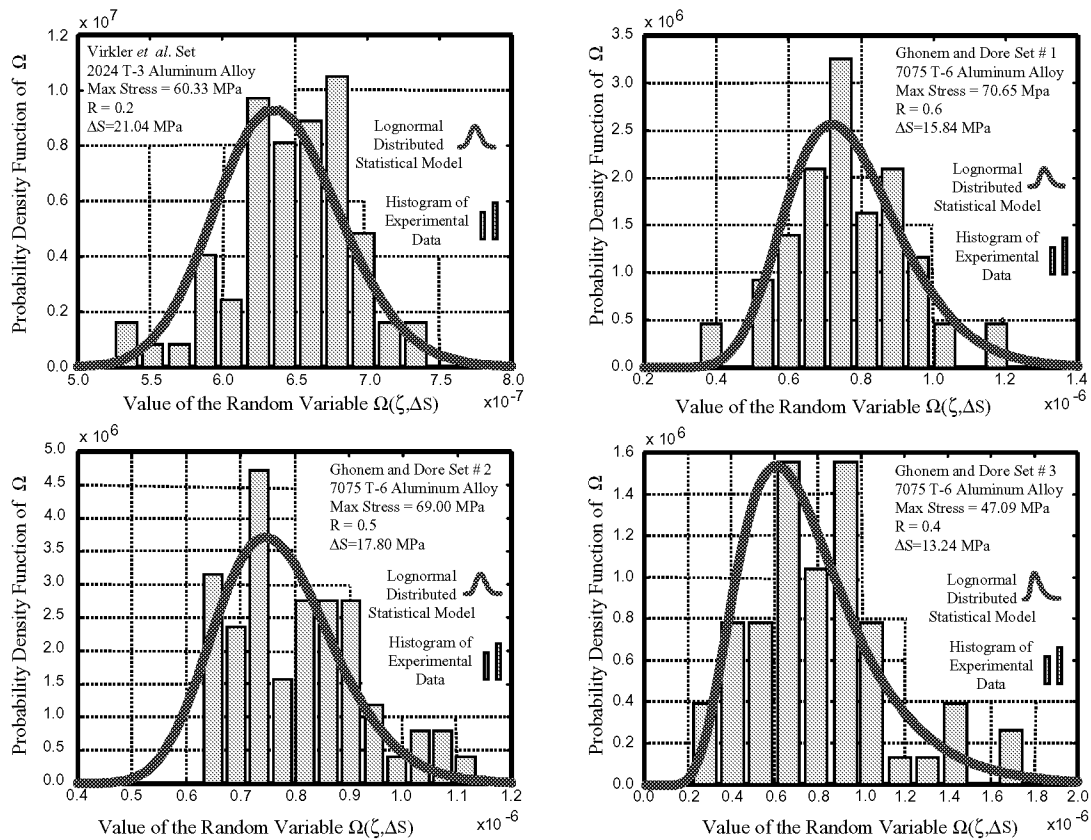


Figure 5-7. Identification of probability density function (PDF) of the model parameter Ω .

Next, model predictions of crack growth were obtained by Monte Carlo simulation of the stochastic difference equation (3) using the parameters listed in Table 5-3. Lognormal distributions of both $\Omega(\zeta, \Delta S)$ and $\rho(\zeta, t)$ were realized by taking exponentials of outputs of the standard normal random number generator with different seed numbers. Test data and model predictions were both used to generate probability distribution functions (PDFs) of service cycles to exceed specified limits c^* of crack length. The Virkler set and each of the three Ghonem sets contain 68 samples and 60 samples, respectively, while the Monte Carlo simulations for model prediction have been conducted with 1000 samples in each case. The PDF plots in Figure 4-8 compare model predictions with the experimental data of Virkler et al. (1979) for three different values of c^* (i.e., 11 mm, 14 mm, and 20 mm). Similarly, the three PDF plots from left to right in Figure 4-9 compare model predictions with the data sets, 2, 1, and 3 (in the decreasing order of the effective stress range ΔS) of Ghonem and Dore (1987) for $c^*=11$ mm. The agreement of the predicted PDFs in Figures 5-8 and 5-9 with the respective experimental data is a consequence of fitting the key model parameter $\Omega(\zeta, \Delta S)$ to a high level of statistical significance as seen in Figure 5-7. The small differences between the model-based and experimental PDFs in Figures 5-8 and 5-9 could be further reduced for larger ensemble size of the data sets. Figure 5-10 compares the results of Monte Carlo simulation with the test data of Virkler (1979) and Ghonem and Dore (1987) in a two-column format.

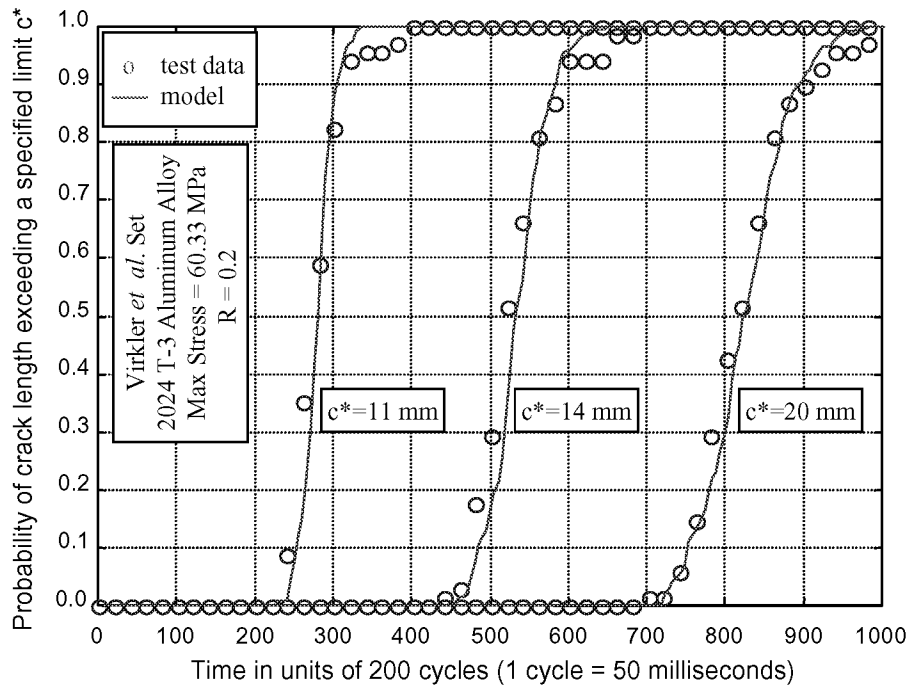


Figure 5-8. Probability distribution of crack length exceeding specified limits. Data source: Virkler et al. 1979.

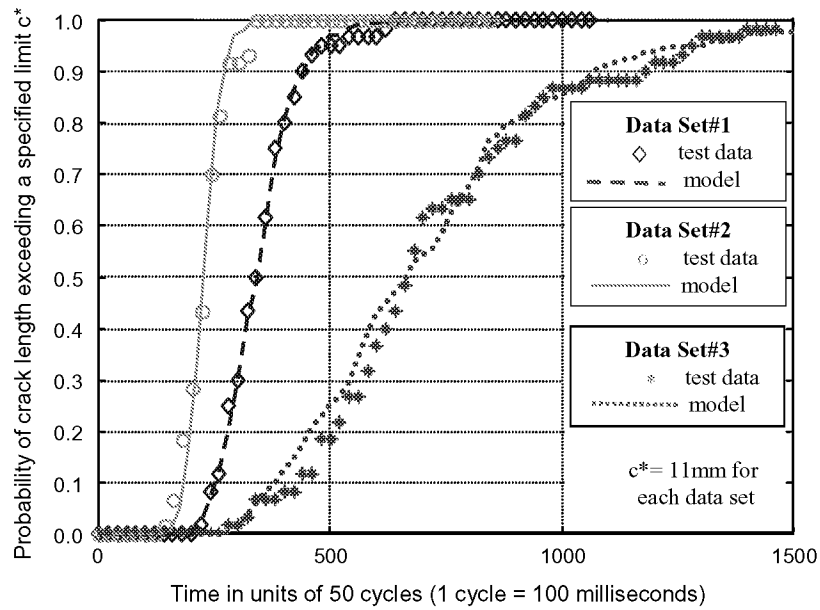


Figure 5-9. Probability distribution of crack length exceeding specified limits. Data source: Ghonem & Dore 1987.

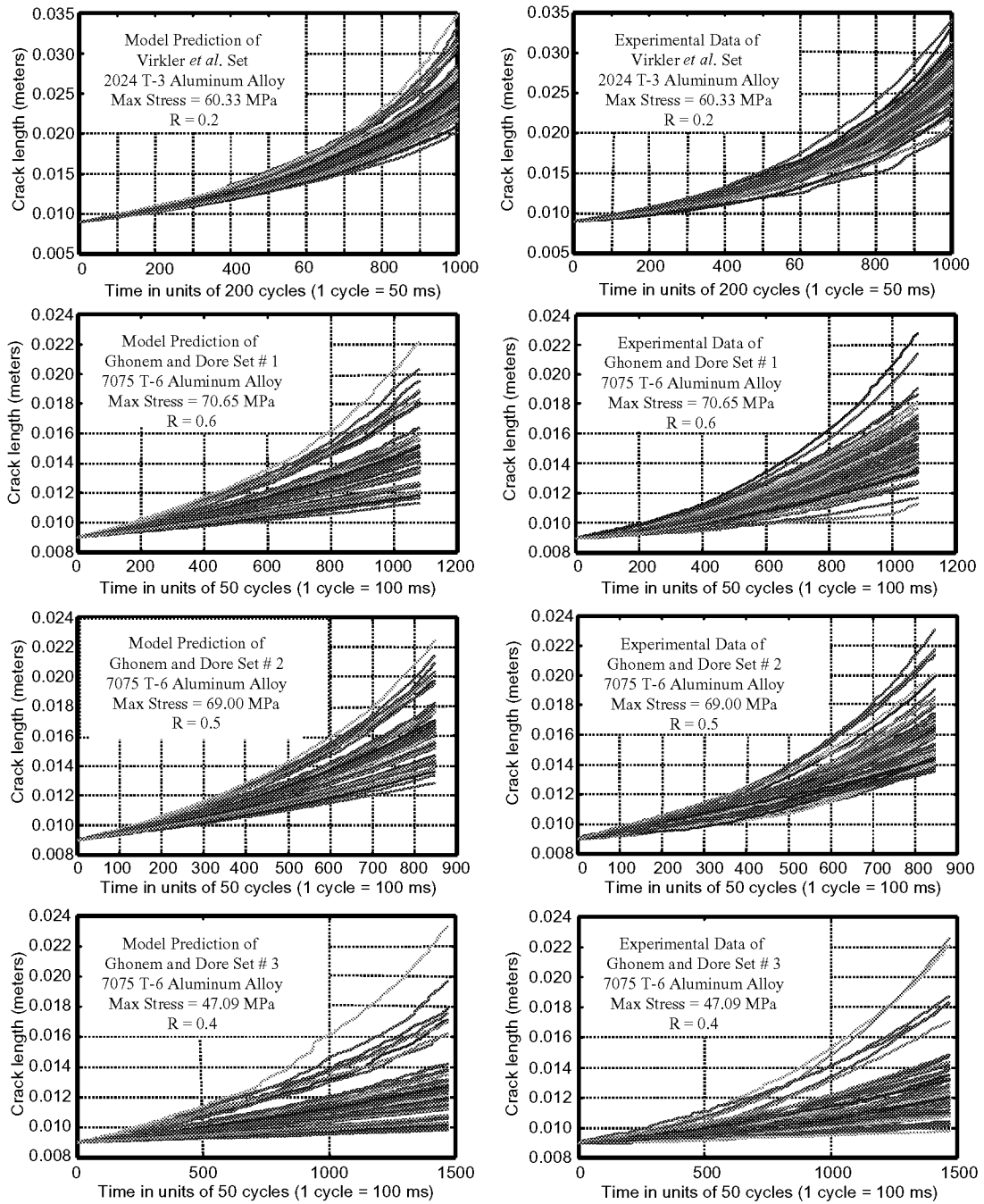


Figure 5-10. Comparison of Monte Carlo simulation of the fatigue crack model with experimental data. Each plate in the left column presents model prediction and the corresponding plate in the right column presents experimental data (crack growth vs. cycles for each sample).

5.2.3 Risk Analysis and Remaining Life Prediction

The stochastic model can be used for risk analysis and remaining life prediction of critical components. As pointed out earlier, the impact of $\rho(\zeta, t)$ on overall scatter of the crack growth profile is not significant for large $(t - t_0)$. In general, t_0 signifies the starting time of a machine after maintenance or inspection. Because risk analysis and life prediction become important after a significant lapse of time (i.e., when $(t - t_0)$ is sufficiently large), it is reasonable to make these decisions based only on the PDF of $\Omega(\zeta, \Delta S)$.

Potential failures were identified by multi-level hypotheses testing based on the stochastic measure of fatigue crack damage (see Eq. (8)). Multi-level hypotheses testing provided a more precise characterization of potential faults than bi-level fail/no-fail hypothesis testing, and is essential for early warning and timely detection and identification of soft failures in gradually degrading components of aircraft structures. In general, if M different types of failure modes are considered, then $M+1$ distinct modes (including the normal mode) could be designated by $M+1$ levels of hypotheses.

$M+1$ hypotheses were defined based on a partition of the crack length in the range $[\bar{c}_0, \infty)$ where \bar{c}_0 is the (known) minimum threshold of the initial crack length $c(\zeta, t_0)$, which is assumed to be measured with good precision, i.e., $\sigma_{\bar{c}_0}^2 \approx 0$. The first M hypotheses are defined on the range $[\bar{c}_0, \bar{c}_M]$ where \bar{c}_M is the critical crack length beyond which the crack growth rate rapidly becomes very large leading to complete rupture:

$$\begin{aligned} H_0(t, t_0) &: c(\zeta, t) \in [\bar{c}_0, \bar{c}_1) \\ H_1(t, t_0) &: c(\zeta, t) \in [\bar{c}_1, \bar{c}_2) \\ &\vdots \\ H_{M-1}(t, t_0) &: c(\zeta, t) \in [\bar{c}_{M-1}, \bar{c}_M); \text{ where } \bar{c}_i = \bar{c}_0 + i \frac{(\bar{c}_M - \bar{c}_0)}{M}, i = 1, 2, \dots, (M-1) \end{aligned} \quad (21)$$

The last (i.e., the M^{th}) hypothesis is defined as $H_M: c_\tau \in [\bar{c}_M, \infty)$, which is popularly known as the unstable crack region in the fracture mechanics literature (Suresh 1991). Each of these $M+1$ hypotheses represents a distinct range in the entire space of crack lengths from an initial value till rupture occurs, and together they form an exhaustive set of mutually exclusive regions in the state-space of crack length. The first M hypotheses were generated as:

$$c(\zeta, t) \in H_j(t, t_0) = [\bar{c}_j, \bar{c}_{j+1}) \Rightarrow \psi(\zeta, t; t_0) \in [\psi_j, \psi_{j+1}) \quad \text{for } j = 0, 1, 2, \dots, M-1 \text{ and a given } \Delta S \quad (22)$$

where $\psi_j \equiv \frac{(\bar{c}_j / w)^{1-m/2} - (\bar{c}_0 / w)^{1-m/2}}{1-m/2} - m \left(\frac{\pi}{4} \right)^2 \left(\frac{(\bar{c}_j / w)^{3-m/2} - (\bar{c}_0 / w)^{3-m/2}}{3-m/2} \right)$ follows the

structure of Eq. (7). As discussed earlier, the process $\psi(\zeta, t; t_0)$ was approximated by

ignoring the effects of the noise term $(\rho(\zeta, t) - 1)$, i.e., by setting the integral within parentheses on the right side of Eq. (8) to zero as:

$$\psi(\zeta, t; t_0) \approx w^{m-2} \Omega(\zeta, \Delta S) (\Delta S)^m (t - t_0) \quad (23)$$

The probability that the j^{th} hypothesis, $H_j(t, t_0)$ was obtained from the instantaneous (conditional) probability distribution function $F_{\psi|c(\zeta, t_0)}(\bullet; t|\bar{c}_0)$ of $\psi(\zeta, t; t_0)$. This was directly generated, without any computationally expensive integration, from the two-parameter lognormal distribution of $\Omega(\zeta, \Delta S)$. Probabilities of the individual hypotheses become:

$$\begin{aligned} P[H_j(t, t_0)] &= F_{\psi|c(\zeta, t_0)}(\psi_{j+1}; t|\bar{c}_0) - F_{\psi|c(\zeta, t_0)}(\psi_j; t|\bar{c}_0) \text{ for } j = 0, 1, 2, \dots, M-1 \\ P[H_M(t, t_0)] &= 1 - \sum_{j=0}^{M-1} P[H_j(t, t_0)] \end{aligned} \quad (24)$$

Examples based on Virkler and Ghonem data sets are presented to elucidate the concept of hypothesis testing for risk analysis and life prediction. The probability that the random crack length $\{c(\zeta, t): t \geq t_0\}$ at a given time t is located in one and only one of these segments was computed in real time by Eq. (24). For each data set, it was observed that $\bar{c}_0 = 9.0$ mm with probability 1. The critical crack length was chosen based on the geometry of the test specimens:

- $\bar{c}_M = 45.0$ mm for the Virkler experiment (in which the specimen half-width is 76.2 mm)
- $\bar{c}_M = 27.0$ mm for the Ghonem experiments (in which the specimen half-width is 50.4 mm)

The space $[\bar{c}_0, \infty)$ was partitioned into $M+1$ regions. In these examples, 11 hypotheses (i.e., $M=10$) were chosen for both data sets. The range of each hypothesis was defined as depicted in Table 5-4 and Table 5-5. The time evolution of probability of the hypotheses for the four data sets is shown in the four plates of Figure 5-11. In each case, the plot of H_0 begins with a probability equal to 1 at time $t = t_0$ and later diminishes as the crack grows with time (i.e., number of load cycles applied). The probability of each of the hypotheses H_1 to H_9 is initially zero and then increases to a maximum and subsequently decreases as the crack growth process progresses with time. The probability of the last hypothesis H_{10} (on the extreme right in each plate of Figure 5-11) of unstable crack growth beyond the critical crack length \bar{c}_M initially remains at zero and increases rapidly only when the specimen is close to rupture. At this stage, the probability of each of the remaining hypotheses is zero or rapidly diminishes to zero.

Table 5-4. Crack Damage Hypotheses for Virkler et al. Data

Description	Range of Fatigue Crack Length
Hypothesis H ₀	9.00 mm ≤ c(t) < 12.6 mm
Hypothesis H ₁	12.6 mm ≤ c(t) < 16.2 mm
•	•
•	•
•	•
Hypothesis H ₉	41.4 mm ≤ c(t) < 45.0 mm
Hypothesis H ₁₀	45.0 mm ≤ c(t) (Unstable Crack Growth)

Table 5-5. Crack Damage Hypotheses for Ghonem & Dore Data

Description	Range of Fatigue Crack Length
Hypothesis H ₀	9.00 mm ≤ c(t) < 10.8 mm
Hypothesis H ₁	10.8 mm ≤ c(t) < 12.6 mm
•	•
•	•
•	•
Hypothesis H ₉	25.2 mm ≤ c(t) < 27.0 mm
Hypothesis H ₁₀	27.0 mm ≤ c(t) (Unstable Crack Growth)

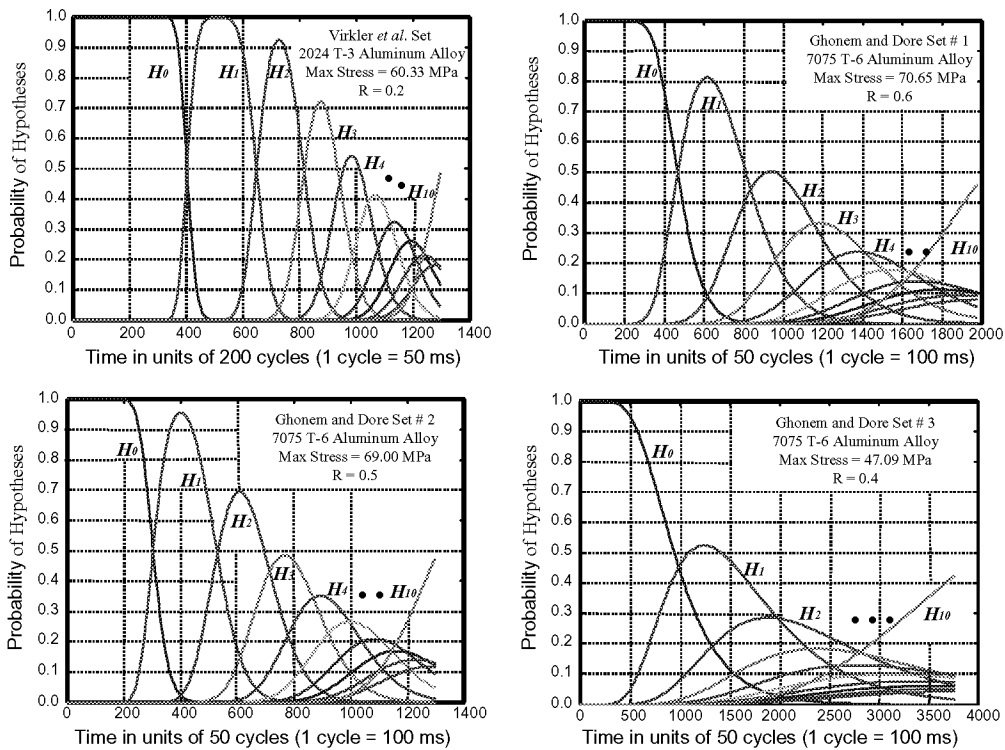


Figure 5-11. Probabilities of hypotheses for fatigue crack propagation for each hypothesis described in Tables 5-4 and 5-5.

The hypotheses testing procedure can be executed in real time on inexpensive platforms such as a Pentium processor in the plant instrumentation and control system for issuing alerts and warnings while the machine is in operation. For example, the space of crack length, defined by $[\bar{c}_0, \infty)$, can be partitioned into four hypotheses denoting three regions of green, yellow and red alert conditions for the first three hypotheses and catastrophic conditions for the fourth hypothesis. Although alerts and warnings are useful for operational support and safety enhancement, operations planning and maintenance scheduling require remaining life prediction. Equipment readiness assessment and failure prognosis based on current condition and projected usage of the machinery are important tools for operations and maintenance planning, especially in an information-based maintenance environment.

If the instantaneous (conditional) probability distribution function $F_{\psi|c_0}(\bullet; t|\bar{c}_0)$ of $\psi(\zeta, t, t_0)$ is known, the remaining life $T(t, Y_d(t), \varepsilon)$ can be computed on-line at any specified time instant t based on a desired plant operational profile $Y_d(t) = \{y(\theta) : \theta \geq t\}$ and a confidence level $(1 - \varepsilon)$. This implies that if the plant operation is scheduled to yield the desired output $Y_d(t)$, then $T(t, Y_d(t), \varepsilon)$ is the maximum time of operation such that the probability of the crack length $c(\zeta, t + T)$ to exceed \bar{c}_M is less than a positive fraction ε . The algorithm for prediction of remaining life is:

$$T(t; Y_d(t); \varepsilon) = \text{Sup} \{ \theta \in [0, \infty) : P[c_{t+\theta} \leq \bar{c}_M] > (1 - \varepsilon) \} \quad (25)$$

The prediction algorithm in Eq. (25) is executed in real time based on the current information. The generated results can then be conveyed to a decision making module such as ACAMS for failure prognosis, life extending control, and maintenance scheduling.

5.3 DISCUSSION

This section presented formulation and validation of (1) a deterministic state-space model for fatigue crack growth prediction under variable-amplitude loading and (2) a stochastic model of fatigue crack damage. Both models were evaluated with published fatigue data.

5.3.1 State-Space Model

The state-space model was built on fracture-mechanistic principles of the crack-closure concept and experimental observations of fatigue test data. The model state variables are crack length and crack opening stress, and the model inputs are maximum stress and minimum stress in the current cycle and the minimum stress in the previous cycle. The crack growth model was represented in the autoregressive moving average (ARMA) setting by a second order nonlinear difference equation that recursively computes the state variables without the need for storage of stress history.

Although there are similarities between the structure of the state-space model for crack growth prediction and that of FASTRAN (Newman 1992), the major difference is in the formulation of transient behavior of the crack opening stress. Because the crack opening stress in FASTRAN is calculated asynchronously based on a relatively long history of stress excitation (~300 cycles), it does not follow a state-space structure. The state-space model of fatigue crack growth captures the effects of stress overload and reverse plastic flow and is applicable to various types of loading including single-cycle overloads, irregular sequences, and random loads. The state-space model was validated with fatigue test data for 7075-T6 and 2024-T3 aluminum alloys. The model predictions were also compared with those of FASTRAN for identical input stress excitation. While the results derived from these two models are comparable, the state-space model enjoys significantly smaller computation time and memory requirements.

Previously, simplistic state-space models, meant for constant-amplitude loads (Holmes and Ray, 1998), have been used for monitoring and control applications. With the availability of the state-space model, reliable strategies can now be formulated for real-time decision and control of damage-mitigation and life-extension.

5.3.2 Stochastic Model

The stochastic model of fatigue crack damage enables risk analysis and life prediction of aircraft structures fabricated from ductile alloys. The measure of fatigue crack damage at an instant (i.e., at the end of a stress cycle) is expressed as a continuous function of the current crack length and initial crack length. The uncertainties in the crack damage measure were shown to accrue primarily from a single lognormal-distributed random parameter associated with individual specimens and, to a much lesser extent, from the random noise due to material inhomogeneity. This conclusion is consistent with the findings of other investigators.

The constitutive equation of the damage model was based on the physics of fracture mechanics and was validated by Karhunen-Loève analysis of fatigue test data for 2024-T3 and 7075-T6 aluminum alloys at different levels of (constant-amplitude) cyclic load. A systematic procedure for parameter identification was also established. The predicted probability distribution function (PDF) of service cycles to exceed a specified crack length was shown to be in close agreement with that generated from the test data. The (non-stationary) probability distribution function of crack damage was obtained in a closed form without numerically solving stochastic differential equations in the Wiener integral or Itô integral setting. The model allows formulation of risk assessment and life prediction algorithms for real-time execution on conventional processing platforms such as a Pentium processor. Consideration of other uncertainties (e.g., variable-amplitude and multi-axial and loading, stress corrosion) in crack growth will enhance applications of the stochastic model.

SECTION 6 CONCLUSIONS AND RECOMMENDATIONS

6.0 INTRODUCTION

The purpose of this project was to develop a multiplexed airframe structural sensor prototype for on-board characterization of multiple and synergistic failure modes in current and future airframes and to demonstrate the technologies in a laboratory setting. In order to achieve the goals of the program, the ARINC team completed the following tasks:

- Established requirements for structural health monitoring systems
- Identified and characterized a prototype structural sensor system and demonstrated the sensors on realistic test articles
- Developed sensor interpretation algorithms

The structural sensing system was designed to provide data sources for ARINC's Aircraft Condition Analysis and Management System (ACAMS), which was developed in a complementary program.

This section summarizes the results, draws conclusions, and makes recommendations that will lead to the implementation of structural health monitoring capabilities

6.1 HEALTH MONITORING SYSTEM REQUIREMENTS

Requirements were developed for a health monitoring system for commercial airframe structures. These system requirements were developed based on an assessment of operators maintenance programs and an analysis of aircraft structural degradation modes.

6.1.1 Maintenance Program Requirements

The purpose of introducing SHM into commercial transports is to enhance aviation safety by improving the effectiveness of the operators' continued airworthiness programs. The primary consideration for assessing the effect of SHM systems on continued airworthiness is to determine their potential influence on scheduled maintenance programs and the potential to reduce unscheduled maintenance actions. SHM systems could be an important factor in improving the effectiveness of inspection and maintenance programs and enabling on-condition maintenance. Section 2 of this report included a review of maintenance practices that are employed by the air carriers and the identification of the potential role for health monitoring technologies. The following conclusions were drawn from this analysis:

- Once the applicability and reliability of SHM systems has been proven, the overall acceptance by the end user will require integration of SHM systems with existing systems and capabilities. In order for SHM systems to be an integral part of the operator's structural maintenance programs, they would be required to automate or improve inspections and tests, detect fault precursors so that

maintenance or replacement activities can be anticipated and scheduled, and include the data collection and analysis functions associated with maintenance program review.

- HM systems could provide benefit to the operators for each of the current preventive maintenance approaches. First, hard-time components could be converted to one of the reliability-based approaches by identifying faults that are precursors to failure and monitoring the components using a SHM system. Second, SHM systems could be used to automate the inspection, measurements, and tests for on-condition components. Finally, SHM systems could be used to detect the precursors to failure for condition-monitored components so that maintenance or replacement activities can be anticipated and scheduled.

6.1.2 Degradation Modes

An important area of emphasis of this project was on sensors to detect aging mechanisms for metallic airframe structures. An understanding of potential damage mechanisms, structural design criteria and fail-safe features, and structural maintenance philosophy was needed to assess the efficacy of sensor-based system to monitor structural condition. Section 2 of this report also includes a discussion of structural degradation modes. The following structural degradation modes and sensing strategies were considered for commercial transport aircraft:

- Low-cycle fatigue (fatigue cracking emanating from pre-existing flaws or defects) – The SHM system will be required to detect the presence of subcritical fatigue cracks, monitor crack growth, and alert the maintenance organization that maintenance or repair should be accomplished before the crack reaches critical length.
- Widespread fatigue damage (the simultaneous presence of small cracks initiating from normal quality structural details) – The SHM system will be required to detect damage events (initiation and subcritical growth of small cracks), characterize damage accumulation and assess fail-safe residual strength, and alert the maintenance organization that maintenance should be accomplished to preclude occurrence of the onset of WFD.
- High-cycle fatigue (fatigue damage resulting from exposure to high-frequency load cycles from aerodynamic, mechanical, and acoustic sources). – Because high frequency loads can lead to significant damage in very short times, the only workable strategy to monitor structural health is to sense the conditions for HCF and make repairs to avoid crack initiation and growth.
- Corrosion (and stress corrosion cracking) – The strategy for monitoring for corrosion damage is to focus on early detection of incipient corrosion or, preferably, detection of when the corrosion prevention scheme has failed. The SHM system could (1) identify when corrosion protection has broken down to a point where moisture can intrude, and (2) identify the presence of corrosion by detecting corrosion products. For stress corrosion cracking, the system will also be required to detect crack initiation or the early stages of crack growth.

- Accidental damage (damage resulting from unexpectedly severe operating conditions, operations and maintenance handling, or thermal and environmental exposure). – The SHM system will be required to monitor for discrete damage incidents and trigger the appropriate sensors to characterize the extent of damage in case an event is detected.

6.2 SENSOR SYSTEM DEVELOPMENT

A sensing approach based on the potential damage mechanisms, component design criteria, and operators' maintenance practices, was developed to monitor selected aircraft structures. It was determined that multiple types of structural sensors were needed to detect the indications of degradation because of the wide range of structural damage mechanisms.

This program focused on fiber optic sensors because of their small size, amenability to multiplexing of sensor elements, low probability for interference with adjacent flight systems, and insusceptibility to electromagnetic interference effects. The selected sensors were evaluated to validate their suitability for monitoring aging degradation, characterize the sensor performance in aircraft environments, and demonstrate placement processes and multiplexing schemes. Corrosion sensors (i.e., LPG moisture and metal ion sensors) and fatigue sensors (i.e., EFPI strain and extension, Bragg grating strain, and EFPI acoustic emission sensors) were evaluated under this program. In addition, a unique micromachined multimeasurand sensor concept was developed and demonstrated.

6.2.1 Corrosion

This program focused on LPG optical fiber chemical sensors because they have been shown to effectively discern the presence of significant moisture, the metal ions indicative of corrosion products, or the pH of a potential electrolyte solution. Performance of LPG-based sensors depends critically on the location and use of the sensor element and the environment surrounding the sensor (e.g., sensor elements could be placed over or embedded within corrosion protection coatings in new aircraft and retrofit applications). The LPG moisture and metal ion sensors were tested to demonstrate the use of the LPG sensor in applications where sensors are either embedded under corrosion preventative compounds (CPC), aircraft sealant, and primer; embedded within lap joints or attached to the surface of structures. The conclusions are summarized below:

- Embedded sensor elements were able to sense target molecules (water and metal ions) that were able to penetrate the corrosion protection schemes
- LPG-based metal ion sensors are capable of detecting the presence of corrosion by-products within an occluded region in a simulated lap joint.

6.2.2 Fatigue

Three types of sensors were evaluated during this program—distributed Bragg grating sensors to monitor changes in strain field distribution as fatigue damage propagates; EFPI strain sensors to detect deformation resulting from fatigue damage; and EFPI acoustic

emission sensors to detect crack initiation and very small crack growth. The conclusions from these evaluations are described in the following:

- Distributed Bragg grating sensors provided a survey of strain distribution that was shown to be effective in detecting and isolating fatigue damage in metallic structure by monitoring changes in strain distribution. This system was easily multiplexed because a large number of sensing elements (hundreds or thousands) could be combined on the same fiber.
- Strategically placed EFPI strain sensors and extensometers were able to sense indications of load redistribution around a growing defect and detect the presence of growing fatigue damage. EFPI could provide a very important measure of crack opening deflection that would be helpful in monitoring critical crack growth.
- EFPI acoustic emission sensors did not have sufficient sensitivity at high frequencies to detect certain AE events, including fatigue crack initiation and propagation. Even though the developments of this program improved the capabilities dramatically over previous systems, this system still does not have the sensitivity to detect extremely low-level events.

6.2.3 Combined Damage Modes

A unique multimeasurand microsensor device, based on silicon micromachining and EFPI technologies, has been developed and demonstrated as a prototype. This device combines multiple sensing elements into one sensing system in a small, lightweight package. The prototype was a single Si-chip, multi-microcantilever beam sensor consisting of three sensing elements and three optical fiber leads. The prototype sensor was able to monitor wet and dry moisture state, vibration/AE, and temperature.

6.2.4 Sensor System Implementation

Section 3 of this report showed that structural degradation of aircraft materials can be effectively detected and characterized using available sensors. The ability to multiplex moderate (10's) to large (100's) numbers of sensors was demonstrated, but multiple sensor types cannot yet be multiplexed in a single source/sensor/demodulation system.

In general, migration of fiber optic sensors and associated optical and electronic systems to flight environments requires careful consideration of the effects of environmental factors, most notably temperature, on the optical components. Optical sources, couplers, connectors, filters and detectors demonstrate significant performance sensitivity to variations in temperature.

6.3 SENSOR DATA INTERPRETATION

A key component of the structural health monitoring capability is the ability to interpret the information provided by sensor system to characterize the structural condition. Section 4 of this report describes a deterministic state-space fatigue growth model and stochastic model that accounts for the statistical nature of damage development processes.

These models were developed to perform real time characterization and assessment of structural fatigue damage.

The state-space model was built on fracture-mechanistic principles of the crack-closure concept and experimental observations of fatigue test data. The model state variables are crack length and crack opening stress, and the model inputs are maximum stress and minimum stress in the current cycle and the minimum stress in the previous cycle. The crack growth model was represented in the autoregressive moving average (ARMA) setting by a second order nonlinear difference equation that recursively computes the state variables without the need for storage of stress history. The state-space model was validated with fatigue test data for 7075-T6 and 2024-T3 aluminum alloys. The model predictions were also compared with those of FASTRAN for identical input stress excitation. The following conclusions result from the development and evaluation of the state-space model:

- The agreement of model predictions with experimental data supports the state-space model and its fundamental hypothesis that the crack opening stress can be treated as a state variable
- The model captures the effects of stress overload and reverse plastic flow and is applicable to various types of loading including single-cycle overloads, irregular sequences and random loads
- The state-space model enjoys significantly smaller computation time and memory requirements than comparable analytic tools
- The state-space model enables reliable strategies to be formulated for real-time decision and control for damage mitigation and life extension in airframe structures

The stochastic model of fatigue crack damage enables risk analysis and life prediction of aircraft structures fabricated from ductile alloys. The measure of fatigue crack damage at an instant (i.e., at the end of a stress cycle) is expressed as a continuous function of the current crack length and initial crack length. The model was validated against published fatigue data sets. The following conclusions were drawn based on this evaluation:

- Uncertainties in the crack damage measures were shown to accrue primarily from variability in individual specimens and, to a much lesser extent, from material inhomogeneity; this conclusion is consistent with the findings of other investigators
- The constitutive equation of the damage model was based on the physics of fracture mechanics and was validated through analysis of fatigue test data for 2024-T3 and 7075-T6 aluminum alloys at different levels of constant-amplitude cyclic load
- Predicted probability distribution functions of service cycles to exceed a specified crack length were shown to be in close agreement with that generated from the test data

- The model allows formulation of risk assessment and life prediction algorithms for real-time execution on conventional processing platforms such as a Pentium processor

6.5 RECOMMENDATIONS

The following recommendations have been developed based on the results of the SHM development and demonstration described in this report.

- Continue interaction with air carriers and regulatory agencies to ensure that the SHM remains responsive to air carrier needs and applicable on commercial transport aircraft.
- Continue to develop structural sensor systems with a focus on long-term durability and environmental effects on sensor performance and on the development of robust optical components, durable packaging and application bonding techniques, and miniaturization of electronics and demodulation systems.
- Expand the applicability of the sensor suite to structural degradation modes that were not considered in this program, especially detection and characterization of aging of high-strength steel structures and accidental damage of metallic and composite structures.
- Integrate the deterministic state-space model of fatigue crack growth into the diagnostic processor developed for the ACAMS and refine the stochastic model formulation by considering other uncertainties (e.g., variable-amplitude and multi-axial and loading, stress corrosion) in crack growth
- Expand sensor data interpretation capabilities to develop tools to map physical behavior to expected sensor response.
- Validate the functionality of SHM with one-to-one verification of structural diagnoses with physically introduced known faults.
- Perform detailed laboratory testing of structural elements and components for expanded sensor fusion and development of diagnostic and prognostic algorithms.

REFERENCES

- Ake, D. 2000. Personal communication between R. Beard and T. Munns (ARINC) and D. Ake (Airborne Express), February 7, 2000.
- Anderson, T.L. 1995. *Fracture Mechanics*, 2nd ed. Boca Raton, Florida: CRC Press.
- ARINC. 2001. *Aircraft Condition Analysis and Management System*. Final Technical Report. Annapolis, Md.: ARINC, Inc.
- ATA, 1993, *Airline/Manufacturer Maintenance Program Development Document (Revision 2)*, Maintenance Steering Group 3 (MSG-3) Task Force, Washington, D.C.: Air Transport Association of America.
- Bannantine, J.A., J.J. Comer, and J.L. Handrock. 1990. *Fundamentals of Metal Fatigue Analysis*. Englewood Cliffs, NJ: Prentice-Hall.
- Boeing, 1994, *Aging Airplane Corrosion Prevention and Control Program: Model 737-100/200*, Boeing Document D6-38528.
- Bogdanoff, J.L., and F. Kozin. 1985. *Probabilistic Models of Cumulative Damage*. New York: John Wiley.
- Bolotin, V.V. 1989. *Prediction of Service Life for Machines and Structures*. New York: ASME Press.
- Casciati, F., P. Colombi, and L. Farvelli. 1992. Fatigue crack size probability distribution via a filter technique. *Fatigue & Fracture of Engineering Materials & Structures* 15(5): 463–475.
- Childers, B.A., M.E. Froggatt, S.G. Allison, T.C. Moore, D.A. Hare, C.H. Batten, and D.C. Jegley. 2001. *Use of 3000 Bragg Grating Strain Sensors Distributed on Four Eight-Meter Optical Fiber during Static Load Tests of a Composite Structure*. SPIE 8th International Symposium on Smart Structures and Materials, Newport Beach, California, March 4–8, 2001.
- Claus, R.O., M.F. Gunther, A. Wang, and K.A. Murphy. 1992. Extrinsic Fabry-Perot sensor for strain and crack opening displacement measurements from -200 to 900 degrees C. *Smart Materials and Structures* 1(3): 237-242.
- Dai, X., and A. Ray. 1996. Damage-mitigating control of a reusable rocket engine: Parts I and II. *Journal of Dynamic Systems, Measurement and Control, ASME Trans.* 118(33): 401–415.
- Dakin, J., and B. Culshaw. 1988. *Optical Fiber Sensors: Principles and Components*. Boston, Mass.: Artech House.
- Ditlevsen, O. 1986. Random fatigue crack growth — A first passage problem. *Engineering Fracture Mechanics* 23(2): 467–477.
- Edwards, T.E. 2000. Personal communication between A. Bartolini, R. Kent, and T. Munns (ARINC) and T. Edwards (United Airlines), February 2, 2000.
- Elster, J., J. Greene, M. Jones, T. Bailey, S. Lenahan, W. Velander, R. VanTassell, W. Hodges, and I. Perez. 1999. *Optical Fiber-Based Chemical Sensors for Detection of Corrosion Precursors and By-Products*, Proc. SPIE Vol. 3540, pp. 251-257 in Chemical, Biochemical, and Environmental Fiber Sensors X, Robert A. Lieberman; Ed.
- Elster, J.L., J.A. Greene, M.E. Jones, T.A. Bailey, S.M. Lenahan, and I. Perez. 1998. *Optical Fiber-Based Corrosion Sensors for Aging Aircraft*, DoD/FAA/NASA Conference on Aging Aircraft, Williamsburg, VA.
- FAA, 1988, *Maintenance Control by Reliability Methods*, Advisory Circular AC 120-17A, Washington, DC: The Federal Aviation Administration.
- FAA. 1980. *Continuous Airworthiness Maintenance Programs*. FAA Advisory Circular AC 120-16C, Washington, DC: The Federal Aviation Administration.

- Froggatt, M., and J. Moore. 1998. Distributed measurement of static strain in an optical fiber with multiple Bragg gratings at nominally equal wavelengths. *Applied Optics* 37: 1741–1746.
- Fukunaga, K. 1990. *Introduction to Statistical Pattern Recognition*, 2nd ed. Boston, Mass.: Academic Press.
- Ghonem, H., and S. Dore. 1987. Experimental study of the constant probability crack growth curves under constant amplitude loading. *Engineering Fracture Mechanics* 27:1–25.
- Harris, C.E., J.C. Newman, Jr., R.S. Piascik, and J.H. Starnes, Jr. 1996. *Analytical Methodology for Predicting the Onset of Widespread Fatigue Damage in Fuselage Structure*. NASA-TM-110293.
- Hidano, L.A. and U.G. Goranson. 1995. *Inspection Programs for Damage Tolerance: Meeting the Regulatory Challenge*. Pp. 193–211 in Proceedings of the FAA-NASA Sixth International Conference on the Continued Airworthiness of Aircraft Structures, DOT/FAA/AR-95/86. Washington, DC: Federal Aviation Administration.
- Holmes, M., and A. Ray. 1998. Fuzzy damage mitigating control of mechanical structures. *ASME Journal of Dynamic Systems, Measurement and Control* 120(2): 249–256.
- Holmes, M., and A. Ray. 2001. Fuzzy damage mitigating control of a fossil power plant. *IEEE Trans. on Control Systems Technology* 9(1): 140–147.
- Ibrahim, F.K., J.C. Thompson, and T.H. Topper. 1986. A study of the effect of mechanical variables on fatigue crack closure and propagation. *International Journal of Fatigue* 8(3): 135–142.
- Ishikawa, H., A. Tsurui, H. Tanaka, and H. Ishikawa. 1993. Reliability assessment based upon probabilistic fracture mechanics. *Probabilistic Engineering Mechanics* 8: 43–56.
- Jazwinski, A.H. 1970. *Stochastic Processes and Filtering Theory*. New York: Academic Press.
- Johnston, W. M. and Helm, J. D. 1998. *Experimental Results from the FAA/NASA Wide Panel Fracture Tests*, Presented at The Second Joint NASA/FAA/DoD Conference on Aging Aircraft, Williamsburg, VA.
- Jones, M. 1996. *Bragg Grating Sensor Interrogation Using In-line Dual Mode Fiber Demodulator*, Thesis, Electrical Engineering Department, Blacksburg, Va.: Virginia Polytechnic Institute and State University.
- Kallappa, P., M. Holmes, and A. Ray. 1997. Life-extending control of fossil fuel power plants. *Automatica* 33(6): 1101–1118.
- Keller, E.E. 2001. *Real-Time Sensing of Fatigue Crack Damage for Information-Based Decision and Control*, PhD Dissertation. Department of Mechanical Engineering, State College, Penn.: Penn State University.
- Kent, R.M., and D.A. Murphy. 2000. *Health Monitoring System Technology Assessments: Cost Benefits Analysis*. NASA/CR-2000-209848. Hampton, VA: NASA Langley Research Center.
- Kloeden, P.E., and E. Platen. 1995. *Numerical Solution of Stochastic Differential Equations*. Berlin: Springer-Verlag.
- Lin, Y.K., and J.N. Yang. 1985. A stochastic theory of fatigue crack propagation. *AIAA Journal* 23(1): 117–124.
- Meller, S.A. 1996. *Extrinsic Fabry-Perot Interferometer System Using Wavelength Modulated Source*. Masters Thesis, Department of Electrical Engineering, Blacksburg, VA: Virginia Polytechnic Institute and State University.
- Munns, T.E., R.E. Beard, A.M. Culp, D.A. Murphy, and R.M. Kent. 2000. *Analysis of Regulatory Guidance for Health Monitoring*, NASA/CR-2000-210643, Hampton, Va.: NASA Langley Research Center.
- Murphy, K., M. Gunther, A. Vengsarkar, and R.O. Claus. 1991. Quadrature phase-shifted, extrinsic Fabry-Perot optical fiber sensors, *Optics Letters* 16(4): 173–275.

- Newman, J.C., Jr. 1984. A crack opening stress equation for fatigue crack growth. *International Journal of Fracture* 24: R131–R135.
- NRC. 1996a. *Accelerated Aging of Materials and Structures: The Effects of Long-Term Elevated Temperature Exposure*. NMAB-479. National Materials Advisory Board. Washington, D.C.: National Academy Press.
- NRC. 1996b. *New Materials for Next-Generation Commercial Transports*. NMAB-476. National Materials Advisory Board. Washington, D.C.: National Academy Press.
- NRC. 1997. *Aging of U.S. Air Force Aircraft*. NMAB-488-2. National Materials Advisory Board. Washington, D.C.: National Academy Press.
- NTSB (National Transportation Safety Board). 1988. Aircraft Accident Report: Aloha Airlines, Flight 243, Boeing 737-200, N73711, Near Maui, Hawaii, April 28, 1988. NTSB/AAR-89/03. Washington, D.C.: NTSB.
- Ozekici, S., ed. 1996 *Reliability and Maintenance of Complex Systems*, Series F: Computer and Systems Sciences, Vol. 154, Berlin: NATO Advanced Science Institutes (ASI).
- Paris, P.C., and F. Erdogan. 1963. A critical analysis of crack propagation laws. *Journal of Basic Engineering, Trans. ASME* D85: 528–534.
- Patankar, R., and A. Ray. 2000. State-space modeling of fatigue crack growth in ductile alloys. *Engineering Fracture Mechanics* 66: 129–151.
- Poland, S.H., J.-P. Bengtsson, M. Bhatnagar, K.C. Ravikumar, M.J. de Vries, and R.O. Claus, 1994, *Multimeasurand Multiplexed Extrinsic Fabry-Perot Interferometric Sensors*, Pp. 58–66 in *Smart Structures and Materials 1994: Smart Sensing, Processing, and Instrumentation*, SPIE Proceedings Vol. 2191, J.S. Sirkis, Ed., Bellingham, Wash.: SPIE Publications.
- Ray, A., and J. Caplin. 2000. Life extending control of aircraft : Trade-off between flight performance and structural durability. *The Aeronautical Journal* 104(1039): 397–408.
- Ray, A., and R. Patankar 1999. Stochastic modeling fatigue crack propagation under variable amplitude loading. *Engineering Fracture Mechanics* 62: 477–493.
- Ray, A., S. Phoha, and S. Tangirala. 1998. Stochastic modeling of fatigue crack propagation. *Applied Mathematical Modeling* 22: 197–204.
- Schijve, J. 1976. Observations on the Prediction of Fatigue Crack Growth Propagation Under Variable-Amplitude Loading. Pp 3–23 in *Fatigue Crack Growth Under Spectrum Loads, ASTM STP 595*. Philadelphia, Penn.: American Society for Testing and materials.
- Sobczyk, K., and B.F. Spencer. 1992. *Random Fatigue: Data to Theory*. Boston, Mass.: Academic Press.
- Spencer, B.F., J. Tang, and M.E. Artley. 1989. A stochastic approach to modeling fatigue crack growth. *The AIAA Journal* 27(11): ,1628–1635.
- Spencer, F.W. 1996. *Visual Inspection Research Project Report on Benchmark Inspections*, DOT/FAA/AR-96/65. Washington, D.C.: Federal Aviation Administration.
- Suresh, S. 1991. *Fatigue of Materials*, Cambridge, UK: Cambridge University Press.
- Tsurui, A., and H. Ishikawa. 1986. Application of the Fokker-Planck to a stochastic fatigue growth model. *Structural Safety* 4: 15–29.
- Virkler, D.A., B.M. Hillberry, and P.K. Goel. 1979. The statistical nature of fatigue crack propagation. *ASME Journal of Engineering Materials and Technology* 101(2): 148–153.
- Wong, E., and B. Hajek. 1985. *Stochastic Processes in Engineering Systems*. New York: Springer-Verlag.
- Yang, J.N., and S.D. Manning. 1996. A simple second order approximation of stochastic crack growth analysis. *Engineering Fracture Mechanics* 53(5): 677–686.
- Zhang, H., A. Ray, and S. Phoha. 2000. Hybrid life extending control of mechanical structures: Experimental validation of the concept. *Automatica* 36(1): 23–36.
- Zuliani, G., D. Hogg, K. Liu, and R. Measures. 1991. *Demodulation of a Fiber Fabry-Perot Strain Sensor Using White Light Interferometry*. Pp 308–313 in *Fiber Optic Smart*

Structures and Skins IV, SPIE Proceedings Vol. 1588. Bellingham, Wash.: SPIE Publications.

APPENDIX: STATE-SPACE MODEL VALIDATION

This appendix includes the detailed data validating the state-space model with fatigue test data for two aluminum alloys—7075-T6 aluminum alloy specimens under different types of variable amplitude cyclic loading (Porter 1972) and 2024-T3 aluminum alloy specimens under spectrum loading (McMillan and Pelloux 1967)—as well as comparisons with predictions of the other fatigue growth models—FASTRAN and AFGROW.

Porter (1972) collected fatigue crack data under tensile load for 12 in. by 36 in. center-notched panels made out of 0.16 in. thick 7075-T6 aluminum alloy sheets. Figure A-1 shows a schematic of Porter’s specimen for which the constraint factor α_k in Eq. (SS-3) of Section 4 varies between 1.1 and 1.8 (Newman 1992).

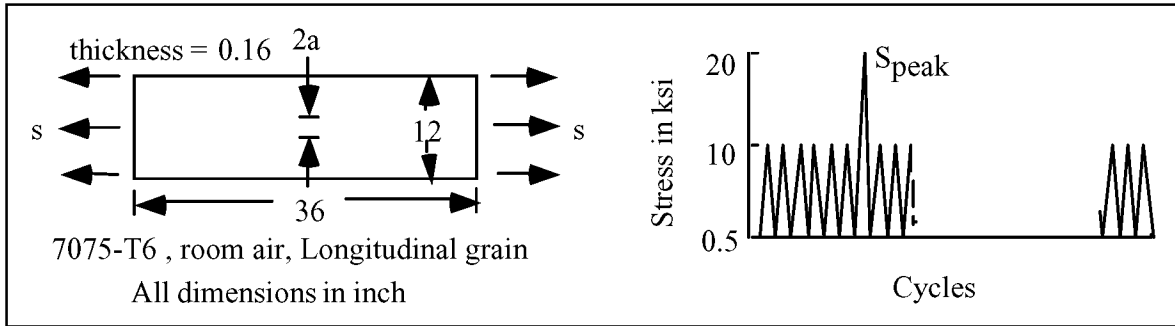


Figure A-1. Porter specimen and load for single overload data.

A crack growth look-up table was used instead of a closed form crack growth equation while generating predictions of both the state-space model and the FASTRAN for Porter’s data on 7075-T6 aluminum alloy specimen.

Figure A-2 illustrates a profile of block loading applied to the specimen to collect data used to validate the crack growth model constructed in state space setting. The positive integers n and m in Figure A-2 indicate that a block of n constant amplitude cycles is followed by a block of m cycles of a different constant amplitude.

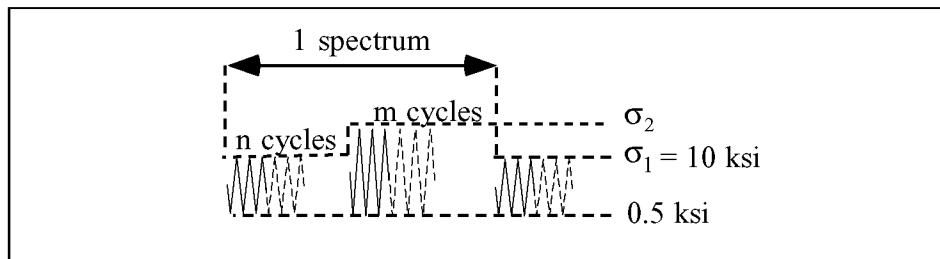


Figure A-2. Cyclic stress excitation profile for Porter data

The details of the loading profiles are presented below.

Porter Data Inputs

Material Type: 7075 – T6
 Type of the Crack: Center Through Crack
 Width of the Specimen: 304.8 mm
 Thickness of the Specimen: 4.064mm
 Length of the Specimen: 915mm
 Initial Half Crack Length: 6.35 mm
 Final Half Crack Length: 70mm
 Young's Modulus , E: 69,600 MPa
 Yield Strength σ_{ys} : 520MPa
 Ultimate Strength σ_{ult} : 575 Mpa

The analysis of the Porter data uses the following look-up table instead of a closed form expression for the crack growth rate:

$\Delta K_{eff} (MPa\sqrt{m})$	$\frac{da}{dN} (m / cycle)$
0.90	1.00e-11
1.35	1.20e-09
3.40	1.00e-08
5.20	1.00e-07
11.9	1.00e-06
18.8	1.00e-05
29.0	1.00e-04

Rate 1: 5e-7
 Alpha 1: 1.8
 Beta1: 1.0
 Rate2: 5e-6
 Alpha2: 1.1
 Beta2: 1.0

McMillan and Pelloux Data Inputs

Material Type: 2024 – T3
Type of Crack: Center Through Crack
Width of Specimen: 228.6 mm
Thickness of the Specimen: 4.064mm
Length of the Specimen: 915mm
Initial Half Crack Length: 6.35 mm
Final Half Crack Length: 70mm
Young's Modulus , E: 71750 MPa

For Samples P1 to P7 and P11 to P13:

Yield Strength σ_{ys} : 327.9 MPa

Ultimate Strength σ_{ult} : 473.3 MPa

For Samples P8 to P10:

Yield Strength σ_{ys} : 315.0 MPa

Ultimate Strength σ_{ult} : 483.6 MPa

Closed form expression for crack growth analysis used :

C= 5.00e-11

M= 4.07

Rate 1: 9.0e-7

Alpha 1: 1.73

Beta1: 1.0

Rate2: 7.5e-6

Alpha2: 1.1

Beta2: 1.0

Table A-1: Load Profiles for Porter Data

Program	Max. Stress	Min. Stress	Cycles/Block
P1	103.42	3.45	50
P2	68.95	3.45	50
P3	68.95	3.45	50
	103.45	3.45	1
P4	68.95	3.45	50
	103.45	3.45	3
P5	68.95	3.45	50
	103.45	3.45	6
P6	68.95	3.45	50
	103.45	3.45	10
P7	68.95	3.45	50
	103.45	3.45	25
P8	68.95	3.45	50
	103.45	3.45	50
P9	68.95	3.45	29
	76.53	3.45	1
P10	68.95	3.45	29
	103.45	3.45	1
P11	68.95	3.45	29
	120.66	3.45	1
P12	68.95	3.45	29
	137.89	3.45	1
P13	68.95	3.45	29
	103.42	3.45	1
P14	68.95	3.45	50
	103.42	3.45	1
P15	68.95	3.45	300
	103.42	3.45	1
P16	68.95	3.45	1000
	103.42	3.45	1
P17	103.42	51.71	50
	103.42	5.171	1
P18	103.42	51.71	50
	155.13	5.171	1
P19	103.42	51.71	50
	155.13	31.03	1
P20	103.42	51.71	50
	134.45	31.03	1
P21	103.42	51.71	50
	206.84	5.171	1
P22	103.42	51.71	49
	103.42	5.171	1
	155.13	51.71	1
P23	103.42	51.71	49
	103.42	31.03	1
	155.13	51.71	1
P24	103.42	51.71	49
	103.42	31.03	1
	134.45	51.71	1
P25	103.42	51.71	49
	103.42	5.171	1
	206.84	51.71	1
P26	103.45	51.71	1
P27	103.42	51.71	50
	155.13	51.71	1

Table A-2: Load Profiles for Mcmillan and Pelloux Data

Program	Max. Stress	Min. Stress	Cycles
P1	82.788	68.99	9
	82.788	27.596	8
	82.788	4.1394	7
P2	82.788	4.1394	7
	82.788	27.596	8
	82.788	68.99	9
P3	82.788	4.1394	10
	82.788	27.596	8
	82.788	41.394	6
P4	82.788	4.1394	20
	82.788	27.596	8
	82.788	41.394	12
	82.788	27.596	8
P5	82.788	4.1394	3
	82.788	41.394	1
	82.788	27.596	1
	82.788	4.1394	1
	82.788	27.596	1
	82.788	41.394	1
	82.788	4.1394	1
	82.788	27.596	1
	82.788	41.394	1
	82.788	4.1394	1
	82.788	41.394	1
	82.788	4.1394	1
	82.788	27.596	1
	82.788	4.1394	1
	82.788	27.596	2
	82.788	41.394	1
	82.788	27.596	1
	82.788	4.1394	1
82.788	41.394	1	
82.788	4.1394	1	
82.788	27.596	1	
P6	96.586	48.293	4
	82.788	34.495	5
	68.99	20.697	6
	55.192	6.899	7
P7	55.192	6.899	6
	55.192	20.697	1
	68.99	20.697	5
	68.99	34.495	1
	82.788	34.495	4
	82.788	48.293	1
	96.586	48.293	3
96.586	6.899	1	
P8	96.586	48.293	20
	82.788	34.495	16
	68.99	20.697	12
P9	68.99	20.697	12
	82.788	34.495	16
	96.586	48.293	20

Table A-2 (Contd.): Load Profiles for Mcmillan and Pelloux Data

P10	96.586	48.293	1
	68.99	48.293	1
	82.788	34.495	1
	82.788	48.293	1
	68.99	48.293	1
	82.788	48.293	1
	82.788	20.697	1
	96.586	48.293	1
	68.99	48.293	1
	96.586	34.495	1
	96.586	20.697	1
	96.586	34.495	1
	96.586	48.293	1
	82.788	48.293	1
	82.788	34.495	1
	68.99	20.697	1
	96.586	48.293	1
	82.788	20.697	1
	96.586	48.293	1
	96.586	34.495	1
	96.586	20.697	1
	68.99	48.293	1
	96.586	48.293	1
	82.788	20.697	1
	82.788	34.495	1
	68.99	34.495	1
	82.788	48.293	1
	68.99	34.495	1
	68.99	34.495	1
	68.99	48.293	1
	82.788	48.293	1
	82.788	20.697	1
	96.586	20.697	1
	96.586	34.495	1
	82.788	48.293	1
	96.586	20.697	1
	96.586	34.495	1
	96.586	20.697	1
	82.788	34.495	1
	68.99	20.697	1
68.99	34.495	1	
68.99	20.697	1	
96.586	48.293	1	
82.788	48.293	1	
96.586	34.495	1	
96.586	48.293	1	
82.788	34.495	1	
96.586	34.495	1	
P11	82.788	34.495	20
	96.586	48.293	3
	96.586	34.495	1
P12	96.586	48.293	20
	96.586	34.495	1
	82.788	34.495	3
P13	82.788	34.495	20
	96.586	34.495	9
	96.586	48.293	10
	96.586	34.495	1

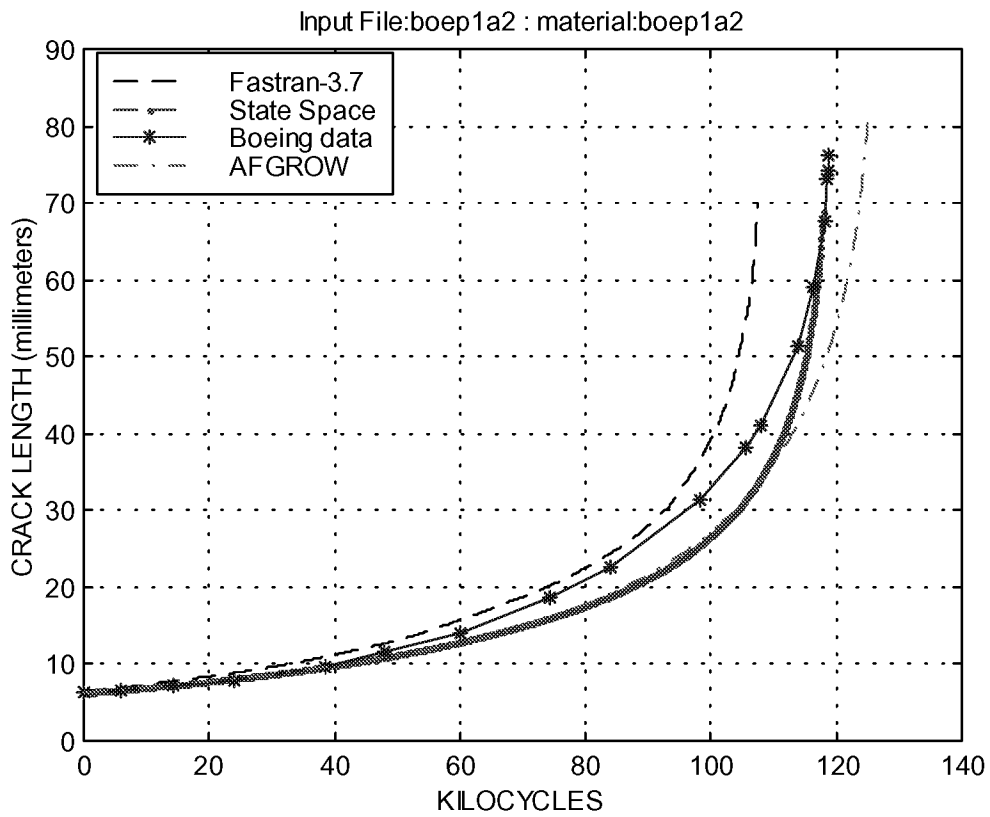
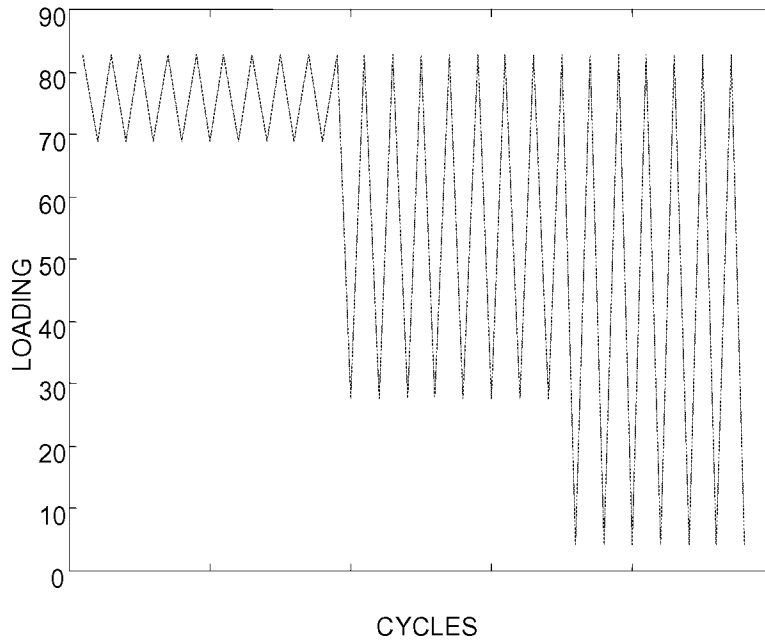


Figure A-3. Mcmillan and Pelloux Program P1

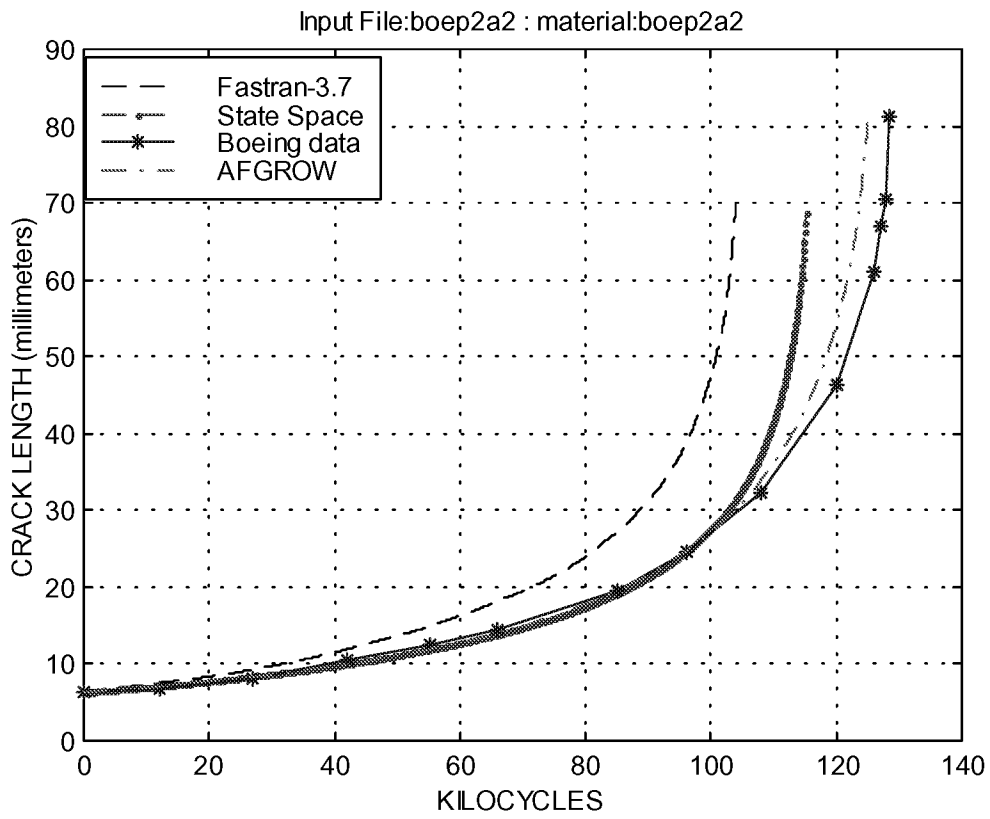
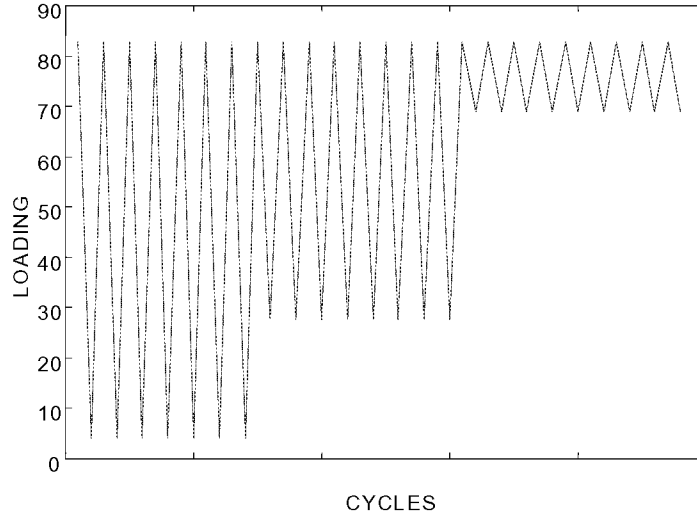


Figure A-4. Mcmillan and Pelloux Program P2.

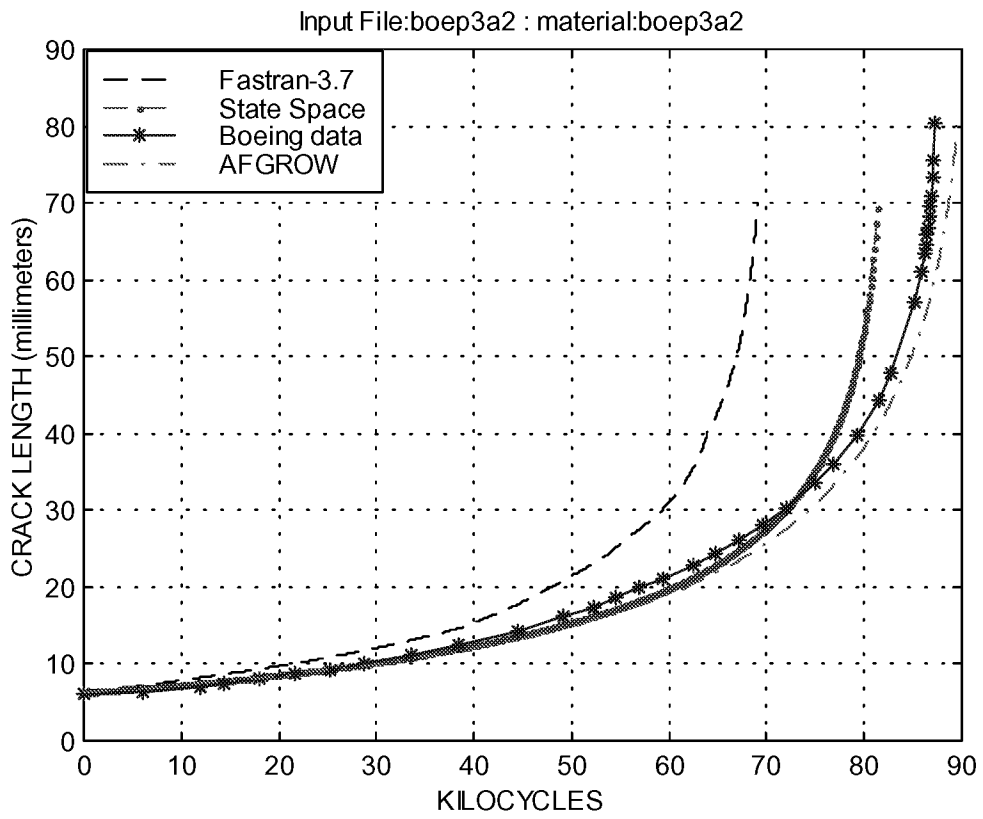
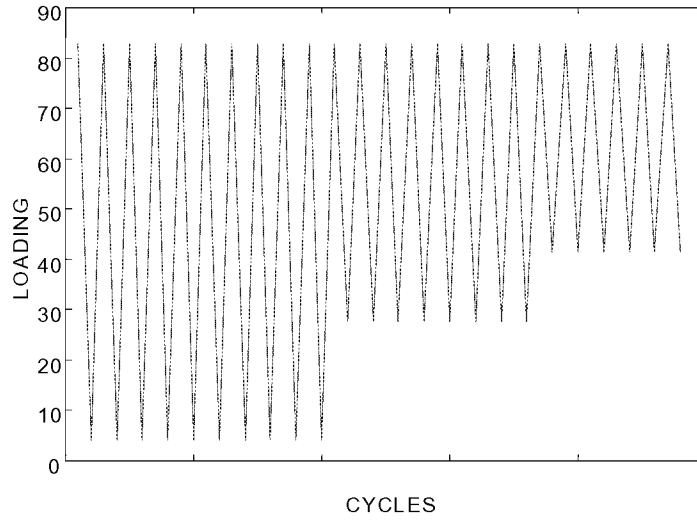


Figure A-5. Mcmillan and Pelloux Program P3

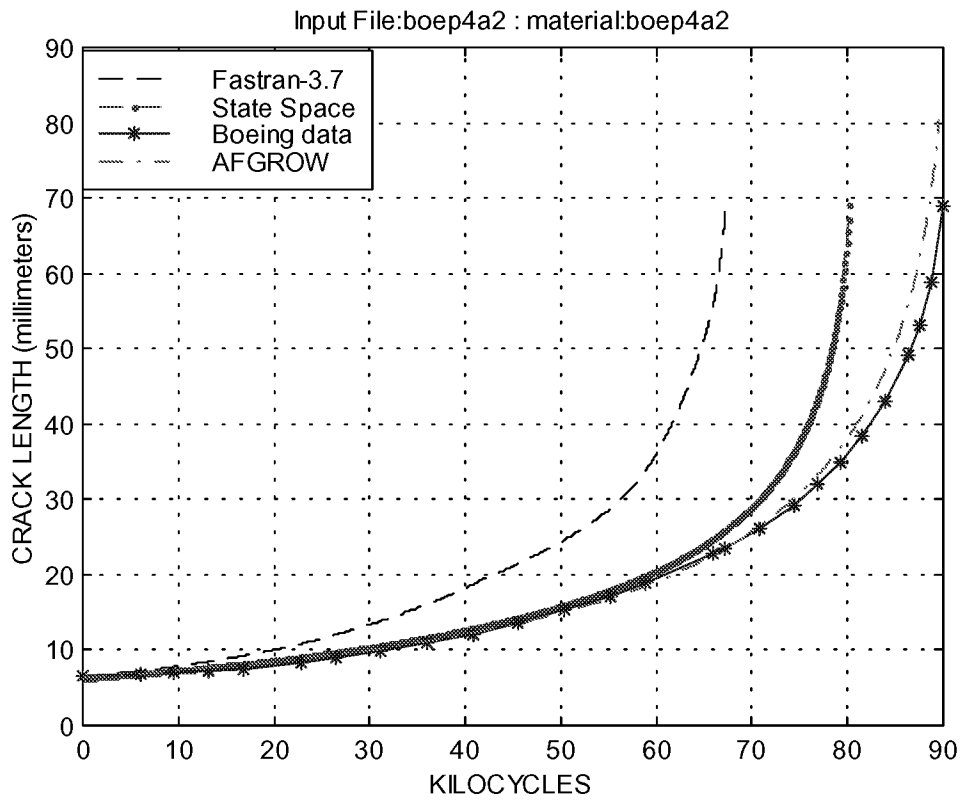
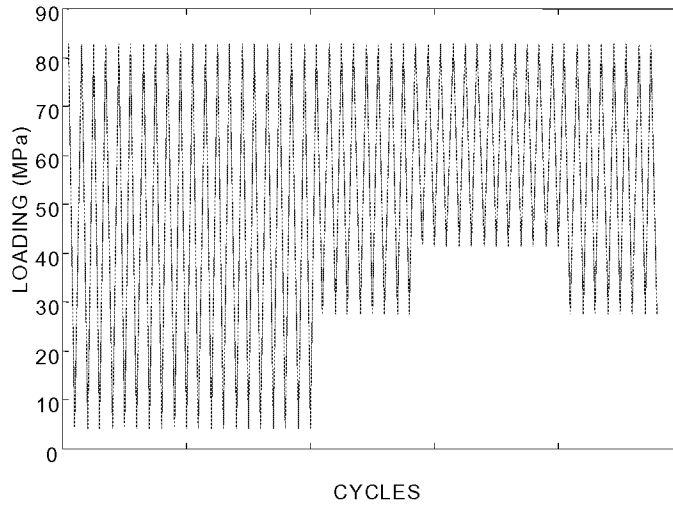


Figure A-6. Mcmillan and Pelloux Program P4.

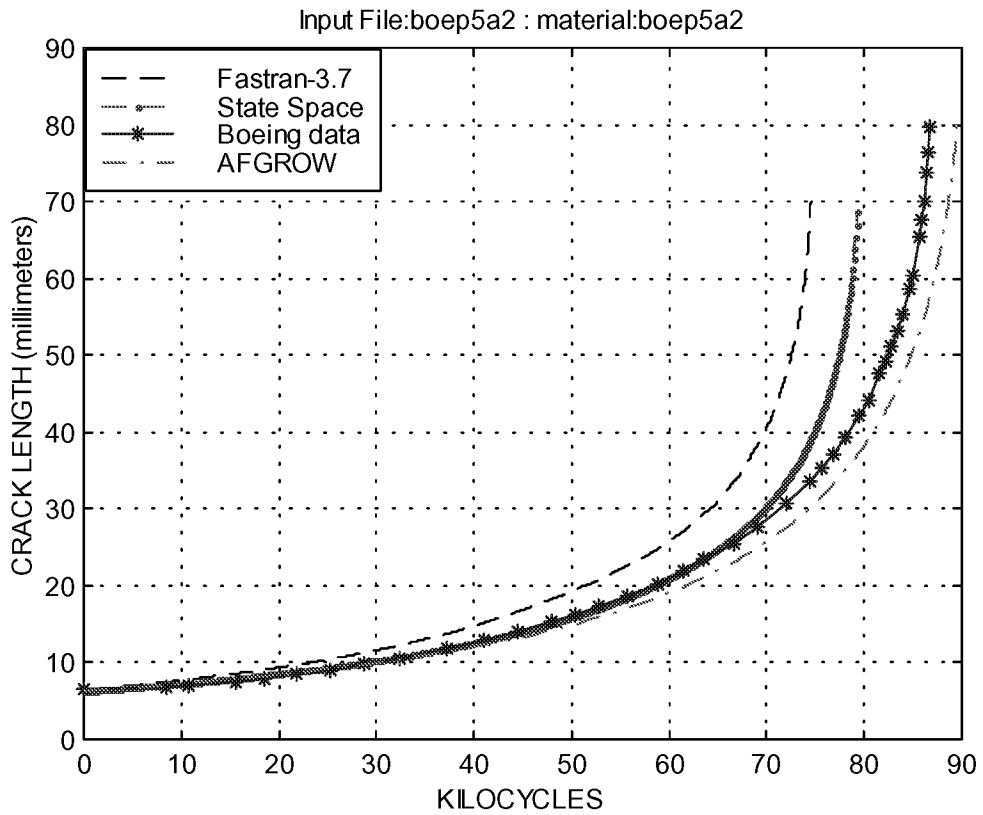
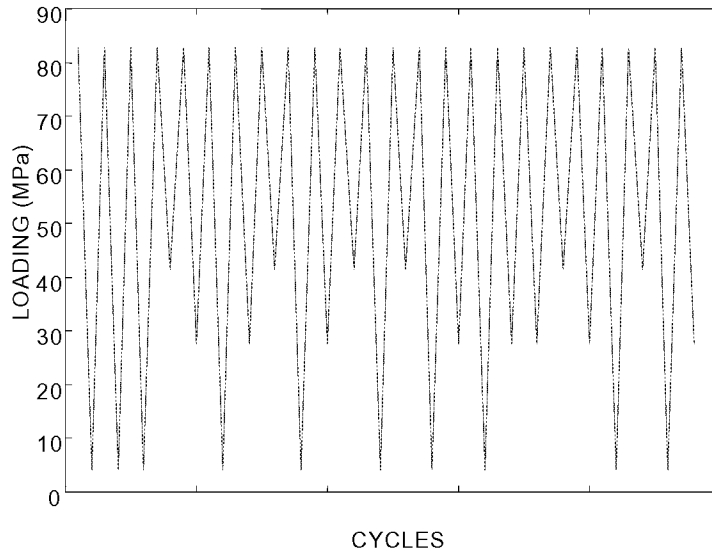


Figure A-7. Mcmillan and Pelloux Program P5.

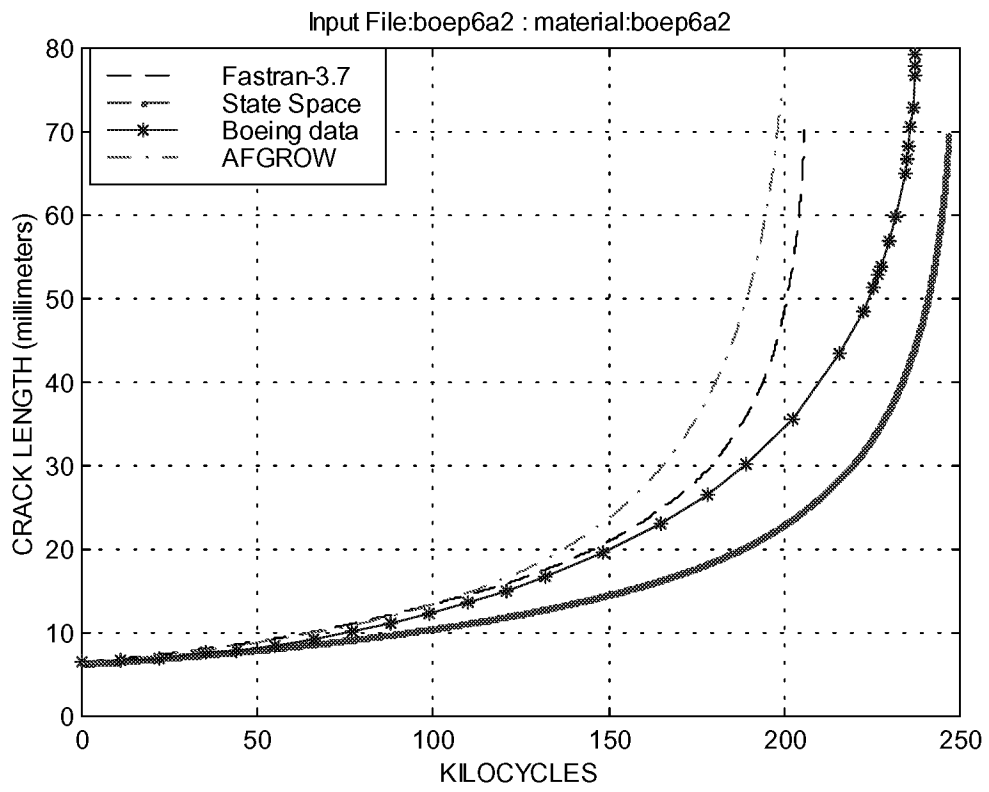
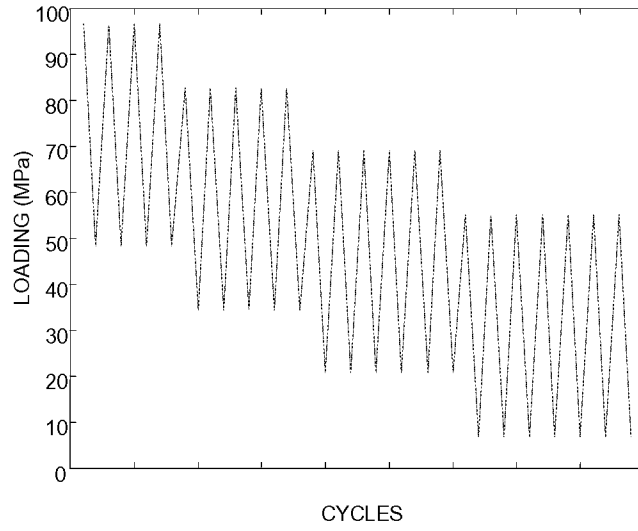


Figure A-8. Mcmillan and Pelloux Program P6.

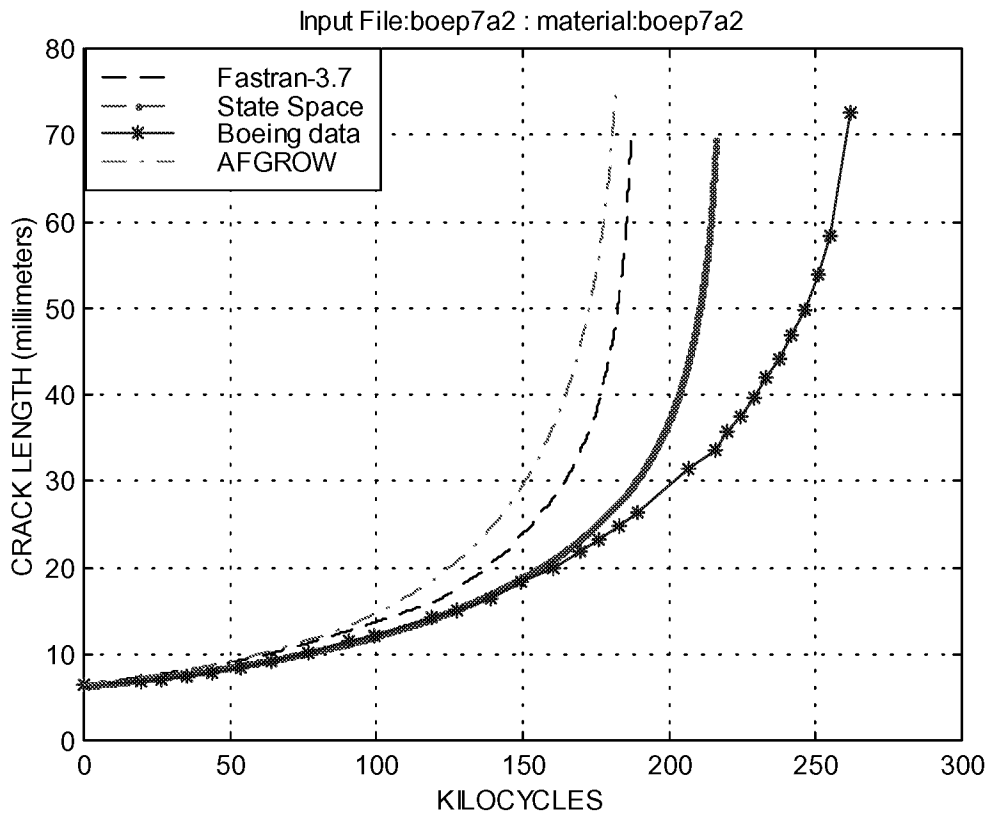
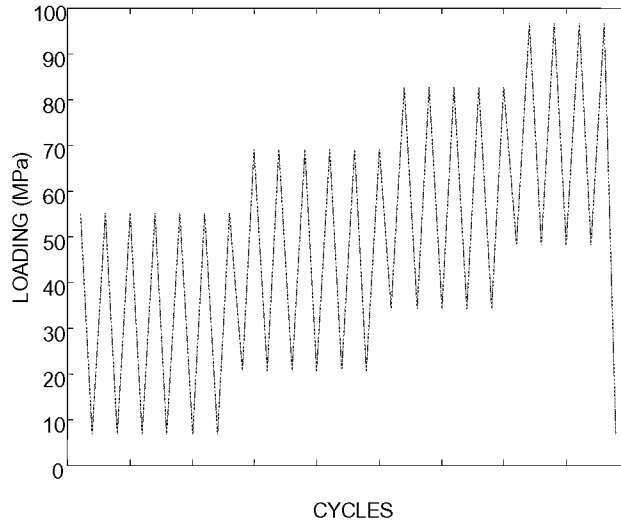


Figure A-9. Mcmillan and Pelloux Program P7.

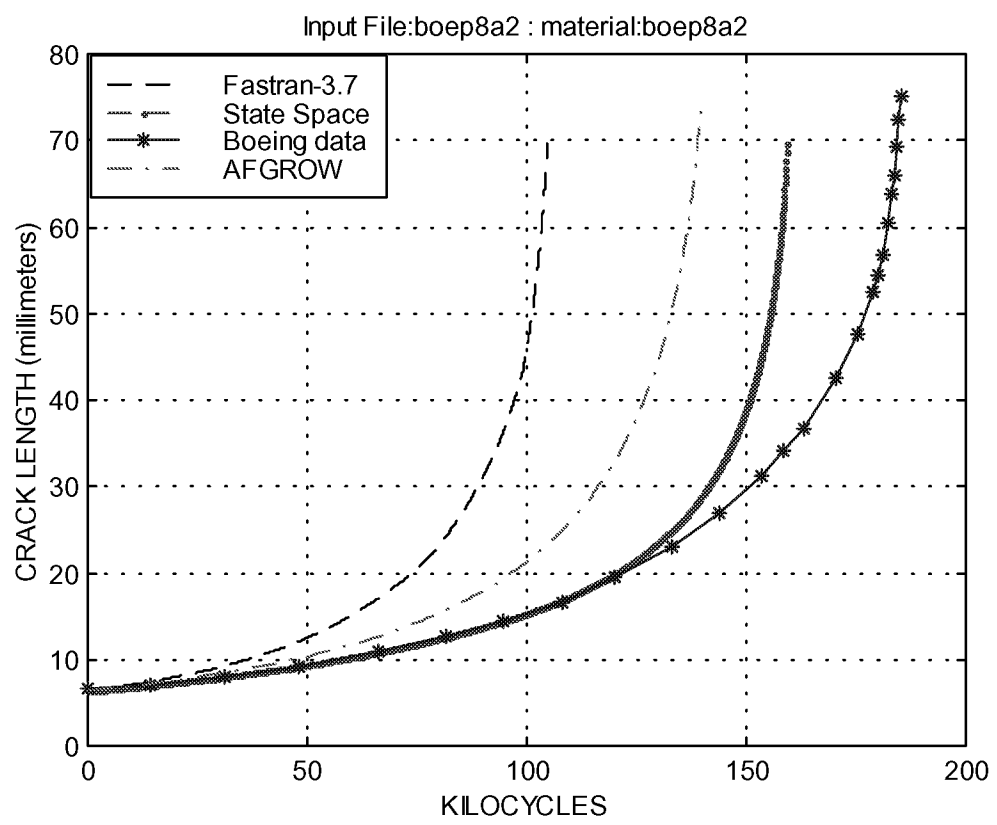
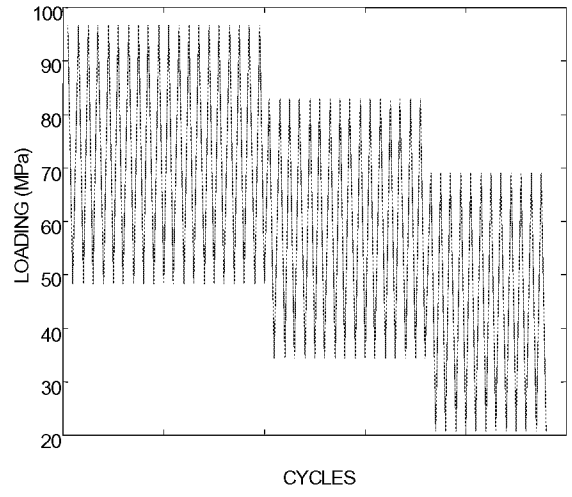


Figure A-10. Mcmillan and Pelloux Program P8.

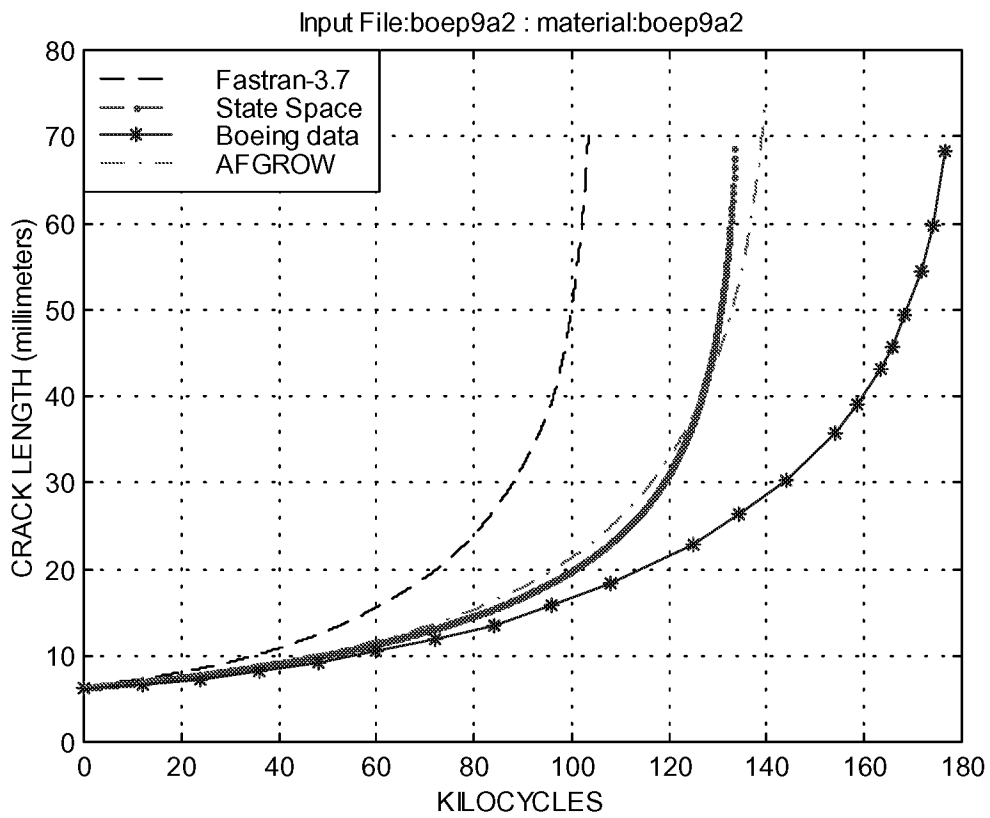
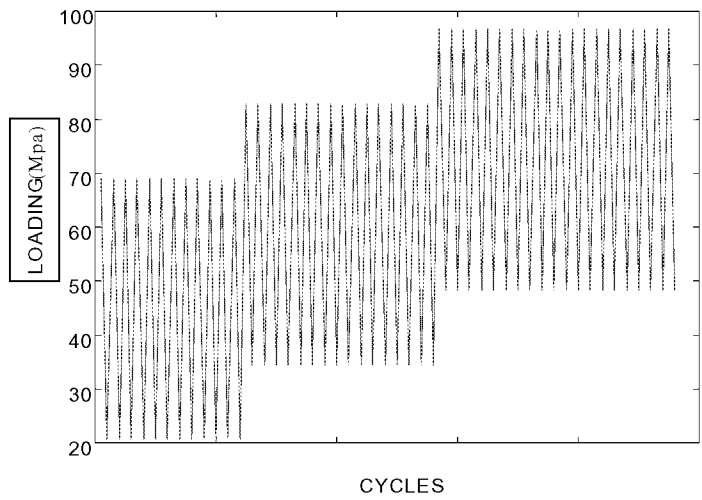


Figure A-11. Mcmillan and Pelloux Program P9.

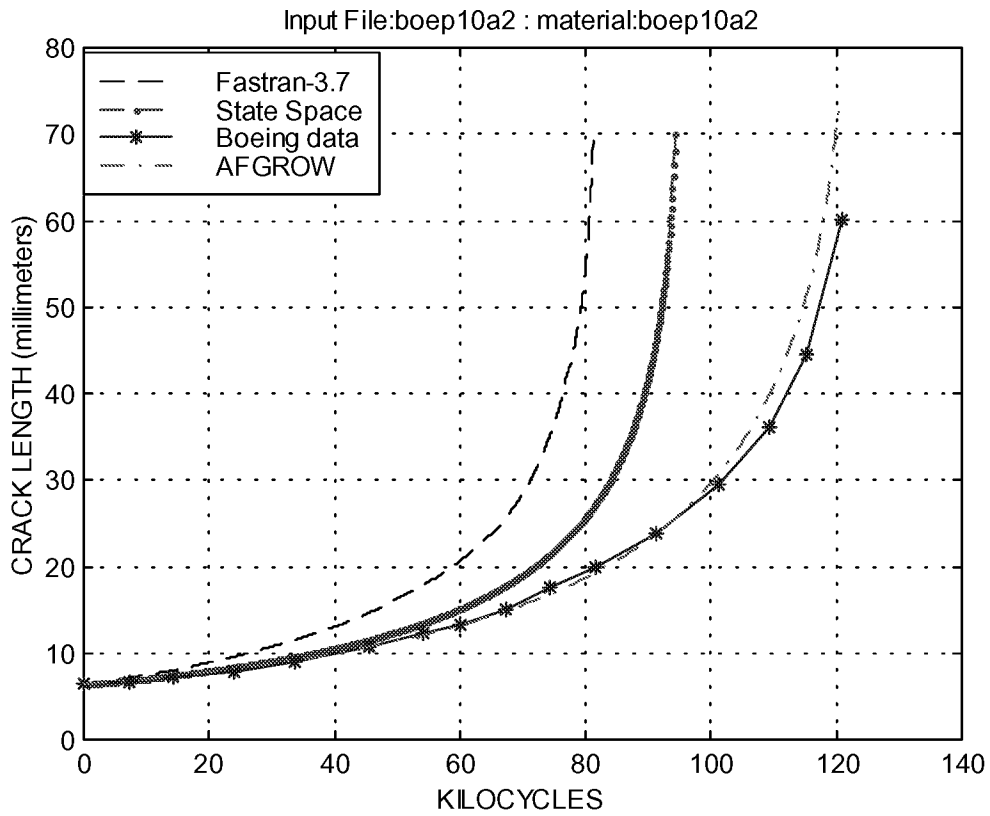
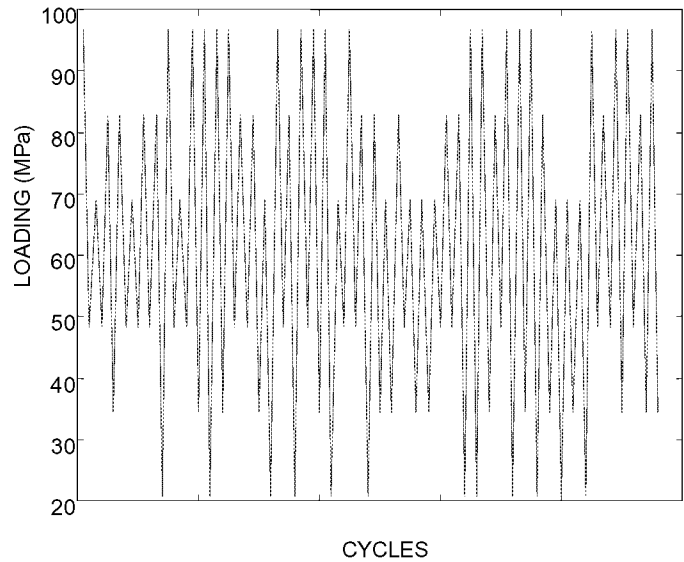


Figure A-12. Mcmillan and Pelloux Program P10.

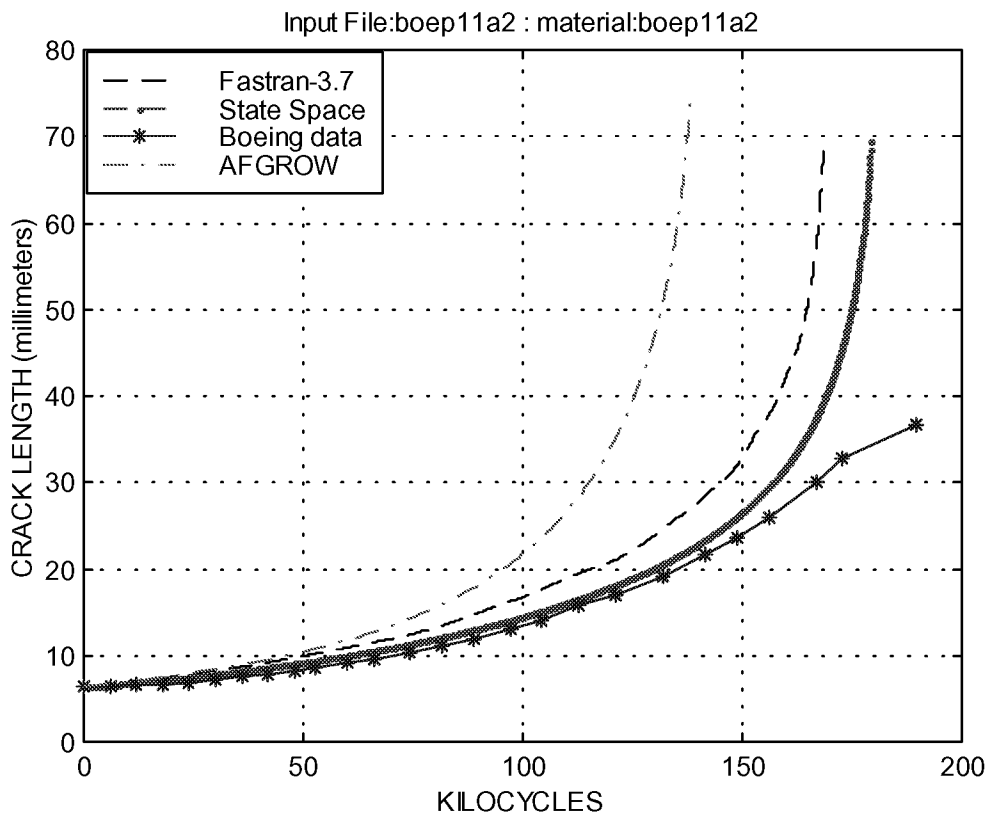
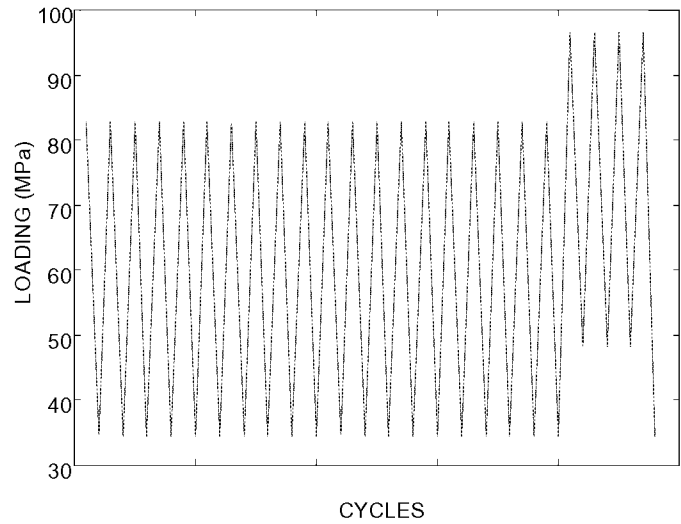


Figure A-13. Mcmillan and Pelloux Program P11.

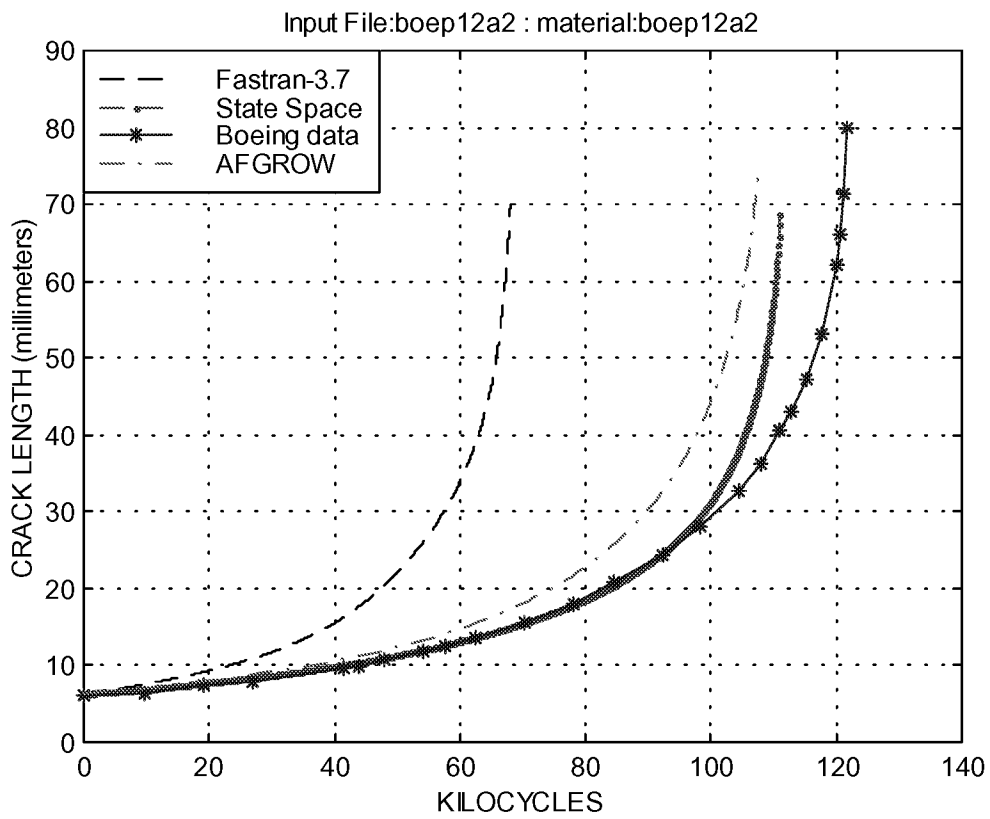
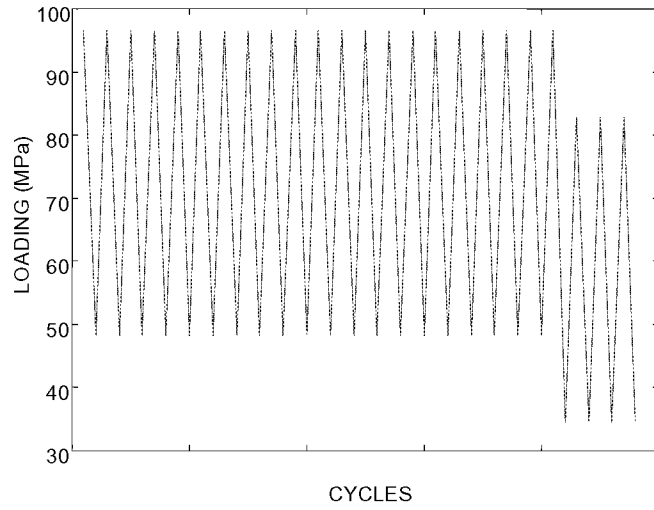


Figure A-14. Mcmillan and Pelloux Program P12

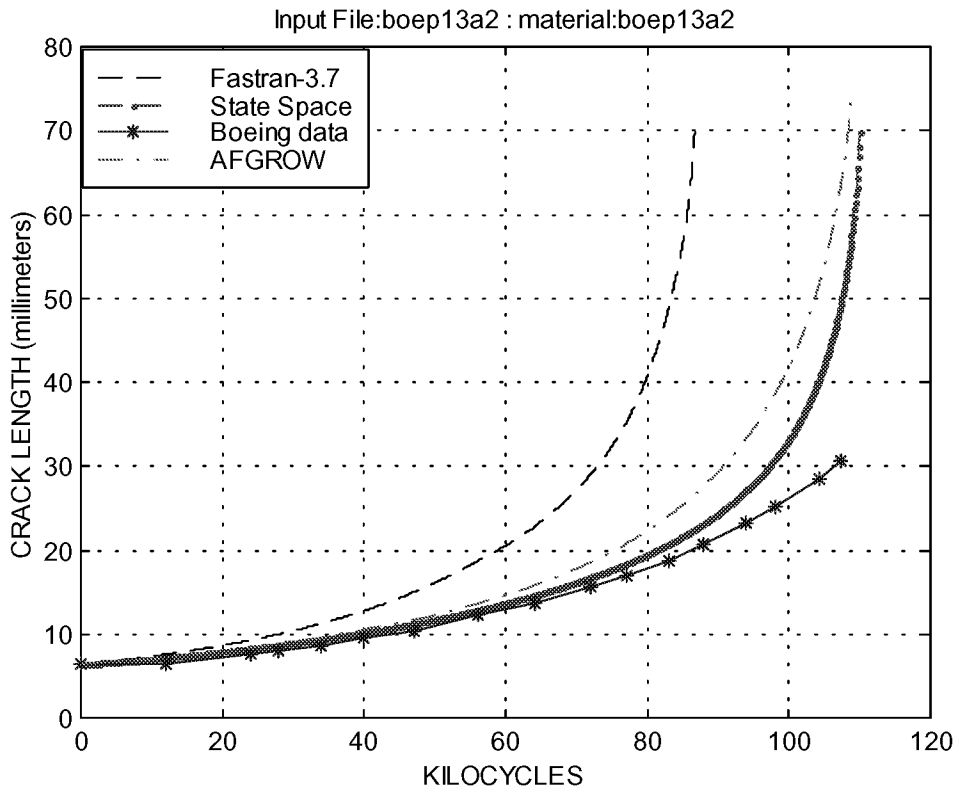
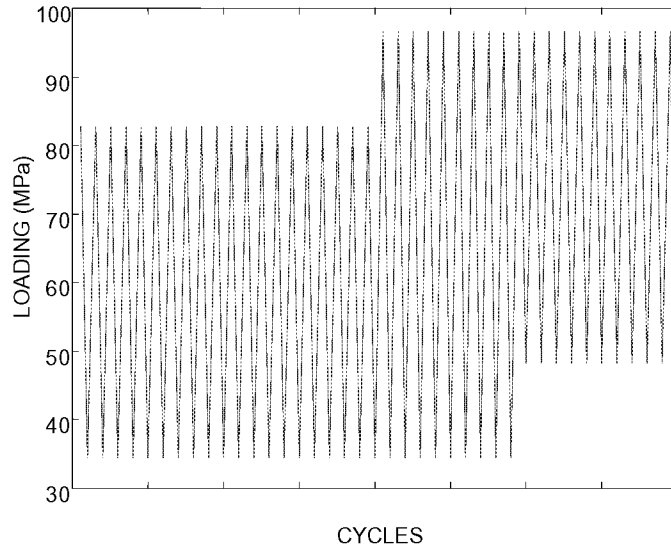


Figure A-15. Mcmillan and Pelloux Program P13.

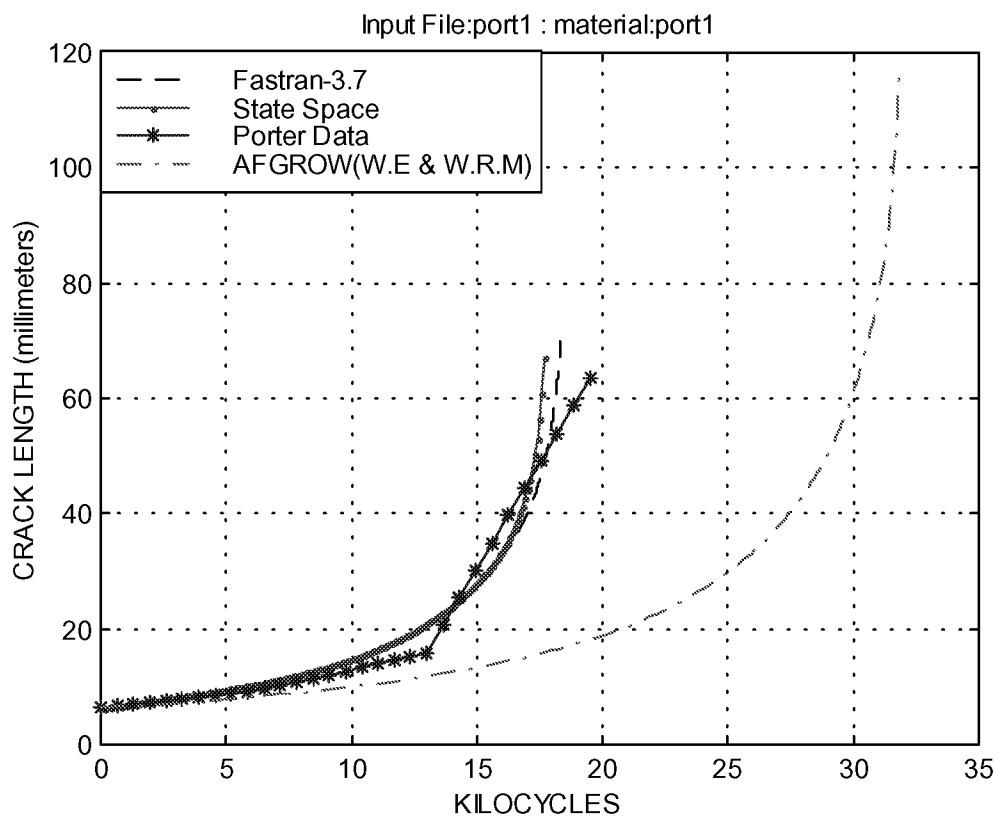
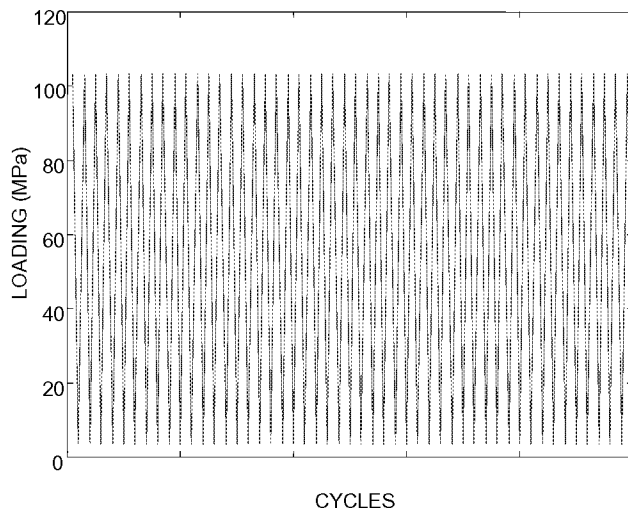


Figure A-16. Porter Program P1.

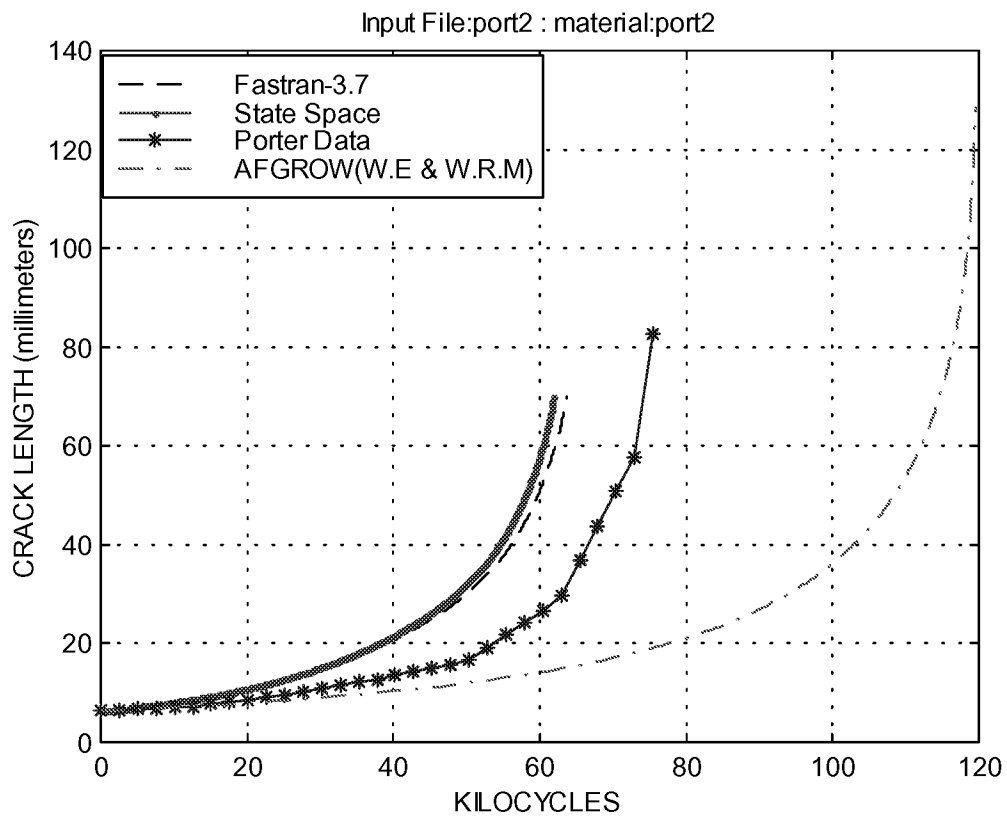
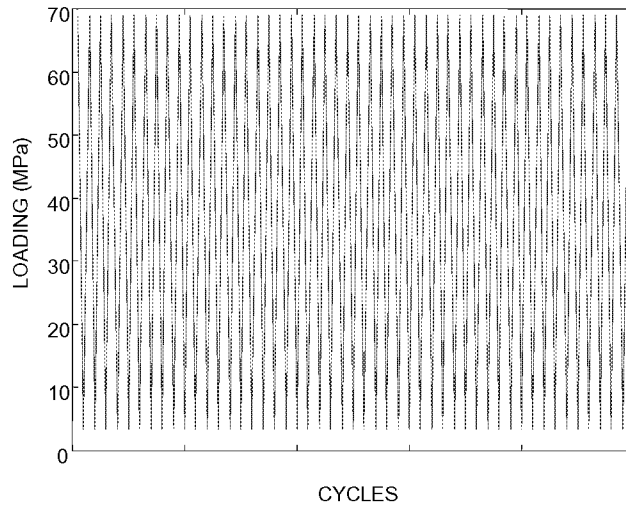


Figure A-17. Porter Program P2.

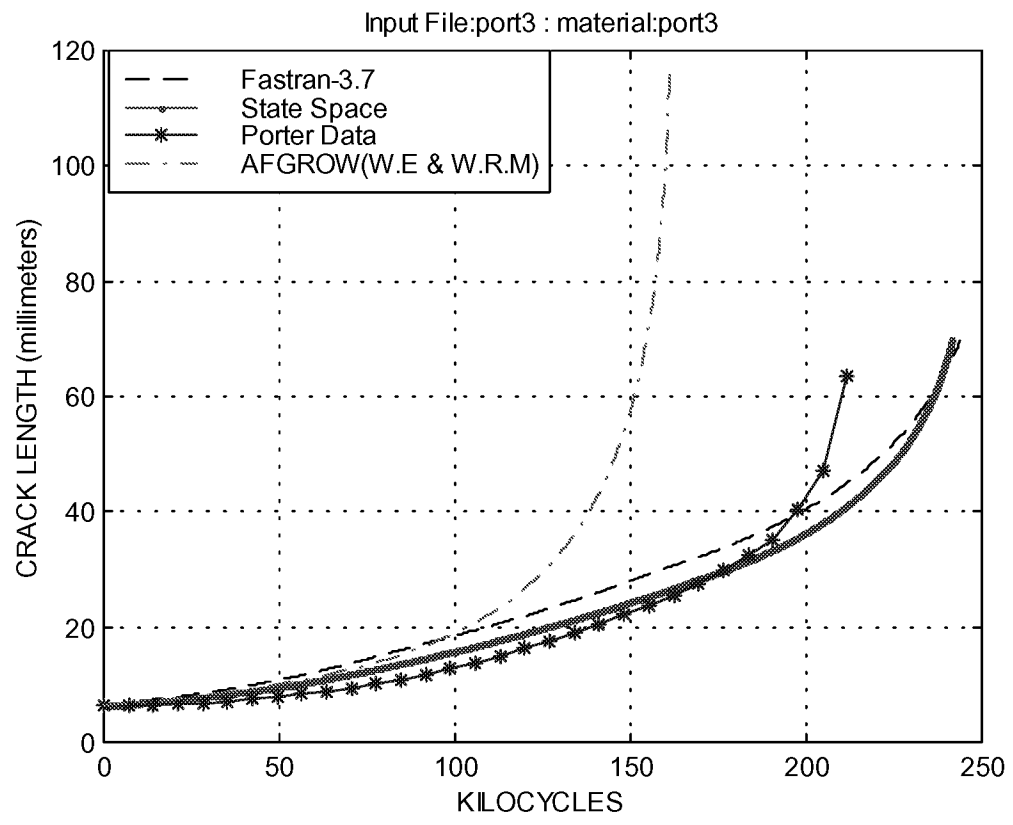
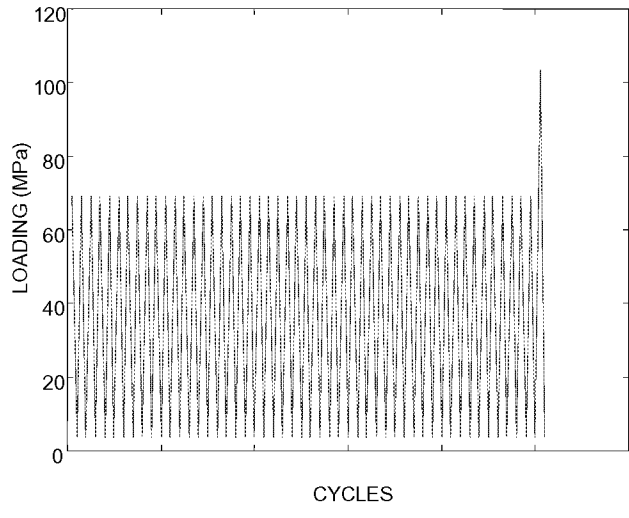


Figure A-18. Porter Program P3.

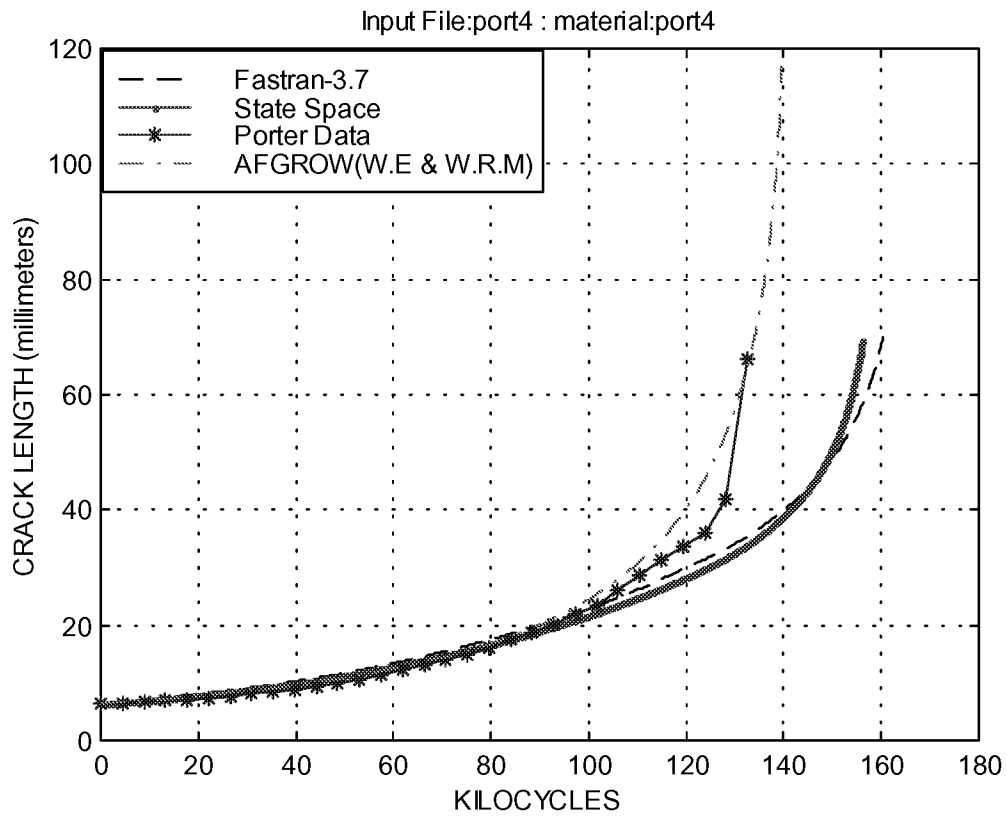
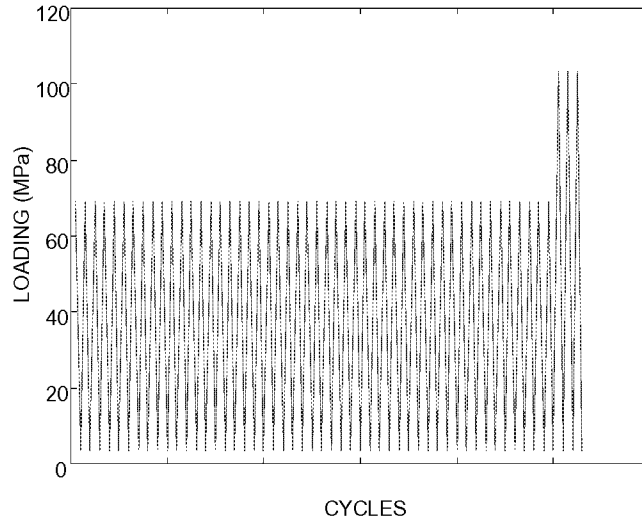


Figure A-19. Porter Program P4.

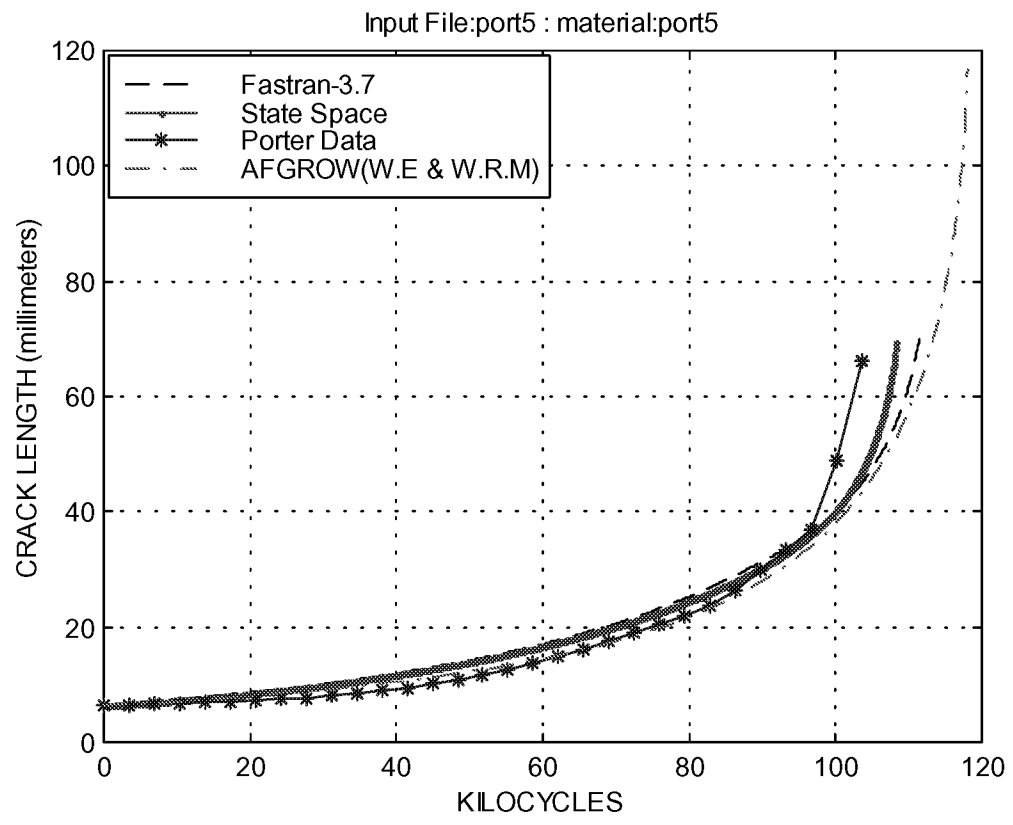
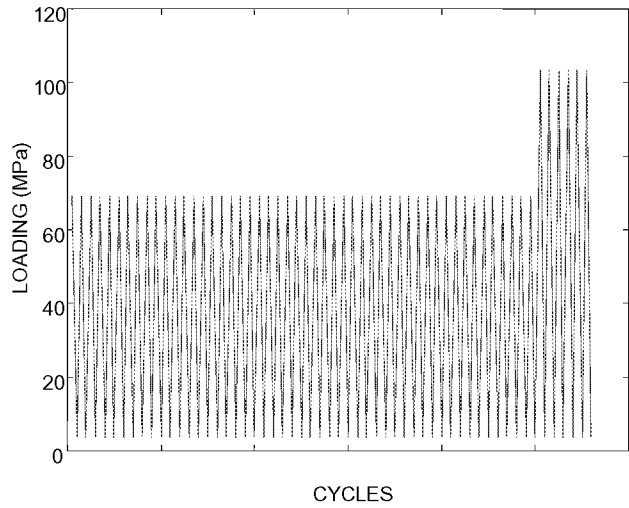


Figure A-20. Porter Program P5.

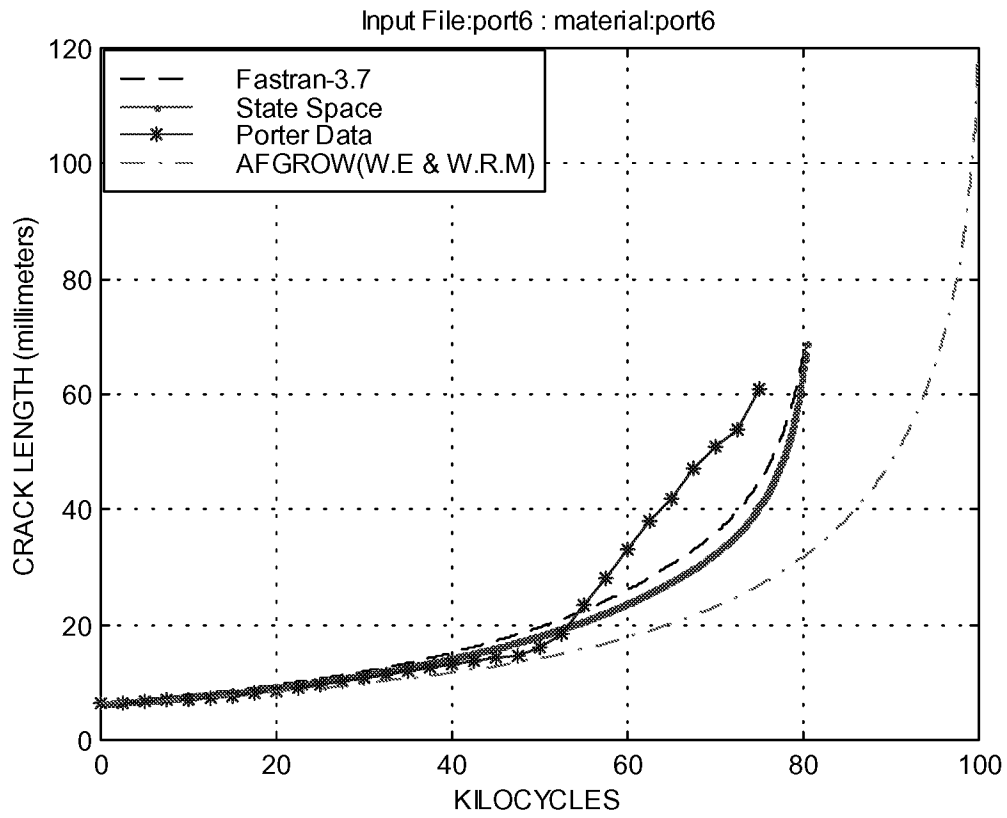
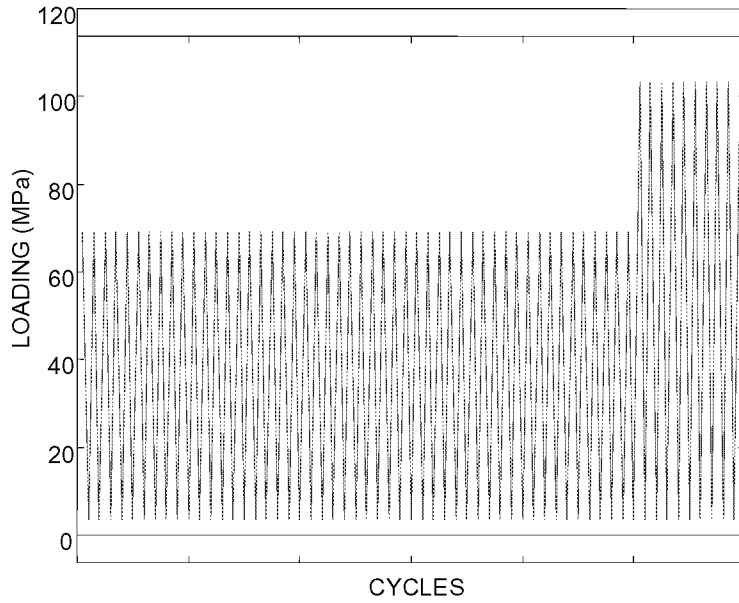


Figure A-21. Porter Program P6.

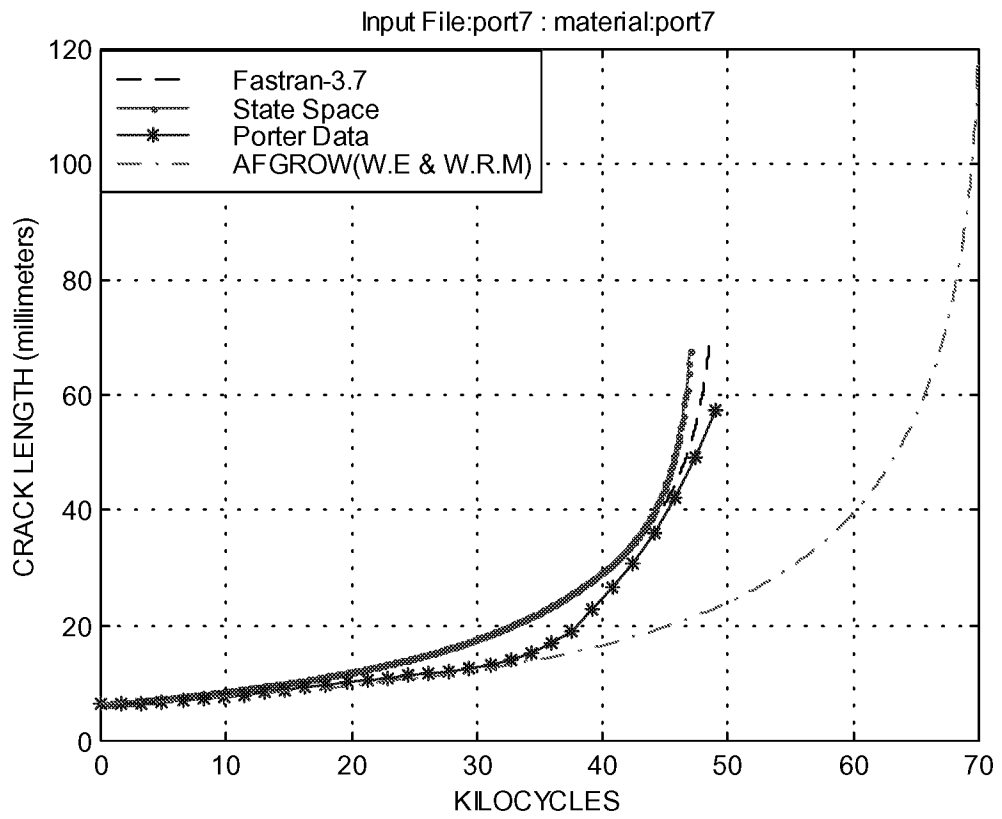
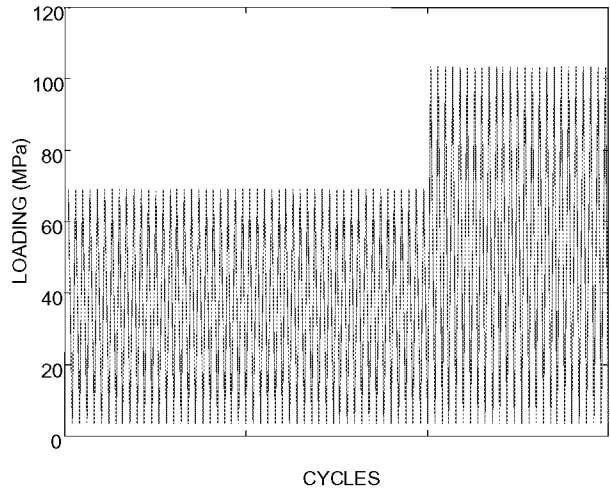


Figure A-22. Porter Program P7.

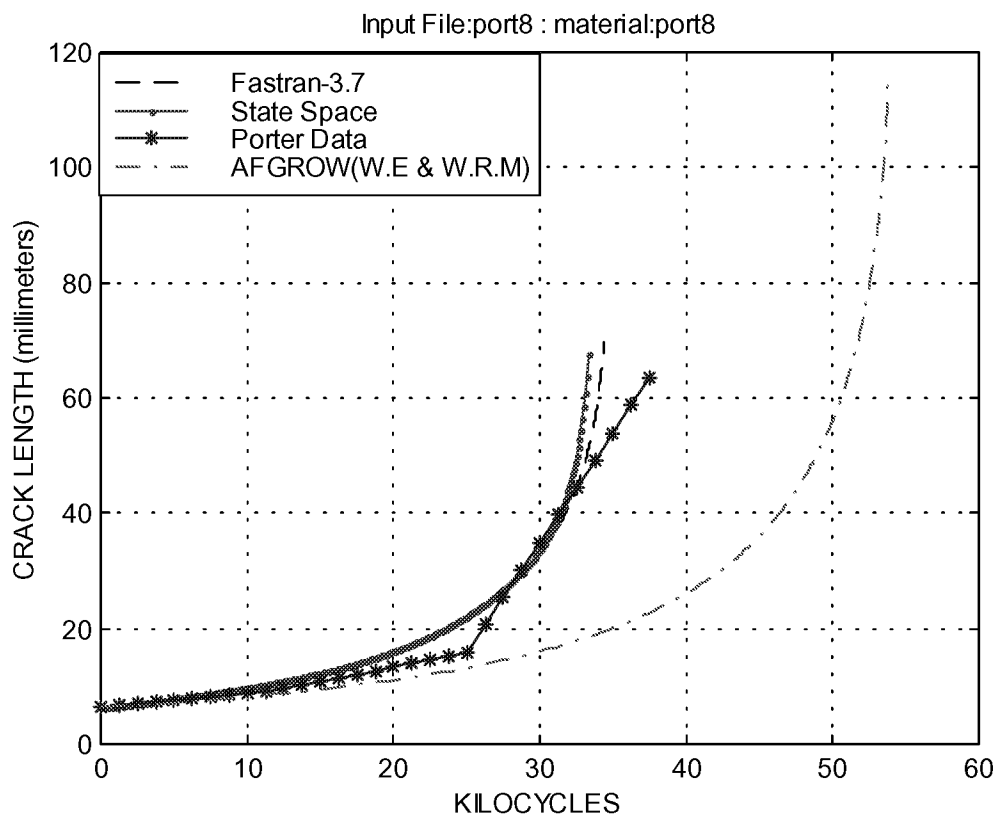
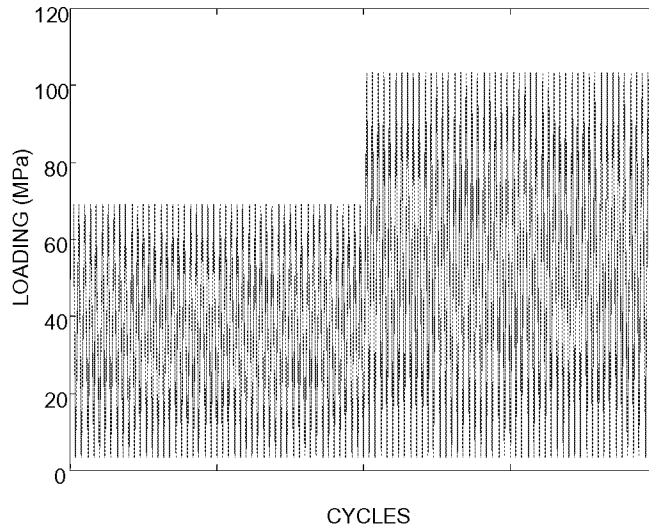


Figure A-23. Porter Program P8.

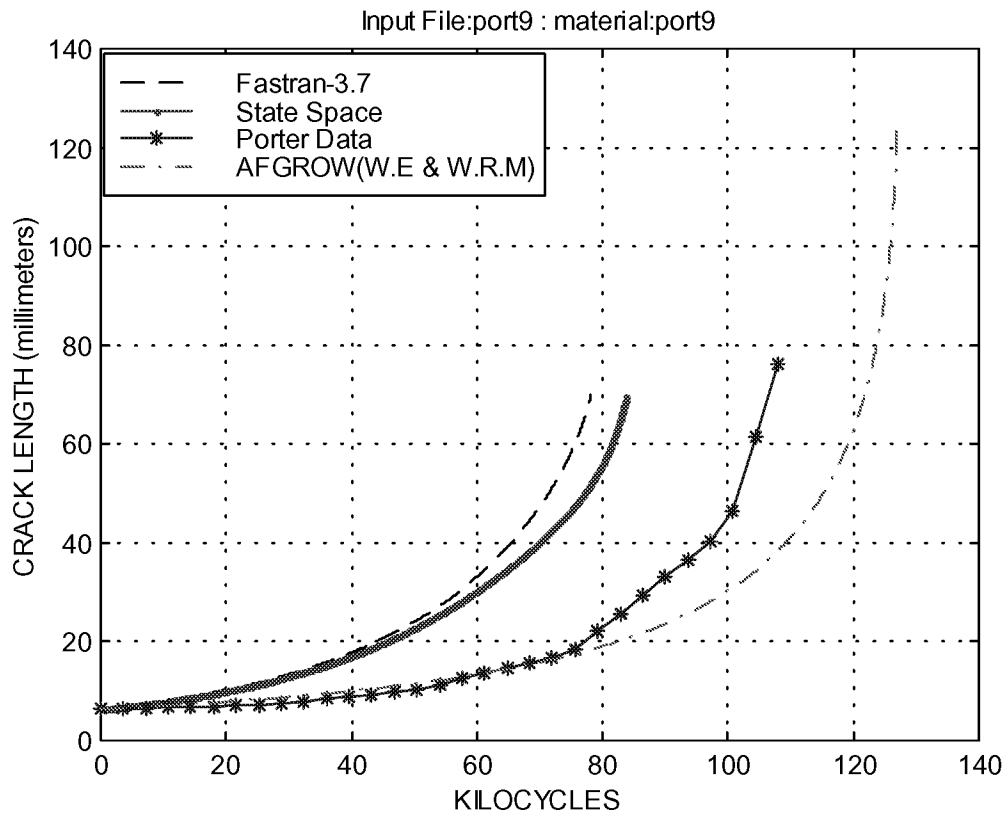
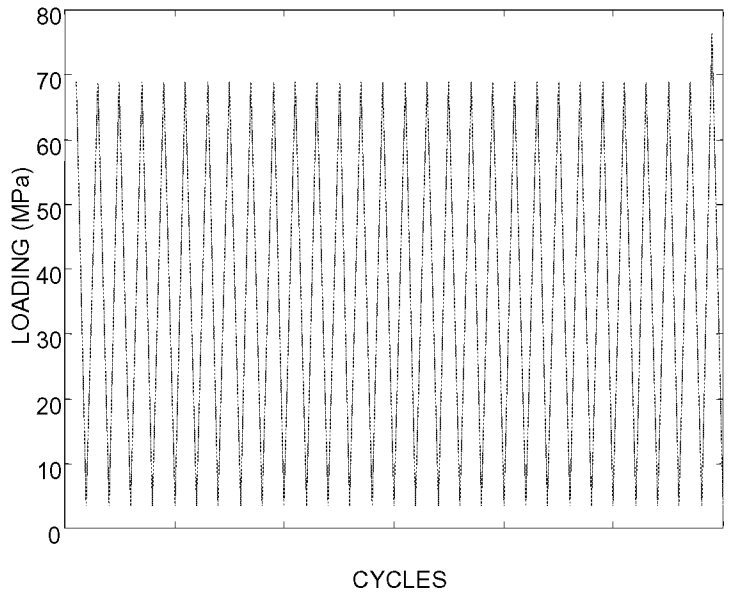


Figure A-24. Porter Program P9.

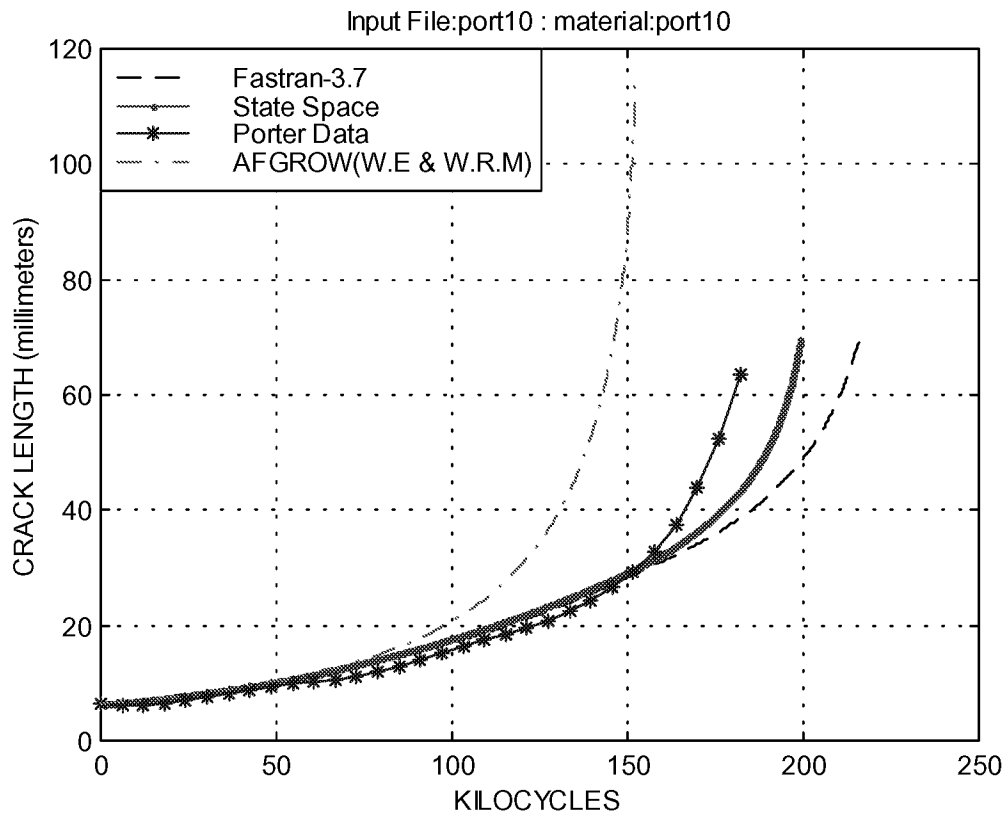
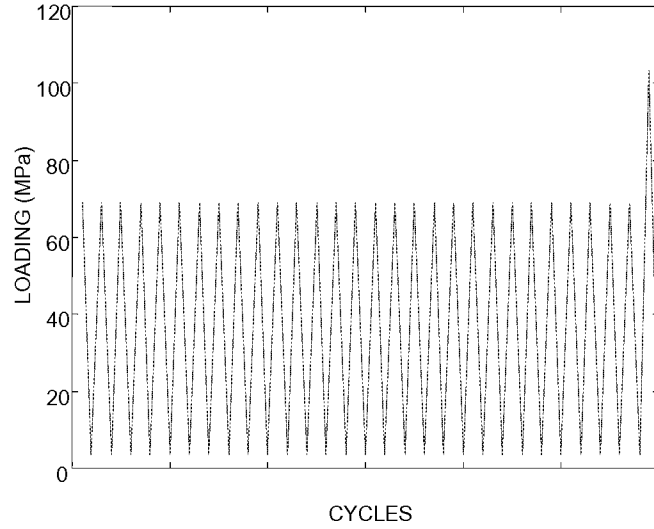


Figure A-25. Porter Program P10.

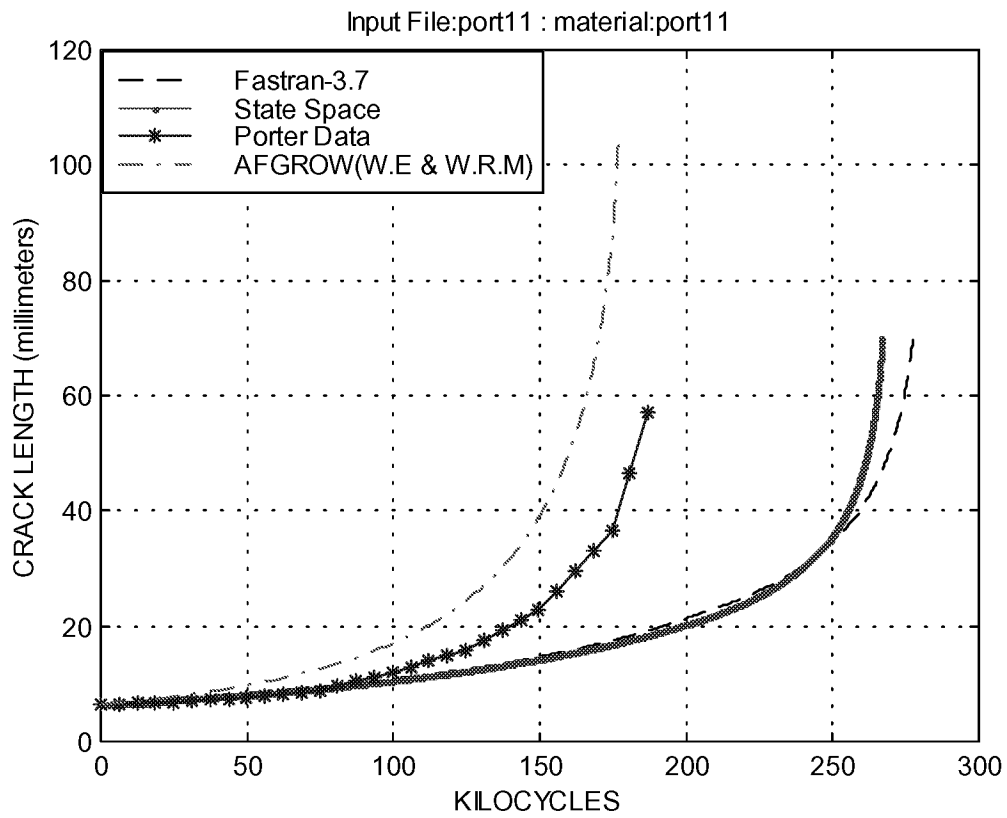
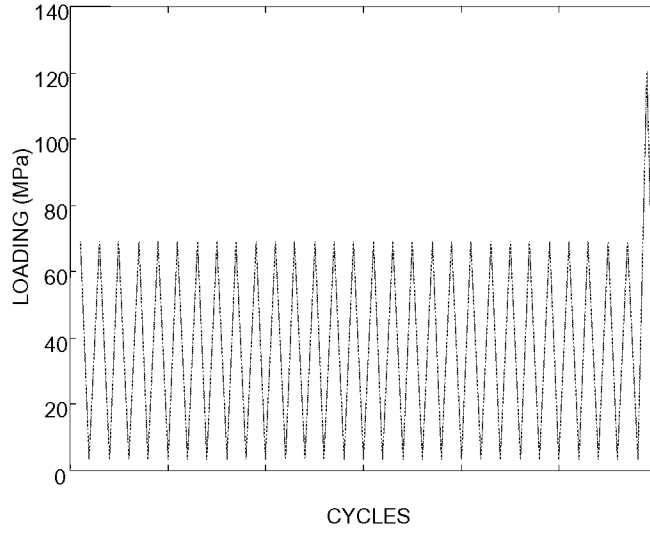


Figure A-26. Porter Program P11.

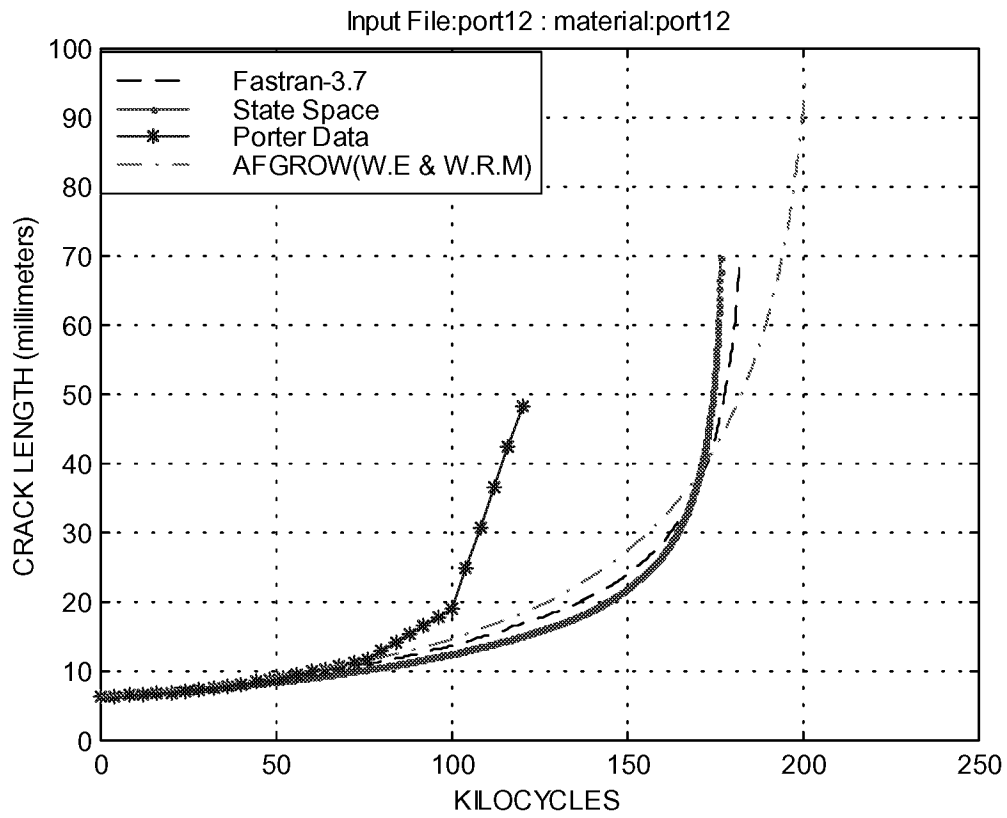
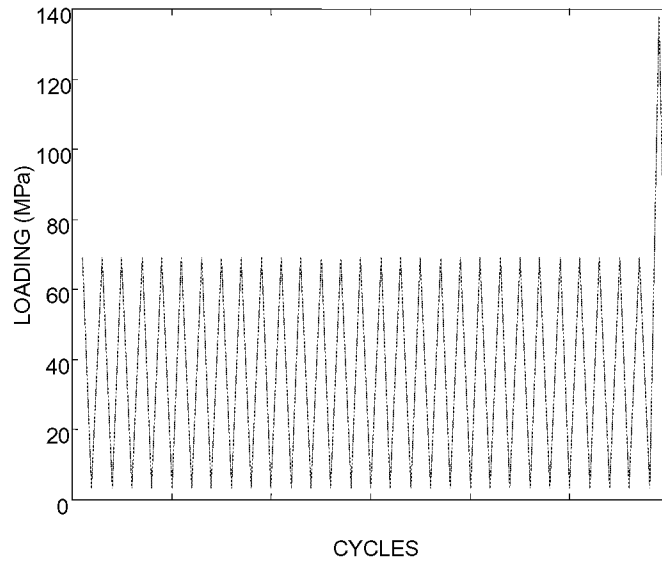


Figure A-27. Porter Program P12.

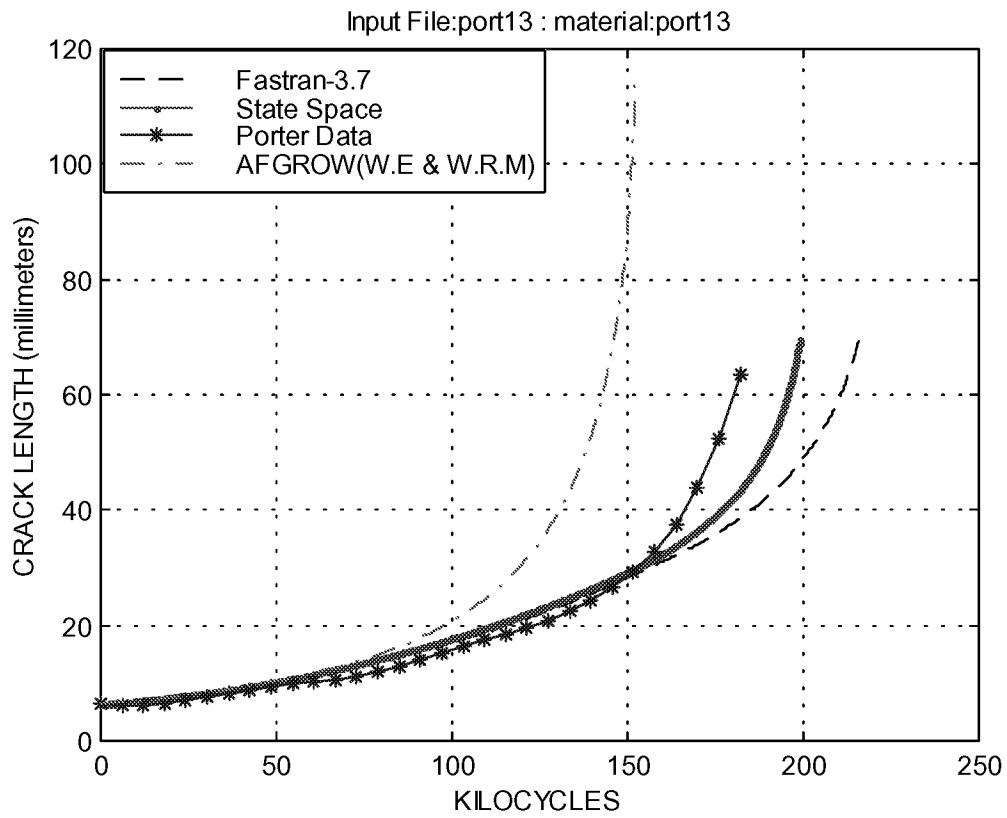
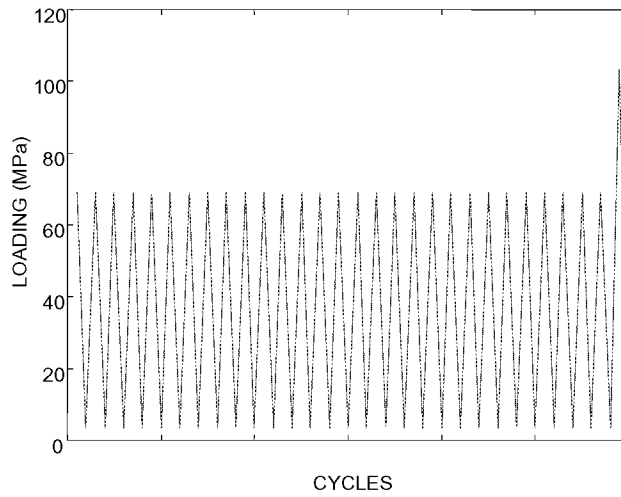


Figure A-28. Porter Program P13.

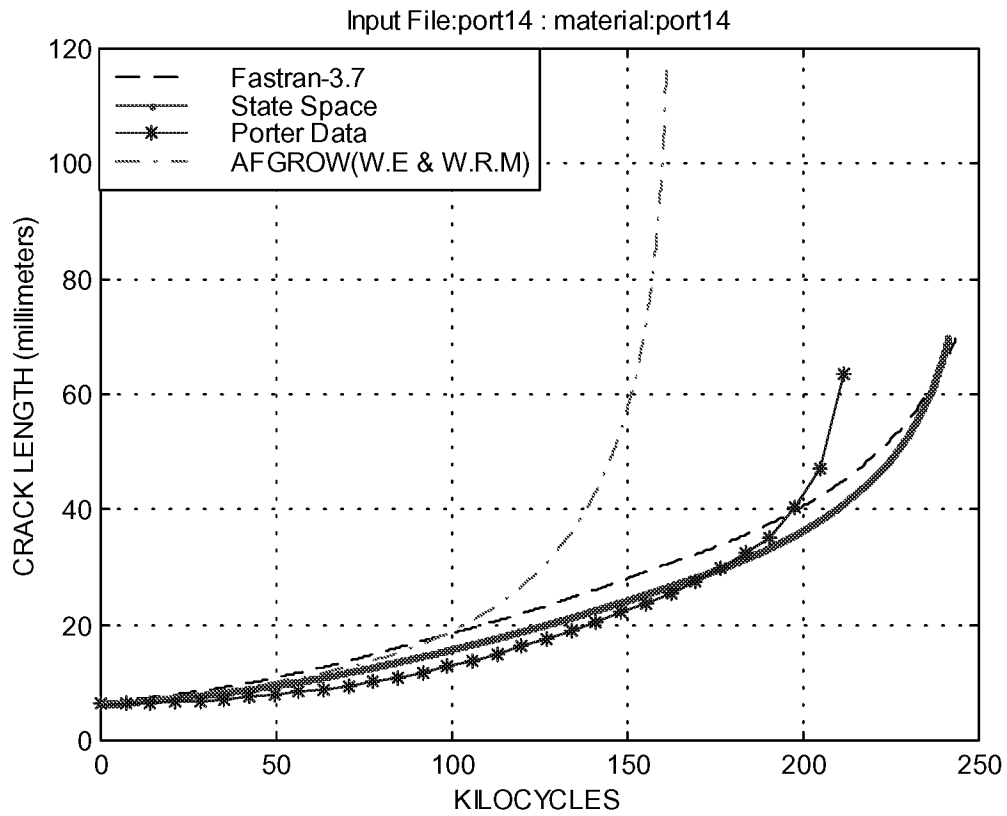
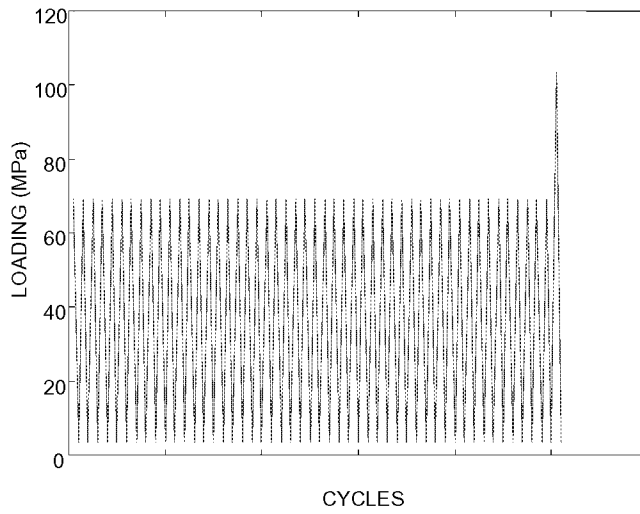


Figure A-29. Porter Program P14.

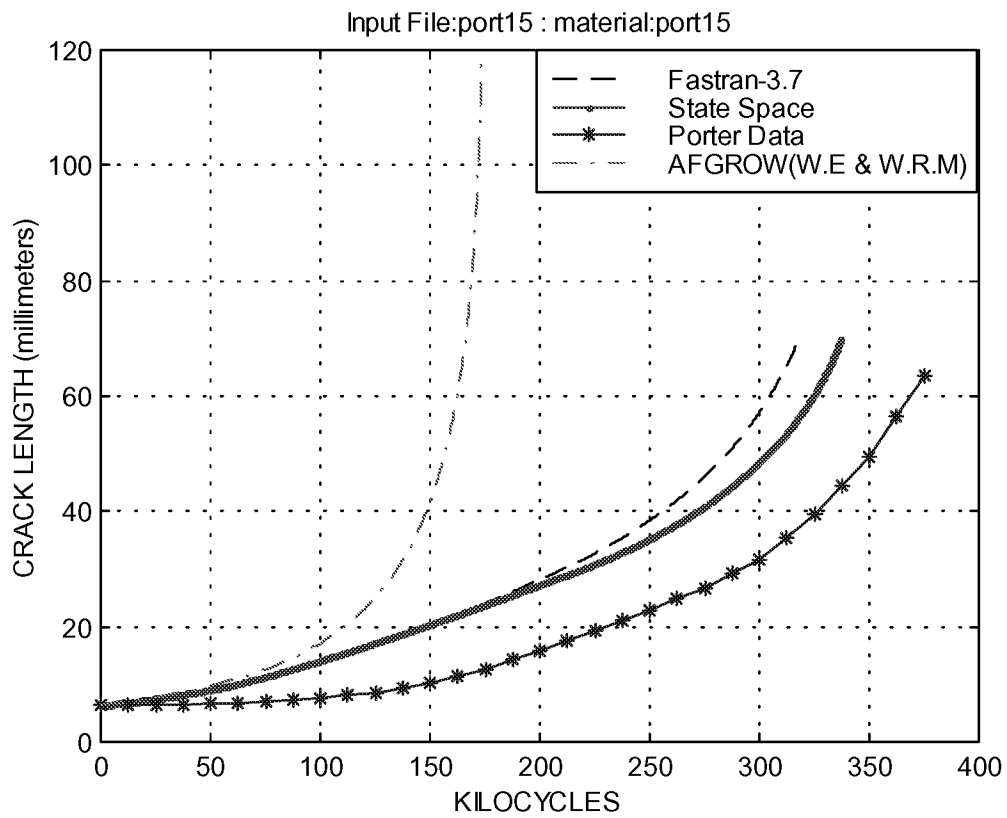
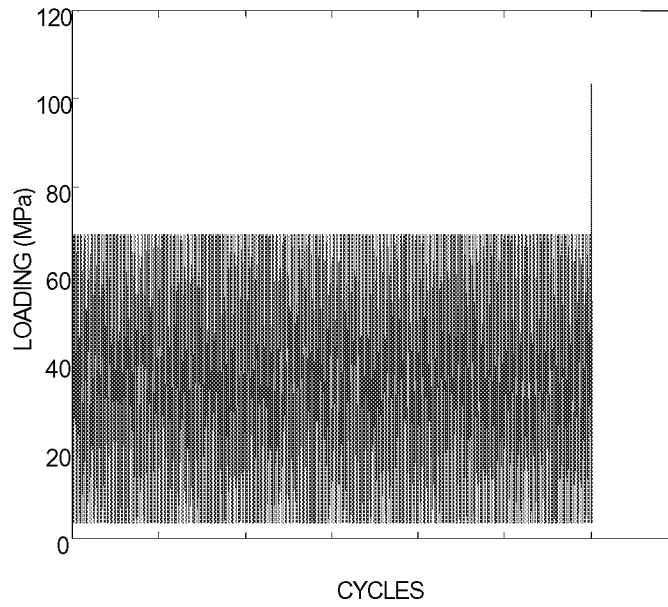


Figure A-30. Porter Program P15.

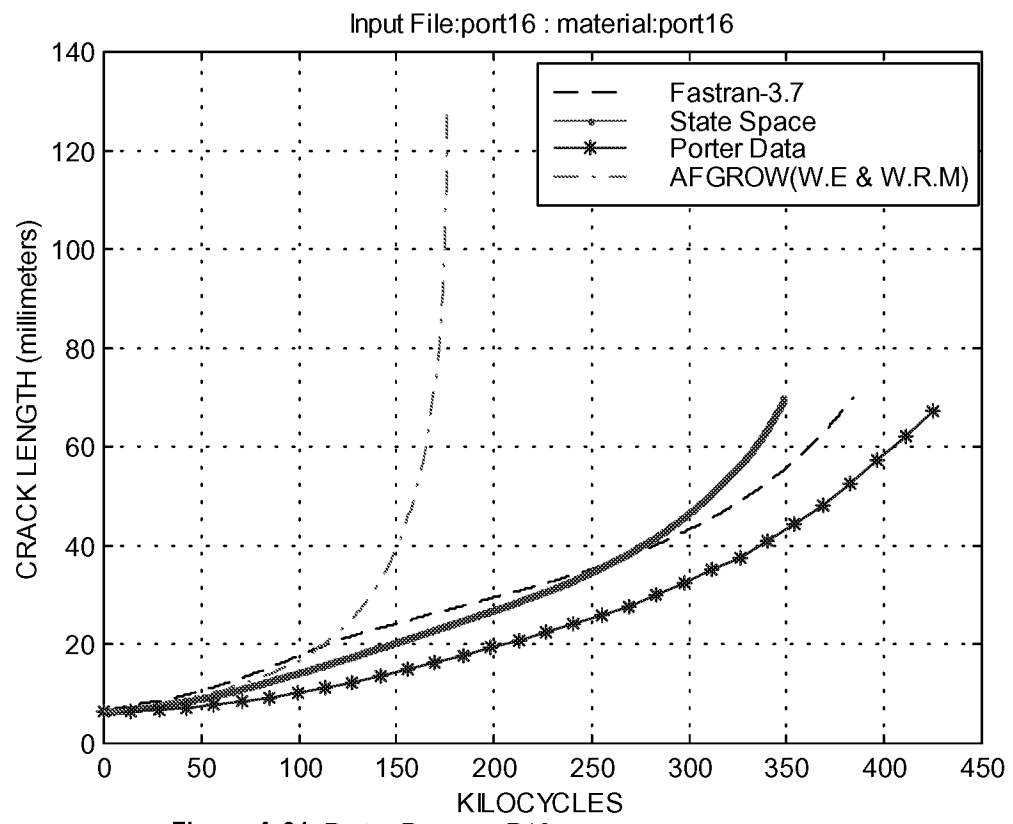
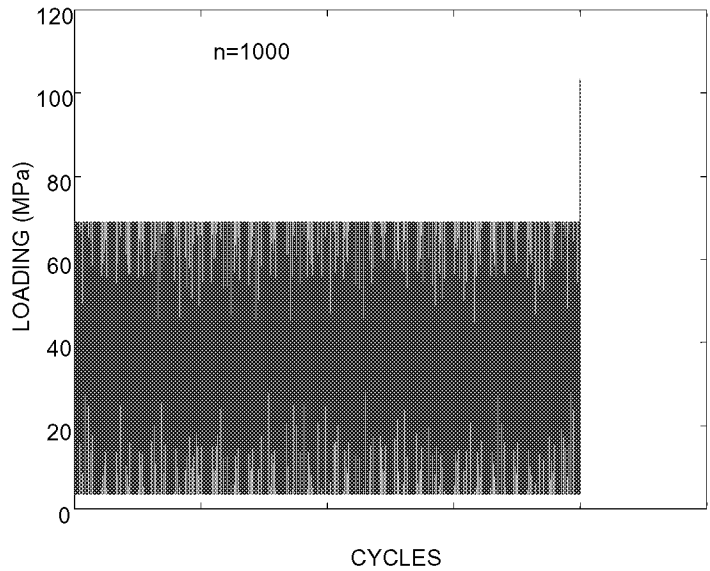


Figure A-31. Porter Program P16.

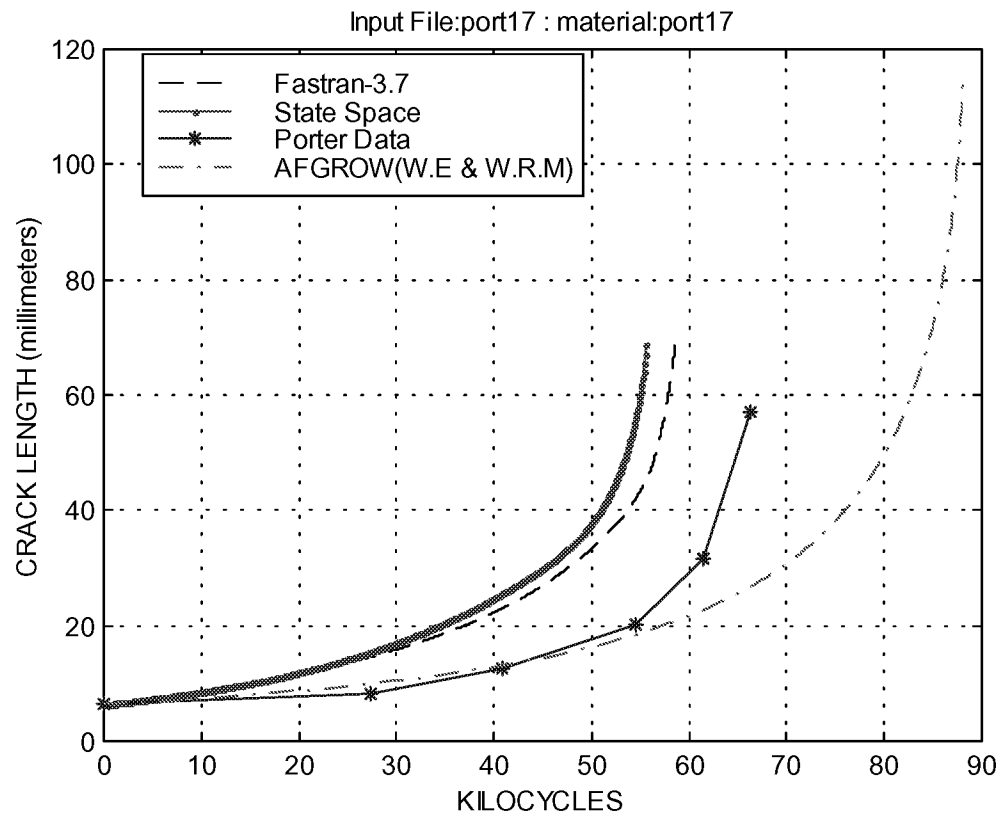
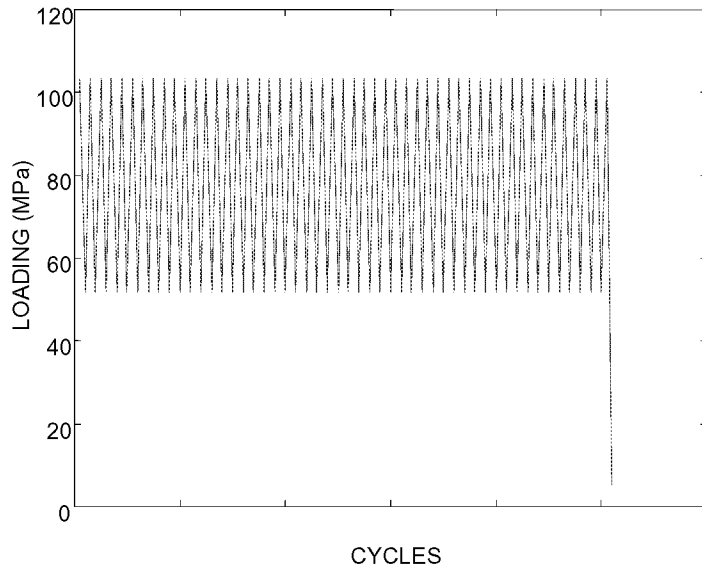


Figure A-32. Porter Program P17.

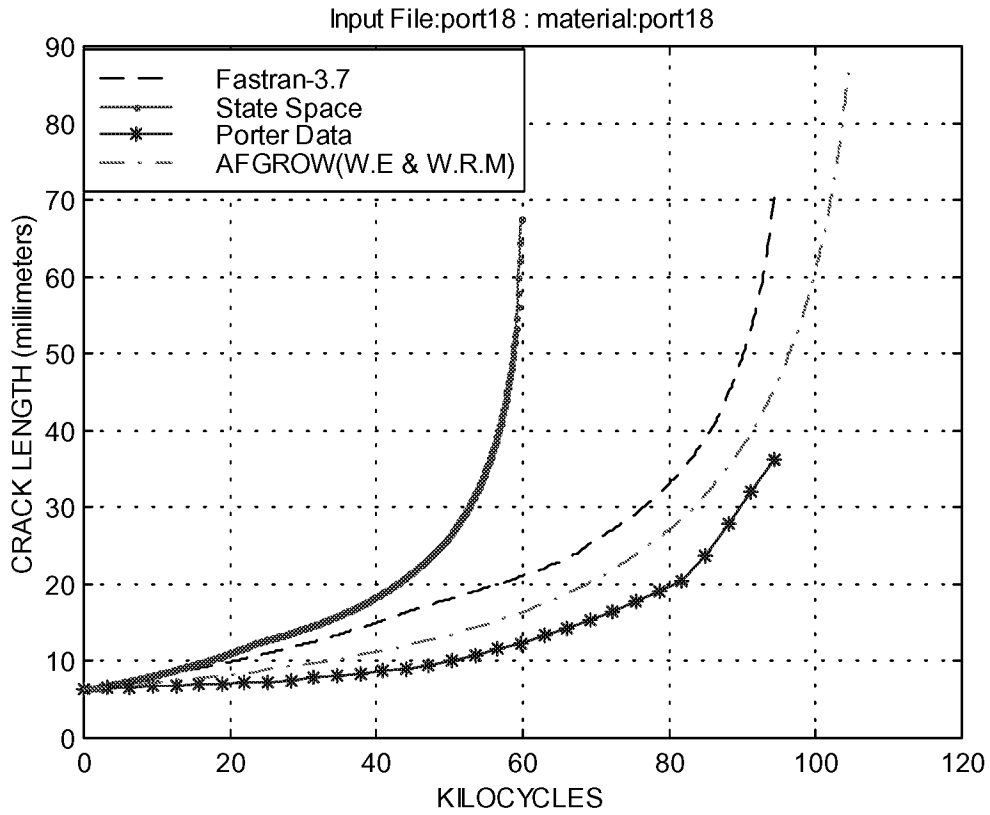
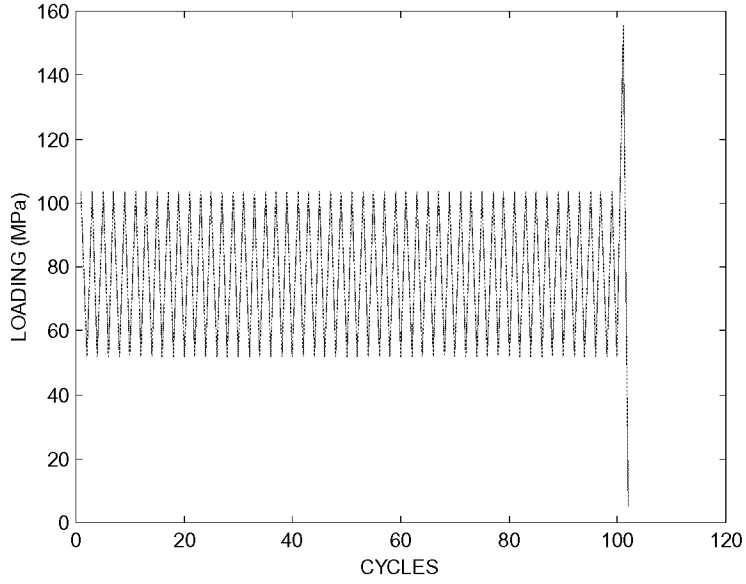


Figure A-33. Porter Program P18.

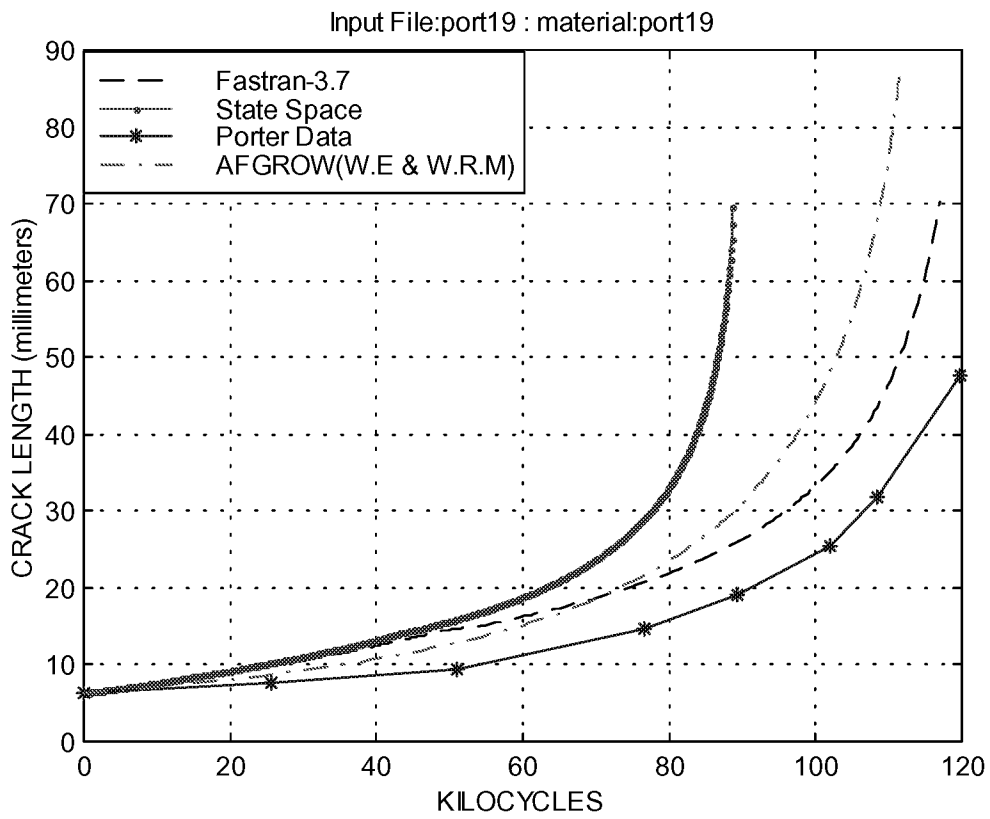
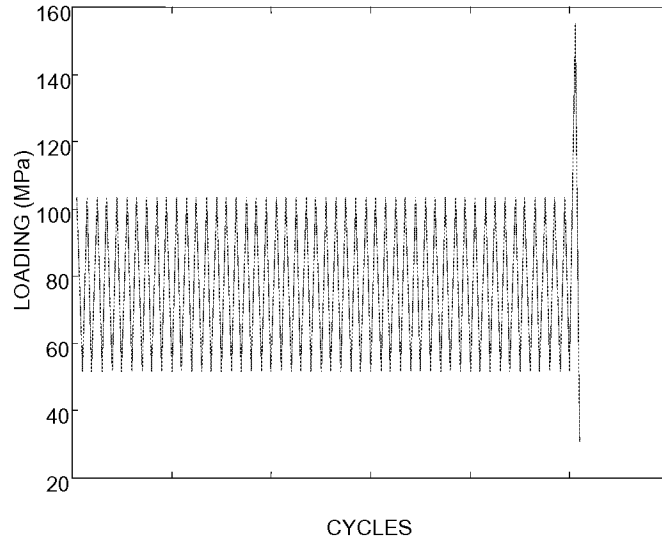


Figure A-34. Porter Program P19.

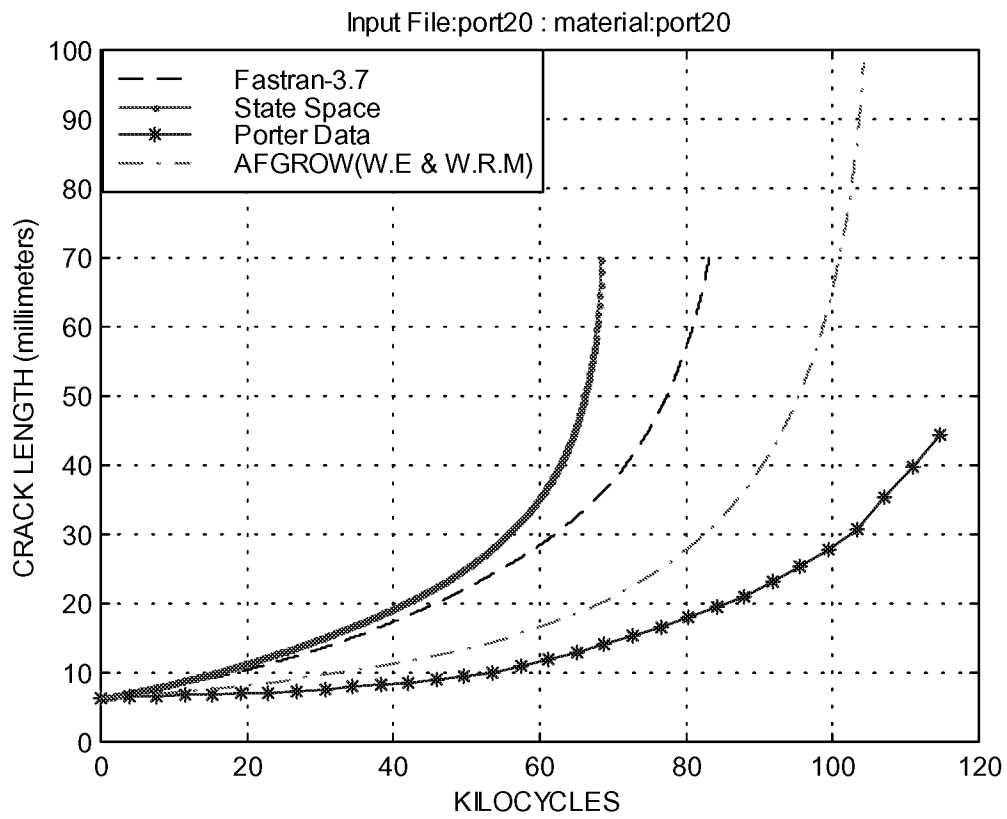
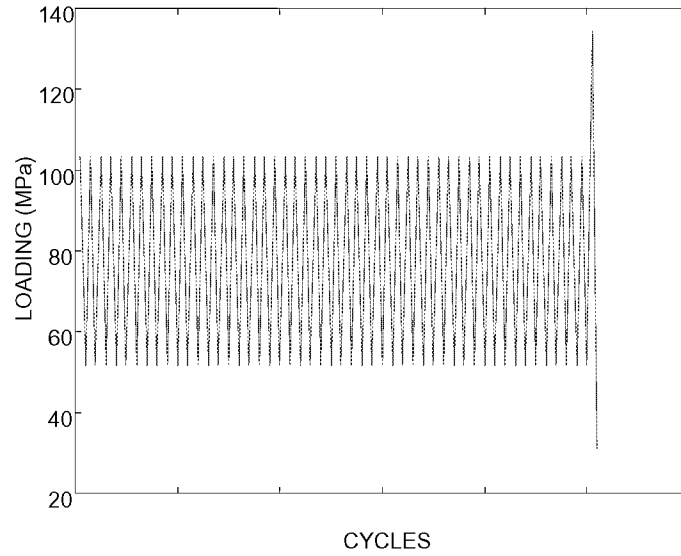


Figure A-35. Porter Program P20.

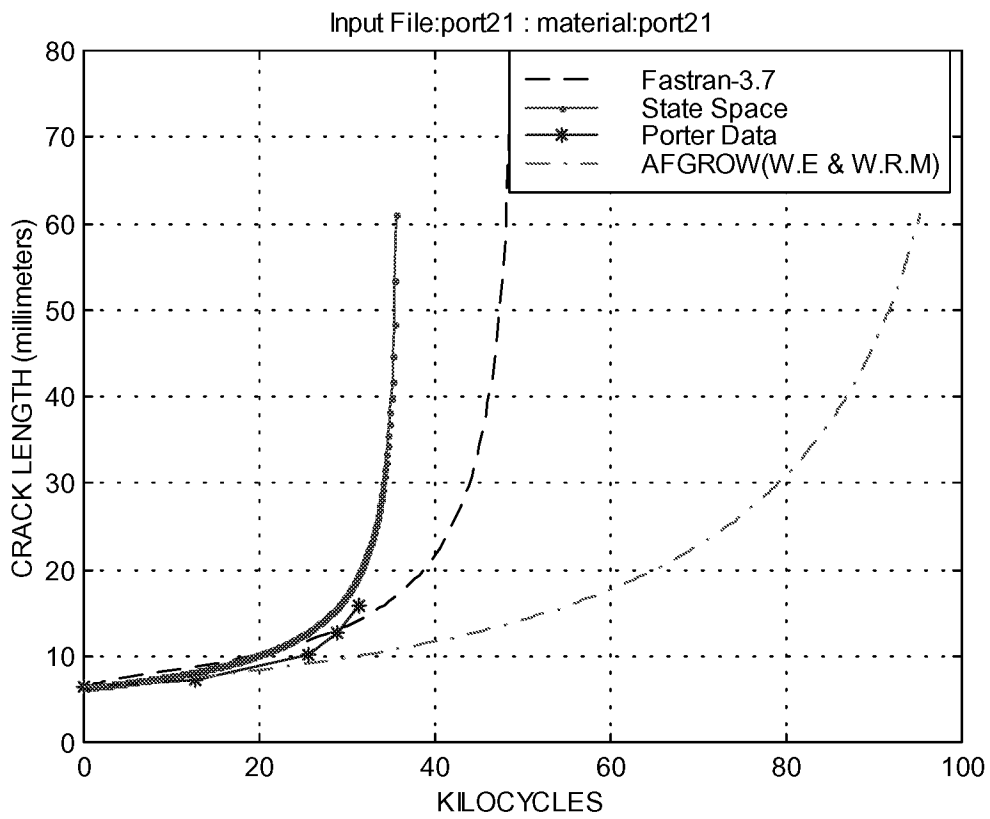
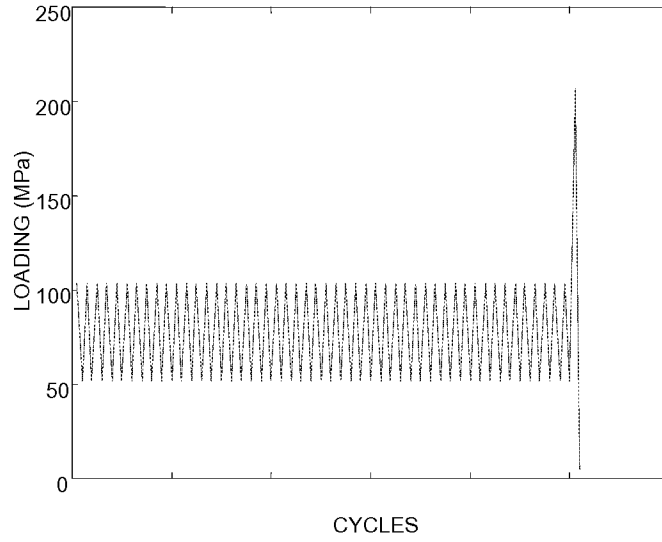


Figure A-36. Porter Program P21.

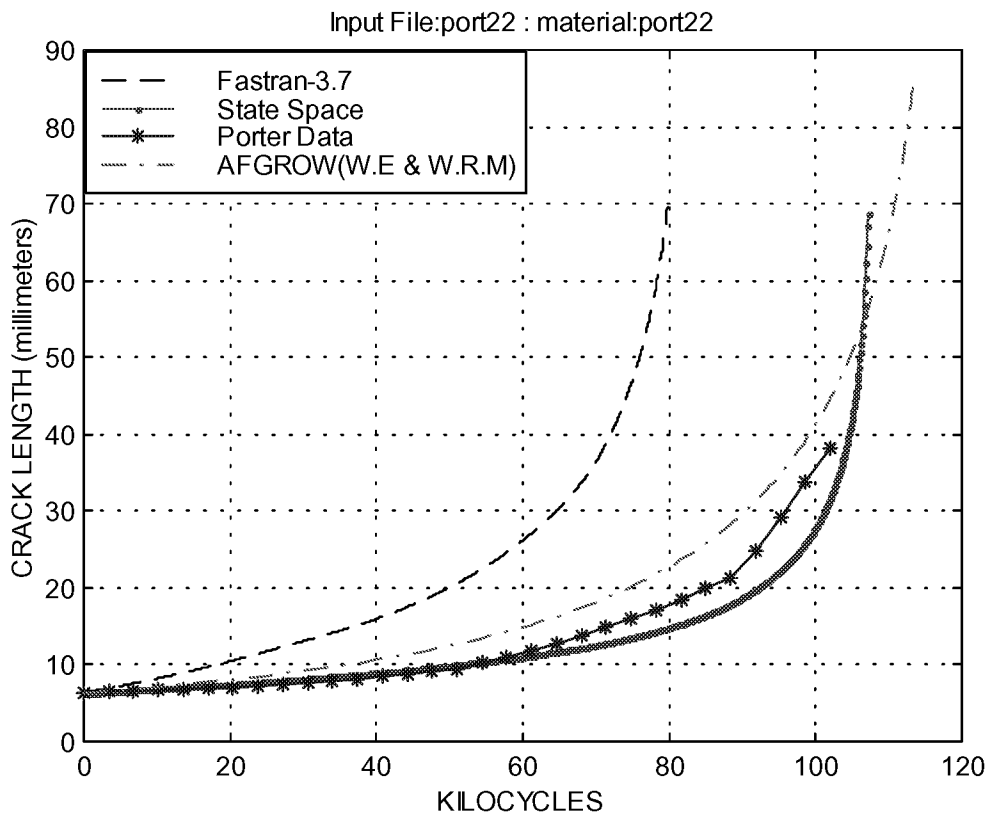
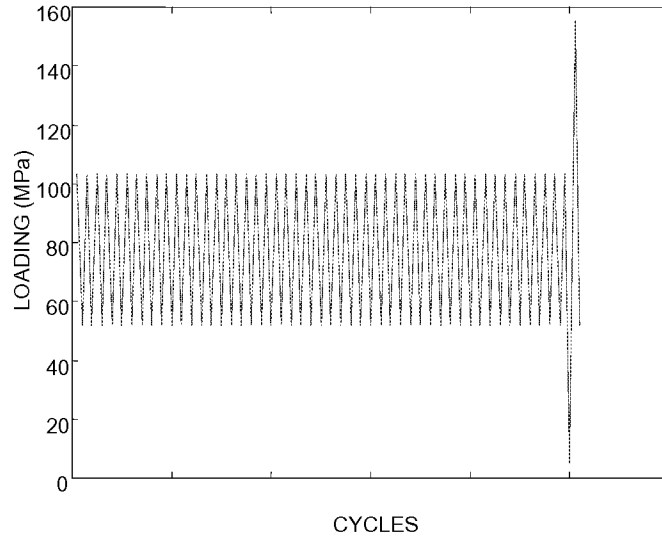


Figure A-37. Porter Program P22.

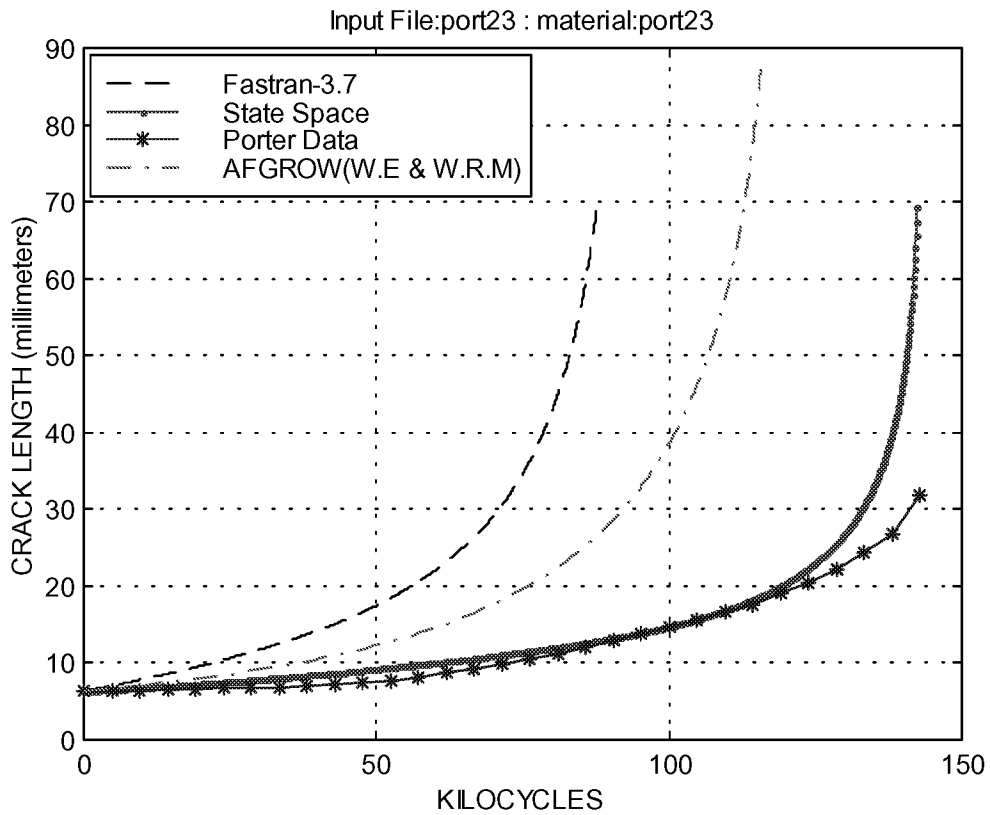
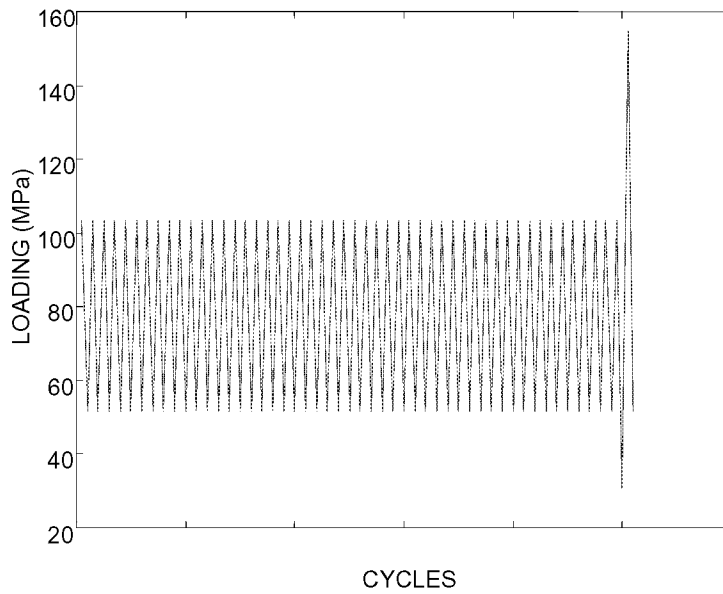


Figure A-38. Porter Program P23.

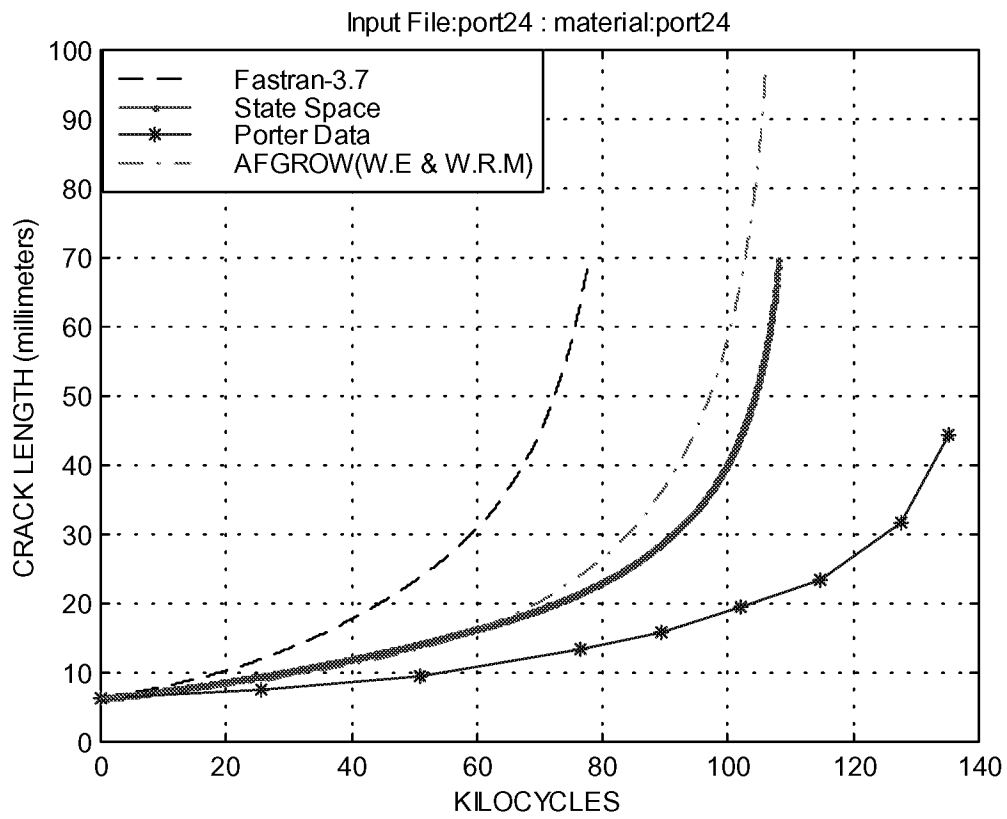
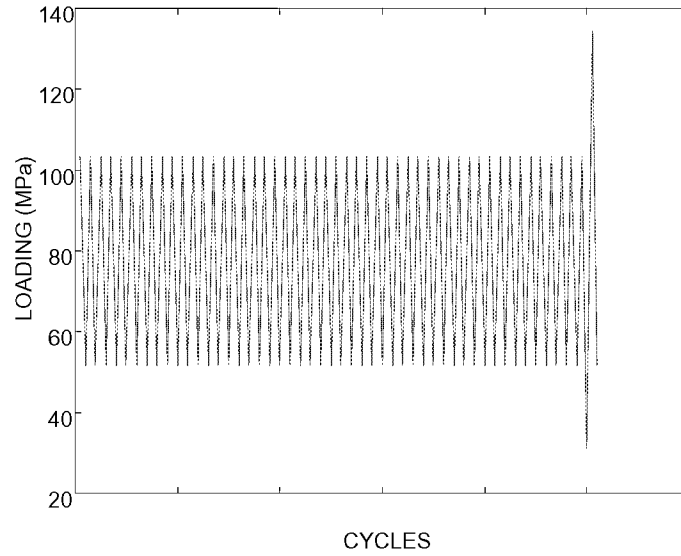


Figure A-39. Porter Program P24.

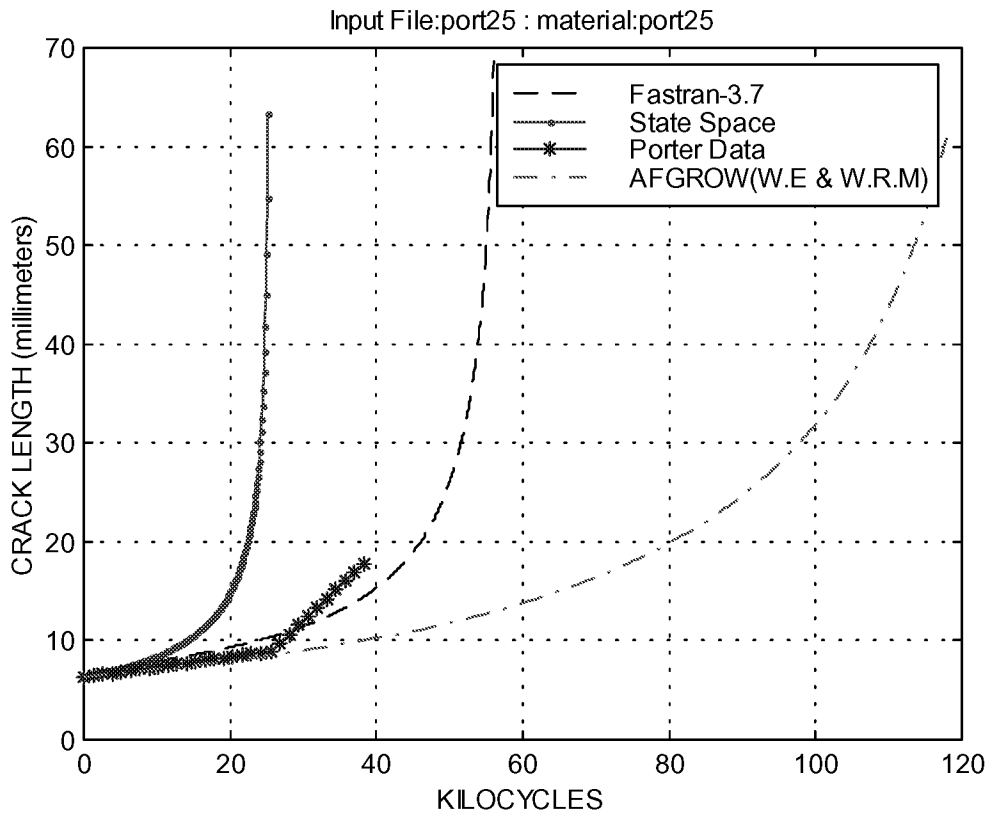
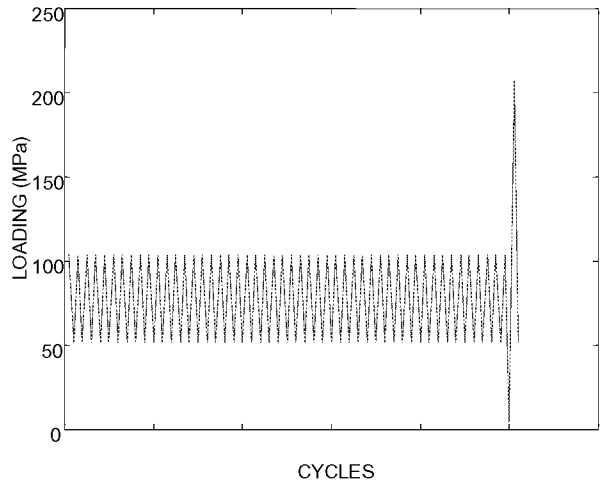


Figure A-40. Porter Program P25.

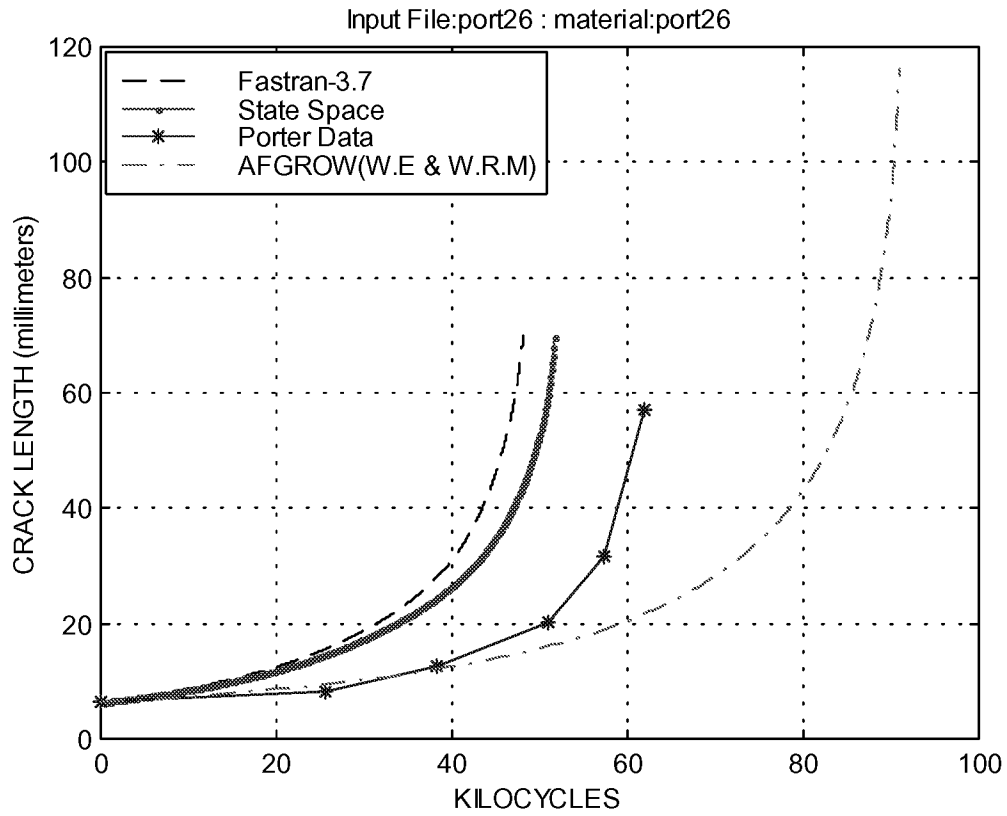
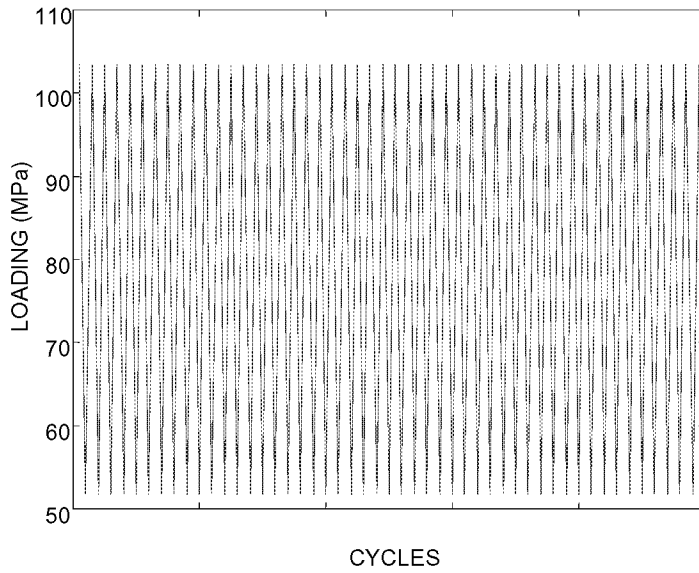


Figure A-41. Porter Program P26.

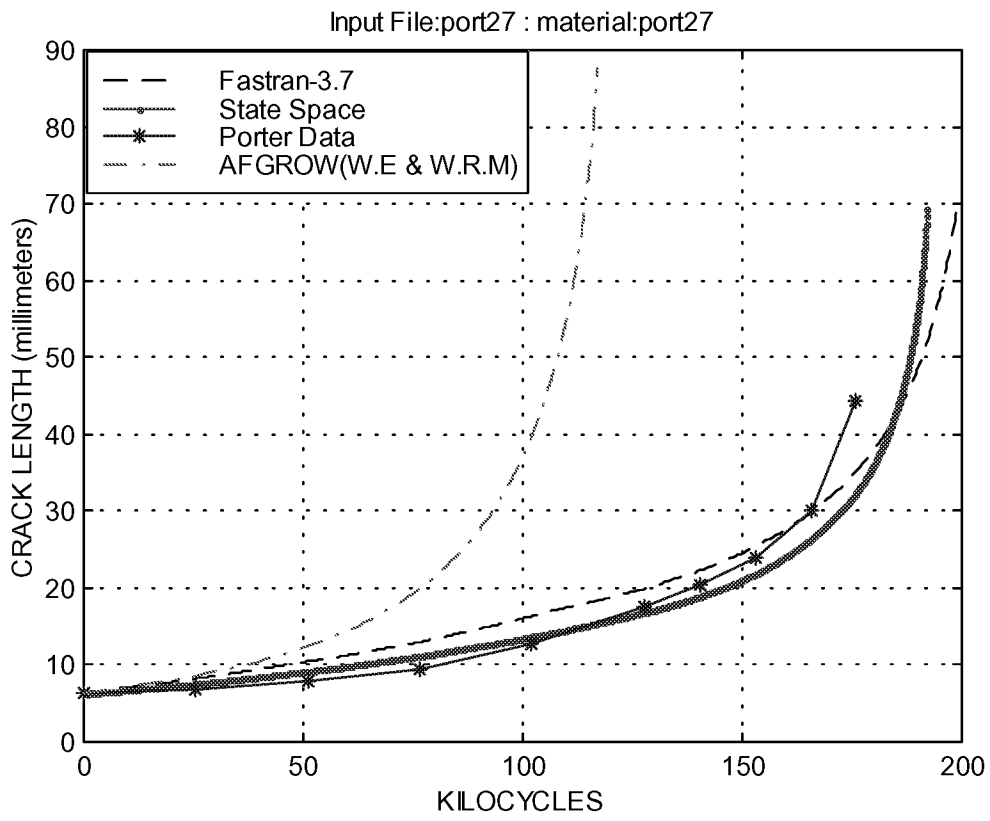
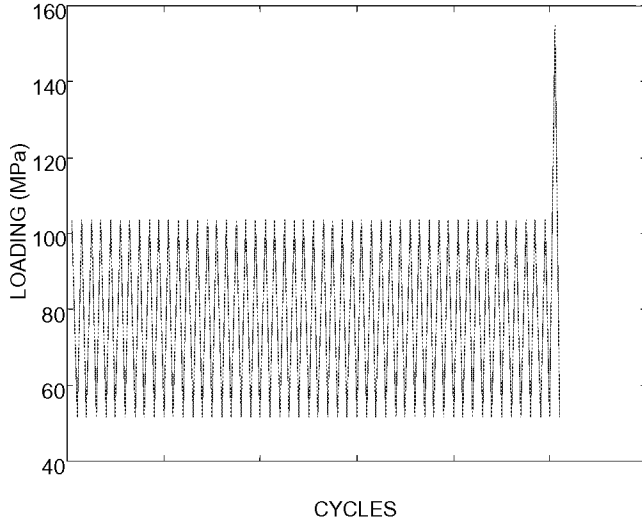


Figure A-42. Porter Program P27.

